THE UNIVERSITY of ADELAIDE

Application of Rotating Fluidized Bed to Solar Gasification

Zhao Lu

The School of Mechanical Engineering

The University of Adelaide

South Australia, 5005

A Thesis Submitted in Fulfilment of the Requirements for the Degree of Doctor of Philosophy

December 2018

Abstract

The development of sustainable energy technologies such as Concentrated Solar Thermal (CST) is attracting growing attention. One of the applications of CST technology is solar thermal gasification of carbonaceous feedstocks. This thermochemical process combines a gasification agent, either steam or CO_2, with widely available carbonaceous feedstocks to produce a useful mixture of H_2 and CO, commonly known as syngas. Syngas can be burned directly in power generation cycles to produce electricity or used as a chemical feedstock in the Fischer-Tropsch process to produce hydrogen based chemicals.

The present thesis reports the development of a directly irradiated solar receiver concept termed Rotating Fluidized Bed Receiver (RFBR) for solar thermal gasification. The RFBR concept involves rotating a cylindrical cavity containing feedstock particles about its axis of symmetry and injecting a radially inward gas flow through the porous cylindrical wall. The centrifugal acceleration generated through rotation forms an annular particle bed on the cylindrical wall for solar radiation absorption, and the radially injected gas flow fluidizes the particle bed with a drag force that counters the centrifugal force acting on the particles.

A comprehensive analytical model was developed to track the movement of a single biomass char particle undergoing gasification in the RFBR under typical solar receiver conditions. The analytical assessment found that: the particle residence time was highly dependent on the rate of particle gasification; the centrifugal force generated through rotation could effectively retain char particles in the receiver cavity until sufficient particle mass is lost to gasification conversion. It was shown that operating the RFBR at a rotational

speed of 70 rad/s or greater could result in gasification conversion extents greater than 85% for char particle sizes between 100 and 450 microns.

A CFD analysis of the flow field in the RFBR concept was also conducted to determine the effects of control parameters such as receiver rotational speed and velocity of the radially injected gas on the propensity of particles depositing on the receiver window and investigate the aerodynamic mechanisms involved. The analysis found the receiver rotational speed to be the most effective parameter in preventing entrained particles from entering the receiver aperture and depositing on the window. Operating at a relatively low rotational speed of 42.1 rad/s could limit the rate of particle deposition on the window to 0.25 % of the injected 10 μm diameter particles, which is comparable to the deposition rate in other solar receivers.

Lastly, an experimental campaign was conducted to investigate the fluidization characteristics and bed surface profile in a non-reacting rotating fluidized bed (RFB) which is integral to the RFBR concept. It was found that at relatively low rotational speeds between 21 rad/s (200 RPM) to 31 rad/s (300 RPM), there was insufficient centrifugal force to create a uniformly distributed annular bed in the investigated vertical RFB. The greatly varied radial bed thickness in the axial direction led to highly non-uniform fluidization quality. A bed redistribution procedure was devised to redistribute the bed particles and reduce the variation in radial bed thickness prior to low rotational speed fluidization. The implementation of this redistribution procedure was observed to significantly improve the uniformity of radial bed thickness and fluidization quality. This confirmed that the RFBR could be operated at relatively low rotational speeds that are unlikely to introduce excessive mechanical energy loss or component wear.

Declaration

I certify that this work contains no material which has been accepted for the award of any other degree or diploma in my name in any university or other tertiary institution and, to the best of my knowledge and belief, contains no material previously published or written by another person, except where due reference has been made in the text.

In addition, I certify that no part of this work will, in the future, be used in a submission in my name for any other degree or diploma in any university or other tertiary institution without the prior approval of the University of Adelaide and where applicable, any partner institution responsible for the joint award of this degree.

I give permission for the digital version of my thesis to be made available on the web, via the University's digital research repository, the Library Search and also through web search engines, unless permission has been granted by the University to restrict access for a period of time.

I acknowledge the support I have received for my research through the provision of an Australian Government Research Training Program Scholarship.

Signed: 

Zhao Lu 11/12/2018

Acknowledgement

This thesis would not have been completed without the tremendous help and contributions from many people.

I would like to first acknowledge the exceptional support provided by my PhD supervisors, A/Prof. Maziar Arjomandi, Dr. Mehdi Jafarian and Prof. Graham 'Gus' Nathan, all of whom dedicated significant amounts of their time to guide me in my research and help me develop independent research skills. I would like to thank: Dr. Mehdi Jafarian for his invaluable expertise on developing numerical models; A/Prof. Maziar Arjomandi for his helpful research advice, motivational talks and infinite patience; and Prof. Graham 'Gus' Nathan for his immense knowledge of all things related to solar energy technologies.

Secondly, I would like to acknowledge the generous support provided by Dr. Alfonso Chinnici, Dr. Zhao Tian and the staff of Mechanical and Electrical Engineering Workshops. Their advice and efforts contributed significantly to this thesis. To them, I express my heartfelt thanks.

I would also like to thank my friends and colleagues at the University of Adelaide. They made the whole journey more enjoyable and less stressful. I will always treasure our shared memories.

Last but not least, I would like to thank my parents, Jing and Ray for their continued support and encouragement. Without them, I would not be where I am today.

Nomenclature

Symbols

A	Area
C	Constant
D	Diameter
f	Ratio of volumes
F	Mass fraction of particles
g	Gravitational acceleration
L	Conventional fluidized bed height
n	Molar flow rate of species
N	Number of holes 10 cm^2
r	Radius
Re	Reynolds number
U	Fluid velocity
V	Wake volume in a conventional fluidized bed
X	Carbon conversion
Y	Segregation distance
ΔH	Change in enthalpy
ΔP	Change in pressure
ε	Fluidized bed void fraction
$\emptyset$	Sphericity of particle
ρ	Fluidizing gas density
μ	Fluidizing gas dynamic viscosity
θ	Bubble wake angle in a conventional fluidized bed
ω	Rotational speed

Subscripts

0	Location of the gas distributor in a conventional fluidized bed
b	Bubble in a fluidized bed
bed	Conventional fluidized bed
C	Carbon
CH_4	Methane
CO	Carbon monoxide
CO_2	Carbon dioxide
f	Fluid
fb	Location of the fluidization boundary
flo	Flotsam

i	Location of the inner bed surface in a rotating fluidized bed
jet	Jetsam
mb	Minimum bubbling
mf	Minimum fluidization velocity in a conventional fluidized bed
mfc	Critical minimum fluidization velocity in a rotating fluidized bed
mfi	Surface minimum fluidization velocity in a rotating fluidized bed
noz	Nozzle
o	Location of the gas distributor in a rotating fluidized bed
p	Particle
s	Solid
t	Particle terminal velocity
w	Bubble wake

Acronyms

CFD	Computational Fluid Dynamics
CST	Concentrated Solar Thermal
DAEM	Distributed Activation Energy Model
DPM	Discrete Phase Model
FV	Finite Volume
IPCC	International Panel on Climate Change
MC	Monte Carlo
PCM	Progressive Conversion Model
PV	Photovoltaic
RFB	Rotating Fluidized Bed
RFBR	Rotating Fluidized Bed Receiver
SCM	Shrinking Core Model

Table of Contents

List of Figures

Chapter 1

Introduction

1.1 Background and Motivation

The significant increase in the atmospheric concentrations of greenhouse gases has been linked to anthropogenic emissions and is suspected to be the primary cause for the increase in the global mean temperature which adversely affects the environment, biodiversity and global economy (Metz et al., 2005; Figueroa et al., 2008). The atmospheric concentration of CO_2, one of the main greenhouse gases, has risen sharply from 280 ppm prior to the industrial revolution to 405 ppm in 2017 largely due to the combustion of fossil fuels for energy production (He et al., 2011; Tans & Keeling, 2014; Dlugokencky et al., 2018). The atmospheric concentration of CO_2 is expected to increase further due to increasing energy demand and the subsequent increase in the consumption of fossil fuels. (Edenhofer et al., 2011). The US Department of Energy has estimated that the rate of consumption of fossil fuels would increase by around 27% in the next 20 years (Figueroa et al., 2008). It has been estimated that if the current trends continue, the world could become 4 ˚C warmer by the end of the century compared to pre-industrial levels (Peters et al., 2013). The consequences of this temperature rise would be very severe and affect the land use, water supply and agriculture of many nations (IPCC, 2007). To prevent these disastrous consequences, the rise in mean global temperature by the end of the century must not exceed 2 ˚C which corresponds to a maximum atmospheric concentration of CO_2 limit of 450 ppm(IPCC, 2007).

Therefore, it is imperative to develop novel energy technologies that could replace the established fossil fuel energy generation technologies and significantly reduce atmospheric CO_2 emissions. Renewable energy technologies based on solar, wind and hydropower offer great potential to reduce reliance on fossil fuels and meet the demand for clean energy (Edenhofer et al., 2011).

Solar energy technologies stand out amongst various available renewable energy technologies because the Sun is a vast and virtually unlimited energy source. It is estimated that the total amount of solar energy incident on the Earth's surface in one hour is sufficient to meet the energy demand of the entire humanity for one year (Lewis & Nocera, 2006). At the present, solar energy is either harnessed directly through Solar Photovoltaic (PV) panels or as process heat in Concentrated Solar Thermal (CST) systems. A major challenge associated with large scale solar energy utilization is its variable and intermittent nature (Saw et al., 2017). CST technologies are currently better positioned to overcome this challenge because they can be easily coupled with relatively cheap thermal energy storage or fossil fuel combustion hybrids technologies (Nathan et al., 2017). Moreover, it has been estimated that CST power plants are more economical than PV systems at locations with annual global irradiance higher than 1300 kWh/m^2 (Quaschning, 2004). In addition, CST technologies can involve high temperature thermochemical processes that produce dispatchable energy carriers which can be easily stored and transported to areas lacking solar resources (Steinfeld, 2005).

Solar driven steam gasification is an attractive thermochemical process (Figure 1.1) which converts steam and carbonaceous feedstock materials such as petroleum coke, coal and

biomass into a useful gas mixture consisting of H_2 and CO, commonly known as synthesis gas or syngas. The product syngas can be used in many applications including as the chemical source in the Fischer-Tropsch process for hydrogen, ammonia and methanol production or fuel feedstock in integrated power generation cycles. Compared to the conventional auto-thermal gasification process which relies on combustion to provide the process heat, the solar gasification process leads to higher purity syngas without combustion product gases (Steinfeld, 2005). As a result, the downstream impurity filtering process is simplified, and there is potential for reduction in capital investment. Furthermore, less carbonaceous feedstock is required in solar gasification to produce the same yield of syngas due to the elimination of combustion reactions. The product syngas derived from solar gasification is calorifically upgraded by an amount of solar energy equal to the enthalpy change of the reaction (von Zedwitz & Steinfeld, 2003; Saw et al., 2017). It has been estimated via a second law analysis that generating electricity using the syngas from solar gasification of petroleum coke has the potential to double the specific electricity output, and consequently, halving the specific CO_2 emission compared to petroleum coke fired power plants (von Zedwitz & Steinfeld, 2003; Trommer et al., 2005). For the above reasons, solar gasification has been gaining growing attention since the 1980s and continues to be a key area of solar energy research (Gregg et al., 1980; Baykara & Bilgen, 1985).

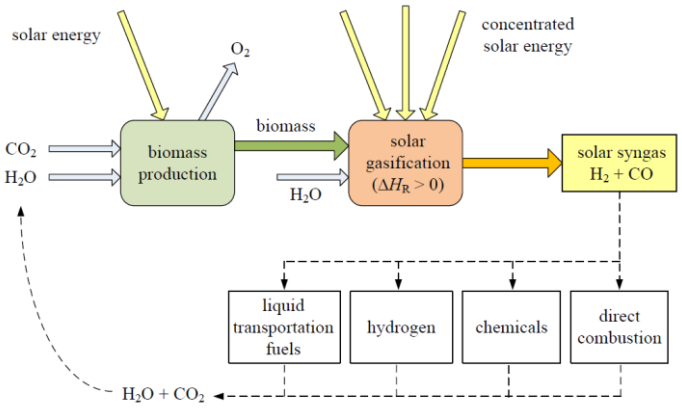

Figure 1.1: Exemplary solar steam gasification process using biomass as feedstock. Reproduced from Krusi (2014).

Owing to the geometrical distance between the Sun and Earth, the incident solar radiation on the Earth's surface is highly diluted. The maximum terrestrial solar irradiance is estimated to be around 1 kW/m^2 (Romero & Steinfeld, 2012). Thus, point-focus optical concentrator systems with high concentrating ratios (>500) are required to provide sufficiently concentrated solar radiative flux to drive the solar gasification process at a typical operating temperature above 1000 K (Steinfeld & Palumbo, 2003). For large scale CST systems, this is often achieved through a solar tower and a heliostat field (Figure 1.2a). The location of the solar receiver in which gasification occurs can be mounted on top of the tower in the beam up configuration. However, mounting the solar receiver on the tower imposes constraints on the size and weight of the receiver, reducing the ease of scalability (Krusi, 2014). Alternatively, the solar receiver can be mounted on the ground below the tower. Concentrated solar radiation from the heliostat field is reflected downward into the solar receiver via a secondary set of optics installed on the tower (Figure 1.2b). The beam

down configuration allows for more scalability and simplifies the tower design at the expense of reduced optical efficiency due to the secondary set of optics.

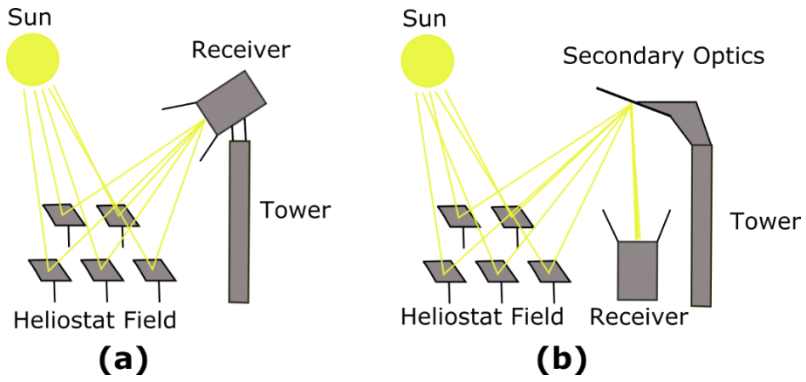

Figure 1.2: Solar tower configurations: (a) beam up with the receiver mounted on top of the tower and (b) beam down with the secondary optics on the tower and the receiver on the ground

The cavity-receiver configuration is particularly favoured for solar thermochemical processes because the absorption efficiency of the aperture approaches that of a black body absorber and the re-radiation heat losses through the aperture are relatively low compared to other receiver configurations such as the absorber tubes used in parabolic trough and linear Fresnel concentrator systems. (Steinfeld & Palumbo, 2003; Steinfeld & Schubnell, 1993). Concentrated solar radiative flux is passed through an aperture into the cavity to create the high temperature environment necessary for the thermochemical processes. The large volume to surface ratio of the cavity type configuration also ensures that less heat is lost through the receiver surface (Nathan et al., 2017).

The transfer of concentrated solar radiative heat to the gasification reaction sites in a cavity-receiver can be achieved through two methods; direct irradiation and indirect irradiation. Directly irradiated receivers are found to achieve higher reaction temperatures and faster reaction kinetics as well as lower exergetic losses due to the direct absorption of radiation

by the feedstock materials (Wu & Narayama, 1988). However, directly irradiated receivers require a transparent window to seal the aperture and prevent the leakage of gasification product gases. Maintaining the transparency and integrity of the window in the presence of feedstock particle clouds has been a major challenge to operating a directly irradiated receiver (Hirsch, 2005). There are also limitations to the size and mechanical strength of the quartz window that can be manufactured with current technology (Steinfeld, 2005; Nathan et al., 2017). The use of quartz glass window as the receiver window has been successfully demonstrated in lab scale receivers with auxiliary window cleaning gas injection (Steinfeld, 2005). Nevertheless, these auxiliary gas injection methods for window cleaning introduce thermodynamic inefficiency and dilute the gasification product gases, requiring additional downstream filtering steps (Kogan & Kogan, 2002). In addition, the mechanical strength of the quartz window at high temperatures limits the operating pressure inside the receiver. Therefore, scaling up lab scale directly irradiated receivers can be very complicated (Trommer et al., 2005).

Indirectly irradiated receivers generally contain two separate cavities for solar radiation absorption and gasification reactions. The absorbed solar heat is transferred between the two cavities through wall conduction. This physical separation removes the need for a transparent receiver window at the expense of decreased heat transfer efficiency due to the irreversibility associated with indirect heat transfer (Steinfeld, 2005). Furthermore, indirect heat transfer imposes stringent limitations on the properties of the receiver construction materials, including chemical stability, thermal conductivity, operating temperature, radiative absorptance, and resistance to thermal shock (Piatkowski et al. 2011)

Both directly and indirectly irradiated receiver configurations possess unique advantageous characteristics which have led to the development of a variety of solar gasification receiver concepts for a range of feedstock types and properties (Z'Graggen & Steinfeld, 2008; Melchior et al., 2008; Kodama et al., 2008; Piatkowski et al., 2009). The state of the art in solar receiver is briefly reviewed in the following section. It is worth noting that sometimes solar receivers are referred to as reactors due to the various thermochemical reactions that occur in their cavities. In the context of the present thesis, the terms, receiver and reactor, are used interchangeably.

1.2 State of the Art

1.2.1 Entrained Flow Receivers

The operation of entrained flow receivers relies on the entrainment of small pulverized feedstock particles in a flow of gasification agent, either H_2O or CO_2. For feedstock particles to be entrained effectively, they are required to have an effective hydrated diameter of less than 100 μm (Z'Graggen & Steinfeld, 2008). The residence time of particles in industrial scale entrained flow gasifiers ranges from 0.5 to 4 seconds (Van Eyk et al., 2013). To achieve high reaction extent in such short residence time, entrained flow gasifiers typically operate at temperatures above 1673K (1400 ˚C) (Basu, 2010). At these elevated temperatures, tar and oils are completely destroyed, and very high carbon conversion and low methane concentration are achieved (Basu, 2010).

A well-studied directly irradiated entrained flow receiver is the Solar Vortex Reactor termed SVR (Figure 1.3). It has been used to study intense radiation driven steam gasification of coal, coke and vacuum residue derived from the processing of crude oil (Z'Graggen &

Steinfeld, 2008). The reactor employs a vortex flow to increase the gas-solid slip velocity and enhance heat transfer as well as extend particle residence time. To keep the receiver window clean, an inert window cleaning gas such as argon was injected into the secondary concentrator volume through tangentially positioned purging nozzles. The lab-scale 5 kW SVR prototype was found to be capable of achieving a solar to chemical energy conversion efficiency of up to 9% and gasification conversion of up to 87% for dry coke feedstock particles with a mean diameter of 2.2 μm (Z'Graggen & Steinfeld, 2008).

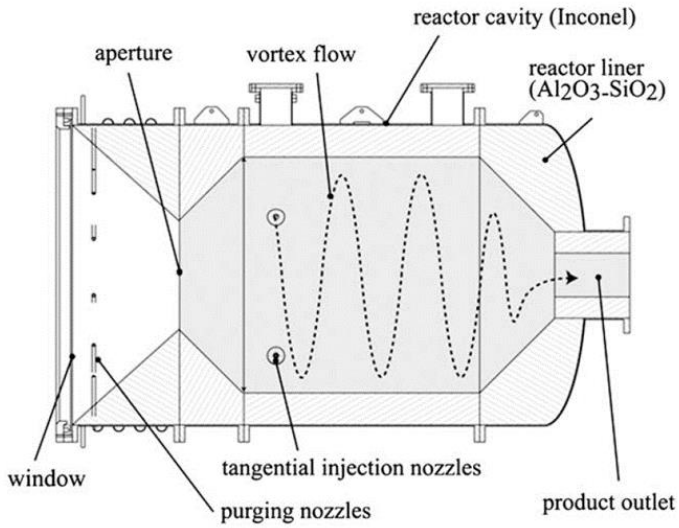

Figure 1.3: Schematic diagram of Solar Vortex Reactor for steam gasification of coke. Reproduced from Z'Graggen and Steinfeld (2008).

Chinnici et al. (2015) proposed the Solar Expanding Vortex Reactor termed SEVR (Figure 1.4) concept which utilizes aerodynamic mechanisms to prevent particle deposition onto the receiver window and reduce the flow of window cleaning gas. Experiments and Computational Fluid Dynamics (CFD) analysis were conducted to study the aerodynamic mechanisms responsible for particle deposition on the window and the precessing vortex core in the SEVR cavity (Chinnici et al., 2016; Chinnici et al., 2017). The cone angle and

the ratio of the vortex core to aperture diameters were found to be important parameters for mitigating particle deposition.

Kogan & Kogan (2002) proposed an entrained flow receiver concept (Figure 1.5) that utilized a small and fast vortex flow termed tornado flow to mitigate particle deposition onto the receiver window while maintaining low a flow rate of window cleaning gas. They estimated that the tornado flow design could reduce the window cleaning gas flow rate to as low as 5% of the mainstream flow rate as opposed to the 30-80% required by other entrained flow receiver concepts (Kogan & Kogan, 2002).

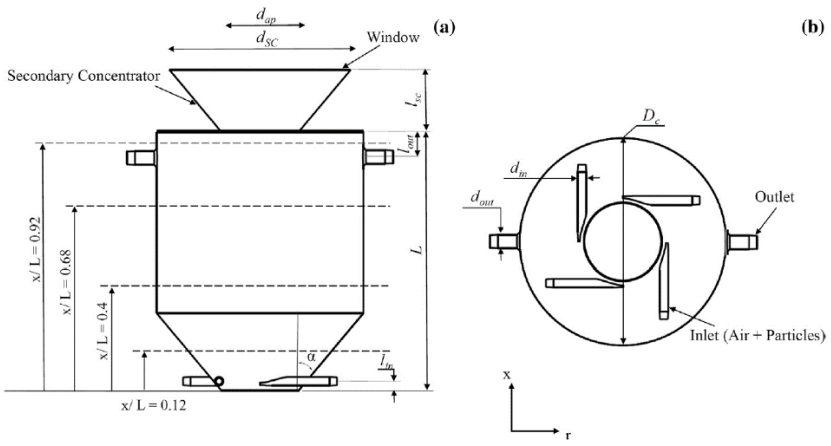

Figure 1.4: Schematic diagram of the Solar Expanding-Vortex Reactor, showing (a) a side view (b) and an end view. Reproduced from Chinnici et al. (2016).

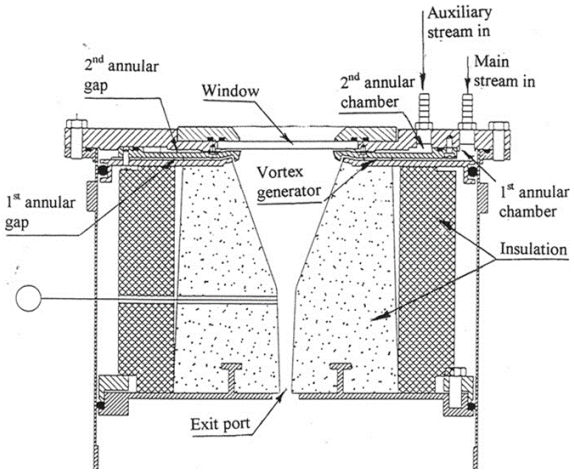

Figure 1.5: Tornado flow receiver for reduced particle deposition onto the window. Reproduced from Kogan & Kogan (2002).

For the indirectly irradiated configuration, various drop-tube entrained flow receiver concepts have been developed (Melchior et al., 2008; Lichty et al., 2010; Perkins et al., 2015). In a drop-tube receiver, the concentrated solar radiation is first absorbed by the absorber tubes, and then, transferred to the gasification agent and entrained feedstock particles via convection and tube wall radiation. The drop-tube receiver concept developed by Melchior et al. (2008) is shown in Figure 1.6. Numerical simulation of the continuous operation of the 3 kW prototype estimated the peak solar to chemical energy conversion efficiency to be 28% at 2300 K (Melchior et al., 2008). Re-radiation through the aperture and conduction through the absorber tube wall was found to be major contributors to heat loss.

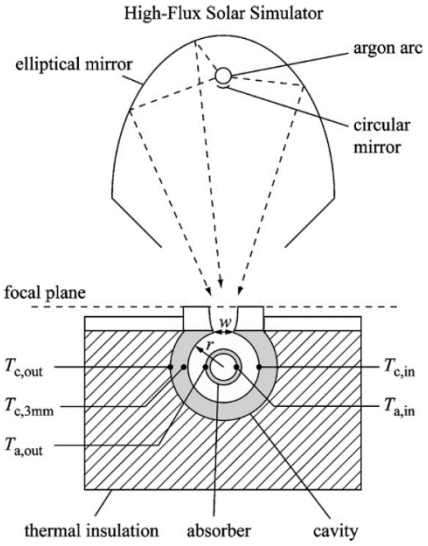

Figure 1.6: Schematic diagram of the indirectly irradiated drop-tube solar receiver. Reproduced from Melchior et al. (2008).

1.2.2 Packed Bed Receiver

In packed bed solar receivers, the feedstock particles are confined in a packed bed exposed to direct or indirect solar radiation. The gasification agent is blown through the bed to facilitate the gasification process and transport product gases. The residence time of in a packed bed receiver can be up to hours and as a result, very high gasification conversion extents can be achieved. However, the extended residence time may not be fully utilized as there are only limited hours of sunlight every day. Unlike entrained flow and fluidized bed receivers, there are no stringent constraints on the feedstock particle size and density. Thus, the cost of feedstock preparation is lower.

The packed bed receiver configuration suffers from poor heat transfer due to high extinction of radiation and relatively poor mixing within the bed (Piatkowski et al., 2009). The maximum flux of solar radiation that can be concentrated on a packed bed is severely limited by the rate of heat transfer from the surface to the bed volume. Hotspots and large

temperature gradients can appear and adversely affect receiver solar to chemical energy conversion efficiency if the solar flux is not carefully controlled. Trommer (2006) demonstrated that the rate of petroleum coke gasification could be significantly reduced if the coke samples are heated to temperatures higher than 1310K. The reduction in gasification rate was thought to be due to the reduction of pore volume and loss of total reactive surface caused by thermal annealing.

An indirectly irradiated packed bed receiver concept (Figure 1.7) for steam gasification has been developed by Piatkowski and Steinfeld (2008). This packed bed receiver concept consists of two cavities separated by an absorber/emitter plate. The first cavity absorbs concentrated solar radiation and directs the heat to the absorber/emitter plate which, in turn, passes the heat to the packed bed of feedstock materials in the second cavity through convection and radiation to drive the gasification process. The absorber/emitter has the main purpose of preventing the deposition of particles and condensation of gases on the receiver window. It has a secondary purpose of redistributing the concentrated solar flux more evenly onto the bed. Due to the relaxed requirements on feedstock size and properties, various carbonaceous feedstocks such as coal, beech charcoal, scrap tire powder and sewage sludges were experimentally tested in a 5 kW lab-scale prototype. A peak solar to chemical energy conversion efficiency of 29% has been achieved in the lab-scale prototype (Piatkowski & Steinfeld, 2008).

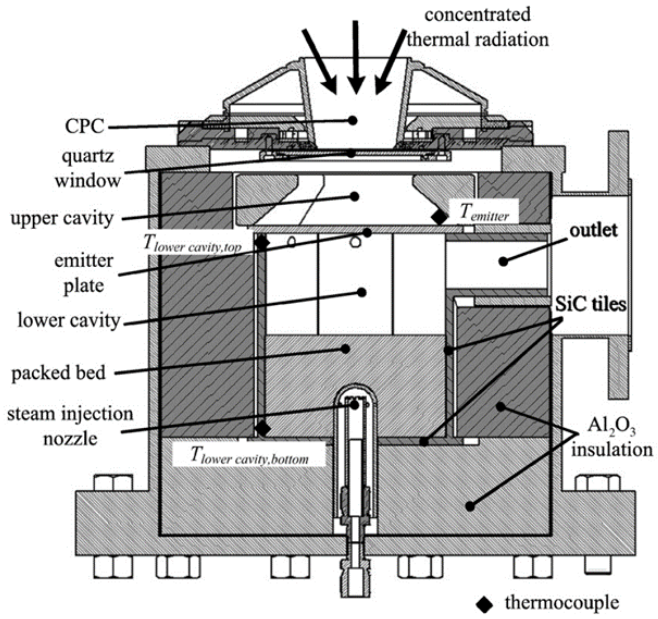

Figure 1.7: Schematic diagram of the indirectly irradiated packed bed solar receiver for steam gasification of carbonaceous feedstock. Reproduced from Piatkowski & Steinfeld (2008).

The packed bed configuration has been considered to be the most difficult to scale up. In laboratory scale prototypes, packed bed solar gasification reactors could easily operate in batch mode. However, on a large scale, the timely removal of hot waste materials and the addition of new feedstock pose great technical challenges (Taylor et al. 1983).

1.2.3 Fluidized Bed Receiver

Fluidized bed solar receivers share similar geometrical features to packed bed receivers. They are typically cylindrical and contain a bed of feedstock particles through which the gasification agent is blown (Gregg et al., 1980; Taylor et al., 1983; Kodama et al., 2008). The main difference between these two configurations is that the flow rate of gasification agent passing through a fluidized bed is sufficiently high for the fluid drag force on the particles to become equal or greater than the gravitational force that keeps the particles in the bed. These two almost equal but opposite forces suspend the bed particles in random,

turbulent motion, resulting in significantly increased gas-solid mixing and high rates of mass and heat transfer. As a result, the temperature within fluidized beds is often assumed to be uniform, and some heat transfer models for fluidized bed only consider the heat transfer between the first surface layer of particles and the external environment to be important (Chandran & Chen, 1982). The high flow rate of gasification agent also helps transporting product gases, ashes and feedstock impurities out of the bed. Thus, it is possible for fluidized bed solar receivers to operate in a continuous manner. The residence time of feedstock particles in a fluidized bed receiver depend entirely on the rate of gasification conversion and flow velocity of the gasification agent (Basu, 2010). Particles cannot leave the bed until they lose sufficient mass to gasification conversion and shrink to a sufficiently small size for entrainment by the gasification agent.

Kodama et al. (2008) have developed a directly irradiated internally circulating fluidized bed reactor for the CO_2 gasification of bitumous coal, as shown in Figure 1.8. A draft tube was installed in the centre of the cavity to create recirculation within the bed volume, which enhances mixing and improves bed temperature uniformity. A lab-scale prototype was constructed and tested using with 6 kW Xeon lamp. It was found that the concept could achieve a peak solar to chemical energy conversion efficiency of 12% for a total radiation input flux of 0.9 kW (Kodama et al., 2008).

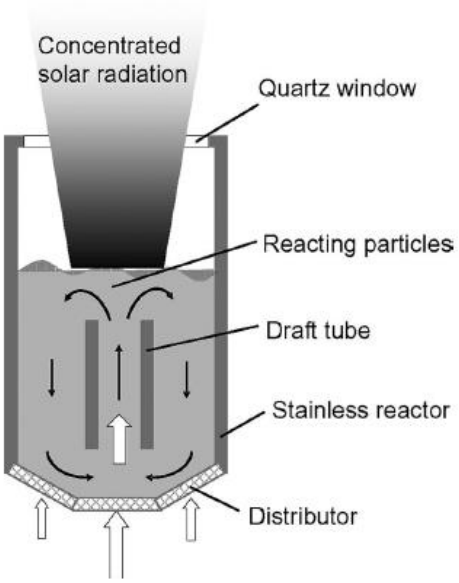

Figure 1.8: Schematic of the directly irradiated internally circulating fluidized in a beam down solar concentrating system. Reproduced from Gokon et al. (2012).

Kodama et al. (2008) reported observing fine coal ash depositing on the receiver window and finding a melted ash mass at the gas distributor, possibly spoiling the fluidization quality within the bed. This indicates that the directly irradiated fluidized bed concept also suffers from the problem of particle deposition on the receiver, and in addition, the input radiation flux is severely limited by the heat transfer rate between the bed surface and internal volume. Particle deposition on the receiver window can be largely resolved through injecting an auxiliary flow of window cleaning gas and increasing the distance between the bed surface and receiver window (Kodama et al., 2008). However, the limitation imposed on the input radiation flux is linked to the fluidized bed surface area and cannot be easily increased without scaling up the bed diameter. It should be noted that scaling up a fluidized bed is a complicated process requiring careful consideration of particle, gas distributor and bed properties (Yates & Lettieri, 2016). Changing the bed diameter affects the ratio of bubble

to bed diameters which could potentially result in a different upward flow pattern of the bubble phase and axial particle movement (Knowlton et al., 2005).

1.3 Rotating Fluidized Bed Receiver Concept

As highlighted in the previous section, the solar receiver is a key component in a solar gasification CST system. Its design and operation can heavily influence the system's energy conversion efficiency, product output, technical robustness, and commercial viability.

The present thesis proposes a new solar receiver concept termed Rotating Fluidized Bed Receiver (RFBR) which has the potential to address some of the common challenges faced by existing solar receiver concepts such as short residence time, poor gas-solid mixing, fine ash/particle deposition on the receiver window, and lack of bed surface area for solar radiation absorption.

A schematic diagram of the RFBR concept is shown in Figure 1.9. The RFBR consists of two sections joined together by a rotary seal. The upper section is stationary and contains the window, secondary concentrator, and tangential outlets. The lower section is a modified rotating fluidized bed (RFB) similar to the simple RFB shown in Figure 1.10 except that the exit port is expanded to match the diameter of the upper stationary section, and a screw feeder is added to the bottom surface of the RFB for the input of solid feedstock particles. The RFB porous cylindrical wall acts as a gas distributor and allows the gasification agent and fluidizing gas, H_2O to be fed into the receiver. The main reason for dividing the receiver into two sections is to minimize the weight of the rotating components and reduce the kinetic energy loss due to rotation.

The concept is oriented vertically for a beam down solar optical concentration system although it can also be used in a beam up system because the centrifugal force generated through rotation can be configured to greatly exceed the gravitational force. The beam down system is selected because it allows for more receiver weight and less complexity in scaling up the receiver structure. The RFBR is expected to be heavier than other receiver concepts due to the additional components required to rotate the lower section.

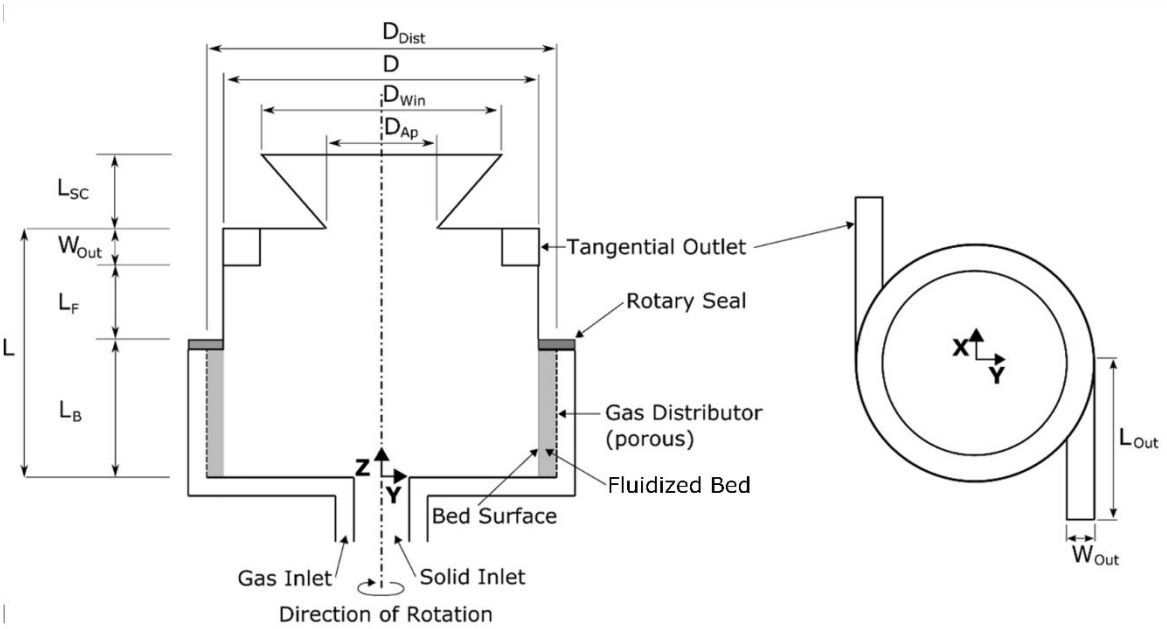

Figure 1.9: Schematic diagram of the Rotating Fluidized Bed Receiver concept.

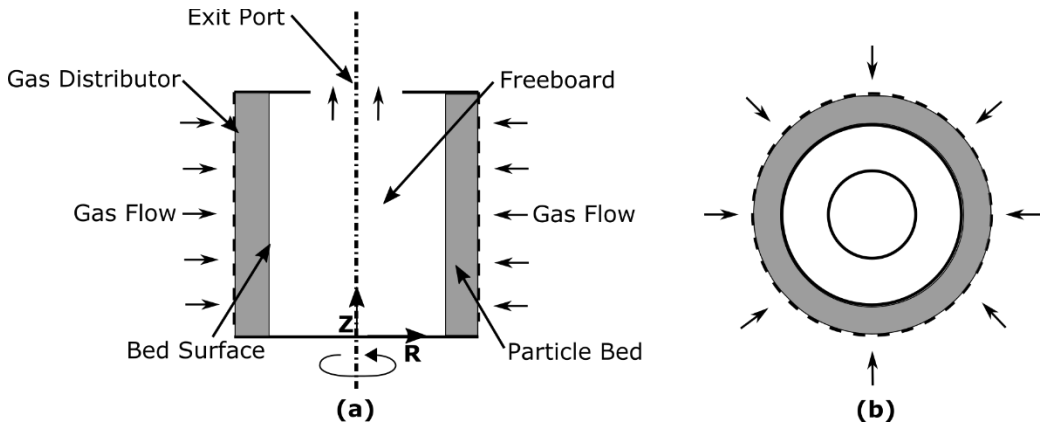

Figure 1.10: Schematic diagram of a simple rotating fluidized bed.

In operation, the rotation of the RFBR lower section generates a centrifugal force which moves the feedstock particles radially outwards away from the central screw feeder. These particles then build up at the cylindrical gas distributor and form a relatively thin annular particle bed. The fluidizing gas is injected radially inwards through the porous cylindrical gas distributor and imparts a fluid drag force on the particles in the bed. The forces acting on a particle in the lower section of the RFBR are shown in Figure 1.11. When the opposing fluid drag and centrifugal forces are approximately equal, the particle bed is minimally fluidized, and the particles within are suspended in random turbulent motion similar to the particles in a conventional fluidized bed receiver. The key difference here is that the centrifugal acceleration in the RFBR is adjustable through bed rotational speed unlike the constant gravitational acceleration in a conventional fluidized bed receiver. This additional control parameter offers more control over the balance of forces acting on the particles regardless of particle density and size. Consequently, the fluidization regime can be precisely shifted using both the fluidizing gas velocity and bed rotational speed. When the feedstock particles are gasified to a sufficiently small size, they are entrained out of the bed and receiver cavity by the flow of fluidizing gas.

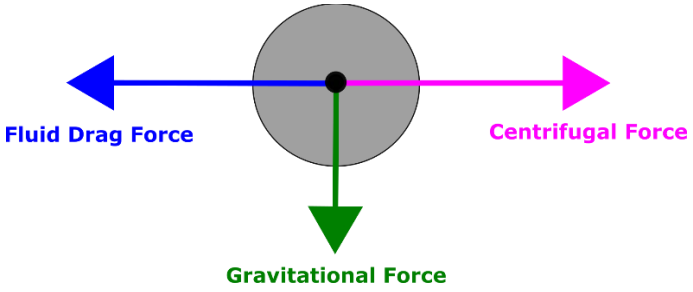

Figure 1.11: Forces acting on a particle in a vertically oriented rotating fluidized bed.

The potential benefits of the RFBR for solar gasification are as follows:

- The RFBR offers controllability over particle entrainment and elutriation from the bed because the centrifugal force acting on the particles can be adjusted through the bed rotational speed. Increasing the rotational speed has been shown to delay particle elutriation and reduce the size of elutriated particles in a non-reacting RFB (Saunders, 1986).
- The RFBR offers controllability over particle residence time and subsequently, gasification conversion because the centrifugal force can be increased to keep the particles in the bed for longer.
- The RFBR could potentially reduce the deposition of ash/particles onto the receiver window because the high speed rotation of the particle bed in the RFBR is expected to generate a high intensity vortex flow in the receiver cavity. Kogan & Kogan (2002) has demonstrated that a fast tornado flow in the receiver cavity can help mitigate particle deposition onto the window.
- The RFBR offers more bed surface area for solar radiation absorption than packed and fluidized beds due to the use of the cylindrical wall as the gas

distributor. This increased bed area could lead to more input radiation flux and higher gasification product output compared to conventional fluidized bed.

- The RFBR could potentially achieve higher mass and heat transfer rates than conventional fluidized bed due to increased gas-solid slip velocity which is determined by the adjustable centrifugal and fluid drag forces acting on the particles.
- The RFBR could be used to fluidize a wider range of particle sizes and densities than conventional fluidized bed because of the adjustable centrifugal force. Uniform fluidization of small cohesive particles, which cannot be fluidized in a conventional fluidized bed, has been demonstrated in a non-solar RFB (Qian et al. 2001).

It is important to note that the potential benefits listed above are based on speculation and conclusions from past studies in literature (Kroger et al., 1979; Chevray et al., 1980; Saunders, 1986; Chen, 1987). Whether these benefits are significant at realisable receiver operating conditions and whether they outweigh any associated negative effects on receiver performance require further investigation. For instance, the operating parameter, rotational speed, has favourable effects on various important receiver performance indicators such as residence time, conversion and elutriated particle size. However, it is not known whether these favourable effects are achievable at sufficiently low rotational speeds that do not incur excessive kinetic energy loss or component wear. Furthermore, the flow rate of the gasification agent is linked to the total bed surface area for radiation absorption. Increasing the solar exposure area and total flow rate could lead to increased product throughput in the

receiver for a given receiver size and capital investment. This capital intensification can reduce investment risks and yield greater returns. However, increasing the total flow rate also has the potential negative effects of causing more particle entrainment and possibly exacerbating the problem of particle deposition on the window. It is uncertain whether the benefit of the increased radiation absorption area outweighs the additional resources required to mitigate particle deposition.

1.4 Research Aim and Objectives

The overall aim of the current research is to develop the RFBR concept which offers potential benefits that could address many of the challenges faced by existing solar gasification receivers and improve the commercial viability of the solar gasification process. These challenges include extending particle residence time and gasification conversion, mitigating particle deposition on the receiver window and increasing the feedstock surface area directly exposed to concentrated solar radiation. However, since the RFBR is an entirely new concept, it is unclear whether these potential benefits are fully realisable under typical solar receiver conditions. Thus, a quantitative assessment of these benefits would need to be conducted, and a better understanding of the operation of the RFBR would need to be developed.

To achieve the overall aim, four objectives have been defined for the current thesis. These are as follows:

1. To identify suitable feedstock particle properties for the RFBR concept.
2. To evaluate the RFBR's potential in precisely controlling the particle residence time and gasification conversion.

3. To evaluate the RFBR's potential in mitigating the deposition of entrained particles onto the receiver window in a directly irradiated configuration.
4. To develop an understanding of the particle bed surface profile and fluidization characteristics in the RFBR operating at relatively low rotational speeds that are unlikely to introduce excessive kinetic energy loss or component wear.

1.5 Thesis Outline

Chapter 1 introduces the RFBR concept and the motivation behind its development.

Chapter 2 provides an overview of the studies concerning conventional and rotating fluidized beds as well as gasification with an emphasis on the gaps related to the mechanisms that could affect the operation of the RFBR.

Chapter 3 reports the development of an unsteady state single char particle gasification model used for the assessment of temperature and conversion of a single char particle undergoing solar radiation driven gasification in typical solar receiver environment.

Chapter 4 presents an analytical assessment of the RFBR concept's potential to increase particle residence time and conversion through varying key receiver operating parameters, namely bed rotational speed, initial feedstock particle size, radiation intensity, and particle release position.

Chapter 5 reports a Computational Fluid Dynamics (CFD) assessment conducted to investigate the potential benefits of the RFBR concept in reducing particle deposition onto the receiver window.

Chapter 6 presents the experimental investigation for examining the fluidization characteristics and bed surface profile in a low rotational speed rotating fluidized bed that resembles the lower section of the RFBR concept.

Chapter 7 concludes the key findings of the present research and provide recommendations for future work.

1.6 Publications Arising from this Thesis

The research presented in the current thesis led to the generation of four academic journal papers and one peer reviewed conference paper. These academic journals and conference proceedings are closely related to the field of research presented in the current thesis. The following list of manuscripts have been published or submitted for publication

1.6.1 Journal Articles

1. Lu, Z., Jafarian, M., Arjomandi, M. and Nathan, G.J., 2016, 'Particle-scale investigation of heat transfer in radiation-driven char gasification', Chemical Engineering & Technology, vol. 39, no. 10, pp.1903-1911
2. Lu, Z., Jafarian, M., Arjomandi, M. and Nathan, G.J., 2016, 'Analytical assessment of a novel rotating fluidized bed solar reactor for steam gasification of char particles', Solar Energy, vol. 140, pp.113-123.
3. Lu, Z., Chinnci, A., Jafarian, M., Arjomandi, M. and Nathan, G.J., 2018, 'Numerical investigation of the isothermal flow field and particle deposition in a rotating fluidized bed solar receiver', (Submitted to Solar Energy).

4. Lu, Z., Jafarian, M., Arjomandi, M. and Nathan, G.J., 2018, 'Fluidization characteristics in a low speed rotating fluidized bed', (Submitted to Experimental Thermal and Fluid Science).

1.6.2 Peer Reviewed Conference Article

1. Lu, Z., Jafarian, M., Chinnici, A., Arjomandi, M. and Nathan, G.J., 2017, June. Flow behavior inside a novel rotating fluidized bed for solar gasification of biomass. In AIP Conference Proceedings (Vol. 1850, No. 1, p. 110009). AIP Publishing.

In addition, the author of the present thesis contributed to the analysis and discussion of the results in the following journal article which is focused on extending the feedstock particle residence time in another novel directly irradiated solar particle receiver, termed Solar Expanding Vortex Receiver.

1. Chinnici, A., Arjomandi, M., Tian, Z.F., Lu, Z. and Nathan, G.J., 2015, 'A novel solar expanding-vortex particle reactor: influence of vortex structure on particle residence time and trajectory', Solar Energy, vol. 122, pp.58-75.

1.7 Thesis Format

The current thesis has been submitted as a portfolio of the aforementioned journal manuscripts according to the requirements of the University of Adelaide. Both the printed and online versions of the thesis are identical. The online version of the thesis is available as a Portable Document File, 'PDF' and can be viewed in its original format using Adobe reader 11.

Chapter 2

Literature Review

This chapter presents a review of previous studies relevant to the RFBR concept. Section 2.1 provides an overview of the gasification process and relevant models for predicting the gasification processes of various carbonaceous materials. Understanding the gasification process would allow for the development of a well-thought out approach to determining the residence time and gasification conversion in the RFBR concept. Section 2.2 presents some of the important fundamental studies on the fluidization characteristics in a conventional fluidized bed and commonly used governing equations for predicting particle transport and incipient fluidization conditions. Since conventional fluidized beds operate using similar principles to RFB's, the fundamental studies on conventional fluidized beds provide valuable insights into the possible fluidization conditions and characteristics in an RFB. Section 2.3 provides an overview of the development of the governing equations for an RFB as well as various aspects related to the current research, including bed surface profile and particle elutriation behaviour in an RFB. This is followed by a brief review of studies on solar gasification receivers in Section 2.4, with an emphasis on the modelling techniques that have been used to analyse existing solar receiver concepts. A summary of the gaps in literature related to the current research is included in Section 2.5, and the research objectives are presented in Section 2.6

2.1 Gasification

The gasification of carbonaceous materials such as biomass, coal and coke is a complex process involving a series of physical and chemical changes. There are usually three essential stages that occur inside a gasifier. These include drying, pyrolysis and solid char gasification.

2.1.1 Drying

Almost all pre-processed carbonaceous feedstocks contain moisture. Before the feedstock can be gasified, it is first heated to temperatures above 100 ˚C where the drying rate becomes significant. The requirements for drying vary greatly depending on the feedstock type. For instance, wood biomass particles contain free liquid water in the void space between wood cell structures, chemically bounded water in the hydroxyl groups of the wood solid constituent and water vapour within wood vessels and capillaries. The moisture content of freshly cut Pinus radiata wood biomass may range from up to 200% in the outer part of the stem to around 40% in the core part of the stem (Xu, 2013). In contrast, the moisture contents in coals are significantly lower but also show a sizable variation. For example, anthracite, bitumous and lignite coals have moisture contents in the ranges of 2.8% to 19%, 2.2% to 19% and 25% to 40% respectively (Xu, 2013). Similar to wood biomass, the moisture content in coal is also trapped in numerous places including pores and micro-capillaries within the coal particle volume, coal surface layer, crevices, and inter-particle void space (Karthikeyan et al. 2009). Therefore, removing moisture from feedstock is a complicated process requiring high energy input. If moisture is not reduced to a sufficient extent, the quality of the products in the subsequent pyrolysis and gasification processes may suffer

(Pang & Mujumdar, 2010). For instance, feedstock with high moisture content such as biomass may result in more condensable long chain hydrocarbons (tar) in the pyrolysis process (Demirbas, 2008). Drying at elevated temperatures can be a very fast process and thus, it is often integrated in the pyrolysis step. The moisture content in feedstock is sometimes treated as water vapour, a gasification agent, in gasification models (Bilbao et al., 1996; de Diego et al., 2002; Massaquoi & Riggs, 1983).

2.1.2 Pyrolysis

Pyrolysis begins when the feedstock reaches a temperature above 200 ˚C. At this point, the drying process is typically finished, leaving the solid feedstock almost free of moisture. Pyrolysis may involve hundreds of chemical processes which break up the chemical bonds in large organic molecules and polymers and form smaller hydrocarbon groups and other simpler molecules. The products of pyrolysis can be categorized into three different groups based on their state: permanent gases (H_2, CO, CO_2, CH_4, and H_2O), condensable gases (tar consisting of large hydrocarbons) and solid char (pure carbon with traces of other elements). The proportions of gases, tar and char depend heavily on pyrolysis temperature, heating rate and pressure. High temperature and heating rate typically favour the formation of lighter hydrocarbons (tar cracking) and lead to increased yield of permanent gases. Low temperature and long residence time generally lead to increased formation of solid char. Pyrolysis processes can be broadly categorised as fast or slow depending on the operating temperature. For the gasification process which requires solid char as feedstock, the pyrolysis process is often operated at a temperature above 700 ˚C which places it in the fast pyrolysis category (Xu, 2013).

Depending on the feedstock type, the pyrolysis process can be very difficult to model. Thus, simplified reaction mechanisms have been proposed in literature based on experimental data to approximate the products of the pyrolysis of coal, biomass and other feedstocks. These models are as follows:

- The simplest model is the one-component model which considers the solid feedstock as a single component (Solomon et al., 1988; Thurner & Mann, 1981). Gases, tar and char are produced from a one general reaction. Each species in the generated gases, tar and char is treated as an independent species with its own kinetics (Shafizadeh & Chin, 1977).

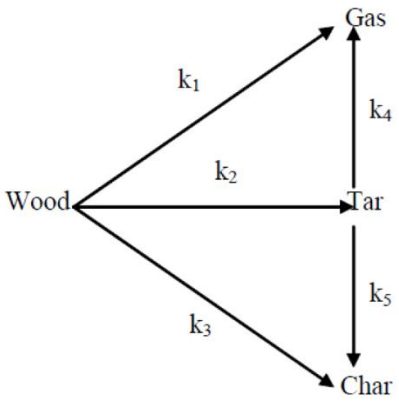

Figure 2.1: Pyrolysis of wood using the one component approach. Reproduced from (Shafizadeh & Chin, 1977).

- A more complicated model is the multi-component model which considers a multitude of reaction mechanisms in pyrolysis. For the pyrolysis of wood, main components such as cellulose, hemicellulose and lignin are treated independently with different reactions and kinetics (Helsen & Van den Bulck 2000; Orfao et al., 1999).

- The Distributed Activation Energy Model (DAEM) also considers multiple components. However, it utilizes a series of first order reaction kinetics for each element and compound in the generated species (Navarro et al., 2009; Please et al., 2003; Ulloa et al., 2004). The production of the generated species is proportional to the content in the feedstock from which it is generated. The reaction for the generation of each component species has corresponding activation energy and pre-exponential factor. This model has the advantage of calculating the reaction rate of each species generated at any time.

In terms of complexity, the one-component model is the simplest to implement, and the DAEM is the most complicated. While DAEM has shown good accuracy for low temperature slow pyrolysis, its accuracy is comparable with that of the one-component model for fast pyrolysis which often taken less than a second at elevated temperatures (Xu, 2013).

2.1.3 Char Gasification

After the feedstock material undergoes pyrolysis, the solid char can be gasified with CO_2 or H_2O to produce syngas which is a mixture of H_2 and CO.

Without combustion, the main gasification reactions are as follows (Higman & Burgt, 2008):

Water-Gas Reaction:

$$C + H_2O \leftrightarrow CO + H_2 \qquad \Delta H_{298K} = 131\ \text{kJ/mol} \qquad \text{Eq. 1}$$

Boudouard Reaction:

$$C + CO_2 \leftrightarrow 2CO \qquad \Delta H_{298K} = 172\ \text{kJ/mol} \qquad \text{Eq. 2}$$

Hydrogasification Reaction:

$$C + 2H_2 \leftrightarrow CH_4 \qquad \Delta H_{298K} = -75\ \text{kJ/mol} \qquad \text{Eq. 3}$$

Water-Gas Shift Reaction:

$$H_2O + CO \leftrightarrow H_2 + CO_2 \qquad \Delta H_{298K} = -41\ \text{kJ/mol} \qquad \text{Eq. 4}$$

Steam Reforming Reaction:

$$CH_4 + H_2O \leftrightarrow 3H_2 + CO \qquad \Delta H_{298K} = 206\ \text{kJ/mol} \qquad \text{Eq. 5}$$

In terms of heterogenous reaction rate, the Water-Gas Reaction is the fastest, followed by the Boudouard and Hydrogasification Reactions (Higman & Burgt, 2008). The Hydrogasification Reaction is sometimes neglected in gasification models because of its slow rate of reaction.

The homogenous Water-Gas Shift Reaction can be used to alter the ratio of CO and H_2 downstream of the gasification process to achieve the desired syngas quality.

2.1.4 Single Particle Modelling

Two commonly used idealised single particle modelling approaches for heterogenous gas-solid reactions are the Progressive Conversion Model (PCM) and Shrinking Core Model (SCM) as shown in Figure 2.2. The Progressive Conversion Model (PCM) assumes constant particle diameter and very fast diffusion rate of gas reactant into the particle compared to the rate of gas reactant being consumed by reaction. The concentration of gas reactant and rate of reaction everywhere in the particle are assumed to be uniform. The whole particle is

completely converted at the same time. The particle conversion rate is solely limited by the reactivity of the solid material. The Shrinking Core Model (SCM), on the other hand, assumes a lack of gas reactant in the unreacted particle volume and very fast reaction rate compared to diffusion rate. The heterogenous reaction is assumed to occur only on the surface of the gradually shrinking unreacted particle volume. For the gasification of materials with high inert material content, a spherical shrinking reaction front is formed within the particle between the reacted and unreacted volumes. For the gasification of petcoke, which contains very low content of inert material, the shrinking reaction front is on the particle surface.

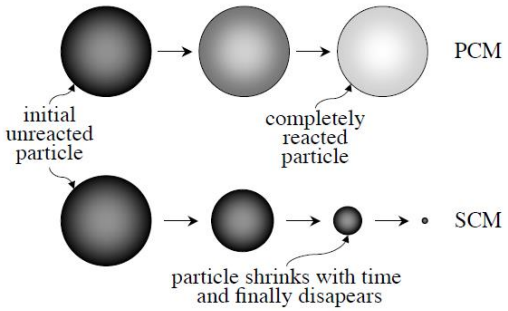

Figure 2.2:Schematic diagram demonstrating the PCM and SCM modelling approaches. Reproduced from (Trommer, 2006).

The SCM and PCM idealisations represent the two extremes of the reaction spectrum, namely diffusion and reaction kinetics limited regimes. In reality, most heterogenous reactions are situated between these two extremes and exhibit features of both. In literature, combinations of these two idealisations have been explored by various researchers.

Szekely and Evans (1970, 1971) developed the Grain Model for heterogenous gas-solid reactions (Figure 2.3). The Grain Model assumes that a solid reacting particle is an aggregation of smaller spherical particles of uniform size, termed grains (Figure 2.3). These

grains are assumed to be non-porous and heterogenous gas-solid reactions occur only on the grain surface. Essentially, each grain is treated as if it was a single reacting particle in the Shrinking Core Model. The diffusion of the gas reactant into the unreacted particle volume is dependent on the rate of gas reactant consumption by the grains. At high temperatures where the rate of consumption is high, the behaviour of the Grain Model approaches that of the Shrinking Core Model. Conversely, at low temperatures, more gas reactant can diffused into the unreacted particle volume, and the Grain Model resembles the Progressive Conversion Model. Kajitani et al. (2002) successfully employed the Grain Model to analyse the gasification of coal char particle in a pressurised drop tube furnace.

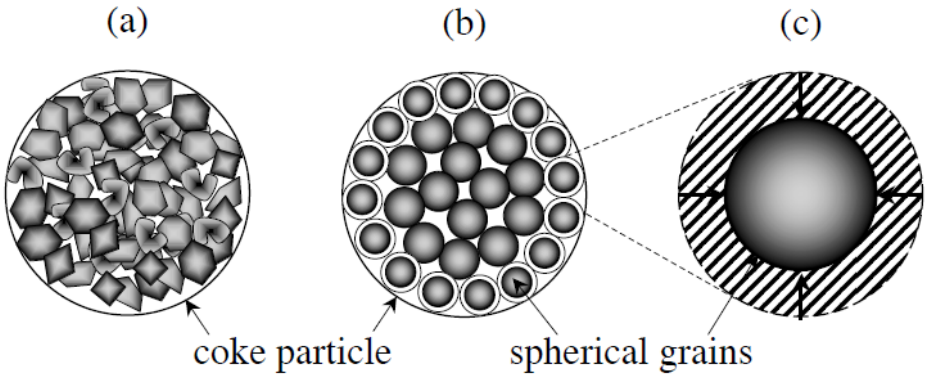

Figure 2.3: Schematic diagram of the grain model, showing (a) aggregation of grains that form a coke particle, (b) uniform grain size assumption and (c) Shrinking Core Model treatment of each grain. Reproduced from (Trommer, 2006).

Bhatia and Perlmutter (1980) proposed a Random Pore Model based on the assumptions that a reacting particle contains cylindrical pores of a distribution of sizes, and heterogenous gas-solid reactions occur on the internal surfaces of these pores (Figure 2.4). As the particle conversion progresses, the pores are enlarged by the consumption of solid material, and the internal reaction surface area is increased. This leads to an increase in reaction rate. When

the particle conversion is close to completion, some pores overlap and collapse, resulting in the loss of internal surface area and a decrease in reaction rate. The evolution of pore structure and variation of internal surface area with respect to conversion allow the Random Pore Model to predict the maximum reaction rate that has been observed in some experimental gasification studies (Dutta et al., 1977; Dutta and Wen, 1977).

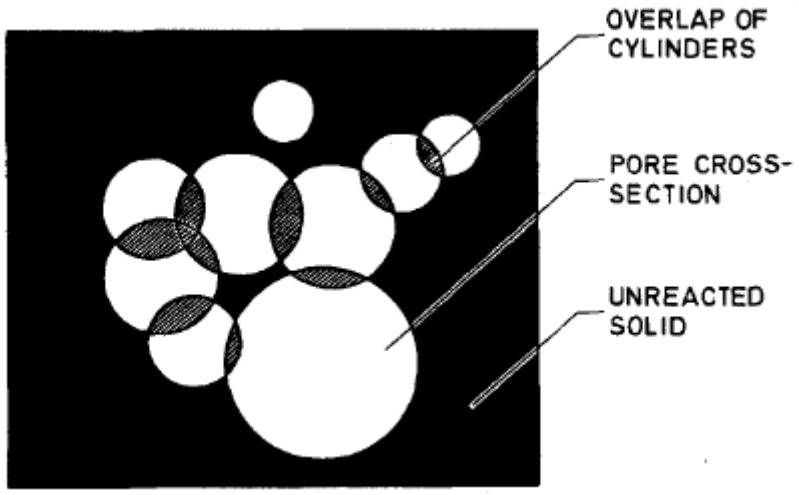

Figure 2.4: Schematic diagram showing the cylindrical pores in a reacting particle. Reproduced from Bhatia & Perlmutter (1980).

Wang and Bhatia (2001) developed a generalized model for single particle char gasification which takes into account the evolution of pores as well as peripheral fragmentation behaviour. The peripheral fragmentation behaviour was modelled using an experimentally determined critical porosity parameter for fragmentation. Mermoud et al. (2006) and Xu et al. (2011) adopted similar modelling approaches to investigate the steam gasification of wood char particles and biomass-coal blend char particles, respectively.

2.2 Conventional Fluidized Bed

Fluidized bed technologies have been an interest to researchers since the beginning of the twentieth century due to their advantageous heat and mass transfer characteristics which are particularly suited to heterogenous gas-solid reacting systems. The relatively high heat and mass transfer rates in fluidized beds enable excellent bed temperature and reactant concentration homogeneity. For this reason, many industrial chemical processes such as fluid catalytic cracking, gasification and combustion utilize fluidized bed technologies. The knowledge related to the fluidization characteristics in a conventional fluidized bed is useful to the development of the RFBR concept mainly because the two types of fluidized bed operate using similar principles. The following sections provide an overview of the fundamental conventional fluidized bed research.

2.2.1 Fluidization Regime

In a conventional fluidized bed, the feedstock particles are confined in a vertically oriented cylindrical vessel with a mesh or porous gas distributor as the bottom surface (Figure 2.5a). The fluidizing gas is injected through the gas distributor vertically upward, countering the effect of gravity. The balance of the fluid drag and gravitational forces keeps the particles in a semi-suspended condition and gives the particle bed fluid like behaviours. For instance, an object denser than the bed's bulk density would sink while another lighter object would float. In this semi-suspended state, the particles are well mixed with the gas forming a mixture termed "emulsion" which possesses high rates of mass and heat transfer between the gas and solid phases. If the fluidizing gas flow rate in the bed is too high, bubbles may form and cause particles to splash when they burst at the bed surface. Smaller particles

maybe elutriated out of the bed and entrained upward by the fluidizing gas. Some of these particles eventually fall back to the bed, and others escape through the vessel outlet. Most of the falling occurs in a zone denoted Transported Disengagement Height (TDH) (Basu, 2010). The general suspension density profile of the gas and solid suspension along the vessel height is shown in Figure 2.5b.

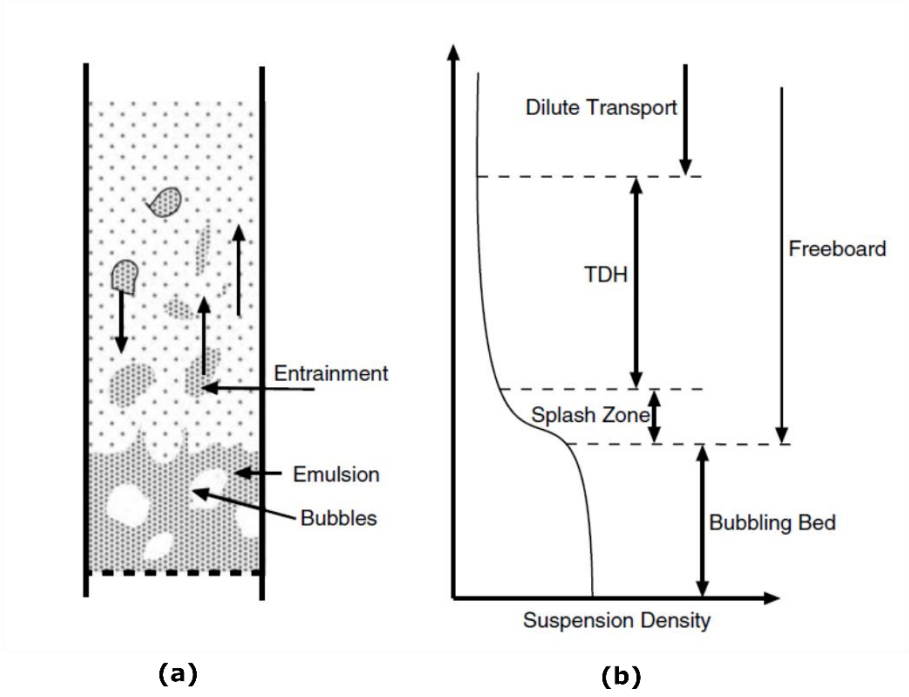

Figure 2.5: (a) schematic representation of a bubbling fluidized bed and (b) Suspension density along the bed height. Reproduced from Basu (2010).

Since the gravitational force acting on the particles is constant, increasing the fluidizing gas velocity leads to changes in the fluidization regime. Kunii & Levenspiel (2013) identified six main fluidization regimes each with its own unique characteristics (Figure 2.6).

Initially, the velocity of the fluidizing gas flow passing through the particle bed is very small. The drag force of the fluidizing gas on the particles is very small compared to the gravitational force. Most of the particles are stationary relative to each other, and the height

of the bed is the same as when there is no fluidizing gas flow. The particle bed is said to be in the fixed or packed bed regime (Figure 2.6a).

As the fluidizing gas velocity gradually increases, a point is reached where the drag force of the fluidizing gas becomes equal to the weight of the particles. At this point, the particle bed shifts to the minimally fluidized regime (Figure 2.6b). The distance between particles is slightly increased as well as the volume and height of the particle bed. The velocity of the fluidizing gas is designated as the minimum fluidization velocity, U_{mf}. This velocity is the same everywhere in a bed consisting of monodisperse particles of the same density because the gravitational acceleration is constant.

If the fluidizing gas velocity is increased further, the formation of fluidization bubbles appears in the bed volume. The particle bed shifts to the bubbling bed regime as shown in Figure 2.6c. The fluidization gas velocity at which bubbles first appear is termed minimum bubbling velocity, U_{mb}.

As the fluidizing gas velocity is increased further still, the bubbles in the particle bed coalesce and grow as they rise through the bed. For sufficiently high bed height to diameter ratios, the bubbles may grow to be as big as the diameter of the bed and form gas slugs. The particle bed is said to be in the slugging bed regime (Figure 2.6d).

If the fluidizing gas velocity is increased to the point that it exceeds the terminal velocity of the particles, the upper surface of the particle bed disappears and is replaced by turbulent mixing of solid clusters and voids of gas of various sizes and shapes. The bed is said to be in the turbulent bed regime (Figure 2.6e). The transition from bubbling bed to turbulent bed

does not take place instantly across the whole bed. Instead, it starts at the upper bed surface and moves down gradually to the gas distributor.

Any further increase in fluidizing gas velocity results in the severe entrainment of bed particles. The particle bed shifts to the pneumatic transport regime (Figure 2.6f). The freeboard region above the particle bed is filled with a diluted concentration of particles.

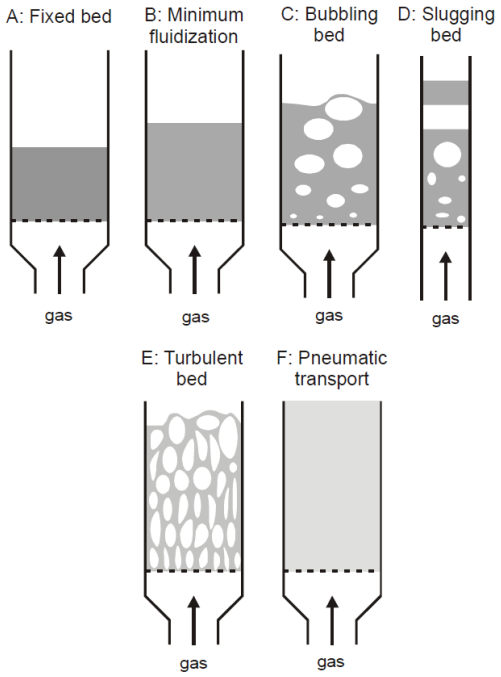

Figure 2.6: Fluidization regimes according to Kunii & Levenspiel (2013).

For relatively slow heterogenous gas-solid reactions such as gasification, fluidized bed gasifiers sometimes operate in the bubbling bed regime where the fluidizing gas velocity is just sufficient to enable fast heat and mass transfer rates and not too high that it would cause the formation of slugs or severe entrainment of unreacted particles.

2.2.2 Classification of Particles in a Fluidized Bed

Experimental observation by Geldart (1973, 1978) showed that the particles behave differently in fluidized beds depending on their size and density. Geldart (1978) classified particles into four distinct categories based on their fluidization behaviour:

- Group A particles are termed 'aeratable' particles. These particles are characterised by their small mean particle size (between 20 μm and 100 μm) and/or low particle density (<~1.4 g/cm^3). Group A particles can be easily and smoothly fluidized at low fluidizing gas velocities without the formation of bubbles. Minimum fluidization always occurs before bubbling in a bed consisting of Group A particles.
- Group B particles are called 'sandlike' particles. These particles typically have size in the range of 40 μm to 500 μm and density between 1.4 and 4 g/cm^3. Group B particles are prone to bubble formation. The excess fluidizing gas flow after minimum fluidization appears in the form of bubbles. Thus, the bubbles in a bed of Group B particles can grow to a large size.
- Group C particles are referred to as 'cohesive' particles. These particles consist of very fine powders with diameters typically smaller than 30 μm. Group C particles are extremely difficult to fluidize because the interparticle forces are relatively large, compared to fluidizing gas drag and gravitational forces. Group C particles are prone to slugging and channelling in small diameter beds.
- Group D particles are known as 'spoutable' particles. These particles are either very large or very dense. They are difficult to fluidize in thick beds because their

density and weight give rise to uneven distribution of fluidizing gas and formation of a gas jet in the bed. This gas jet may blow particles out of the bed in a spouting motion at high fluidizing gas velocities. Uneven gas distribution, spouting behaviour and severe channelling can be typically expected in a bed consisting of Group D particles.

Geldart (1973) plotted his experimental findings and created the Geldart Powder Classification Chart shown in Figure 2.7 for fluidization characteristics at ambient conditions and fluidizing gas velocity less than $10U_{mf}$. This chart provides a clear indication of the type of fluidization and likelihood of bubbles, slugs and spouts that could be expected for any bed material of a known density and mean particle size.

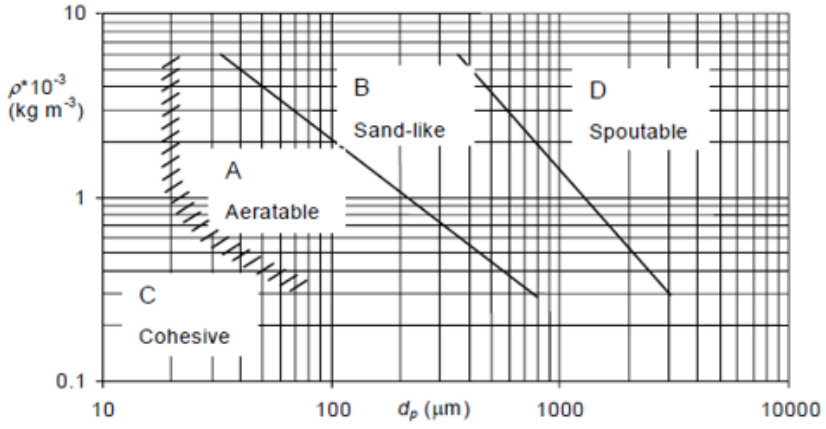

Figure 2.7: Geldart Powder Classification Chart. Reproduced from Geldart (1978).

2.2.3 Fluidized Bed Modelling

Numerous models have been developed to predict the transfer of mass and heat in a fluidized bed. The most commonly used modelling approach divides the contents of a fluidized bed into two "pseudo-phases", L-Phase (Low density) or bubble phase and H-Phase (High density) or emulsion phase, to identify distinctive features and regions in the bed as shown in Figure 2.8 (Machechar-Botero et al., 2009). This modelling approach is based on the two-phase theory of Toomey and Johnstone (1952) which assumes that most of the fluidizing gas flow in excess of the amount required for minimum fluidization passes through the particle bed in the form of bubbles. One phase and three phase fluidized bed models have also been developed but they are less used in literature because of various restrictions. For instance, one-phase models that assume all bed properties are the same everywhere in the bed may only be applied to very slow kinetically controlled reacting systems (Edwards & Avidan, 1986; Foka et al., 1994; Chen et al., 2004). Three-phase models (Fryer & Potter, 1972; Raghuraman & Potter, 1978; Kunii & Levenspiel, 2013) that divide the bed contents into three phases, such as emulsion, cloud and bubble, add complexity to the modelling process while showing little to negligible improvement in accuracy (Clift, 1983).

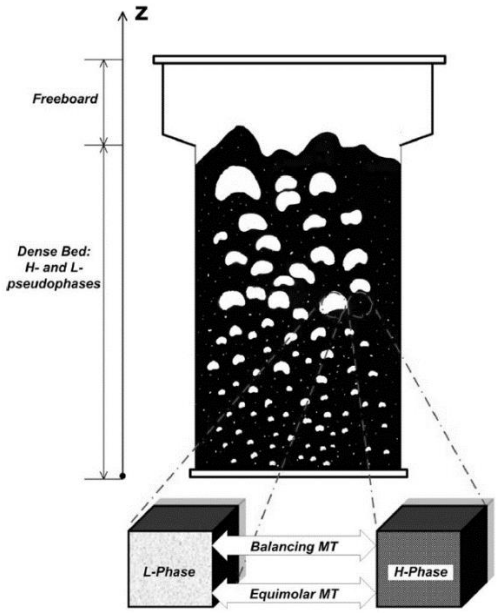

Figure 2.8: Schematic representation of phase division and fluidization. MT denotes mass transfer. Reproduced from Machechar-Botero et al. (2009).

At minimum fluidization, the drag force imparted on the bed particles is approximately equal to the gravitational force. Thus, the weight of the particle bed can be related to the fluidizing gas velocity at minimum fluidization, commonly referred to as the minimum fluidization velocity U_{mf}. The pressure drop across the bed per unit height $\frac{\Delta P}{L}$, can be linked to U_{mf} through the Ergun (1952) equation for the pressure drop in a packed bed as shown in Eq. 6.

$$\frac{\Delta P}{L} = 150\frac{\left(1-\varepsilon_{mf}\right)^2}{\varepsilon_{mf}^3}\frac{\mu U_{mf}}{\left(\emptyset D_p\right)^2} + 1.75\frac{(1-\varepsilon_{mf})}{\varepsilon_{mf}^3}\frac{\rho_f U_{mf}^2}{\emptyset D_p} \qquad \text{Eq. 6}$$

where, ε_{mf} is the bed voidage at minimum fluidization, $\emptyset$ is the sphericity, μ is the dynamic viscosity, D_p is the diameter of the particle, and ρ_f is the density of the gas.

Solving Eq. 6 leads to Eq. 7 which gives the Reynolds number of the fluidizing gas at minimum fluidization.

$$Re_{mf} = \frac{D_p U_{mf} \rho_f}{\mu} = \sqrt{C_1^2 + C_2 \frac{D_p^3 \rho_f (\rho_s - \rho_f) g}{\mu^2}} - C_1 \quad \text{Eq. 7}$$

where, C_1 and C_2 are experimentally determined constants, ρ_s is the density of the solid particle and g is the gravitational acceleration.

For $Re_{mf} \leq 10$, a simpler empirical expression for U_{mf} obtained by Leva (1959) can also be used.

$$U_{mf} = 7.9x10^{-3} D_p^{1.82} (\rho_s - \rho_f)^{0.94} \mu^{-0.88} \quad \text{Eq. 8}$$

For a fluidized bed consisting of Group B or D particles, bubbles immediately form the in the bed for any fluidizing gas velocity that exceeds U_{mf}.

A fluidized bed consisting of Group A particles behaves slightly differently and expands for a fluidizing gas velocity that exceeds U_{mf}. Bubbles do not appear in a fluidized bed of Group A particles until the fluidizing gas velocity becomes greater than the minimum bubbling velocity, U_{mb} which is given by Abrahamsen and Geldart (1980):

$$U_{mb} = 2.07 \exp\left(0.716 F_{D_p<45}\right) D_p \left[\frac{\rho_f^{0.06}}{\mu^{0.347}}\right] \quad \text{Eq. 9}$$

where, $F_{D_p<45}$ is the mass fraction of particles with a diameter smaller than 45 μm.

Knowing the minimum fluidization velocity, it is possible to estimate the flow rate of excess fluidizing gas passing through the bed in the form of bubbles and subsequently bubble size.

An empirical correlation for the mean bubble size in a fluidized bed $D_{b,mean}$, is given by Geldart (1973):

$$D_{b,mean} = \frac{1.43}{g^{0.2}}\left(\frac{\left(U - U_{mf}\right)\pi D_{bed}^2}{4N_0}\right)^{0.4} + 2.05\left(U - U_{mf}\right)^{0.94} L \qquad \text{Eq. 10}$$

where $D_{b,mean}$ is the mean bubble diameter, D_{bed} is the bed diameter, U is the fluidizing gas velocity, N_0 is the number of holes per 10 cm^2 of the distributor plate, and L is the bed height.

The mean bubble size given in Eq. 10 is an important parameter in measuring the amount of solid particles travelling upward through the fluidized bed (Kunii & Levenspiel, 2013).

The diameter of a bubble D_b, at a height Z, above the gas distributor can be estimated using the expression by Darton et al., (1977):

$$D_b = 0.54\left(U - U_{mf}\right)^{0.4}\left(Z + 4\sqrt{A_{noz,0}}\right)^{0.8} g^{-0.2} \qquad \text{Eq. 11}$$

where A_0 is the nozzle area of the gas distributor.

The maximum stable bubble size $D_{b,max}$, can be found using the correlation by Grace (1982):

$$D_{b,max} = \frac{2(U_t)^2}{g} \qquad \text{Eq. 12}$$

where U_t is the terminal velocity of particles with a diameter that is equal to $2.7D_p$.

The initial bubble size $D_{b,0}$, near the gas distributor can be estimated using the following correlation (Kunii & Levenspiel, 2013):

$$D_{b,0} = \frac{2.78\left(U - U_{mf}\right)^2}{g} \quad \text{Eq. 13}$$

The upward velocity of a single bubble rising in a fluidized bed can be found using (Kunii & Levenspiel, 2013):

$$U_b = U - U_{mf} + 0.711\sqrt{gD_b} \quad \text{Eq. 14}$$

It has been observed that as bubbles rise, they carry some amounts of particles inside them. The amount of particles carried inside each bubble is termed 'wake'. An idealised bubble is shown in Figure 2.9 which consists of an approximately spherical bubble and a wake at the bottom with volume defined by the wake angle θ_w. The wake is picked up by the bubbles as they are formed at the gas distributor and travel through the bed.

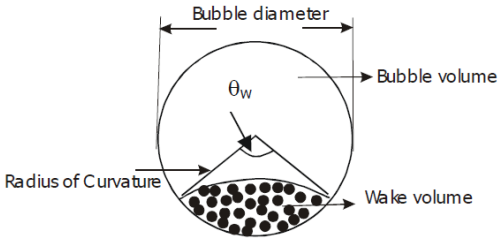

Figure 2.9: An idealised bubble with wake inside. Reproduced from Dechsiri (2004).

Naimer et al. (1982) gave an empirical expression for the variation of the wake angle with the bubble diameter. This expression was later modified and improved by Hoffmann (1983) who proposed the following:

$$\theta_w = 160 - 160\exp(-60D_b) \quad \text{Eq. 15}$$

The volume of the wake V_W, can be estimated using θ_w, D_b and bubble radius r_b,. The ratio of the wake volume to the bubble volume is termed the wake fraction f_W which provides an

important parameter for estimating the amount of particles being transported upward and recirculated in the bed. The expression for f_W is as follows:

$$f_W = \frac{3V_W}{4\pi r_b^3} \quad \text{Eq. 16}$$

Yates (2013) estimates that for spherical materials, the wake makes up approximately 30% of the bubble volume.

2.2.4 Movement of Bubbles and Particles

Davidson (1961) proposed the Davidson Model which describes the movement of both solid and gas in a fluidized bed. He used a stream function to describe the superficial gas flow and found that the geometry of the stream function was influenced by the bubble rise velocity. If the bubble rise velocity is slower than the fluidizing gas velocity in the emulsion phase, the gas in the emulsion phase enters the bubble at the bottom and leaves at the top, effectively using the bubble as a shortcut (Figure 2.10). If the bubble rise velocity is faster than the fluidizing gas velocity in the emulsion phase, significant circulation appears around the bubble, forming a "cloud". The size of the circulation zone is inversely proportional to the ratio of bubble rise to superficial gas velocities. When the bubble rise velocity is significantly faster than the superficial gas velocity, the circulation zone becomes confined within the bubble. The rest of the gas in the emulsion phase moves past the bubble without any mixing. Mass transfer is limited to dispersion only because the gas in the bubble is essentially isolated.

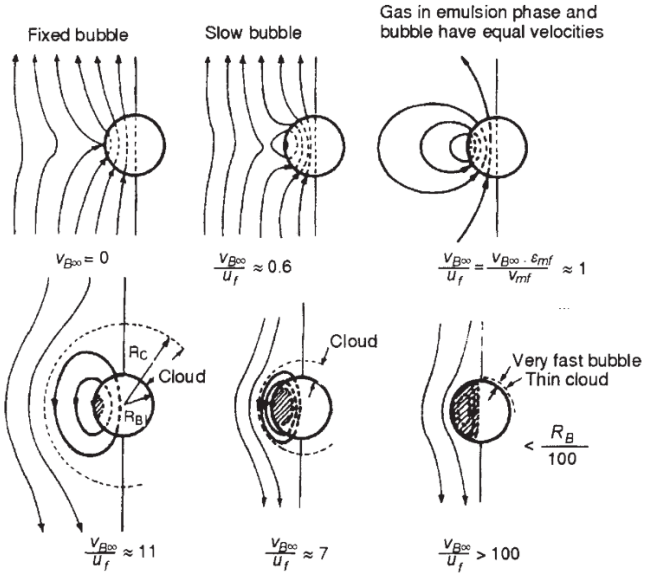

Figure 2.10: Gas streamlines around a bubble in fluidized bed. $v_{B\infty}$ and u_f denote the bubble rise and superficial gas velocities respectively. Reproduced from Kunii & Levenspiel (2013).

The Davidson Model was later extended by many researchers such as Jackson (1963) and Murray (1965) to offer more realistic descriptions of bubble and solid movement. It is worth noting that the Davidson Model does not account for bubble breakage. It has been found that in dense beds, if the bubble rise velocity exceeds the terminal velocity of the bed particles, the bubble becomes unstable and tends to break into smaller bubbles (Kunii & Levenspiel, 2013). Thus, the maximum size of stable bubble and the location where the bubble breaks are influenced by particle properties. Geldart Group A particles produce smaller stable bubbles than Geldart Group B particles. Group D particles exhibit a different bubbling behaviour. Due to their relative high density, the gas flow distribution within the bed is highly skewed and jets form instead of bubbles.

As mentioned earlier, bubbles coalesce as they rise upward through the bed. They can either move up and incorporate other bubbles on top of them or move sideways and incorporate

bubbles next to them, as shown in Figure 2.11. The bubbles near the wall of the bed always move away from the wall due to the wall boundary effects that generates a denser emulsion phase near the wall. Therefore, the upward movement of particles near the wall is always less than the movement in the centre because the more active bubbling zone away from the wall. Because of the difference between the bubbling activity in these two regions, particles tend move upward in the centre and fall downward near the wall. This particle recirculation pattern can be modified through the addition of tubes and baffles in the fluidized bed volume. For example, Kodama et al. (2008) added a draft tube in the centre of their fluidized bed solar receiver to create more axial recirculation in the centre where the solar flux is the highest.

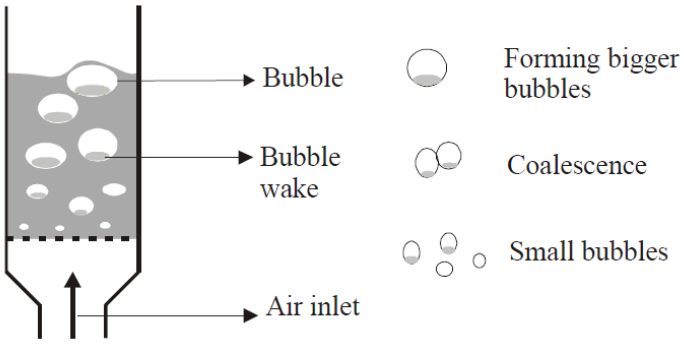

Figure 2.11: Coalesce behaviour of bubbles. Reproduced from Dechsiri (2004).

Sometimes, the bubble flow rising through the bed is non-uniform and leads to a phenomenon termed gulf streaming (Merry & Davidson, 1973). Gulf streaming creates a strong upward flow of bubbles and particles in one part of the bed and an equally strong downward flow in another part of the bed. The net effect of gulf streaming is increased recirculation of particles along the axial direction and faster bubble rising velocity than that predicted using minimum fluidization velocity.

Nienow et al. (1987) conducted experiments to better understand the mechanisms governing the particle transport processes in fluidized bed. Solid circulation was found to be mainly determined by the fluidizing gas velocity. The key mechanisms for particle transport in the bed are upward moving bubble wake, downward moving solid phase not in a bubble and dispersion caused by the disturbance of the emulsion phase by bubble movement and breakage (Figure 2.12). While particle movement occurs in both axial and radial directions, the particle movement in the radial direction was found to be typically many times smaller than that of the axial direction (Kunii and Levenspiel, 2013). The downward movement of particles is also slower than the upward movement due to the upward drag force of the fluidizing gas.

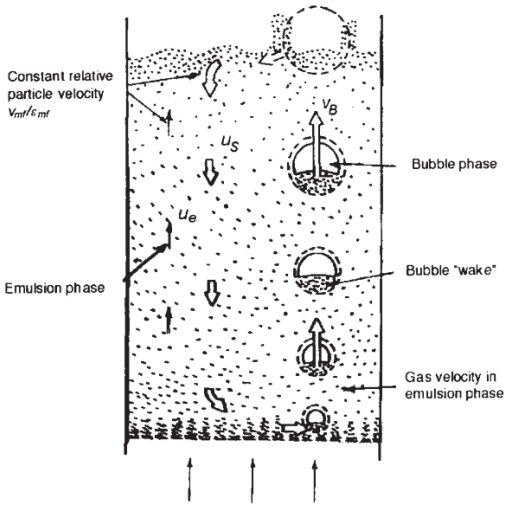

Figure 2.12: Schematic diagram of the particle phase flow pattern in a fluidized bed. Reproduced from Kunii & Levenspiel (2013).

In a fluidized bed with particles of varying sizes and densities, segregation of particles can take place because of the different ratio of drag and gravitational forces acting on the particles. Larger or denser particles with low drag per unit weight move downward while

smaller or lighter particles with high drag per unit weight move upward. These two types of particles are termed, jetsam and flotsam, respectively.

Gibilaro and Rowe (1974) modelled a segregating fluidized bed consisting two types of particles and found that particle segregation is heavily dependent on bubble movement and varies with the height from the gas distributor. In some cases, particle segregation was found to cause de-fluidization due to jetsam particles depositing on the bottom.

Tanimoto et al. (1981) proposed a quantifiable parameter termed segregation distance Y to measure particle segregation. The segregation distance is non-dimensionalized with the radius of the fluidization bubble and characterises the distance over which the jetsam particles sink with the passage of a single particle. The expression for segregation distance is given in Eq. 17.

$$Y = 0.8\frac{\rho_{jet}}{\rho_{flo}}\left(\frac{d_{jet}}{d_{flo}}\right)^{\frac{1}{3}} - 0.8 \qquad \text{Eq. 17}$$

Naimer et al. (1982) suggested that jetsam particles falling through bubbles may be a segregation mechanism for their faster downward flow compared to flotsam particles.

Hartholt et al., (1996) found that inserting baffles in a fluidized bed increases the segregation of larger and denser particles and decreases axial mixing. Experiments showed that baffles reduce the amount of solid wake carried upward by bubbles (van Dijk et al. 1998).

2.3 Rotating Fluidized Bed

The top view of the schematic diagram of a simple Rotating Fluidized Bed (RFB) is shown in Figure 2.13. In an RFB, the centrifugal force due to rotation is responsible for keeping the particles on the cylindrical gas distributor and countering the drag force of the fluidizing gas. If the centrifugal force is significantly greater than the gravitational force, the effect of gravity can be ignored. At minimum fluidization, these two opposing forces are equally balanced and suspend the particles in a random turbulent motion. Since the centrifugal force acting on the particles is a function of particle radial position, minimum fluidization across the bed does not occur at a single fluidizing gas velocity. The particles at the inner bed surface are under the least amount of centrifugal force due to their proximity to the centre of rotation and thus become fluidized before any other part of the bed. The fluidizing gas velocity at which the inner surface particles are minimally fluidized is termed surface minimum fluidization velocity U_{mfi}. As the fluidizing gas velocity and drag force increase, the fluidization boundary gradually moves from the inner bed surface radially outward. The particles at the gas distributor are furthest away from the centre of rotation and therefore become fluidized last. The fluidizing gas velocity at which the particles at the gas distributor are minimally fluidized is termed critical minimum fluidization velocity U_{mfc}. The difference between U_{mfi} and U_{mfc} is dependent on the radial thickness and rotational speed of the RFB.

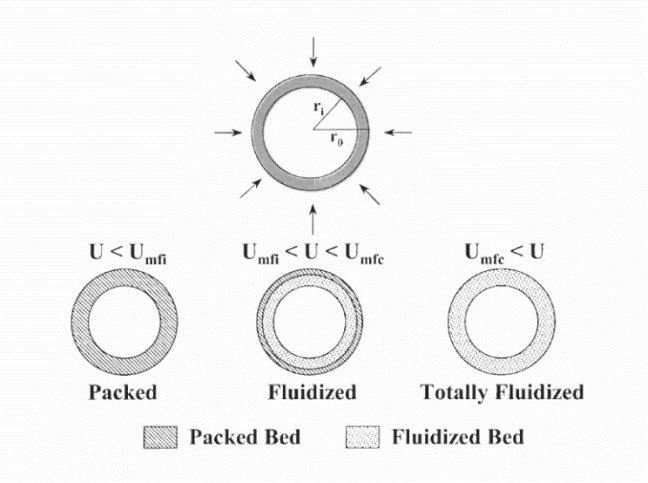

Figure 2.13: Transition from packed bed to fluidized bed in an RFB. Reproduced from Qian (2003).

It is important to note that the area of the gas distributor is greater than that of the inner bed surface. Therefore, for the same flow rate, the fluidizing gas velocity at the inner bed surface is higher than that at the gas distributor. For very thick beds, it is possible for the inner bed volume close to the surface to be in the turbulent bed regime while the outer bed volume close to the gas distributor being in the packed bed regime. Thus, to achieve uniform fluidization quality, it is desirable to operate an RFB with a shallow particle bed of small radial thickness.

2.3.1 Pressure Drop

RFBs have been investigated by numerous researchers since the 1960s. Many investigations focus on the bed pressure drop and incipient fluidization conditions. Two types of pressure drop responses have been reported in literature. Takahashi et al. (1984), Fan et al. (1985) and Hao et al. (2000) reported the existence of a maximum pressure drop as opposed to the pressure drop plateau reported by Kroger et al. (1979), Metcalfe et al. (1977), Demircan et al. (1978), and Levy et al. (1978). The difference in reported experimental pressure drop

curves indicates the complexity of the gas-solid interaction behaviour in the RFB. The experimental curves obtained by Fan et al. (1985) and Metcalfe et al. (1977) are shown in Figure 2.14 to demonstrate the two types of pressure drop responses. The curve of Fan et al. (1985) exhibits a pressure drop plateau after minimum fluidization, similar to the pressure drop response in a conventional fluidized bed, whereas the curve of Metcalfe et al. (1977) shows a maximum pressure drop at minimum fluidization.

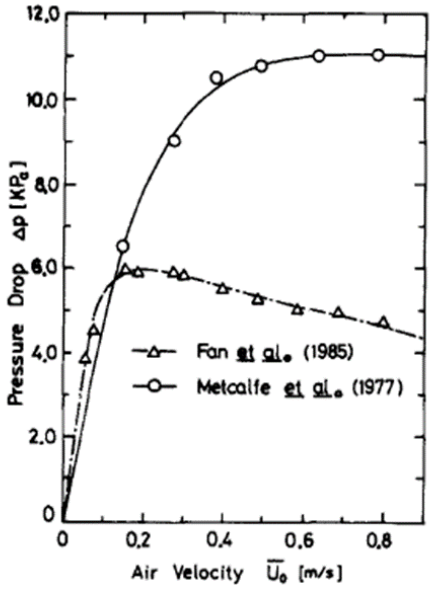

Figure 2.14: Pressure drop across the rotating fluidized bed as a function of fluidizing gas superficial velocity (Kao et al. 1987)

Kao et al. (1987) conducted RFB experiments using beds of different radial thicknesses (1-3 cm) and were able to observe both types of pressure drop response (Figure 2.15). The radial thickness appears to be a key parameter in determining the pressure drop response. Kao et al. (1987) attributed the occurrence of a maximum pressure drop to particle elutriation. In a thick bed, the difference between U_{mfi} and U_{mfc} is large, and the drag force at the bed surface may be significantly greater than at that the gas distributor. Thus, particle

elutriation is likely to occur in a thick RFB after minimum fluidization, and the loss of effective bed weight causes the pressure drop to decrease. In contrast, the difference between U_{mfi} and U_{mfc} is relatively small in a shallow bed. Particle elutriation is less likely to occur, and the constant effective bed weight maintains a pressure drop plateau after minimum fluidization. The theoretical pressure drop in Figure 2.15 was calculated using the correlations of Chen (1987). It can be seen that as the radial thickness increases, the correlations become less accurate.

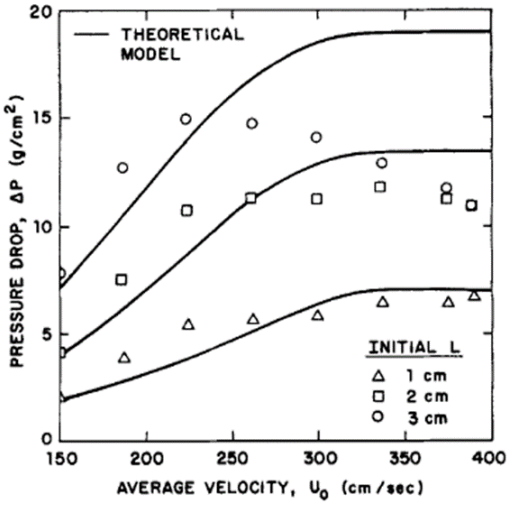

Figure 2.15: Pressure drop across fluidized beds of varied thicknesses (1cm, 2cm and 3cm) as a function of fluidizing gas velocity curves obtained experimentally and using Chen (1987) theoretical model. Reproduced from Kao et al. (1987).

Qian et al. (1998) conducted experiments in RFBs with sintered and slotted metal gas distributors. The pressure drop measurements made with the sintered gas distributor showed the characteristic features previously observed by Fan et al. (1985). The slotted metal gas distributor produced a one-time sudden drop in the pressure drop curve that had never been observed (Figure 2.16). The sudden drop can only be observed as the RFB makes the transition from the packed bed to fluidized bed regime, denoted FF. The reverse transition

from fluidized bed to packed bed regime, denoted B/S, shows a smooth pressure drop curve without any notable feature. The gradient of the reverse transition is also slightly lower than the forward transition, indicating some loss of effective bed weight.

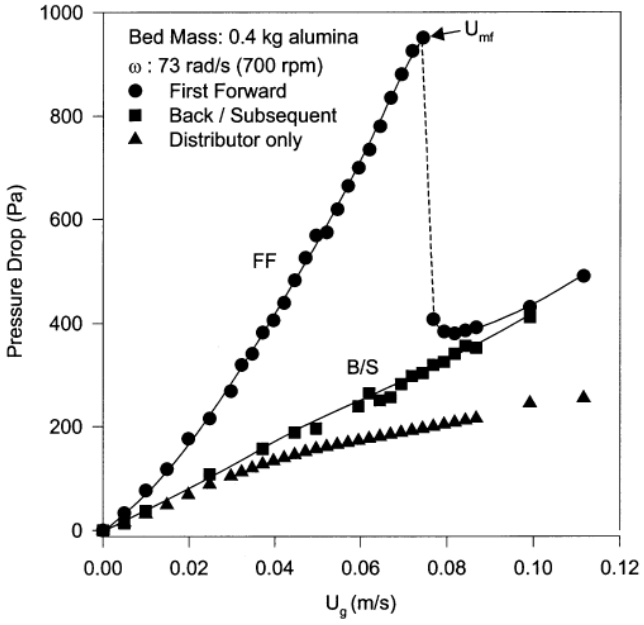

Figure 2.16: Pressure drop in an RFB with slotted gas distributor as a function of fluidizing gas velocity.

Qian et al. (1998) observed that unlike the sintered gas distributor, the slotted gas distributor creates two distinctly different zones of fluidization as shown in Figure 2.17. At minimum fluidization, the bed volume immediately above the open area of the distributor becomes fluidized while the volume above closed area remains packed. Qian et al. (1998) postulated that some of the particles in the fluidized bed portion freely flows over to the packed bed portion, and the sudden reudction in pressure drop in Figure 2.16 is caused by this transfer of particles during the forward transition. Since there is no reverse transfer of particles from the packed bed portion to the fluidized bed portion in the reverse transition, this change in

pressure drop is not repeated in the B/S curve. Qian et al. (1998) highlighted the importance of gas distributor geometry in determining the fluidization quality and uniformity in an RFB.

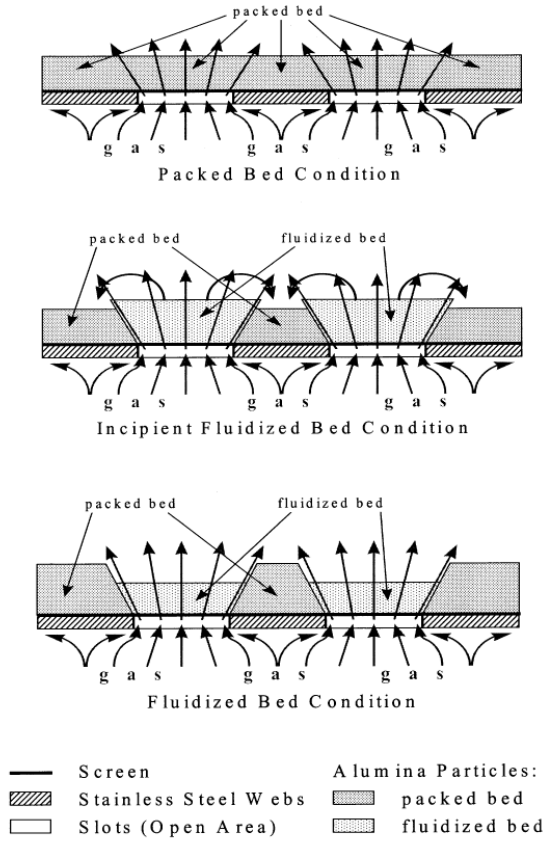

Figure 2.17: Conceptualization of pressure drop behaviour for the slotted gas distributor. Reproduced from Qian (2003).

2.3.2 Rotating Fluidized Bed Modelling

Modelling the incipient fluidization conditions in an RFB was of particular interest to researchers. Various mechanistic models based on the overall force balance in an RFB were developed to predict the minimum fluidization velocities and pressure drop across the bed during the transition from the packed bed to a fully fluidized bed regime (Levy & Chen, 1977; Demircan et al., 1978; Kroger et al., 1979; Fan et al., 1985; Chen, 1987). The model developed by Chen (1987) is the most comprehensive and only model to consider the

influence of variable bed voidage in the radial direction. This allows the model to accurately describe the partial fluidization behaviour in an RFB and predict the pressure drop while the bed is partially fluidized. Chen (1987) compared the predictions of his model with those of the previous models and found that his model showed better agreement with experimental measurements.

Kao et al. (1987) simplified the complex theoretical analysis of Chen (1987) by removing the terms that appeared to have little effects on the results. They proposed a set of simplified and easier-to-use semi-empirical equations for predicting U_{mf_i} and U_{mf_c}, as given in Eq. 18 and 19. A comparison of the results calculated using the simplified equations and the equations of Chen (1987) showed that the deviations less than 5%.

$$\frac{U_{mf_i}\rho_f D_p}{\mu}\frac{r_o}{r_i} = \left[(33.7)^2 + 0.0408\frac{\rho_f(\rho_s-\rho_f)D_p^3\omega^2 r_i}{\mu^2}\right]^{0.5} - 33.7 \qquad \text{Eq. 18}$$

$$\frac{U_{mf_c}\rho_f D_p}{\mu} = \left[(33.7)^2 + 0.0408\frac{\rho_g(\rho_s-\rho_f)D_p^3\omega^2 r_o}{\mu^2}\right]^{0.5} - 33.7 \qquad \text{Eq. 19}$$

where ρ_f, ρ_s, D_p, ω, μ, r_i, and r_o are fluid phase density, solid phase density, particle diameter, bed rotational speed, fluid phase kinematic viscosity, inner bed surface radius, and gas distributor radius respectively.

Using the above definitions, the bed can be categorized into three states depending on the fluidizing gas velocity, U.

For $U \leq U_{mf_i}$, the bed is in the fully packed state. The pressure drop across the bed is determined through Eq. 20 (Kao et al., 1987).

$$\Delta P = C_1 U_o r_o \ln\left(\frac{r_o}{r_i}\right) + C_2 U_o^2 r_o^2 \left(\frac{1}{r_i} - \frac{1}{r_o}\right) \quad \text{Eq. 20}$$

where

$$C_1 = \frac{1650(1-\varepsilon)\mu}{D_p^2}, \quad C_2 = \frac{24.5(1-\varepsilon)\rho_f}{D_p}$$

For $U_{mf_i} \leq U \leq U_{mf_c}$, the bed is partially fluidized, consisting of a fluidized inner portion defined by $r_i \leq r \leq r_{fb}$ where r_{fb} is the radial position of the fluidisation boundary and a packed outer part defined by $r_{fb} < r \leq r_o$. The pressure drop across the bed is the sum of the pressure drops across the two portions and is given through Eq. 21 (Kao et al., 1987).

$$\Delta P = (1-\varepsilon)\left(\rho_s - \rho_f\right)\omega^2\left(r_{fb}^2 - r_i^2\right) + C_1 U_o r_o \ln\left(\frac{r_o}{r_{fb}}\right) + C_2 U_o^2 r_o^2 \left(\frac{1}{r_{fb}} - \frac{1}{r_o}\right) \quad \text{Eq. 21}$$

For $U_{mf_c} \leq U$, the bed is fully fluidized. The pressure drop across the bed can be calculated with Eq. 22 (Kao et al., 1987).

$$\Delta P = \frac{1}{2}(1-\varepsilon)\left(\rho_s - \rho_f\right)\omega^2(r_o^2 - r_i^2) \quad \text{Eq. 22}$$

2.3.3 Flow Field and Particle Entrainment

There exists little information in the public domain about the flow field inside an RFB. The vortex flow structure inside a rotating porous vessel that is geometrically similar to an RFB without particles has been investigated by Donaldson and Snedeker (1962) in a specially designed setup shown in Figure 2.18. Their experimentally obtained flow measurements at the opening plane of the vessel provide useful insights into the influence of vessel rotational

speed and diameter to length ratio on the vortex flow structure in the rotating vessel. Donaldson and Snedeker (1962) observed that the vortex flow inside a high speed rotating vessel with radially inward air injection from the porous cylindrical wall is likely to be a Rankine vortex consisting of a free vortex in the outer region and forced vortex in the core region.

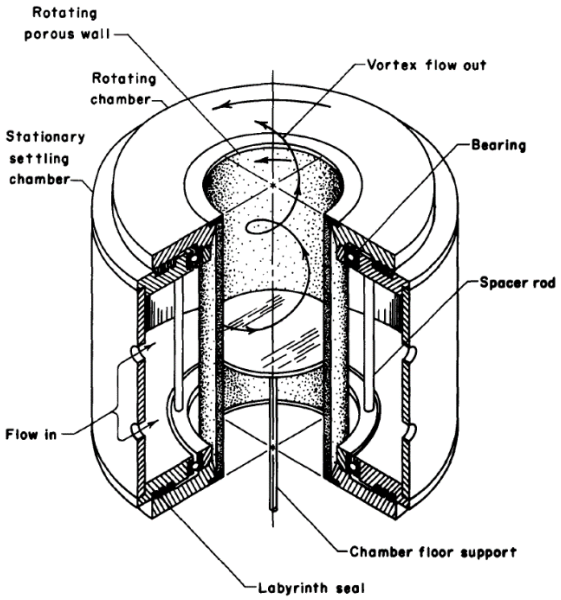

Figure 2.18: Cutaway view of the experimental apparatus of Donaldson and Snedeker (1962). Reproduced from Donaldson and Snedeker (1962).

Based on the measurements and findings of Donaldson and Snedeker (1962), Chevray et al. (1980) proposed a universal representation of the tangential velocity distribution inside a high speed rotating vessel with radially inward inlet air flow (Figure 2.19). This representation can be used to estimate the magnitude and location of the maximum tangential velocity of the Rankine vortex if the rotational speed and fluid properties are known.

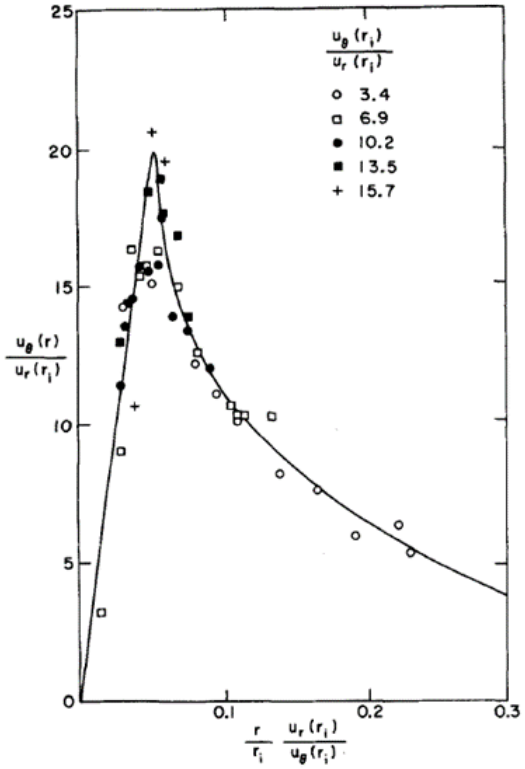

Figure 2.19: Universal representation of tangential velocity distribution based on the data of Donaldson and Snedeker (1962). Reproduced from Chevray et al. (1980).

Chevray et al. (1980) also mathematically derived a set of equations to describe the idealised flow field inside an RFB without end effects. This set of idealised flow field equations was then coupled with single particle motion equations to investigate the movement of an entrained non-reacting particle in an RFB. The trajectories of different sized entrained particles released from two different angles relative to the bed surface are presented in Figure 2.20. It can be seen from Figure 2.20 that the particle trajectories vary significantly depending on the particle size and release angle. Medium sized particles such as the 60×10^{-6}m diameter particle were found to be more likely to be entrained out of the vessel than both larger and smaller particles because their trajectories cross the central viscous core boundary where Chevray et al. (1980) assumed that the upward axial flow to be the strongest.

This highlights the importance of particle size selection in minimising the loss of particles in an RFB.

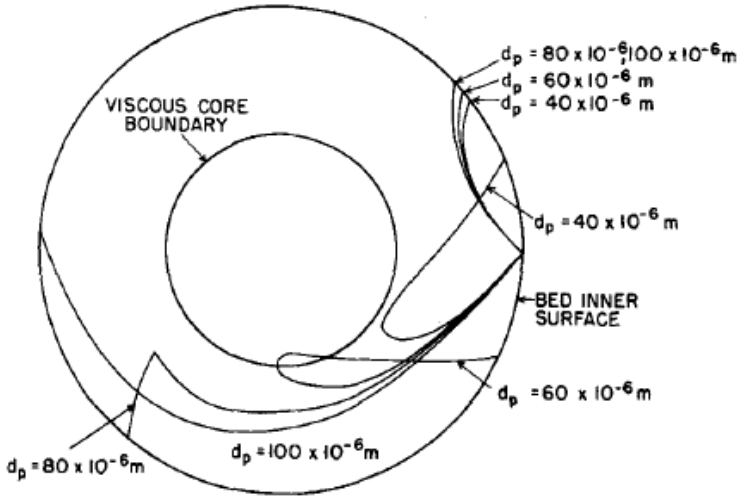

Figure 2.20: Trajectories of entrained particles of various sizes in the freeboard of a rotating fluidized bed. Two different angles of release: $\frac{\pi}{4}$ and $\frac{3\pi}{4}$rad. Reproduced from Chevray et al. (1980).

Saunders (1986) experimentally measured the particle elutriation rates of different sized non-reacting particles in an RFB with various combinations of exit port diameter and rotational speed. His experimental results confirmed that rotational speed is an effective parameter in delaying the onset of particle entrainment and reducing the particle entrainment rate (Figure 2.21). Saunders (1986) reported that the onset of noticeable particle elutriation can be predicted with the ratio of fluidizing gas to particle terminal velocities at the inner bed surface. Saunders (1986) determined this ratio to be 0.25 based on his experimental measurements.

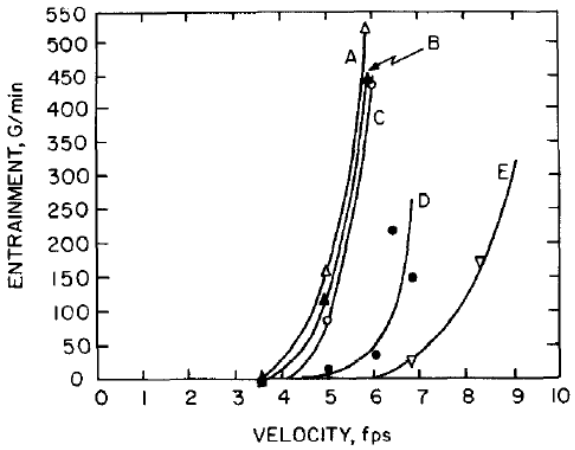

Figure 2.21: Entrainment of glass beads as a function of fluidizing gas velocity for various combinations of particle diameter, exist hole diameter and rotational speed. The combinations are as follows: A - 215 micron particles, 250 RPM, 4.625 in exit hole with 0.5 in exit hole lip extended into the freeboard. B - 215 micron particles, 250 RPM, 4.625 in exist hole. C - 215 micron particles, 250RPM, 6 in exit hole. D - 362 micron particles, 250RPM, 6 in exit hole. E - 215 micron particles, 400 RPM, 6 in exit hole. Reproduced from Saunders (1986).

In recent years, the vast improvement in computational power has enabled various researchers to use Computational Fluid Dynamics (CFD) methods to investigate the flow field and particle movement in RFBs (Ahmadzadeh et al. 2003; Nakamura et al. 2014). Ahmadzadeh et al. (2003) studied the flow field and particle movement in an RFB using a 2D axis-symmetric Eulerian Multiphase CFD model. Figure 2.22 presents the calculated fluid phase flow and pressure fields for an RFB without particles rotating at 40 rad/s for two radial inlet velocities, 0 m/s and 1 m/s (Ahmadzadeh et al. 2003). It can be seen that if there is no inlet air flow, the low pressure central core generated by rotation could draw air in from the outside atmosphere. In the case where the radial inlet velocity is 1 m/s, the tangential momentum of the fluid flow due to rotation leads to significant pressure build up in the near wall region of the cavity. As a result, the upward flow exiting the RFB is the strongest in the near wall region and almost zero in the central region where the pressure remains relatively low. The lack of axial flow in the central region is desirable because it suggests that significant upward particle entrainment is unlikely to occur in the central

region of the RFBR concept where the aperture is located. The strong outlet flow in the near wall region indicates tangential outlets could create a smoother flow than outlets located close to the centre.

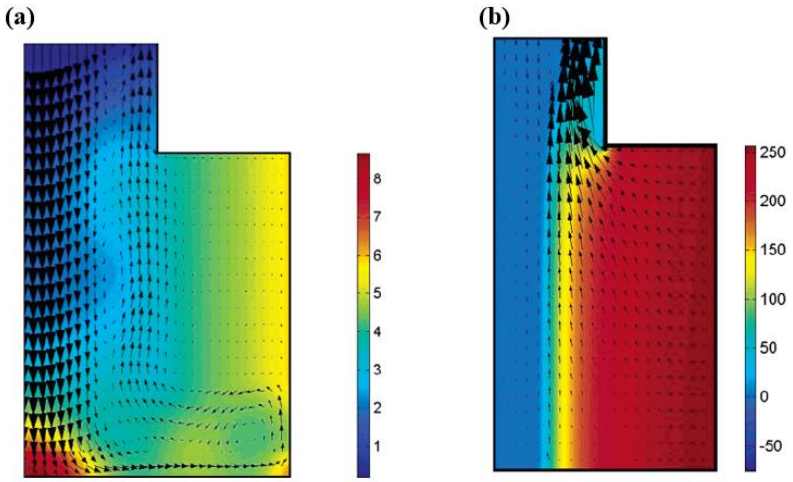

Figure 2.22: Pressure (Pa) and flow field velocity vectors in a rotating fluidized bed vessel without particles for radial inlet flow velocities of (a) U = 0 m/s and (b) U = 1 m/s. The vessel was rotated at a speed of 30 rad/s. Reproduced from Ahmadzadeh et al. (2003).

Nakamura et al. (2014) proposed a novel tapered RFB design for mitigating particle entrainment from the bed in an RFB powder coating device for pharmaceutical applications (Figure 2.23). The tapered design allows the circumferential cross section area to vary with radial position. This has the benefit of reducing the fluidizing gas velocity at the bed surface and subsequently the rate of particle entrainment.

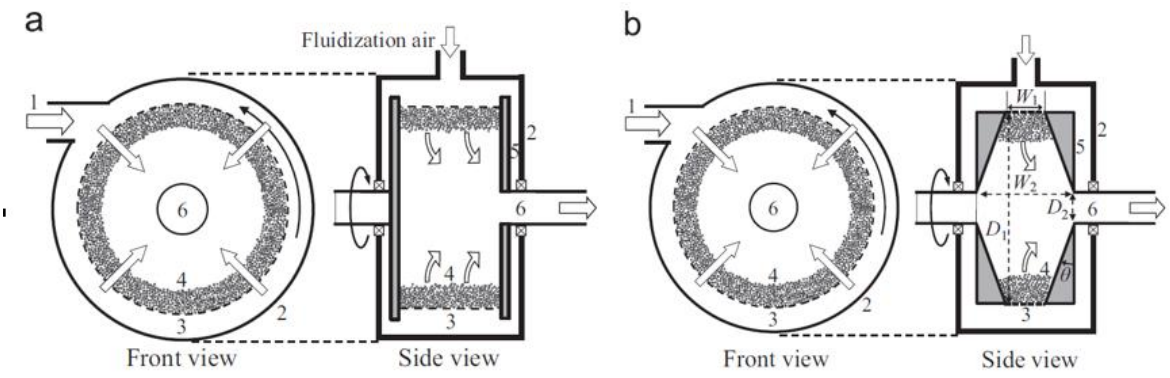

Figure 2.23: Schematic diagrams of (a) conventional and (b) tapered rotating fluidized bed coating device Reproduced from Nakamura et al. (2014).

To quantitatively investigate the sensitivity of particle entrainment rate and maximum entrained particle size to variations in taper angle, Nakamura et al. (2014) developed a coupled CFD model that was then coupled with a Discrete Phase Model (DPM) for particle tracking. The combined model was verified with experimental measurements and found that increasing the taper angle was effective in reducing the maximum entrained particle size. Figure 2.24 shows the maximum entrained particle size as a function of taper angle. It can be seen that the maximum entrained particles particle could be halved by increasing the taper angle from 0 to 23 degrees.

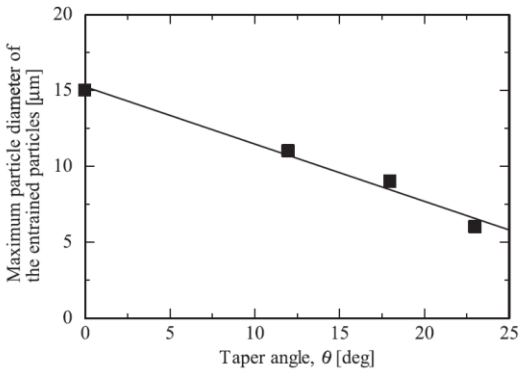

Figure 2.24: Calculated maximum entrained particle diameter as a function of taper angle. Reproduced from Nakamura et al. (2014).

The mass fraction of entrained particles in the RFB coating device outlet was experimentally measured by Nakamura et al. (2014). A significant reduction of 42% in mass fraction was observed through increasing the taper angle from 0 to 23 degrees (Figure 2.25). The trends in both Figures 2.24 and 2.25 appear to be linear, indicating that further reductions are possible with increased taper angle.

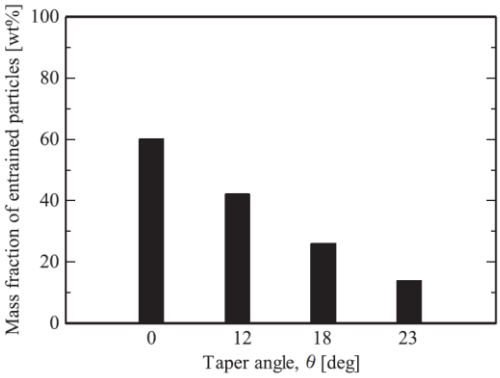

Figure 2.25: Experimentally measured mass fraction of entrained particles in the outlet flow as a function of taper angle. Reproduced from Nakamura et al. (2014).

2.3.4 Rotating Fluidized Bed Surface Profile

Most RFB experiments in literature were conducted at high rotational speeds where the bed fluidized bed surface is almost annular with constant radial thickness. The theoretical RFB models presented in Section 2.3.2 are based on the annular fluidized bed surface assumption. However, to minimize kinetic energy loss due to rotation and rotating component wear, it is desirable to operate the RFBR at the lowest rotational speed that is still able to provide the conditions for desirable fluidization characteristics. Thus, a good understanding of the rotating fluidized bed surface profile at low rotational speeds is crucial.

Kroger et al. (1979) studied the axial distribution of bed thickness and radial gas velocity on the bed surface in a vertically oriented RFB operating at different rotational speeds (Figure 2.26). It was found that increasing the rotational speed moves more particles to the upper portion of the RFB and leads to better uniformity of bed thickness in the axial direction and less variation in pressure drop across the bed and radial gas velocity. For the 305 mm diameter RFB of Kroger et al. (1979), significant variations in bed thickness and radial gas velocity only appear when the rotational speed is reduced to 26.2 rad/s. This suggests that the RFB must be operated at a rotational speed greater than 26.2 rad/s to achieve good, uniform fluidization quality along its axis.

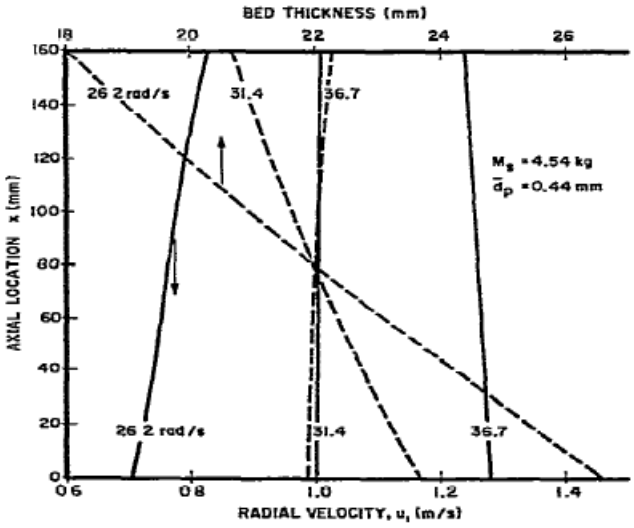

Figure 2.26: Experimentally determined axial variation of bed thickness and radial gas velocity. Reproduced from Kroger et al. (1979).

Ahmadzadeh et al. (2003) developed an axis-symmetric 2D Eulerian Multiphase CFD model of a vertically oriented RFB that shares similar geometrical dimensions with that of Kroger et al. (1979). The solid volume fraction and particle movement vectors predicted using the model for radial gas velocities of 0 m/s (packed bed state) and 1 m/s (fluidized

bed state) are shown in Figure 2.27. It can be seen that in the packed bed state, the particles in the RFB form an approximately parabolic bed surface. Only half of the cylindrical gas distributor is covered by the particles due to strong inter-particle friction and gravitational force. In the fluidized bed state, the particle bed exhibits fluid like behaviours and flows up the cylindrical gas distributor until it reaches the top end surface. The bed surface appears to be flat similar to the experimentally measured bed surface profiles reported by Kroger et al. (1979).

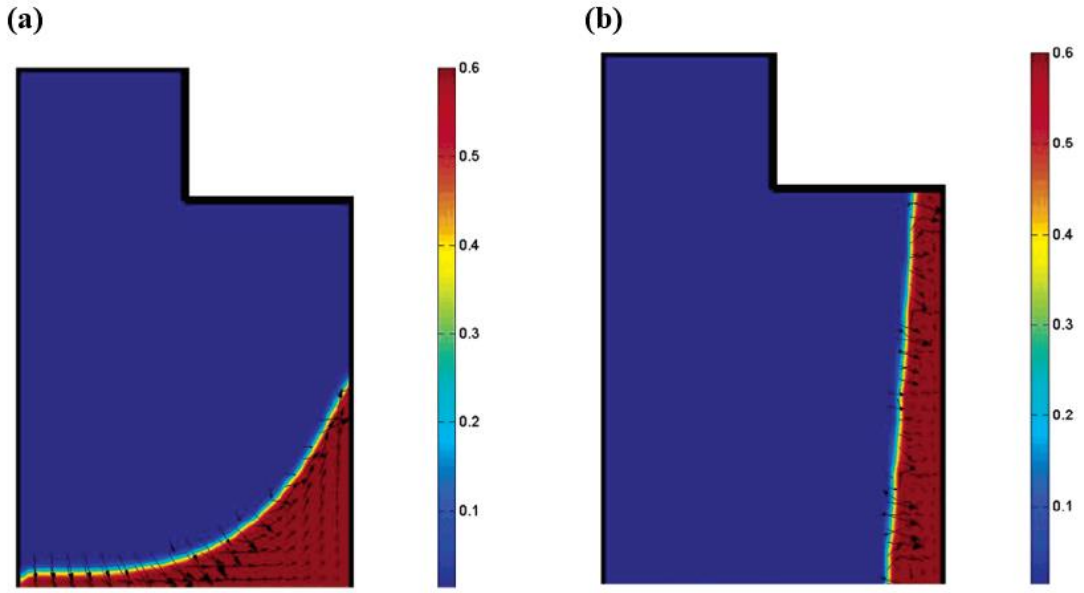

Figure 2.27: Solid volume fraction in a vertically oriented rotating fluidized bed with radial gas velocities of (a) U = 0 m/s and (b) U = 1 m/s. The vessel was rotated at a speed of 30 rad/s. Reproduced from Ahmadzadeh et al. (2003).

Ahmadzadeh & Arastoopour (2008) developed a 3D Eulerian Multiphase CFD Model to investigate the particle movement behaviour in a horizontally oriented RFB with a diameter of 61.5 mm. The calculated solid volume fractions for various rotational speeds are shown in Figure 2.28. For the range of rotational speeds used in the investigation, the bed surface and radial thickness appear to be highly non-uniform, suggesting that higher rotational speeds are required if uniform fluidization is desired. The investigation showed that gravity

has a much greater influence on particle fluidization in a horizontally oriented RFB compared to a vertically oriented RFB. At the upper most point of the horizontally oriented RFB, the gravitational force acts directly opposite to the centrifugal force, and at the lowest point of the RFB, the gravitational force acts in the same direction as the centrifugal force. As a consequence, at low rotational speeds where the centrifugal and gravitational forces are of the same order of magnitude, the tangential distribution of bed thickness is highly non-uniform, and significant particle build up can be expected in the lower portion of the RFB. Increasing the rotational speed results in increased centrifugal force which pushes more particles to the upper portion of the RFB and improves the uniformity of bed thickness. If the centrifugal force is increased to be significantly greater than the gravitational force, the bed thickness is expected to become approximately uniform in all directions.

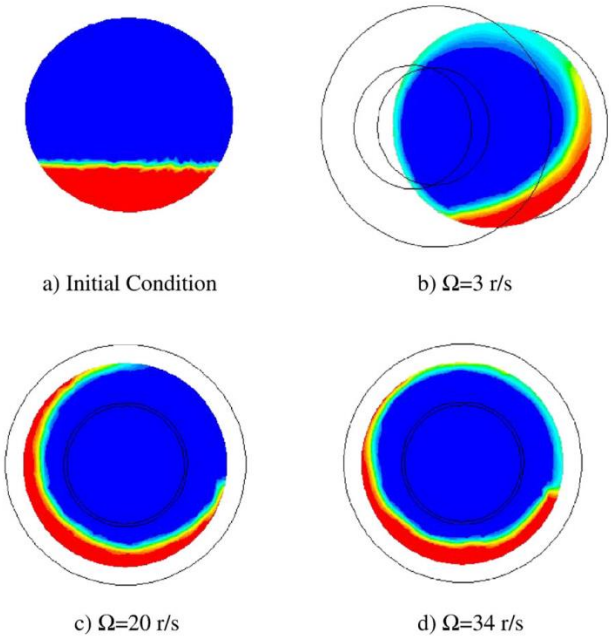

Figure 2.28: Solid volume fraction in a horizontally oriented rotating fluidized bed operating at various rotational speeds: (a) 0 rad/s, (b) 3 rad/s, (c) 20 rad/s, and (d) 34 rad/s. Reproduced from Ahmadzadeh & Arastoopour (2008).

2.4 Solar Gasification

Solar driven steam gasification of carbonaceous materials has a focus of many researchers since the 1980s. Numerous exploratory studies were conducted with coal (Gregg et al., 1980; Beattie et al., 1983; Kubiak and Lohner, 1992) and with oil shales (Gregg et al., 1980; Fletcher and Berber, 1988; Ingel et al., 1992; Flechsenhar and Sasse, 1995). The gasification of coal using CO_2 was investigated by Kodama et al. (2002) in a fluidized bed confined in a quartz tube under intense radiation. Moreover, the heat transfer characteristics of radiation driven gasification were analysed by Belghit and Daguenet (1989), and the reaction kinetics of radiation driven steam gasification were investigated using a quartz tube by Muller et al. (2003). Based on the results of these fundamental studies, several solar receiver concepts for the gasification of various types of carbonaceous feedstock have been developed and experimentally demonstrated on a lab scale (Gregg et al., 1980; Murray & Fletcher, 1994; von Zedtwitz & Steinfeld, 2005; Z'Graggen et al., 2006; Melchior et al., 2009; Piatkowski et al., 2009; Lichty et al., 2010).

A solar gasification receiver's performance is usually described using two solar energy conversion efficiencies, solar to chemical energy conversion efficiency and thermal energy conversion efficiency. The solar to chemical energy conversion efficiency is defined as the portion of input solar energy that is converted to the chemical energy stored in reaction products. The thermal energy conversion efficiency reports the proportion of input solar energy that is converted to both stored chemical energy and recoverable sensible heat. It is important to note that despite the widely agreed definitions of these efficiencies, various authors have used different approaches to calculate them (Puig-Arnavat et al., 2013).

Sometimes, carbon conversion X_c, calculated using Eq. 23, is also reported to indicate the proportion of input carbon that is converted to products in a solar receiver.

$$X_c = \frac{n_{CO} + n_{CO_2} + n_{CH_4}}{n_C} \quad \text{Eq. 23}$$

where n_C, n_{CO}, n_{CO_2}, and n_{CH_4} are the molar flow rates of input carbon and product gases.

To achieve optimal energy conversion efficiency and identify suitable operating regimes, many solar gasification receiver concepts have been analytically modelled. Modelling a solar receiver involves solving the unsteady mass and energy conservation equations describing the interaction between reacting gas and solid phases in the receiver. Because of the elevated operating temperature range of solar receivers, radiative heat transfer dominates over other heat transfer modes such as convection and conduction. Monte Carlo (MC) ray-tracing is a commonly used method for modelling radiative heat transfer in solar receivers (Lipinski et al., 2005; von Zedtwitz et al., 2007). It has the advantage of being able to treat radiative heat transfer in complex 3D geometries and on anisotropic surfaces without simplifying assumptions.

The particle suspension in an entrained flow receiver and the particle bed in a packed or fluidized bed receiver are often modelled using Finite Volume (FV) techniques (von Zedtwitz & Steinfeld, 2005; Z'Graggen, 2008). Figures 2.29 presents the FV discretization approach used by Z'Graggen (2008) to model the SVR for gasification of carbonaceous materials. The reactor volume was divided into axis-symmetric concentric ring volume elements. Each volume element was assumed to be isothermal with uniform concentrations of gas species and particles. The MC ray-tracing method was used to model the radiative

heat absorbed by the polydisperse particle suspension in each element. A CFD model was coupled with the MC ray-tracing model to predict the flow of particle suspension. The model's predictions showed good agreement with the experimental measurements of outlet temperature and product composition. The effects of particle size, reactor geometry, particle feeding rate, and input solar power on the SVR's carbon conversion and solar to chemical energy efficiency were evaluated with the model with the aim of identifying suitable operating regimes.

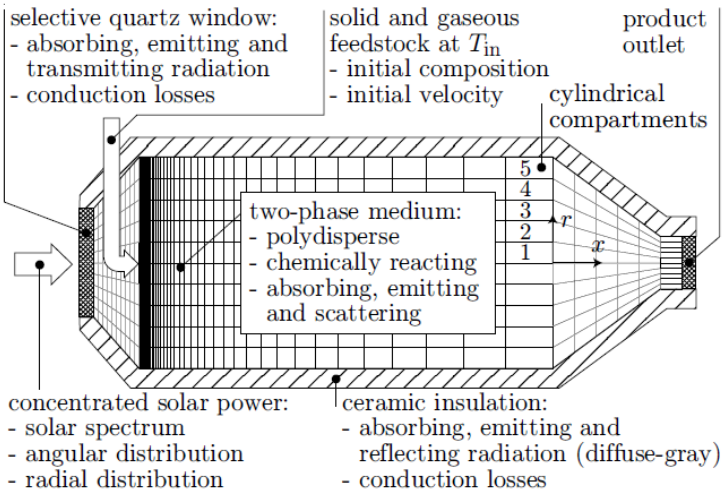

Figure 2.29: Axis-symmetric model domain of the Solar Vortex Reactor. Reproduced from Z'Graggen (2008).

In the quasi-transient model developed by von Zedtwitz and Steinfeld (2005) for investigating radiation driven steam gasification in a tubular quartz fluidized bed reactor, a one-dimensional FV discretization approach was employed to discretise the fluidized bed volume into a series of disc volume elements (Figure 2.30). Similar to the SVR model, each disc volume was assumed to be isothermal with uniform two-phase properties. The MC ray-tracing method was used to model the radiative heat transfer from the argon arc solar simulator to the quartz reactor and within the quartz reactor volume. The reactor model was

validated with experimentally measured radiative power flux distribution in the focal plane of the solar simulator, reactor product composition and temperature profile in the particle bed in both fluidized and packed bed states. Through experimental validation, von Zedtwitz and Steinfeld (2005) found that the one-dimensional discretization approach was appropriate for a fluidized bed because the vigorous mixing and high heat transfer rate within the bed could quickly dissipate the absorbed radiative heat in the bed volume.

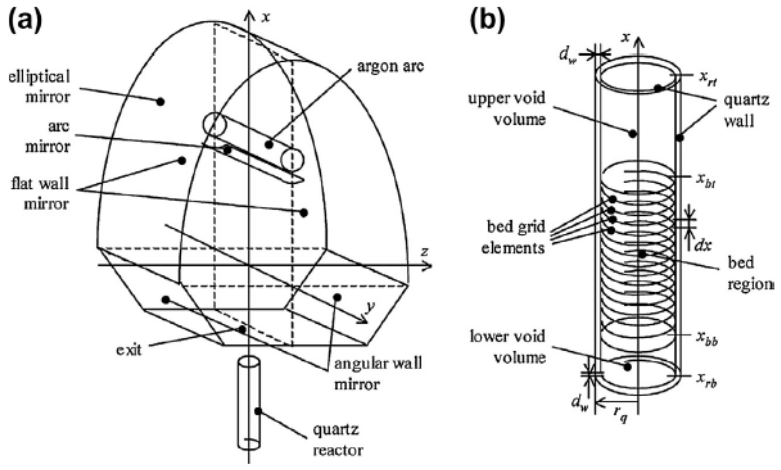

Figure 2.30: Model domain for a directly irradiated fluidized bed in a quartz reactor: (a) High flux solar simulator with the quartz reactor and (b) discretised elements of the quartz reactor. Reproduced from von Zedtwitz and Steinfeld (2005).

In addition, von Zedtwitz and Steinfeld (2005) reported that the fluidization quality inside the tubular reactor was seen to vary along the axial direction because as the fluidizing gas rises through the tubular reactor, it receives increased radiative heat, expands in volume and causes the fluidizing gas velocity to increase. Their video recording of the tubular reactor in operation showed a mostly packed bed in the lower bed region and a strongly bubbling fluidized bed in the upper bed region. This highlights the importance of accounting for gas expansion in solar receiver regions with high intensity radiation. The non-uniformity of

fluidization in the tubular reactor could be mitigated with a tapered fluidized bed design which allows for variable cross-sectional area in the axial direction.

2.5 Summary and Discussion of Research Gaps

Solar to chemical energy conversion efficiency is a commonly used indicator for solar gasification receiver performance. The sensitivity of this performance indicator to various important receiver scale parameters such as receiver length to diameter ratio, particle feeding rate, feedstock reaction kinetics, and input radiation flux have been studied in numerous analytical and experimental investigations (Puig-Arnavat et al., 2013). However, there currently is a gap in the understanding of the effect of particle scale parameters on solar to chemical energy conversion efficiency in the solar gasification process. While it is generally agreed that radiative heat transfer is the dominant heat transfer mode for relatively large particles with sizes greater than 100 microns, there is little information on the precise boundary between radiative and convective heat transfer dominance regimes. This can be attributed to the boundary being highly dependent on receiver operating conditions. Each receiver concept is likely to have a slightly different range of particle sizes for which the radiative heat transfer mode is dominant. Therefore, there is a need to develop a particle scale gasification model and investigate the relative dominance of heat transfer modes as well as the effect of particle scale parameters on the solar to chemical conversion efficiency.

Past studies concerning the particle entrainment and elutriation behaviour in an RFB have been conducted with non-reacting particles that maintain a constant size (Chevray et al., 1980; Saunders, 1986). Therefore, the particle residence time related findings from these studies may not be valid for the RFBR concept in which the feedstock particles undergo

gasification conversion and change in size and density over time. To make the matter more complicated, particle shrinking behaviour is dependent on particle size and gasification conditions. Feedstock particles have been found to exhibit different shrinking behaviours under different conditions in conventional chemical reactors. Therefore, to investigate the residence time and gasification conversion of a particle in the RFBR concept, the movement of the entrained particles need to be coupled with changing particle properties such as shrinking particle size and decreasing density.

CFD analyses of the flow field and particle deposition behaviour in existing entrained flow solar receiver concepts have demonstrated good agreement with experimental measurements (Ozalp et al., 2013; Chinnici et al., 2016). A commonly used CFD modelling approach to investigate the particle deposition on the receiver window is through coupling an established turbulence model such as the k-ε or Reynolds Stress Model with the Lagrangian particle tracking Discrete Phase Model (DPM). This approach has the benefits of relatively low computational cost and good agreement with experimental measurements. Hence, the flow field and particle deposition behaviour inside the RFBR concept can be investigated with the same approach. Unfortunately, the literature review did not yield any experimental flow field measurement inside an RFB with which the CFD model could be verified. However, there is one experimental study on the vortex flow inside a rotating vessel with radially injected air flow from porous cylindrical wall (Donaldson & Snedeker, 1962). While the vortex flow in this study does not necessarily represent the flow field inside an RFB, it is likely to be in the same flow regime and contain similar features because the rotating vessel is geometrically similar to an RFB and shares similar ranges of rotational

speeds and inlet air flow rates. Thus, the experimental measurements from this rotating vessel study could be used to partially verify the CFD model.

Since rotational speed introduces kinetic energy loss and rotating component wear, it is desirable for the RFBR to operate at low rotational speeds. At the present, there is very little information in literature about RFB fluidization characteristics and particle bed surface profile at low rotational speeds. Most studies concerning the fluidization quality in an RFB were conducted at sufficiently high rotational speeds that enable the formation of an evenly distributed particle bed with almost annular surface profile. Only one experimental study was conducted at a relatively low rotational speed of 26.2 rad/s in a vertically oriented RFB which resulted in a slumped particle bed with the top portion of the bed being thinner than the bottom portion. This presumably affected the pressure drop distribution across the bed in the axial direction and caused undesirable non-uniform fluidization. It is important to develop an understanding of bed surface profile and fluidization uniformity at low rotational speeds because the bed surface has a considerable influence on the radiative heat transfer in the RFBR cavity and non-uniform fluidization could lead to poor mixing, high particle entrainment rate and uneven exposure of particles to concentrated radiation.

There is also a gap in the understanding of the movement of the fluidization boundary in a partially fluidized RFB at low rotational speeds. Theoretical models developed for the pressure drop across a partially fluidized RFB assumes that the fluidization boundary is one dimensional and moves in the radial direction only. However, this is only valid for high rotational speed RFBs in which the centrifugal acceleration significantly exceeds the gravitational acceleration. In low rotational speed RFBs, the ratio of centrifugal to

gravitational accelerations is less extreme. Consequently, the fluidization boundary movement is likely to be two dimensional, moving in both radial and axial directions. Developing an understanding of the fluidization boundary movement in low rotational speed RFBs is important for modelling a partially fluidized RFB and predicting the fluidization quality inside the RFBR across a range of conditions.

2.6 Aim and Objectives of Current Research

The overall aim of the current research to is to develop the RFBR concept through quantitatively assessing its perceived benefits and improving the understanding of its operation. Four objectives have been developed to achieve this aim (Section 1.4).

The selection of suitable feedstock particles is very important to the solar to chemical energy conversion efficiency of a solar receiver because a mismatch of particle scale properties and receiver conditions can negatively affect the reaction kinetics, particle surface temperature, rates of heat and mass transfer, and gasification conversion. Therefore, the first objective of the present thesis is to develop a radiation driven single particle gasification model to assist in the matching of particle scale parameters to possible conditions in the RFBR cavity. This model would be used to explore the sensitivity of particle surface temperature, gasification conversion and heat transfer modes to variations in particle size, radiation flux incident on the particle surface and concentration of the gasification agent, H_2O, surrounding the particle. This analysis would provide an understanding of the influence of particle scale parameters on particle surface heat transfer mechanisms and solar to chemical energy conversion efficiency.

Carbon conversion is also an important receiver performance indicator. Less preparation and cycling of feedstock materials are required for solar receivers that can achieve sufficiently long particle residence time and high carbon conversion. Hence, the second objective of the present thesis is to develop an analytical model to assess the particle residence time and gasification conversion in the RFBR concept under various operating conditions. Due to the lack of information about the heat and mass transfer within the fluidized bed volume in the RFBR concept, a single particle modelling approach would have to be used instead of the usual finite volume modelling approach. The previously developed single particle gasification model would be coupled with idealised equations describing the motion of a particle traversing through the RFBR cavity. This analytical model would be used to investigate the sensitivity of particle conversion and residence time to variations in key receiver operating parameters, namely fluidized bed rotational speed, initial feedstock particle radius, radiation intensity, and particle release position. The effect of particle shrinking behaviour on the trajectory of an entrained particle in the RFBR could also be explored.

A major challenge in operating a directly irradiated solar receiver is maintaining the receiver window transparency and integrity in the presence of particle clouds. The injection of auxiliary window cleaning gas lowers the energy conversion efficiency of a solar receiver and adds to its operating cost. The feasibility and commercial viability of a directly irradiated solar receiver are closely linked to its capability to prevent particles from depositing on the receiver window. Thus, the third objective is to develop a CFD-DPM model to assess the RFBR concept's capability to mitigate particle deposition on the receiver window. This numerical model could overcome the limitations of the idealised flow field

assumption applied in the aforementioned analytical model and provide a reliable assessment of the influence of key geometrical and operating parameters, namely bed rotational speed, cavity length to diameter ratio and radial inlet gas velocity, on the flow field and particle deposition behaviour in the RFBR concept. The mechanisms affecting the particle deposition behaviour would be analysed to identify cost effective strategies to mitigate particle deposition on the receiver window or particle leakage through the open aperture in an alternative windowless RFBR configuration.

The fourth objective of the current research is to confirm the feasibility of operating the RFBR at low rotational speeds while maintaining an acceptable fluidization quality in the RFB volume. Physical experiments would be conducted to examine the fluidization characteristics and bed surface profile of an RFB operating at low rotational speeds that are insufficient to produce an annular bed surface. Unlike the previous experiments in literature, this experimental campaign will be conducted using a rectangular transparent acrylic chamber that is geometrically similar to a sector of an RFB. This experimental set up would enable the observation of the RFB tangential cross section and offer a glimpse of the fluidization quality inside the bed volume. More importantly, accurate measurements of the bed surface profile and fluidization boundary within a partially fluidized RFB could be made with high speed photography techniques. Through this experimental campaign, the influence of rotational speed, particle size and radial gas flow on the bed surface profile, movement of fluidization boundary and fluidization characteristics in a low speed RFB can be evaluated. This knowledge could help the development of the RFBR concept as well as other applications that involve a low rotational speed RFB.

Chapter 3

Particle Scale Heat Transfer

This chapter reports the development of a single char particle gasification model used for the assessment of the heat transfer on the particle surface and gasification conversion of a single char particle undergoing high intensity radiation driven gasification under typical solar receiver conditions. The purpose of this assessment is to develop an understanding of the effect of particle scale parameters on the relative dominance of the heat transfer mechanisms on the surface of a feedstock particle undergoing steam gasification. This understanding is essential for matching appropriate feedstock particle properties to specific solar receiver conditions for optimal solar to chemical energy conversion efficiency.

To ensure the reliability of model's predictions, the developed model is comprehensive and considers single particle gasification related phenomena such as the evolution of internal reactive surface area due to changing pore structure and peripheral fragmentation due to the collapse of particle outer structure at high conversion. The peripheral fragmentation behaviour is particularly important here because it changes the particle surface-to-volume ratio during gasification conversion and could significantly affect the relative dominance of heat transfer mechanisms. The mass transport of gas species within the porous particle volume is calculated using the Dusty-Gas Model which accounts for the effects of Knudsen

diffusion and multi-component molecular diffusion. The char specific properties in the model, namely critical porosity value for predicting fragmentation, reaction kinetics and semi-empirical correlation for the evolution of internal reactive surface area, are sourced from the experimental work of Mermoud et al. (2006) who investigated the pyrolysis and steam gasification of wood char particles.

The developed model was used to examine the effects of important feedstock particle parameters, namely radiation intensity incident on the particle surface, initial particle diameter and concentration of H_2O surrounding the particle, on particle surface temperature, gasification conversion and relative dominance of heat transfer modes. It was found that faster reaction kinetics could lead to higher solar to chemical energy conversion efficiency, and the dominant heat transfer mode for heat dissipation from the particle surface is mainly dependent on the particle surface-to-volume and the temperature difference between the particle surface and surrounding environment. Particles with diameters greater than 700 microns were seen to attain higher particle surface temperatures due to their larger surface for radiation absorption and lower convection heat loss. This accelerates the reaction kinetics and allows these particles to convert a greater amount of absorbed radiative heat into stored chemical energy, increasing the solar to chemical energy conversion efficiency. It must be noted that the single particle model presented here cannot account for the volumetric effects of particle clouds. The findings derived are only valid for cases where: the particulate phase is dilute; there is little heat exchange between particles; and the heat dissipated by particles does not noticeably affect the temperature of the surrounding fluid.

Statement of Authorship

Title of Paper	Particle-Scale Investigation of Heat Transfer in Radiation-Driven Char Gasification
Publication Status	☑ Published ☐ Accepted for Publication ☐ Submitted for Publication ☐ Unpublished and Unsubmitted work written in manuscript style
Publication Details	Z. Lu, M. Jafarian, M. Arjomandi, & G. Nathan, 2016, "Particle-Scale Investigation of Heat Transfer in Radiation-Driven Char Gasification", Chemical Engineering & Technology, vol. 39, no. 10, pp.1903-1911

Principal Author

Name of Principal Author (Candidate)	Zhao Lu
Contribution to the Paper	Developed ideas, performed numerical simulations, interpreted data, wrote manuscript, and acted as the corresponding author
Overall percentage (%)	70
Certification:	This paper reports on original research I conducted during the period of my Higher Degree by Research candidature and is not subject to any obligations or contractual agreements with a third party that would constrain its inclusion in this thesis. I am the primary author of this paper.
Signature	Date 17/04/2018

Co-Author Contributions

By signing the Statement of Authorship, each author certifies that:

i. the candidate's stated contribution to the publication is accurate (as detailed above);
ii. permission is granted for the candidate in include the publication in the thesis; and
iii. the sum of all co-author contributions is equal to 100% less the candidate's stated contribution.

Name of Co-Author	Mehdi Jafarian
Contribution to the Paper	Supervised development of work, interpreted data, and edited manuscript
Signature	Date 17/04/2018

Name of Co-Author	Maziar Arjomandi
Contribution to the Paper	Supervised development of work, interpreted data, and edited manuscript
Signature	Date 17/04/2018

Name of Co-Author	Graham Nathan		
Contribution to the Paper	Supervised development of work, interpreted data, and edited manuscript		
Signature		Date	17/04/2018

Particle Scale Investigation of Heat Transfer in Radiation Driven Char Gasification

Zhao Lu*

Mehdi Jafarian

Maziar Arjomandi

Graham J. Nathan

Centre for Energy Technology, School of Mechanical Engineering, The University of Adelaide, SA 5005, Australia

*Corresponding author: zhao.lu@adelaide.edu.au

Keywords: gasification, steam, modelling, heat transfer.

Abstract

A model of the steam gasification of a single char particle driven by high intensity radiation was developed and experimentally verified with available measurements in literature. This was used to explore the sensitivity of particle surface temperature and heat transfer mechanisms to variations in particle diameters (100μm to 1900μm), radiative heat flux (1MW/m^2 to 4MW/m^2) and the concentration of the gasification agent, H_2O (0.2 to 0.8 mole fraction) under typical conditions for solar gasification reactors. The results highlight the importance of particle diameter in influencing solar to chemical energy conversion efficiency and assist in the selection of appropriate feedstock particles to match the conditions in specific solar gasification reactors.

3.1 Introduction

Concentrated Solar Thermal (CST) technology is gradually gaining attention due to the increased awareness of the environmental impacts of fossil fuels. One potential CST application is solar thermal gasification, which transforms steam and solid carbon rich feedstocks such as biomass char into an easily purified and energy rich synthesis gas that can be utilized in Integrated Gasification Combined Cycle (IGCC) power systems, liquid fuels production (Perkins & Weimer, 2009) or as a feedstock for petrochemical products (Gunardson, 1997). Unlike conventional autothermal gasification, solar thermal gasification does not rely on combustion to produce the heat to drive the endothermic gasification process. As a result, it produces a greater output of syngas with higher H_2O to CO ratio and presents a significant opportunity to reduce pollutant discharge.

Numerous studies have been conducted on the solar thermal gasification of carbonaceous materials in both directly and indirectly irradiated reactors, including fluidized bed reactors (von Zedtwitz & Steinfeld, 2005; Tommer, 2006; Kodama et al., 2008), packed bed reactors (Piatkowski et al., 2009), multiple tube vortex flow reactors (Melchior et al., 2009) and vortex flow reactors (Z'Graggen et al., 2006). These exploratory studies provide insight into the relationship between reactor specific heat and mass transfer conditions, feedstock type and product composition. In addition, experimentally verified reactor scale models have been developed to investigate the sensitivity of product composition and solar to chemical energy conversion efficiency to operating parameters such as reactor geometry, particle feed in rate and solar radiation intensity (Kodama et al., 2002; Trommer, 2006). However, these reactor scale models are unable to incorporate the effect of particle physical properties or

investigate particle scale phenomena such as intra-particle mass and heat transport. Furthermore, exposing char particles to high intensity radiation increases the particle surface temperature, resulting in significant changes to the relative dominance of heat transfer modes on the particle surface which influences reactor solar to chemical conversion efficiency. Therefore, the design and optimization of solar gasification reactors require a particle scale model capable of capturing the effects of intra-particle phenomena and predict the response of particle surface temperature to high intensity radiation.

Although numerous single particle gasification models have been developed based on both experimental and theoretical investigations, none of these account sufficiently for heat transfer in sufficient detail to account for the heating by high flux radiation (Srinivas & Amundson, 1980; Wang & Bhatia, 2001; Mermoud et al., 2006). These models are developed to study particle conversion and intra—article mass transport by accounting for temporal evolution of pore structures, multicomponent diffusion, and peripheral fragmentation. Some of these models neglect heat transfer completely and assume the particle is at a constant temperature (Zygourakis & Amundson, 1982: Xu et al., 2011). Others assume uniform intra-particle temperature and only consider external heat transfer, which is an appropriate assumption for a conventional gasifier with moderate heating rates (Wang & Bhatia, 2001; Gomez-Barea et al., 2006). These assumptions cannot be relied on for a particle undergoing solar driven gasification, where significant gradients in temperature are expected due to the high heating rates. The model developed by Mermoud et al. (Mermoud et al., 2006) accounts for both internal and external heat transfer. However, it simplifies internal mass and heat transfer by using Fick's Law for diffusive transport and an empirical correlation for thermal conduction, which is unsuitable for the temperature

range inside a typical solar reactor. There is therefore a need to develop a particle gasification model with a focus on transient thermal transport phenomena relevant to solar reactors.

Nevertheless, heat transfer models are available for other porous solid thermal conversion processes such as calcination and pyrolysis, so that it is possible to adapt their transient thermal modelling approaches and analytical techniques to gasification. For opaque particles, temperature dependent surface emissivity was used by Jafarian et al. (2013) in their study of the heat transfer modes and temperature on the surface of an opaque oxygen carrier particle under high flux radiation. For semi-transparent particles, Yue & Lipinski (2015) used Rosseland Diffusion Approximation to determine the radiative heat transfer within a $CaCO_3$ particle undergoing solar radiation driven calcination. Both Jafarian et al. (2013) and Yue & Lipinski (2015) models assumed constant radius particles and therefore, cannot account for the effect of particle shrinkage in gasification. The effect of particle shrinkage on heat transfer has been considered by Di Blasi (1996) in his model of biomass pyrolysis under thermal radiation. However, the rate of change in particle radius was determined by empirical shrinkage parameters which are only suitable for specific pyrolysis conditions. A more robust approach to modelling particle shrinkage in gasification is detailed in the work of Fuertes and Marban (1994) which utilizes the concept of critical porosity to predict local pore structural integrity and disintegration. Hence, to develop a model suitable for the present investigation, a combination of approaches from previous thermal conversion models is required.

In the light of above, the present work aims to develop an opaque single particle model relevant to solar thermal gasification by combining experimentally verified single particle gasification modelling approaches of Mermoud et al. (2006) and Xu et al. (2011), radiative heat transfer analysis of Jafarian et al. (2013) and Di Blasi (1996), and the critical porosity for predicting peripheral fragmentation by Fuertes and Marban (1994). The present work further aims to generate new understanding of the relatively contributions of heat transfer modes involved in gasification at the particle scale. More specifically, it aims to assess their sensitivity to key solar gasification parameters, namely radiative heat flux, particle diameter and the availability of the gasification agent (H_2O) so that suitable particle physical properties can be matched to reactor conditions for maximum solar to chemical energy conversion efficiency.

3.2 Methodology

3.2.1 Problem statement

An opaque, porous and non-uniform wood char particle is exposed to high intensity radiation in a gasification reactor like environment consisting only of the gasification, steam (H_2O), and the inert carrier gas, N_2. For simplicity and robustness, the present work only considers Steam Gasification reaction shown in Eq. 1:

$$C + H_2O \rightarrow CO + H_2 \qquad \text{Eq. 1}$$

While numerous other reactions such as Boudouard, Methanation and Water Gas Shift reactions often proceed in parallel with Steam Gasification reaction, their effect on solid char conversion is not nearly as influential. For instance, Boudouard reaction, the second

fastest gasification reaction, is estimated to be an order of magnitude slower than the Steam Gasification reaction (Higman, 2008). Mermoud et al. (2006) showed that gasification experimental measurements can be reliably modelled even with only Steam Gasification reaction,

During gasification, H_2O diffuses into the particle's pores to fuel the gasification process, which in turn consumes the solid char to produce CO and H_2. The product gases diffuse in the reverse direction to the particle surface and external environment. Due to the difference in the volumes of the product gases and the bulk gas mixture surrounding the particle, the release of the product gases is assumed to have negligible effect on the composition of the bulk gas mixture.

The main assumptions used in the model are as follows:

1. The feedstock particle is comprised of porous spherical layers, with each layer being of uniform porosity and porosity varying only between the layers (in the radial direction).
2. The feedstock particle has the same chemical properties as the wood char used by Mermoud et al. (2006) for the purpose of model verification, although alternative properties may be specified.
3. Bulk gas mixture composition, temperature and pressure are uniform at the particle's surface.
4. The particle diameter decreases in a step-wise manner as each layer disintegrates by fragmentation as predicted by the critical porosity approach detailed in Fuertes & Marban (1994).

5. The pressure gradient within the highly porous particle is assumed to be sufficiently small to have negligible impact on the transport of gaseous species.
6. The char particle is assumed to be completed devoilatized and thus, is composed of pure carbon.
7. The surface area of the particle exposed to diffuse high flux radiation at any instant is equal to its cross sectional area. This assumption is conservative, but could readily modified for various solar reactor configurations.
8. The particle is assumed to rotate sufficiently quickly for the radiative heat flux to be distributed uniformly over the particle's surface.
9. Gaseous species are non-radiatively participating.
10. The surroundings are black and enclose the particle.
11. The particle surface is assumed to be opaque because char has very high absorptivity and the particle diameters investigated in the present work are sufficiently large, resulting in relatively thick discretised layers, which according to the work of Foster and Howarth (1967) should stop the transmission of approximately 90% of the infrared radiation in a conventional gasifier at 1500K.
12. The concentration of particles in the present study is assumed to be sufficiently dilute such that there is negligible inter-particle radiation heat transfer.

3.2.2 Mass conservation

There are three gas components involved in the Steam Gasification reaction, namely H_2O, H_2 and CO (termed species i = 1 to 3). The diluent, N_2 (termed species i = 4) is included in the model as the inert carrier gas and does not participate in the reaction.

The intrinsic reaction rate $R_{intrinsic}$ is estimated using the Langmuir-Hinshelwood formulation following Dasappa et al., (1994):

$$R_{intrinsic} = -\frac{k_1 p_{h_2 o} + k_4 p_{h_2 o} p_{h_2} + k_5 p_{h_2 o}^2}{1 + k_2 p_{h_2} + k_3 p_{h_2 o}} \quad \text{Eq. 2}$$

The coefficients k_1 to k_5 are described by an Arrhenius law, shown in Eq. 3 that depends on activation energy E, a kinetic pre-exponential factor A and temperature T. The values of kinetic pre-exponential factors and activation energies are taken from Mermoud et al., (2006), whose experimental measurements are used to verify the present model.

$$k_j = A_j \exp(-\frac{E_j}{RT}) \quad \text{Eq. 3}$$

Accounting for the effect of internal reactive surface area S_r and apparent particle density $\rho_{apparent}$, char gasification R_{char} is:

$$R_{char} = R_{intrinsic} S_r \rho_{apparent} \quad \text{Eq. 4}$$

The determination of S_r depends on the pyrolysis process and the source of char. Mermoud et al. (2006) proposed the simple correlation in Eq. 5 to approximate the internal reactive surface area of birch wood char, which has been experimentally verified to be accurate for conversion extents up to 60%.

$$S_r = S_r^0(\frac{1}{1 - X_{conversion}}) \quad \text{Eq. 5}$$

Particle conversion $X_{conversion}$ is defined as follows.

$$X_{conversion} = \frac{m_{init} - m}{m_{init}} \quad \text{Eq. 6}$$

The apparent particle density $\rho_{apparent}$ is a function of particle conversion $X_{conversion}$. ρ_{char} and ρ_{gas} are the solid phase char and gas mixture densities respectively, as reported in Table 1.

$$\rho_{apparent} = \rho_{char}(1 - X_{conversion}) + \rho_{gas}X_{conversion} \quad \text{Eq. 7}$$

The rate of particle conversion $\frac{\partial X_{conversion}}{\partial t}$ can be calculated from R_{char} as shown in Eq. 8.

$$\frac{\partial X_{conversion}}{\partial t} = -\frac{M_{char}}{\rho_{char}}R_{char} \quad \text{Eq. 8}$$

where M_{char} is the molecular weight respectively of solid phase char.

Under the stated assumptions, the mass balance equations for the four gas components can be written in a 1-D spherical coordinate system as:

$$\frac{\partial(\varphi C_i)}{\partial t} + \frac{1}{r^2}\frac{1}{\partial r}(r^2 N_i) = \nu_i R_{char} \quad \text{Eq. 9}$$

with the following initial and boundary conditions:

$$C_i(r,0) = C_{i,bulk} \qquad \text{Eq. 10}$$

$$\frac{\partial C_i}{\partial r}(0,t) = 0, \qquad for\ t \geq 0 \qquad \text{Eq. 11}$$

The net flux of gaseous components is evaluated using the Dusty-Gas Model which incorporates the effects of Knudsen diffusion into the Stefan-Maxwell multi-component molecular diffusion model (Krishna & Wesselingh, 1997). The net flux N_i of a gas component can be related to the component concentration C_i and pressure gradient ∇P through the following equation.

$$-\frac{\varphi}{\tau}\left(\nabla C_i + \frac{B_0}{D_{iK}\mu} C_i \nabla P\right) = \sum_{j=1}^{4} \frac{y_j N_i - y_i N_j}{D_{ij}} + \frac{N_i}{D_{iK}} \qquad \text{Eq. 12}$$

where D_{ij} and D_{iK} are the molecular and Knudsen diffusion coefficients respectively.

Due to the small size and high porosity of the particles modelled in the present work and slow release of gaseous products during gasification, the pressure gradient ∇P present within the modelled particle is assumed to be sufficiently small for the its effects on mass transport to be considered negligible.

The Knudsen diffusion coefficient of the *i*th component $D_{i,K}$ is evaluated using Eq. 13.

$$D_{iK} = \frac{d_{pore}}{3}\sqrt{\frac{8RT}{\pi M_i}} \qquad \text{Eq. 13}$$

where d_{pore} is the mean particle pore diameter which can be approximated using the internal surface area and porosity.

The initial mean diameter of the particle pores was taken from the work of Mermoud et al. (2006) who measured the mean particle pore diameter of wood particles using Scanning Electron Microscopy (SEM).

The binary molecular diffusion coefficient D_{ij}, is calculated using the correlation provided by Welty et al. (2014):

$$D_{ij} = \frac{0.001858T^{3/2}\sqrt{\left(\frac{1}{M_i}\right) + \left(\frac{1}{M_j}\right)}}{P_t{\sigma_{ij}}^2\Omega_D} \qquad \text{Eq. 14}$$

To account for the reduction of radius due to peripheral fragmentation, the concept of critical porosity ε_{cr} is incorporated in the model, and the change in particle radius r_p is as follows:

$$\frac{\partial r_p}{\partial t} = -\frac{\partial \varphi(r_p)}{\partial t} \Big/ \frac{\partial \varphi(r_p)}{\partial r} \quad (for\ \varphi(r_p) > \varphi_{cr}) \qquad \text{Eq. 15}$$

$$\frac{\partial r_p}{\partial t} = 0 \quad (for\ \varphi(r_p) < \varphi_{cr})$$

The surface of the particle is assumed to neither accumulate mass nor react, so that the net flux of gas components through the surface depends only on the external convective mass transfer.

$$\mathbf{N}(r_p) = k_c[\mathbf{C_b} - \mathbf{C}(r_p)] \quad \text{Eq. 16}$$

The concentration of the gaseous species $\mathbf{C_b}$ in the bulk gas flow surrounding the particle is assumed to be constant and are reported in Table 1. Here, k_c is the mass transfer coefficient and can be evaluated from the forced convective mass transfer correlation for a spherical particle in a bulk gas flow with velocity V_{gas} (Bharadwaj et al., 2004). k_c is defined as a function of Sherwood number Sh, effective diffusion coefficient at the particle surface D_{eff} and particle radius r_p.

$$k_c = \frac{ShD_{eff}}{2r_p} \quad \text{Eq. 17}$$

$$Sh = 2 + (0.4Re^{0.5} + 0.06Re^{0.66})Pr^{0.4} \quad \text{Eq. 18}$$

Table 1: Numerical Parameters for the Simulations

Variable	Unit	Baseline Value	Variation	Reference
σ	[$Wm^{-2}K^{-4}$]	5.670e-8		
$d_{pore,0}$	[µm]	10		Mermoud et al. (2006)
ΔH_R	[J/mol]	135.8		Mermoud et al. (2006)
ρ_{char}	[kg/m^3]	1900		Mermoud et al. (2006)
φ_{cr}		0.98		Mermoud et al. (2006)
S_r^0	[m^2cm^{-3}]	275		Mermoud et al. (2006)
V_{gas}	[ms^{-1}]	0.14		
T_{feed}	[K]	773		

T_g	[K]	1273		Piatkowski et al. (2009) Z'Graggen et al. (2006)
T_{srn}	[K]	1273		Piatkowski et al. (2009) Z'Graggen et al. (2006)
P	[atm]	1		
r_p	[µm]	50	50-400	
q_{solar}	[MW/m^2]	1	1-4.5	
$y_{H_2O,bulk}$		0.2	0.2-0.9	
$y_{CO,bulk}$		0		
$y_{H_2,bulk}$		0		
$y_{N_2,bulk}$		0.8	0.8-0.1	

3.2.3 Energy conservation

The present model considers conduction, convection, radiation and reaction. Upon being exposed to high intensity radiation, the particle surface absorbs a fraction of incident solar radiation $\dot{Q}_{abs}$. The absorbed solar radiation is then conducted into the particle as $\dot{Q}_{conduction}$ to drive the endothermic gasification process, re-radiated to the surroundings as $\dot{Q}_{re-radiation}$ or convected to the bulk gas flow as $\dot{Q}_{convection}$.

The governing equation for energy conservation in 1-D spherical coordinate system, according to Jafarian et al., (2013) is:

$$(C_{p,s}\rho_{char}(1-\varphi)+C_{p,g}\rho_{gas}\varphi)\frac{\partial T}{\partial t}+\frac{1}{r^2}\frac{1}{\partial r}(r^2\lambda_{eff}\frac{\partial T}{\partial r})=R_{char}\Delta H_R \qquad \text{Eq. 19}$$

where the effective thermal conductivity λ_{eff} which includes conduction by gas mixture and solid phase and radiative heat transfer within particle pores. According to Larfeldt et al., (2000), λ_{eff} can be expressed as follows:

$$\lambda_{eff} = \lambda_s(1-\varphi) + \lambda_g\varphi + 4\sigma T^3 d_{pore}\varepsilon \qquad \text{Eq. 20}$$

The boundary and initial conditions are given by:

$$T(r,0) = T_{feed} \qquad \text{Eq. 21}$$

$$\frac{\partial T}{\partial r}(0,t) = 0, \qquad for\ t \geq 0 \qquad \text{Eq. 22}$$

$$\underbrace{\lambda_{eff}\ \frac{\partial T}{\partial r}(r_p,t)}_{\dot{Q}_{conduction}} = -\underbrace{\frac{Nu\lambda_g}{2r_p}(T(r_p,t)-T_g)}_{\dot{Q}_{convection}} - \underbrace{\sigma\varepsilon\left(T(r_p,t)^4 - T_{srn}^4\right)}_{\dot{Q}_{re-radiation}} + \alpha\underbrace{\frac{q_{solar}}{4}}_{\dot{Q}_{abs}}$$

$$for\ t \geq 0 \qquad \text{Eq. 23}$$

The total hemispherical absorptivity α is equal to emissivity ε and can be determined using the correlation as reported in Brewster & Kunitomo (1984):

$$\alpha = 0.78 + 0.00269T^{0.5} \qquad \text{Eq. 24}$$

The Nusselt number Nu for a spherical particle in a bulk gas flow with velocity V_{gas} is as follows:

$$Nu = 2 + (0.4Re^{0.5} + 0.06Re^{0.66})Sc^{0.4} \quad \text{Eq. 25}$$

3.3 Model Verification

Figure 3.1 compares the predictions of the present model with the experimental measurements of conversion of a single char particle for three different constant reactor temperature cases without solar irradiation. It can be seen that the model predictions follow the experimental measurements closely for the majority of the gasification process. Slight departures of the calculation from the measurements are seen for T = 1103K and t > 5000s, which is consistent with the limited understanding of peripheral fragmentation towards the end of the gasification process. As can be observed in the comparison, the effect of peripheral fragmentation on conversion is only significant for extended gasification at low reactor temperatures. However, for the higher rates of gasification at temperatures above 1203K, the inaccuracy introduced by peripheral fragmentation can be considered negligible.

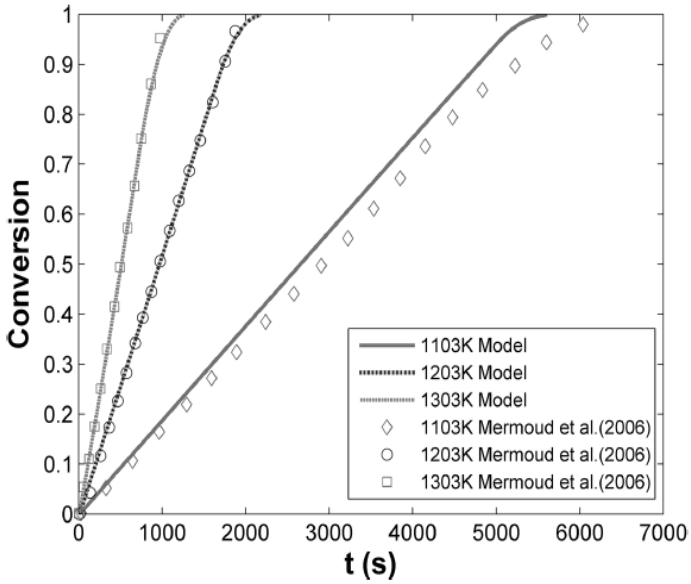

Figure 3.1: Particle conversion as a function of time predicted by the present model for varying reactor temperatures compared with the experimental measurements of Mermoud et al. (2006).

Figure 3.2 compares the predictions of the present model with the experimental measurements for varying particle diameters. The present model agreed with the experimental measurement to within 10%, indicating that it is reliable in assessing the effects of gasification agent availability and particle diameter on particle conversion under these conditions.

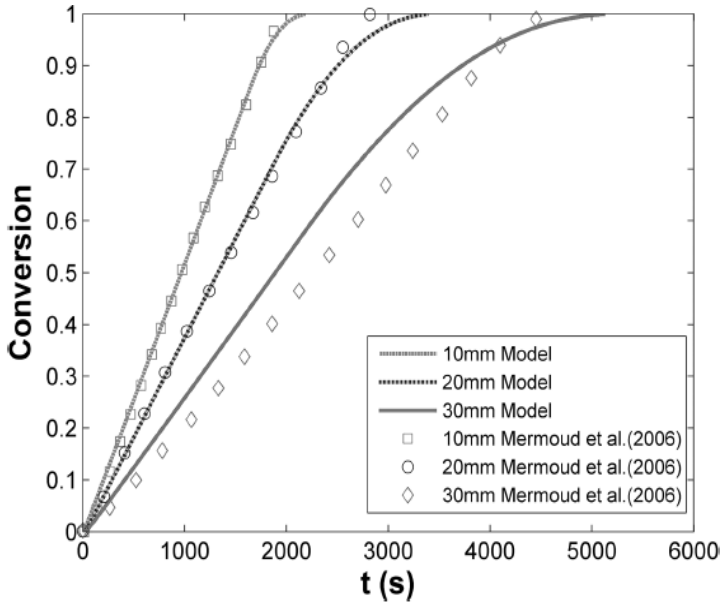

Figure 3.2: Particle conversion as a function of time predicted by the present model for varying particle diameters compared with the experimental measurements of Mermoud et al. (2006).

The close resemblance in the shape of the experimental measurements and model predictions, in Figures 3.1 and 3.2, confirms that the present model accounts reasonably well for the effects of the dominant heat and mass transfer mechanisms that control the rate of particle conversion.

3.4 Results and discussion

3.4.1 Effect of radiation intensity

Figure 3.3 presents the calculated difference between particle surface and surroundings temperatures as a function of time for various radiative heat fluxes under the baseline conditions in Table 1. As expected, the difference in temperatures depends strongly on the radiative heat flux. The stepwise increases in radiative heat flux lead to approximately stepwise increases in particle surface temperature. This implies that, under the baseline conditions, the effect of convection and re-radiation cooling is proportional to radiative heat flux and particle surface temperature. In addition, exponential reductions in conversion time are observed due to approximately stepwise increases in particle surface temperature. This indicates that the gasification process, under the baseline conditions, is in the kinetically controlled reaction regime.

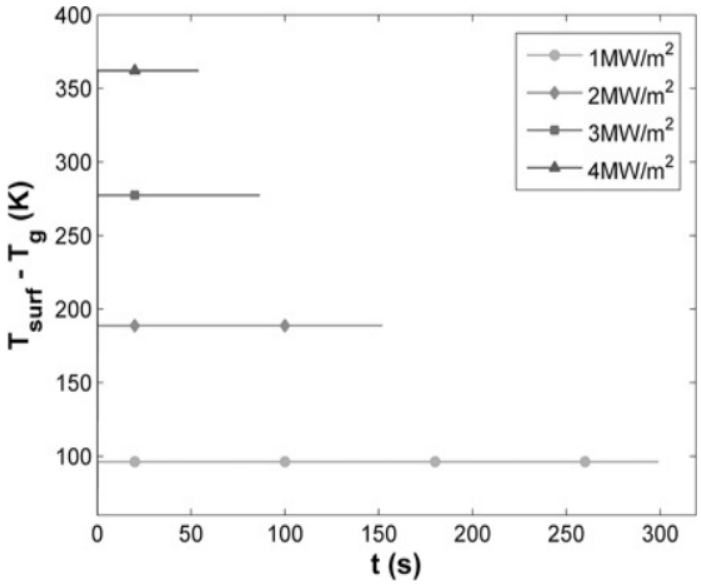

Figure 3.3: Predicted differences between the particle surface temperature and the temperature of the surroundings, as a function of time, for selected radiative heat fluxes.

Figure 4 presents (a) the fraction of solar radiative heat $\dot{Q}_{solar}$ absorbed on the particle surface $X_{absorbed}$, and the fractions of absorbed radiative heat $\dot{Q}_{abs}$ dissipated through (b) conduction $X_{conduction}$, (c) convection $X_{convection}$ and (d) re-radiation $X_{re-radiation}$ during the gasification of a char particle under the baseline conditions in Table 1 exposed to various radiative heat fluxes. It can be seen that both $X_{re-radiation}$ and $X_{absorbed}$ are positively correlated with radiative heat flux, which can be explained by the increased difference between particle surface and surrounding temperatures and emissivity due to higher radiative heat flux. $X_{convection}$ is observed to decrease with increasing radiative heat flux mostly because of increased $X_{re-radiation}$. The effect of radiative heat flux on $X_{conduction}$ is not as clear as the other components. Increasing the radiative heat flux results in increased particle surface temperature and gasification rate which leads a higher demand for energy and rate of solar to chemical energy conversion. Hence, $X_{conduction}$ can be increased with radiative heat flux. On the other hand, increasing the radiative heat flux also leads to a higher temperature difference between the particle and its surroundings. As a result, more heat is lost to the surroundings through convection and re-radiation, resulting in a decreased $X_{conduction}$. The balance of these two opposing mechanisms determines the net effect of radiative heat flux on $X_{conduction}$. For instance, increasing the flux from 1MWm^{-2} to 2MWm^{-2} resulted in a slight decrease in $X_{conduction}$ while a noticeable increase can be seen by increasing the flux from 2 MWm^{-2} to 3 MWm^{-2}.

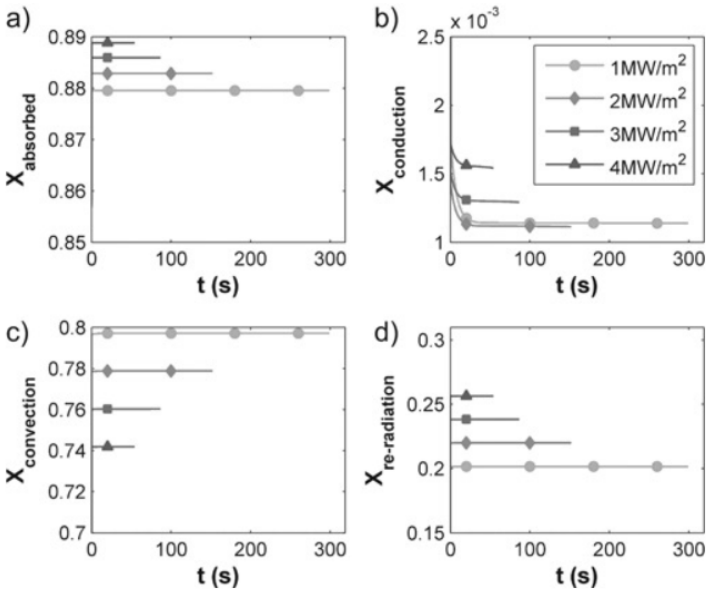

Figure 3.4: Sensitivity to variations in the radiative heat flux of the fractions (a) of heat absorbed by the particle surface to the total radiative heat, (b) of the heat conducted into the particle relative to the absorbed heat, and (c) of the heat lost through re-radiation and (d) convection relative to the absorbed heat.

3.4.2 Effect of particle diameter

The predicted deviations of particle surface temperature from the surroundings as a function of time for variations in particle diameter are presented in Figure 3.5. The relationship between particle diameter and surface temperature appears to be non-linear. An increase of 150K is observed for increasing the particle diameter from 100µm to 700µm. However, this sizeable increase is not repeated for further increments in particle diameter. The increases in particle surface temperature from 700µm to 1300µm and 1300µm and 1900µm are approximately 40K and 10K respectively. This shows that as the particle diameter increases, the radiative heat gained through increased cross sectional area approaches the energy lost to convection and re-radiation due to increased surface area and temperature. As seen in Figure 3.5, larger particles attain faster gasification rates and require less time to achieve complete conversion, which may seem counter-intuitive.

One important thing to note in Figure 3.5, is the more gradual cooling of larger particles near full conversion. One possible explanation for this is the difference in the reaction control regimes of different sized particles. A small particle, such as the 100μm diameter particle, has a low volume to surface ratio, which enables more gasification agent to be diffused into the particle than consumed by the particle's internal reactive surface area, as determined by its volume. In addition, the small particle receives less radiation and therefore, is colder and more uniform in temperature than a larger particle. For these reasons, the conversion rate within the small particle is likely to be uniform, meaning the whole particle reaches critical porosity and disintegrates by fragmentation in a very short period of time. In the case of the 100μm diameter particle, the disintegration time is so short that the time step of the solution procedure is unable to capture its rapid cooling and temperature drop. In contrast, a large particle, for instance, the 1900μm particle, consumes more gasification agent than that can be provided by surface diffusion. Thus, the concentration of gasification agent and conversion rate is skewed towards the particle surface, which incidentally is also at a higher temperature, leading to further skewedness. Therefore, the particle volume near the surface reaches critical porosity far earlier than the inner volume; the reduction of particle diameter occurs at a lower conversion extent and stretches over a relatively long period of time, resulting in the gradual cooling seen in Figure 3.5. Another noteworthy observation in Figure 3.5 is the slight surface temperature increase near the end of conversion for large particles such as the 1900μm diameter particle. This is likely due to the significant changes in particle mass and energy requirement throughout conversion for large particles.

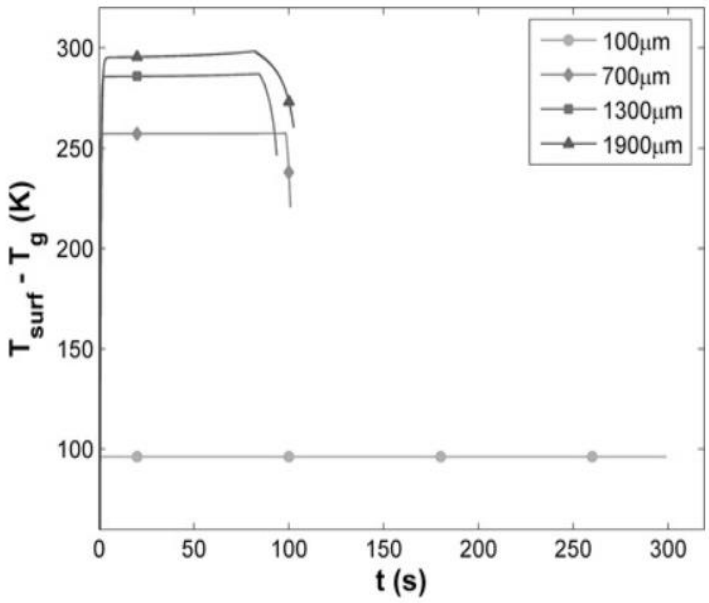

Figure 3.5: Predicted difference between the temperature of the particle surface and its surroundings as a function of time for selected particle diameters.

Figure 3.6 presents the sensitivity of calculated heat transfer component fractions to variations in particle diameter. $X_{absorbed}$ is seen to be higher for larger particles due to greater solar heat absorption and particle surface temperature. $X_{conduction}$ is also seen to increase with particle diameter, which can be attributed to the exponentially increased particle mass and gasification energy requirement of large particles. Because of their greater particle mass, larger particles undergo a more significant reduction in mass and energy requirement throughout conversion. This results in the sharp drop in $X_{conduction}$ and causes the slight increase in temperature before disintegration in Figure 3.5. The relative dominance of $X_{convection}$ and $X_{re-radiation}$ change significantly with particle diameter. Re-radiation cooling is the dominant cooling mechanism for particle diameters of 700µm to 1900 µm and convection cooling for the 200 µm baseline diameter particle. This highlights the importance of selecting appropriate feedstock particle size to suit specific solar reactor conditions.

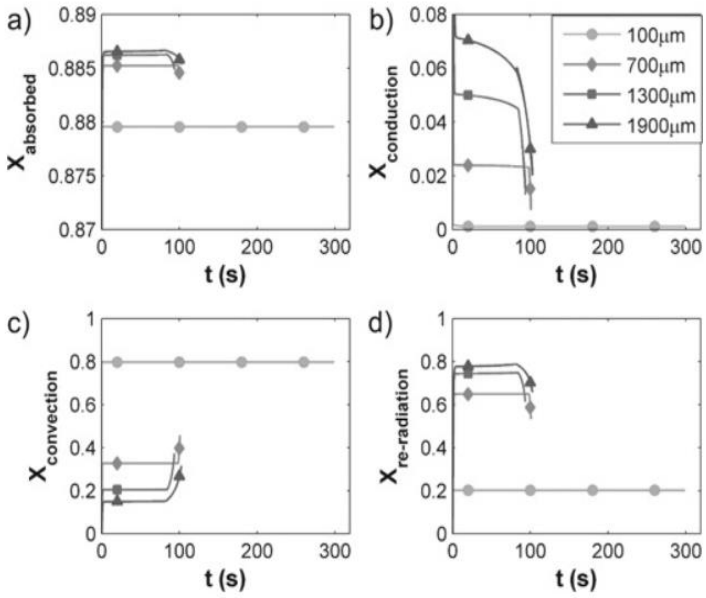

Figure 3.6: Sensitivity to variations in particle diameter of the fractions (a) of heat absorbed by the particle surface to the total radiative heat, (b) of the heat conducted into the particle relative to the absorbed heat, and (c) of the heat lost through re-radiation and (d) convection relative to the absorbed heat.

3.4.3 Effect of H_2O Mole Fraction

Figure 3.7 shows the predicted particle surface temperature as a function of time for different mole fractions of the gasification agent, H_2O. It can be seen that due to the relatively slow gasification conversion rate under the baseline conditions, the particle surface temperature is not greatly influenced by increases in H_2O mole fraction and associated minor increases in gasification rate and energy consumption. Increasing the mole fraction from 0.2 to 0.8 only results in an increase of 10K in particle surface temperature. It is interesting to note that the slight increase in the thermal conductivity of the bulk gas mixture is not sufficient to produce any meaningful changes in particle surface temperature due to the H_2O being a poor conductor in the superheated state. H_2O mole fraction demonstrates a stronger influence on conversion time, with the greatest reduction in conversion time being 40 seconds for the increase from 0.2 to 0.4. Subsequent increases

result in vastly diminished reductions in conversion time due to the gasification process shifting deeper into the kinetically controlled reaction regime.

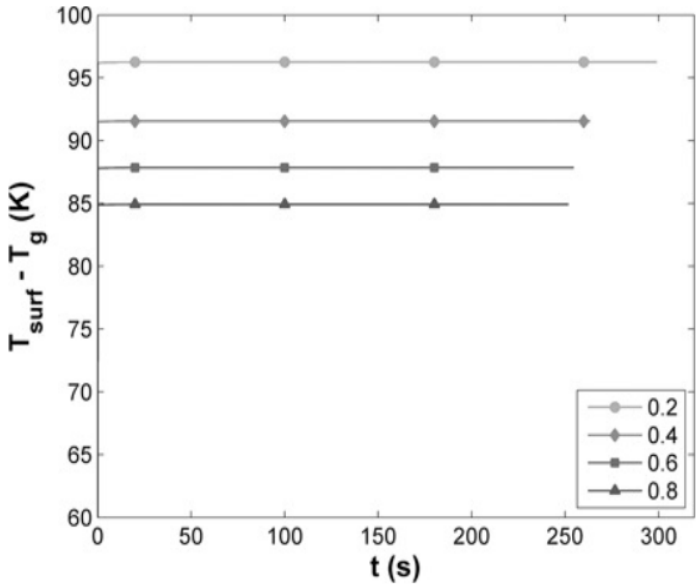

Figure 3.7: Predicted difference between the temperature of the particle surface and its surroundings as a function of time for selected H_2O mole fractions.

Figure 3.8 presents the sensitivity of calculated heat transfer mode fractions to variations in H_2O mole fraction. It can be seen that H_2O mole fraction has very little influence on the relative significance of various heat transfer component fractions on the particle surface and shifts slightly them in a very predictable manner. It should be noted that the present work only considers a single particle undergoing solar radiation driven gasification. In a physical solar gasification reactor containing many particles, the effect of the H_2O mole fraction on heat transfer is expected to be more pronounced but still less influential compared to other reactor parameters.

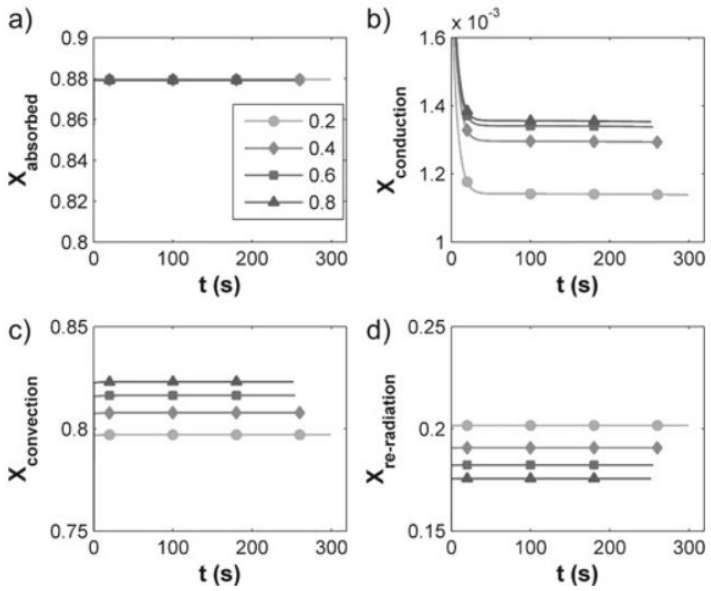

Figure 3.8: Sensitivity to variations in H_2O mole fraction of the fractions (a) of heat absorbed by the particle surface to the total radiative heat, (b) of the heat conducted into the particle relative to the absorbed heat, and (c) of the heat lost through re-radiation and (d) convection relative to the absorbed heat.

3.5 Conclusion

The dynamic model of a single char particle undergoing solar driven gasification has been verified with available experimental measurements and found to yield good agreement. The model produced the following key findings:

- The rate of particle shrinkage determines the significance of particle shrinkage on particle conversion. For instance, the conversion of small particles experience almost no retarding effect due to almost instantaneous disintegration. Large particles shrink over a relatively long period of time and therefore experience increased convective heat loss for longer and undergo gasification at a lower temperature that approaches the temperature of the bulk gas flow. As a result, there is a noticeable reduction in conversion rate during shrinking.

- Particle surface area to volume ratio is found to be an influential factor in determining the proportion of absorbed solar energy being used to drive endothermic gasification. This is because surface area increases heat dissipation through convection and re-radiation while volume increases total reactive surface area and energy conducted into the particle. The influence of surface area to volume ratio is expected to diminish as the particle size increases and shifts gasification to diffusion controlled reaction regime. This means that there is an optimal particle size to achieve maximum solar to chemical energy conversion efficiency in specific reactor conditions.

- Despite of slightly increasing the rate of endothermic gasification, the availability of the gasification agent has negligible influence on particle surface temperature and heat transfer mechanisms. This implies that steam gasification of char driven occurs at a sufficiently slow rate for its rate of energy consumption to be considered insignificant compared to more dominant convective and radiative heat transfer.

3.6 Nomenclature

A_j		Frequency factor
B_o		Gas permeability of the porous char particle
C_i	[mol/m^3]	ith component concentration
C_t	[mol/m^3]	Total concentration of gas components
$C_{i,bulk}$	[mol/m^3]	ith component concentration in the bulk gas
$c_{p,s}$	[J/kg]	Specific heat capacity solid
$c_{p,g}$	[J/kg]	Specific heat capacity gas
$D_{i,eff}$	[m^2/s]	Effective diffusion coefficient of the ith component
$D_{i,K}$	[m^2/s]	ith component Knudsen diffusion coefficient
$D_{i,j}$	[m^2/s]	Molecular diffusion coefficient

d_{pore}	[m]	Pore diameter
k_{eff}	[W/mK]	Effective char thermal conductivity
k_j		Kinetic parameter
k_c	[mol/m^{2}s]	Mass transfer coefficient
m_{init}	[kg]	Initial mass of particle
M_c	[mol/kg]	Molecular weight of carbon
M	[mol/kg]	Molecular weight
N_i	[m^3/mols]	ith component net flux
Nu		Nusselt number
$\rho_{apparent}$	[kg/m^3]	Apparent density of the particle
ρ_{char}	[kg/m^3]	Density of solid phase char
ρ_{gas}	[kg/m^3]	Density of gas mixture
φ		Porosity
φ_{cr}		Critical porosity
τ		Tortuosity of the pores
P	[Pa]	Pressure
P_t	[Pa]	Total Pressure
p_i	[Pa]	ith component partial pressure
$\dot{Q}_{abs}$	[W]	Absorbed radiative heat on the particle surface
$\dot{Q}_{convection}$	[W]	Convective heat on the particle surface
$\dot{Q}_{conduction}$	[W]	Conductive heat on the particle surface
$\dot{Q}_{re-radiation}$	[W]	Re-radiative heat on the particle surface
$\dot{Q}_{solar}$	[W]	Solar radiation heat incident on the particle surface
q_{solar}	[MW/m^2]	Solar heat flux
R	[m^{3}Pa/Kmol]	Universal gas constant
R_{char}	[mol/m^{3}s]	Rate of gasification of char
$R_{intrinsic}$	[mol/m^{3}s]	Intrinsic rate of gasification
r_p	[m]	Particle radius
S_r	[m^2]	Internal reactive surface area
S_r^0	[m^2]	Initial internal reactive surface area
Sh		Sherwood number
T	[K]	Particle Temperature
T_{srn}	[K]	Reactor Wall Temperature
T_g	[K]	Bulk Gas Temperature
T_{feed}	[K]	Temperature of particles entering the reactor
V_{gas}	[m/s]	Gas velocity
v		Stoichiometric coefficient of gas component in the water gas reaction.
$X_{absorbed}$		Fraction of solar radiative heat absorbed on the particle surface
$X_{conversion}$		Particle conversion

$X_{conduction}$		Fraction of absorbed radiative heat conducted into the particle
$X_{convection}$		Fraction of absorbed radiative heat lost to the particle surroundings through convection
$X_{re-radiation}$		Fraction of absorbed radiative heat lost to the particle surroundings through re-radiation
$y_{i,bulk}$		Mole fraction of ith component in the bulk gas
y_i		Mole fraction of ith component in the particle
ΔH_R	[J/mol]	Enthalpy Change due to Steam Gasification Reaction
α		Effective absorptivity
ε		Effective emissivity
σ	[$Wm^{-2}K^{-4}$]	Stefan-Boltzmann Constant
σ_{ij}	[Å]	Collision diameter
Ω_D		Collision integral
μ	[Nsm^{-2}]	Viscosity

Chapter 4

RFBR Residence Time and Conversion

This chapter presents the development of the analytical model for the assessment of the RFBR concept's potential to control particle residence time and gasification conversion. The centrifugal force generated through bed rotation is expected to delay the onset of particle elutriation from the bed and extend the residence time of entrained particles in the freeboard. However, there is little knowledge of the sensitivity of particle residence time and gasification conversion to variation in bed rotational speed. Understanding the influence of rotational speed and other key parameters on particle residence time and conversion would enable a preliminary assessment of the feasibility of the RFBR concept and identify suitable operating regimes that can lead to high feedstock conversion.

Given that there currently is little information on the mass and heat transfer characteristics in the bed volume of an RFB, it would be difficult to use a finite volume modelling approach to model the solar gasification process and determine the residence time and conversion of feedstock particles in the RFBR concept. However, there is information in literature about the flow field, maximum elutriated particle size and possible trajectory of non-reacting particles in the freeboard of a simple RFB which is geometrically similar to the freeboard volume in the RFBR concept. Without considering the geometrical effects of the aperture

and tangential outlets, the flow field in the RFBR freeboard could be quantitatively described with a set idealised flow field equations derived by Chevray et al. (1980). Coupling these idealised flow field equations with the previously developed single particle gasification model in Chapter 3 results in a new analytical model with which the particle residence time and gasification conversion of a single entrained particle moving in the RFBR freeboard could be tracked and calculated.

Using the aforementioned single particle modelling approach, the sensitivity of particle residence time and conversion in the RFBR concept to variations in bed rotational speed and other key parameters, namely initial feedstock particle size, radiation intensity, and particle release position, was evaluated. The results confirm that the RFBR concept is capable of performing at the same level or better in terms of controlling particle residence time and gasification conversion compared to other solar gasification receivers. Therefore, the feasibility of the RFBR concept should be investigated further.

Statement of Authorship

Title of Paper	Analytical Assessment of a Novel Rotating Fluidized Bed Solar Reactor for Steam Gasification of Char Particles
Publication Status	☑ Published ☐ Accepted for Publication ☐ Submitted for Publication ☐ Unpublished and Unsubmitted w ork w ritten in manuscript style
Publication Details	Z. Lu, M. Jafarian, M. Arjomandi, & G. Nathan, 2016, "Analytical Assessment of a Novel Rotating Fluidized Bed Solar Reactor for Steam Gasification of Char Particles", Solar Energy, vol. 140, pp.113-123.

Principal Author

Name of Principal Author (Candidate)	Zhao Lu
Contribution to the Paper	Developed ideas, performed numerical simulations, interpreted data, wrote manuscript, and acted as the corresponding author
Overall percentage (%)	70
Certification:	This paper reports on original research I conducted during the period of my Higher Degree by Research candidature and is not subject to any obligations or contractual agreements with a third party that would constrain its inclusion in this thesis. I am the primary author of this paper.
Signature	Date 15/12/2017

Co-Author Contributions

By signing the Statement of Authorship, each author certifies that:

i. the candidate's stated contribution to the publication is accurate (as detailed above);
ii. permission is granted for the candidate in include the publication in the thesis; and
iii. the sum of all co-author contributions is equal to 100% less the candidate's stated contribution.

Name of Co-Author	Mehdi Jafarian
Contribution to the Paper	Supervised development of work, interpreted data, and edited manuscript
Signature	Date 15,12,17.

Name of Co-Author	Maziar Arjomandi
Contribution to the Paper	Supervised development of work, interpreted data, and edited manuscript
Signature	Date 15/12/2017

Name of Co-Author	Graham Nathan
Contribution to the Paper	Supervised development of work, interpreted data, and edited manuscript
Signature	Date 15/12/2017

Analytical Assessment of a Novel Rotating Fluidized Bed Solar Reactor for Steam Gasification of Char Particles

Zhao Lu*

Mehdi Jafarian

Maziar Arjomandi

Graham J. Nathan

Centre for Energy Technology, School of Mechanical Engineering, The University of Adelaide, SA 5005, Australia

*Corresponding author: zhao.lu@adelaide.edu.au

Keywords: solar, gasification, chemical reactor, fluidized bed.

Abstract

A novel rotating fluidized bed solar reactor for the gasification of carbonaceous materials is presented. A simplified single particle model, in which the particle gasification is coupled with three dimensional equations of motion, is developed and used to study the particle residence time and gasification conversion within the proposed reactor, together with their sensitivity to changes in key operating parameters, namely reactor rotational speed, initial feedstock particle radius, radiation intensity, and particle release position. The proposed reactor is shown to offer potential for increased particle residence time and conversion relative to conventional fluidized beds through adjustments of the operating parameters other than the particle release position. The results presented assist in developing an understanding of the operation of the proposed reactor and optimising its performance.

4.1 Introduction

Solar energy is becoming an increasingly attractive renewable energy source due to its abundance and low environmental impacts (Desideri et al., 2014). Concentrated Solar Thermal (CST) systems for application in electrical power generation are being applied in increasing numbers and scale due to their low cost for energy storage (Ho & Iverson, 2014). An alternative application of CST is for the solar thermal gasification of carbon rich materials which converts solid carbonaceous feedstocks into calorifically upgraded synthesis gas for use in power generation cycles or the Fischer Tropsch process for the production of liquid fuels (Piatkowski & Steinfeld, 2008). Solar thermal gasification has two distinct advantages over auto-thermal gasification; the net carbon emission is reduced, and the quality of syngas is improved due to the lack of combustion and associated by-products (von Zedtwitz & Steinfeld, 2005). Through life cycle analysis, Z'Graggen and Steinfeld (2008) estimated that solar energy could upgrade the calorific value of carbonaceous feedstock by up to 34% and lower the production cost of syngas by up to 14% per unit compared to auto-thermal gasification. However, a number of technical and economic challenges remain to be overcome before this technology can become commercially viable. Among these is the need for more efficient and reliable gasification reactors.

Solar thermal gasification of carbonaceous materials derived from biomass and fossil origins has been studied in a variety of solar reactors to determine their suitability for various feedstocks and operating conditions (Taylor et al., 1983; Trommer, 2006; Kodama et al., 2008; Z'Graggen et al., 2006; Piatkowski & Steinfeld, 2008; Mechoir et al., 2009). The

directly irradiated configuration has received a lot of attention because it directly delivers high flux solar heat to the reaction site, resulting in relatively high temperature and fast reaction rate. The Solar Vortex Reactor (SVR) developed by Z'Graggen et al. (2006) was found to be one of the most promising concepts and currently has the highest lab scale solar to chemical energy conversion efficiency (Piatowski et al., 2011). However, it suffers from the inability to preferentially control particle residence time based on particle size which could result in the premature conversion of small particles and incomplete conversion of large particles. Chinnici et al. (2015) modified the solar vortex reactor and proposed a new vortex reactor concept, referred to as the Solar Expanding Vortex Reactor (SEVR), which utilises an expansion cone in the vicinity of the tangential inlets to alter the vortex structure responsible for particle entrainment. Their CFD analysis showed that the altered vortex structure could significantly increase the sensitivity of particle residence time to particle size and reduce the number of particles depositing on the reactor window. Later, Chinnici et al. (2016) performed PIV experimental measurements in a lab scale SEVR to verify the findings of the CFD analysis. The SEVR's ability to preferentially extend particle residence time greatly improves the conversion of feedstock particles at the reactor exit and the commercial viability of the reactor concept.

An alternative approach with increased particle residence time is the internally circulating bubbling fluidized bed solar reactor proposed by Kodama et al. (2008). In this reactor, feedstock particles are re-circulated in the fluidized bed under the influence of gravity and particle drag until they are reduced to sufficiently small sizes to be entrained by the fluidising gas. One key drawback of using a conventional fluidized bed for solar gasification is the limited bed surface area through which solar heat can be introduced to the bed.

Conventional bubbling fluidized beds are typically tall and narrow in diameter which leads to a small top surface relative to the volume of the bed. The high flux solar heat required to adequately heat the entire bed volume has a high risk of overheating the particles at the top bed surface and creating undesirable melted lumps that were reported in the work of Kodama et al. (2008). A different configuration that increases the relative surface area for radiation absorption is the laterally irradiated fluidized bed confined by transparent a silica glass or quartz tube (Taylor et al. 1983; Kodama et al. 2002). However, Taylor et al. (1983) reported that using a transparent tube exposes the hot bed to the external environment, leading to increased re-radiation heat loss and reduced solar to chemical energy conversion efficiency. Both Taylor et al. (1983) and Kodama et al. (2002) found that the use of either silica glass or quartz tube imposed a maximum temperature limit on the fluidized bed. At temperatures above 1000˚C, the quartz or silica glass tube was prone to permanent damage caused by overheating. Trommer (2006) compared the gasification of coke in both directly and indirectly irradiated fluidized beds and found that the heat transfer mode has negligible effect on chemistry and gasification conversion rate. Nevertheless, he noted that the directly irradiated configuration is more economical due to reduced parasitic heat loss. In the light of the above, the first aim of the present investigation is to introduce a novel concept of using rotating bubbling fluidized bed for solar gasification to address the problem of limited surface area for solar radiation absorption while maintaining reliability and also offering greater control over particle residence time for improved reactor reliability and efficiency.

Rotating fluidized beds, described in more detail below, have been proposed for non-solar applications to offer greater control of residence time and gas flow than conventional fluidized beds (Metcalfe & Howard, 1977). However, to the authors' knowledge, no

previous assessment has been reported of suitability of rotating fluidized bed for solar gasification. Hence, a further aim of the present investigation is to assess the potential benefits of the proposed concept in controlling particle residence time and conversion. This is achieved through (a) developing a numerical model with which the gasification conversion and entrainment trajectory of a single reactant particle can be investigated and (b) assessing the sensitivity of particle residence time and conversion to key operating parameters, namely rotational speed, location of particle release, particle diameter, and radiation intensity, with the aim of determining the underlying reasons.

4.2 Rotating Fluidized Bed Receiver Concept

A schematic diagram of a conventional rotating fluidized bed reactor is presented in Figure 4.1. The cylindrical gas distributor shown employs a porous distributor plate to radially inject the fluidising gas into the cavity. External walls, not shown in Figure 4.1, enclose the cylindrical gas distributor to form a plenum that controls the direction of the pressure gradient for injecting the fluidising gas. The distribution of bed thickness along the axis of symmetry is typically constant in the range of rotational speeds suitable for particle fluidisation. However, unlike conventional bubbling fluidized beds, the dominant force acting against the drag force is the centrifugal force of rotation, which is much stronger than gravity. Because the centrifugal force is a function of particle radial position, the particles at the bed surface are under a smaller centrifugal force than the particles at the gas distributor. Therefore, the minimum fluidisation velocity varies with radial distance and its uniformity depends on the thickness of the bed. The gas velocities required to minimally fluidise the

particles at these two locations are termed the “surface minimum fluidisation velocity” and “critical minimum fluidisation velocity” respectively.

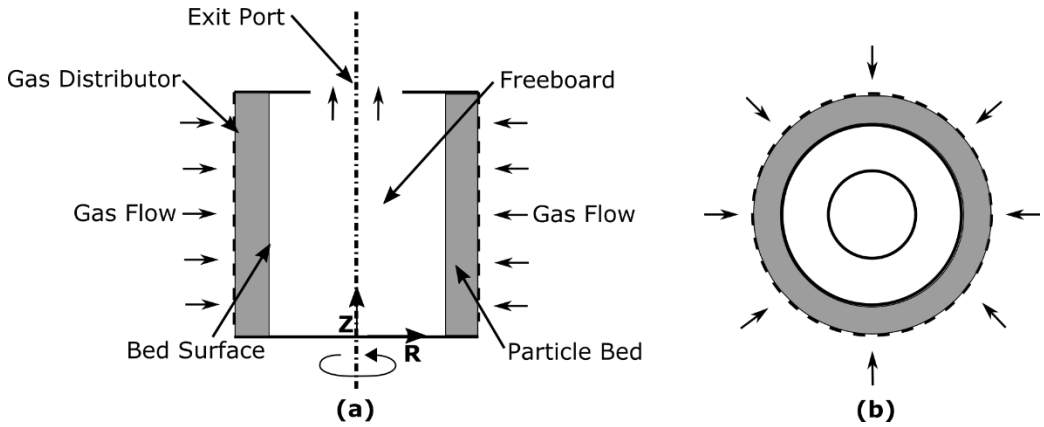

Figure 4.1: Schematic diagram of a simple rotating fluidized bed, showing side view (a) and top view (b).

A schematic diagram of the proposed solar RFB gasifier is shown in Figure 4.2. This configuration is shown oriented vertically, i.e. for a beam down solar optical concentration system, although a beam up configuration is also possible because the forces are controlled by centrifugal motion instead of gravity. For the present assessment, the beam down configuration is selected because it offers the potential advantages of cheaper scaling of support structure, better retention of particles, reduced cost of maintenance, and the possibility of being used to harvest solar radiation from a surround field (Segal & Epstein, 2003; Segal & Epstein, 2000; Hasuike et al., 2006).

As shown in Figure 4.2, the proposed concept comprises a moving cylindrical lower section that rotates about its axis of symmetry and a stationary upper section, which is connected to a secondary concentrator and fixed tangential outlets. Dividing the reactor into two sections has the benefit of reducing the weight of the moving components to improve reactor energy efficiency. The two sections could be joined together with a high temperature steam turbine

brush seal such as the ones developed by General Electric to prevent the leakage of gasification products (Dinc et al., 2001). An annular barrier is installed at the top of moving section to stop particles from reaching to the brush seal. Feedstock particles are proposed to be fed through the inlet at the bottom of the gasifier. At sufficient rotational speeds, the particles can be translated away from the centre by the centrifugal force. The speed of rotation also determines the shape of the bed, whose surface profile depends both on gravitational and centrifugal forces, as shown in Figure 4.2.

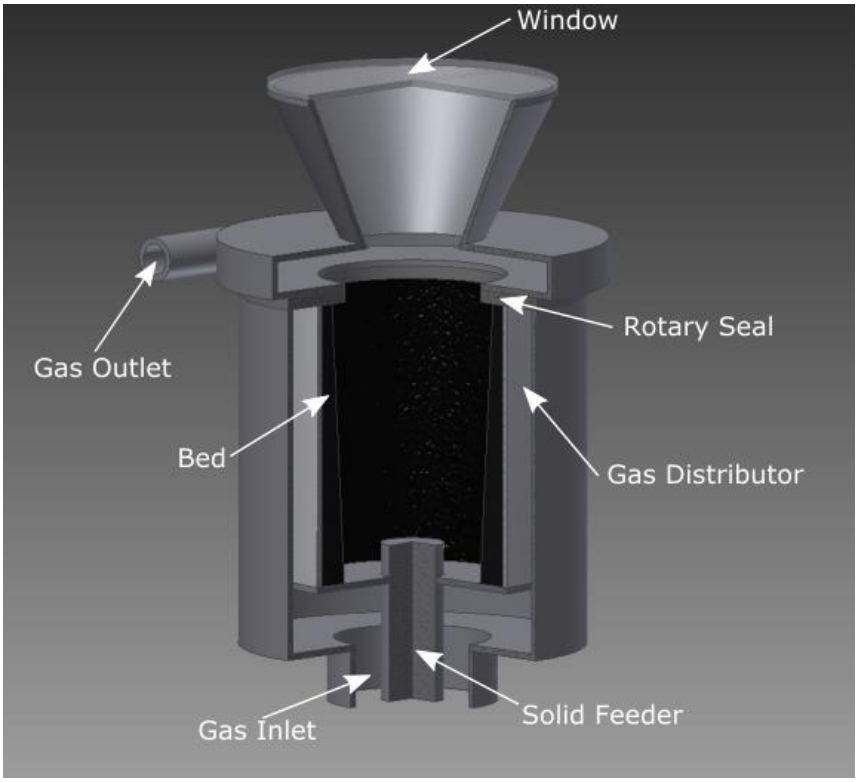

Figure 4.2: Schematic diagram of the proposed Rotating Fluidized Bed Solar Gasification Reactor.

Some of the potential benefits of the rotating solar fluidized bed solar gasification reactor are anticipated as follows:

- Rotating fluidized beds perform better than conventional fluidized beds in terms of minimising the elutriation of particles. Experiments and numerical simulations for non-reacting particles in rotating fluidized bed have shown that increasing rotational speed and centrifugal force is an effective means of reducing particle elutriation and reducing elutriated particle size (Saunders, 1986; Chevray et al., 1980).
- Rotating fluidized beds could achieve a higher bed surface area relative to volume than conventional bubbling fluidized beds (Metcalfe & Howard, 1977). Increasing the absorption surface area offers potential to lower the radiation flux at the bed surface to prevent local overheating. The surface area of the bed is also much larger than the aperture for the reactor, which offers the potential to reduce re-radiation losses through the aperture, while the shorter aspect ratio of the bed offers potential to reduce conduction losses through the cylindrical wall.
- The much higher fluidising velocities of rotating fluidized beds offer potential for improved heat and mass transfer rates over conventional fluidized beds (Chen, 1987). The use of adjustable centrifugal force for particle suspension offers a greater tolerance to variations in particle physical properties, resulting in a reduction in the cost of preparing particles (Chen, 1987).

For accurate and realistic heat transfer assumptions in the present investigation, the inner dimensions of the RFB solar gasification reactor analysed in the present work are the same as the theoretical rotating packed bed solar reactor developed for the reduction of Zinc Oxide by (Schunk et al., 2009). The RFB solar gasification reactor dimensions and operating conditions used in the present investigation are listed in Table 1.

Table 1: Dimensions of the Rotating Fluidized Bed Solar Reactor analysed here.

Variable	Unit	Baseline Value
r_{bed}	[m]	0.25
r_{exit}	[m]	0.15
$r_{distributor}$	[m]	0.3
L	[m]	0.75
$r_{aperture}$	[m]	0.085

4.3 Methodology

The reactor geometry is significantly simplified to remove the influence of complex geometrical features. The effects of inlet and outlet on particle elutriation and gasification are not considered. The modelled reactor domain consists only of the simple rotating fluidized bed shown in Figure 4.1. The bed thickness is assumed to be constant in the Z direction, leading to a perfectly vertical bed surface profile. This assumption is considered to be reasonable based on the visual observation of Saunders (1986) in a rotating fluidized bed of a smaller radius (100mm), but otherwise under similar operating conditions. Nevertheless, the bed thickness is never truly uniform due to the disturbances caused by fluidising gas bubbles bursting at the surface. In addition, at lower rotational speeds, the bed thickness may become thicker at the bottom than the top due to gravity. This will affect the radial velocity profile of the fluidizing gas leaving the bed surface and, hence also, the flow field within the reactor cavity. A systematic investigation of the critical rotational speed at which the uniform thickness assumption breaks down has not been reported. Nevertheless, Saunders (1986) reported that a rotational speed of 26 rad/s is sufficient to generate an approximately uniform thickness. Therefore, rotational speeds of 30-70 rad/s were chosen for the present work.

The gasification conversion has been estimated using a single particle gasification model developed and validated by Lu et al. (2016). The motion of the particle in the freeboard region is determined by balance of forces. The mass and heat transfer conditions within the fluidized bed of the proposed concept are currently not known. Thus, in the present work, ejected particles that fall back to the bed under the influence of centrifugal force are assumed to be immediately ejected into the freeboard region again and repeat the near bed surface bouncing motion until they are converted to a sufficiently low mass that allows them to be entrained into the freeboard permanently. Under this assumption, the present work only considers gasification in the freeboard, where conditions can be reasonably estimated based on the existing directly irradiated entrained flow solar reactors.

4.3.1 Single particle gasification

The particle model is one dimensional and discretised in the radial direction to form concentric spherical layer elements (i.e. onion rings), as is shown in Figure 4.3. Each layer is assumed to have uniform porosity, concentration of gaseous species and temperature. The model adopts Furtes and Marban's (1994) approach to predicting the reduction of particle diameter through a critical porosity value. This means that if the porosity of a layer falls below the critical porosity, the layer is assumed to be too weak to support the char structure and to fragment instantaneously into fines, exposing the next layer to the reactor environment.

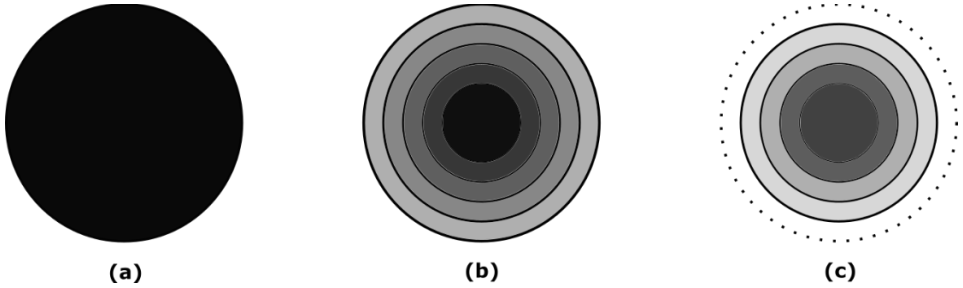

Figure 4.3: Diagram of the particle modelling approach, showing unreacted particle (a), partially reacted particle (b), and partially reacted particle with a collapsed layer indicated by the dash line (c).

For the present assessment, the particle is assumed to be completely devolatilized upon entering the RFB solar gasifier, and the char particle's chemical and physical properties are taken from the work of Mermoud et al. (2006). While several heterogeneous reactions proceed in parallel in char gasification, only the most dominant Steam Gas reaction, shown in Eq.1 , is considered in the present work because other reactions such as Boudouard and Methanation reactions are typically more than an order of magnitude slower (Higman & Van der Burgt 2008). This single reaction approach to model the gasification of a single char particle has been shown to be reliable, while significantly reducing the computational time (Mermoud et al. 2006).

$$C + H_2O \rightarrow CO + H_2 \qquad \text{Eq. 1}$$

Using the single dominant reaction approach, the four gas components present in the internal volume of the particle are H_2O, H_2, CO and N_2, termed i = 1 to 4. The bulk gas flow surrounding the particle is assumed to consist of H_2O and N_2. The composition of the bulk gas flow is constant due to the volume difference between the reactor cavity and particle. N_2 as an inert carrier gas is used to dilute the concentration of the gasification agent H_2O. The composition of the bulk gas flow and other numerical parameters are listed in Table 2.

The intrinsic reaction rate $R_{intrinsic}$ is estimated using the Langmuir-Hinshelwood formulation in Eq. 2 following Mermoud et al. (2006).

$$R_{intrinsic} = -\frac{k_1 p_{h_2o} + k_4 p_{h_2o} p_{h_2} + k_5 p_{h_2o}^2}{1 + k_2 p_{h_2} + k_3 p_{h_2o}} \quad \text{Eq. 2}$$

The work of Wang and Bhatia (2001), who proposed Eq. 3, was used to account for the effects of internal reactive surface area S_r and apparent particle density $\rho_{particle}$ on the rate of char gasification, R_{char}.

$$R_{char} = R_{intrinsic} S_r \rho_{particle} \quad \text{Eq. 3}$$

It should be noted that this rate has been determined through thermo-gravimetric measurements which expose reactants to a much lower heat flux than in a solar reactor. A correction factor, k_{solar} based on the Solar Vortex Reactor measurements of Trommer (2006) is therefore applied to the reaction rate, R_{char} to produce a more realistic reaction rate $R_{char,solar}$ for gasification driven by high flux radiation shown in Eq. 4.

$$R_{char,solar} = R_{char} k_{solar}, \quad \text{Eq. 4}$$

where k_{solar} is:

$$k_{solar} = 498\exp\left(\frac{-5.71 \times 10^4}{\mathcal{R}T}\right) \quad \text{Eq. 5}$$

The mass balance equations for the four gas components, C_i can be expressed in a 1-D spherical coordinate system as:

$$\frac{\partial(\varphi C_i)}{\partial t} + \frac{1}{r^2}\frac{1}{\partial r}(r^2 N_i) = \nu_i R_{char,solar} \quad \text{Eq. 6}$$

The net flux, N_i, of *ith* gas component was evaluated using the Dusty Gas Model (DGM). The application of DGM to single particle gasification can be found in Xu et al. (2011).

$$-\frac{\varphi}{\tau}\left(\nabla C_i + \frac{B_0}{\mathcal{D}_{iK}\mu} C_i \nabla P\right) = \sum_{j=1}^{4} \frac{y_j N_i - y_i N_j}{\mathcal{D}_{ij}} + \frac{N_i}{\mathcal{D}_{iK}} \quad \text{Eq. 7}$$

Pressure variation, ∇P within particle is neglected due to the high porosity and small particle diameters that are used in the present study.

The reduction of particle radius, r_p is tracked by comparing the porosity of individual spherical layer elements to the experimentally determined critical porosity value, φ_{cr} by Mermoud et al. (2006).

$$\frac{\partial r_p}{\partial t} = -\frac{\partial \varphi(r_p)}{\partial t} \Big/ \frac{\partial \varphi(r_p)}{\partial r} \quad (for\ \varphi(r_p) > \varphi_{cr}) \quad \text{Eq. 8}$$

$$\frac{\partial r_p}{\partial t} = 0 \quad (for\ \varphi(r_p) < \varphi_{cr})$$

The authors showed in their previous work that the rate of particle radius reduction strongly depends on particle diameter, which significantly influences the variation in the rate of gasification within a particle (Lu et al. 2016). Greater variation in gasification rate is observed in larger particles and leads to earlier onset of particle radius reduction and lower radius reduction rate, $\frac{\partial r_p}{\partial t}$.

The unsteady heat transfer conservation equation in spherical coordinate system can be expressed as:

$$(C_{p,s}\rho_{char}(1-\varphi)+C_{p,g}\rho_{gas}\varphi)\frac{\partial T}{\partial t}+\frac{1}{r^2}\frac{1}{\partial r}(r^2\lambda_{eff}\frac{\partial T}{\partial r})=R_{char,solar}\Delta H \quad \text{Eq. 9}$$

where the effective thermal conductivity λ_{eff} includes conduction by the gas mixture and solid char and radiative heat transfer within particle pores. According to Larfeldt et al. (2000), λ_{eff} can be estimated as follows:

$$\lambda_{eff}=\lambda_s(1-\varphi)+\lambda_g\varphi+4\sigma T^3 d_{pore}\varepsilon \quad \text{Eq. 10}$$

The solid char conductivity λ_s is interpolated from the work of Kantorovich & Bar-Ziv (1999). The gas mixture conductivity λ_g is calculated using the conductivity values for the gas components in Poling et al. (2001).

The boundary and initial conditions are given by:

$$T(r,0)=T_{feed} \quad \text{Eq. 11}$$

$$\frac{\partial T}{\partial r}(0,t) = 0, \qquad for\ t \geq 0 \qquad \text{Eq. 12}$$

$$\underbrace{-\lambda_{eff}\ \frac{\partial T}{\partial r}(r_p,t)}_{\dot{Q}_{conduction}} = \underbrace{\frac{Nu\lambda_g}{2r_p}(T(r_p,t) - T_g)}_{\dot{Q}_{convection}} + \underbrace{\sigma\varepsilon\left(T(r_p,t)^4 - T_{srn}^4\right)}_{\dot{Q}_{re-radiation}} + \alpha\underbrace{\frac{q_{solar}}{4}}_{\dot{Q}_{abs}}$$

$$for\ t \geq 0 \qquad \text{Eq. 13}$$

The total hemispherical absorptivity, α, is equal to the emissivity, ε, and can be determined using the correlation as reported in Brewster & Kunitomo (1984):

$$\alpha = 0.78 + 0.00269T^{0.5} \qquad \text{Eq. 14}$$

The Nusselt number, Nu for a spherical particle is as follows:

$$Nu = 2 + (0.4Re^{0.5} + 0.06Re^{0.66})Sc^{0.4} \qquad \text{Eq. 15}$$

Table 2: Parameters and values employed in the Particle Gasification Model

Variable	**Unit**	**Baseline Value**	**Range assessed in the model**	**Reference**
σ	[W m^{-2} K^{-4}]	5.670e-8		
$d_{pore,0}$	[µm]	10		Mermoud et al. (2006)
ΔH_R	[J mol^{-1}]	135.8		Mermoud et al. (2006)
ρ_{char}	[kg m^{-3}]	1900		Mermoud et al. (2006)
φ_{cr}		0.98		Mermoud et al. (2006)

S_r^0	[m^2 cm^{-3}]	275		Mermoud et al. (2006)
v_{gas}	[m s^{-1}]	0.14		
T_{feed}	[K]	773		
T_g	[K]	1273		Z'Graggen et al. (2006) Piatowski & Steinfeld (2008)
T_{srn}	[K]	1273		Z'Graggen et al. (2006) Piatowski & Steinfeld (2008)
P	[atm]	1		
$r_{p,0}$	[µm]	50	50-450	
q_{solar}	[MW m^{-2}]	1	2-6	
$y_{H_2O,bulk}$		0.2		
$y_{CO,bulk}$		0		
$y_{H_2,bulk}$		0		
$y_{N_2,bulk}$		0.8		

4.3.2 Particle motion in the freeboard

To the best of the authors' knowledge, the flow field inside a rotating fluidized bed has never been measured. However, Donaldson and Snedeker (1962) have experimentally obtained the pressure and velocity profiles at the opening plane of a porous cylindrical vessel completely open on one side with gas radially injected through its porous wall. Based on these experimental measurements, idealised approximations of the flow field inside the cylindrical vessel, which is the freeboard region of a rotating fluidized bed, have been proposed by Chevray et al. (1980) and Saunders (1986) and used in their investigations on particle dynamics and elutriation in non-reacting rotating fluidized beds. These methods were therefore chosen to estimate the flow-field within the rotating fluidized bed gasifier.

In the present work, particle movement in the freeboard is tracked using a rotating reference frame. According to the work of Donaldson and Snedeker (1962), the flow field in a rotating

porous cylinder appears to be a Rankine vortex consisting of a free vortex in the near wall region and forced vortex in the core region. In literature, the forced vortex in the core region is sometimes referred to as the 'viscous core' (Chevray et al. 1980; Saunders 1986). For a vessel with a full top opening, the location of the boundary, r_m, separating the forced and free vortices has been found to largely depend on the ratio of the tangential and radial components of the initial flow at the wall (Donaldson & Snedeker 1962). For a vessel with a partial top opening, the vortex flow investigation by Roschke (1966) indicates that the boundary r_m coincides with exit port radius r_{exit}, for small vessel length to diameter ratios. In the present work, the modelled domain has a length to diameter ratio of 1.5 so r_m is assumed to be located at the exit radius, r_{exit}.

From the measurements of Donaldson and Sendeker (1962), Chevray et al. (1980) constructed a quantitative description of the relationship between tangential to radial velocity component ratio and the location of maximum tangential velocity, r_m. Combining this empirical correlation, continuity and known initial flow components at r_{bed}, they were able to mathematically derive the idealised freeboard flow field expressions in both rotational and irrotational regions of the RFB freeboard without considering end effects. The present assessment adopts these expressions to calculate particle drag force and particle motion.

For tangential gas velocity u_θ:

$$u_\theta(r) = \frac{100(v_f A_{dis})^2}{\omega \pi^2 r_{bed}^4 h^2} \; for \; 0 \leq r \leq r_{exit} \qquad \text{Eq. 11}$$

$$u_\theta(r) = \frac{\omega r_{bed}^2}{r} \; for \; r_{exit} \leq r \leq r_{bed} \qquad \text{Eq. 12}$$

For radial gas velocity u_r:

$$u_r(r) = -\frac{v_f A_{dis}}{2\pi r_m^2 h} r \; for \; 0 \leq r \leq r_{exit} \qquad \text{Eq. 13}$$

$$u_r(r) = -\frac{v_f A_{dis}}{2\pi r h} \; for \; r_{exit} \leq r \leq r_{bed} \qquad \text{Eq. 14}$$

For axial gas velocity u_z:

$$u_z(r) = \frac{v_f A_{dis}}{\pi r_m^2 h} z \; for \; 0 \leq r \leq r_{exit} \qquad \text{Eq. 15}$$

$$u_z(r) = 0 \; for \; r_{exit} \leq r \leq r_{bed} \qquad \text{Eq. 16}$$

The drag force acting on a particle in the freeboard can be evaluated using Eq. 17.

$$F_{drag} = \frac{1}{2} \rho_{fluid} |\boldsymbol{U}|^2 A_p C_D \qquad \text{Eq. 17}$$

where C_D, $\boldsymbol{U}$, and A_p are drag coefficient, particle velocity and particle cross sectional area respectively.

The drag coefficient C_D can be determined by (Chevray et al. 1980):

$$C_D = \frac{24}{Re} + \frac{4.6}{Re^{0.38}} \quad \text{Eq. 18}$$

The motion of the particle is influenced by centripetal, Coriolis, gravitational and drag forces. The equations of motion can be derived from the summation of these forces. Expressed in cylindrical coordinate system, the equations of motion for the centre of mass of a particle are as follows (Chevray et al. 1980):

$$\ddot{r} - r\dot{\theta}^2 = \omega^2 r + 2r\omega\dot{\theta} - BC_D|\boldsymbol{U}|\dot{r} \quad \text{Eq. 19}$$

$$2\dot{r}\dot{\theta} + r\ddot{\theta} = -2\omega\dot{r} - BC_D|\boldsymbol{U}|r\dot{\theta} \quad \text{Eq. 20}$$

$$\ddot{z} = -g - BC_D|\boldsymbol{U}|\dot{z} \quad \text{Eq. 21}$$

where B and $|\boldsymbol{U}|$ are:

$$B = \frac{3}{8}\frac{\rho_{fluid}}{\rho_{particle}}\frac{1}{r_p} \quad \text{Eq. 22}$$

$$|\boldsymbol{U}| = \sqrt{(\dot{r}^2 + (r\dot{\theta}\,)^2 + \dot{z}^2)} \quad \text{Eq. 23}$$

Particles are initially injected into the freeboard with the radial velocity that is the same as the fluidising gas velocity v_f. The particle is assumed to have zero initial tangential and axial velocity. The initial dimensionless axial position of the particle or the height of release $H_{release}$ is selected to be half of the reactor length L. It should be noted that $H_{release}$ is later varied for sensitivity study. The values of operating parameters are listed in Table 3.

Changes in particle properties due to gasification per time step are fed into the particle motion equations Eq. 19-21 which are solved using Fourth Order Runge-Kutta Method to determine the changes in particle position, velocity and acceleration.

Table 3: Operating Parameters of the Rotating Fluidized Bed Solar Reactor

Variable	Unit	Baseline Value	Variation
ω	[rad s^{-1}]	30	30-70
v_f	[m s^{-1}]	2.4	
$H_{release}$		0.5	0.1-0.9

4.4 Results and discussion

4.4.1 Baseline case

Under the conditions specified in Tables 2 and 3, the calculated particle trajectory of a 50μm radius char particle is shown in Figure 4.4. The outer red circles indicate the top and bottom edges of r_{bed} in the RFB cavity. The inner red circle shows r_{exit} which is also the boundary of the outer irrotational region and inner viscous core. It can be seen from the particle trajectory that the radial component of the particle velocity reduces as the particle approaches the inner viscous core. This can be explained by the greatly increased tangential velocity and centrifugal force in the vicinity of the boundary of the viscous core. Figure 5

also shows that the 50μm particle is sufficiently small to be permanently elutriated from the bed after release and orbit towards the center in the outer irrotational region where the upward flow is assumed to be negligible. Upon crossing the boundary r_{exit} and entering the viscous core where there is assumed upward flow, the particle gains significant upward velocity and exits the RFB cavity. According to the number of orbits the particle travels in the inner and outer regions, the particle motion in the outer region makes up the majority of the freeboard residence time. Hence, to increase freeboard residence time for greater particle conversion before exit, key parameters to consider are size of the inner viscous core and the maximum tangential velocity at the boundary which forms a barrier to entrained particles.

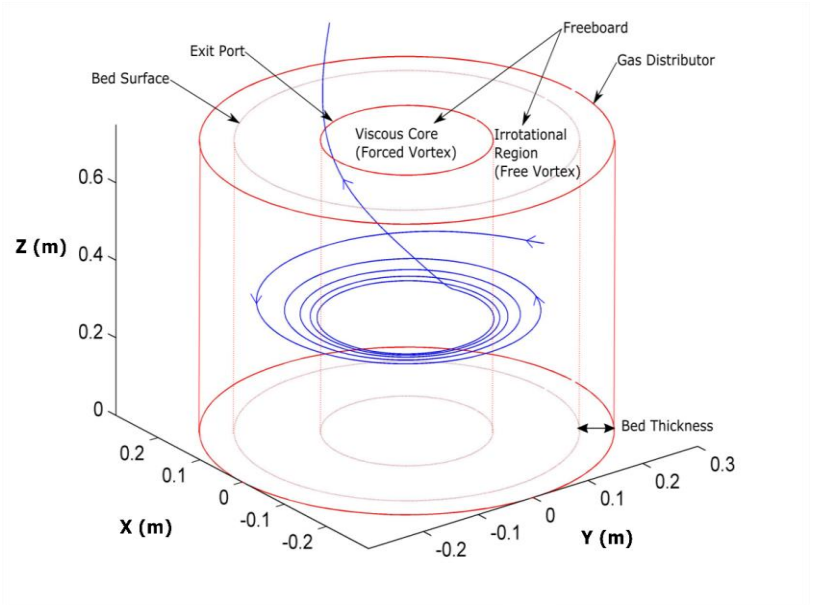

Figure 4.4: Calculated trajectory of a 50μm radius char particle in the reference RFB solar gasifier using the parameters specified in Tables 1, 2, and 3.

4.4.2 Effect of rotational speed

Figure 4.5 presents the dependence of the calculated particle residence time and conversion as a function of rotational speed under the conditions in Tables 1, 2, and 3. The particle residence time is divided into two sections to show the times taken for the particle to bounce near the bed surface and move through the freeboard to the exit. As expected, increasing the reactor rotational speed and centrifugal force results in greatly increased particle residence time and conversion in the reactor cavity. However, the dependence of residence time and conversion on rotational speed is seen to be non-linear. The most significant increase in residence time occurs between the rotational speeds of 30rad/s and 40rad/s. This can be attributed to the immediately entrainment of the particle after ejection and the lack of near bed surface bouncing, which means in these cases, the particle residence time depends entirely on the particle motion within the freeboard whose idealised flow field is highly sensitive to rotational speed. The increases in particle residence time for the rotational speeds of 50rad/s, 60rad/s, and 70 rad/s are seen to be less sensitive and almost proportional to the changes in rotational speed. This can be explained by the self-regulating effect of near bed surface bouncing, which prevents a particle from being entrained into the freeboard until its mass reduces sufficiently to tip the balance of the particle drag and centrifugal forces.

Another trend observed for the cases with near bed surface bouncing is the gradual decrease in the time taken for a particle to travel through the freeboard, which is a reversal of the trend for the rotational speed cases without near bed surface bouncing. This suggests that the reduction in entrained particle mass due to increased rotational speed has a greater influence on the particle centrifugal force than the associated increase in the rotational speed

of the freeboard vortex. The net result is that the particle is subjected to a decreased centrifugal force and moves through the freeboard in a shorter time. The increase in particle conversion with respect to rotational speed closely mirror the increases in particle residence time. Figure 4.6 shows that the average conversion rate is almost independent of rotational speed. The very small increase in conversion rate observed between the rotational speeds of 30rad/s and 50rad/s can be attributed to the increase in gas-particle slip velocity and particle mass transfer caused by a faster rotating vortex. The influence of the vortex on the conversion rate is significantly diminished by a further increase in rotational speed due to the shorter particle residence time in the freeboard and a possible shift to the kinetic-limited reaction regime.

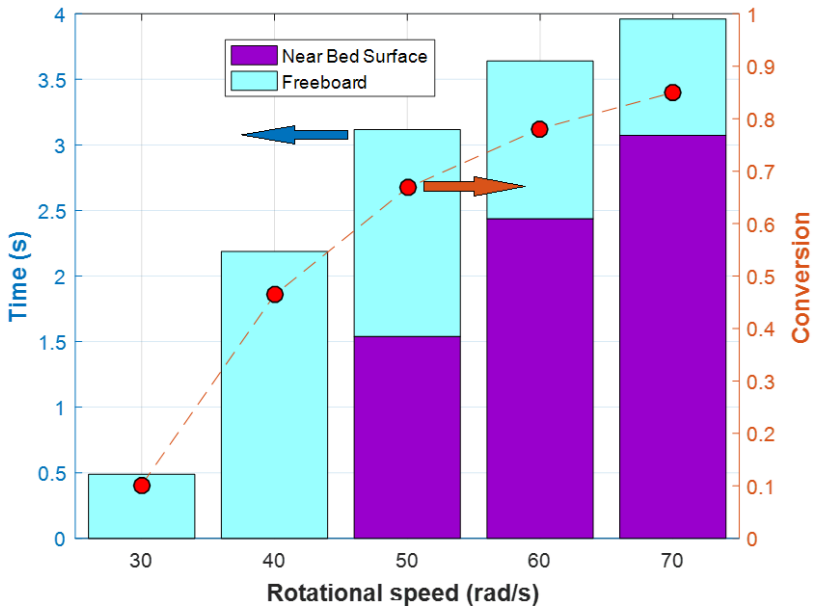

Figure 4.5: Calculated particle residence time τ_{res},, on the left, and conversion X, on the right, as a function of rotational speed ω under the conditions shown in Tables 1, 2, and 3.

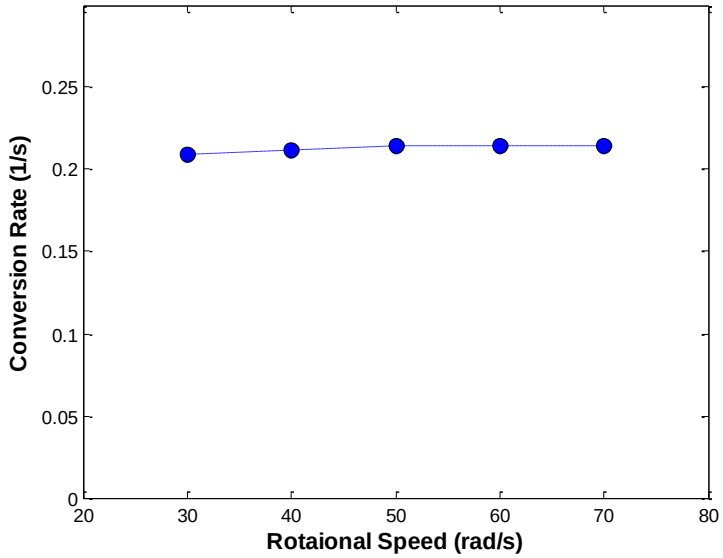

Figure 4.6: Calculated average particle conversion rate $\frac{\Delta X}{\Delta t}$ as a function of rotational speed ω under the conditions shown in Tables 1, 2, and 3.

4.4.3 Effect of particle diameter

Figure 4.7 presents the particle residence time and conversion as a function of initial particle radius under the conditions shown in Tables 1, 2, and 3. It can be seen that increasing the initial particle radius increases particle residence time. However, the increase in residence time is highly non-linear and varies greatly depending on the initial particle radius. The residence time increases by 2.7s for an increase in the the initial particle radius from 50μm to 150μm. In contrast, increasing the radius from 150μm to 350μm only increases the residence time by 1.5s. A further increase in initial particle radius from 350μm to 450μm leads to a residence time increase of almost 3s. This complex and non-linear dependence of the residence time on the particle radius is attributed to the different roles of the underlying phenomena that influence the balance of forces acting on the particle, some of which increase the particle residence time with respect to radius and others which decrease it. The

centrifugal force is proportional to the cube of the radius while the drag force is proportional to the square of radius. Therefore, an increase in radius generates an increase in the ratio of centrifugal to drag force, causing a reduction in entrainment and an increase in the particle residence time near to the bed surface as shown in Figure 4.7.

The dominant heat transfer mode also depends on particle radius. Radiative heat transfer scales with particle surface area ($\propto r_p^2$), which is proportional to radius squared, while convective heat transfer scales with the product of convective heat transfer coefficient ($\propto 1/r_p$) and surface area ($\propto r_p^2$), which is only proportional to radius. As a result, the dominant particle cooling mode changes from convection to re-radiation with an increase in particle radius. This interpretation is supported by the radiation driven single particle oxidation model of Jafarian et al. (2013). Under the assumed reactor conditions in the present work, larger particles reach a higher equilibrium temperature than do smaller particles and also undergo more rapid conversio. This explains the increase in the average conversion rate caused by increasing the particle radius from 50um to 150um shown in Figure 4.8. Faster average conversion leads to reduced residence time because the centrifugal force responsible for delaying particle entrainment is proportional to particle mass. Nevertheless, larger particles may reach a lower equilibrium temperature than smaller particles under some conditions.

It is also clear from Figure 4.8 that the average conversion rate does not increase indefinitely with increasing particle radius, but decreases for particle radii greater than 150μm. The downward trend in average conversion rate is most likely due to the shift to the diffusion limited reaction regime for sufficiently large particles. As the surface to volume ratio

decreases, the rate of consumption of gasification agent by the particle volume exceeds the rate of its diffusion through the particle surface. The decreased rate of mass reduction prolongs the particle residence time near to the bed surface.

The peripheral fragmentation behavior is also strongly dependent on particle radius and affects the particle residence time by altering the rate of change of the particle cross sectional responsible for the drag force. Sufficiently small porous particles are approximately isothermal and contain almost uniform concentrations of gas components throughout. Thus, the whole particle reaches the critical porosity almost simultaneously, causing the particle radius reduce to zero instantly (Singer & Ghoniem 2013). Larger porous particles, however, do not exhibit this instantaneous disintegration. Instead, the presence of thermal and concentration gradients within these particles causes the edge of the particle to gasify faster than the core. The outer volume reaches the critical porosity faster than the inner volume so the fragmentation front gradually moves from the outer volume of the particle inwards, causing the particle radius to slowly decrease. The rate of particle radius reduction increases as the particle becomes smaller and gradients flatter (Lu et al. 2016). Because of the difference in the rate of particle radius reduction, peripheral fragmentation increases the residence time of the larger particles entrained in the freeboard region.

Finally, the particle heating rate determines the time taken for a particle to reach its equilibrium temperature. Smaller particles reach their equilibrium temperature faster than larger particles due to their larger surface to volume ratio and higher absorption of solar energy per unit volume before equilibrium. Therefore, smaller particles typically reaches full conversion and leave the reactor faster than larger particles. The effect of particle

heating rate on particle residence time and conversion becomes less significant as the initial particle radius and time required for full conversion increase.

Figure 4.8 also presents the calculated particle conversion as a function of initial particle radius. It can be seen that relatively high conversion extents (>90%) can be achieved for the large particles that are retained near the bed surface by centrifugal force. However, it is obvious that increasing the initial particle radius shifts the particle gasification into the diffusion limited reaction regime which results in a decrease in average conversion rate and conversion extent, seen in the case of the 350μm radius particle. It is important to note that the complete conversion achieved by the largest 450μm radius particle is unrealistic. Because of its heavy mass, the 450μm radius particle fell to the bottom surface of the reactor before it could be entrained into the inner viscous core and exit the reactor like the smaller particles. It became trapped on the bottom surface due to the idealised flow field assumptions which ignore end effects and turbulence. For this reason, the 450μm radius particle attained complete conversion and a much higher freeboard residence time than the smaller particles. In a real physical reactor, there is expected to be a particle pile on the bottom surface, and particles added to the pile may re-join the fluidized bed under gravitational and centrifugal forces or be entrained by upward turbulent flow if they are sufficiently small.

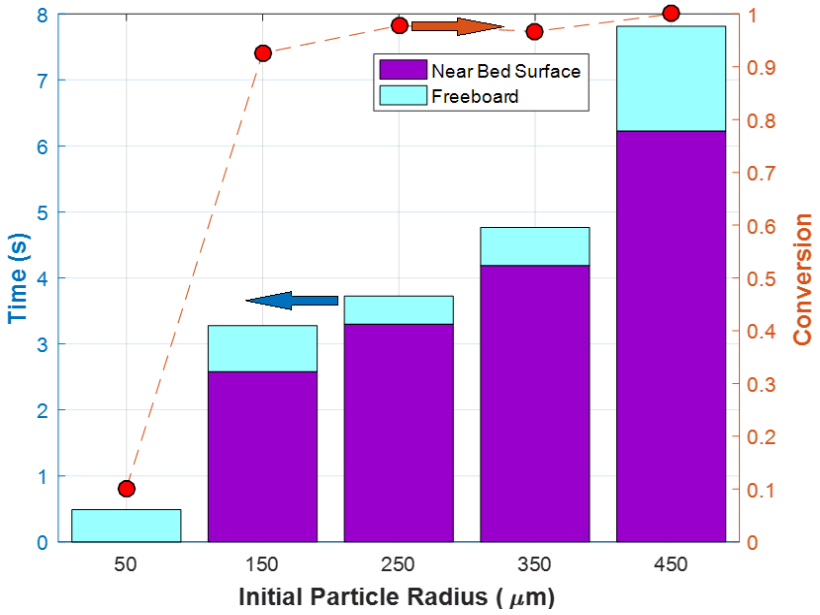

Figure 4.7: Calculated particle residence time τ_{res} and conversion X as a function of initial particle radius $r_{p,0}$ under the conditions shown in Tables 1, 2, and 3.

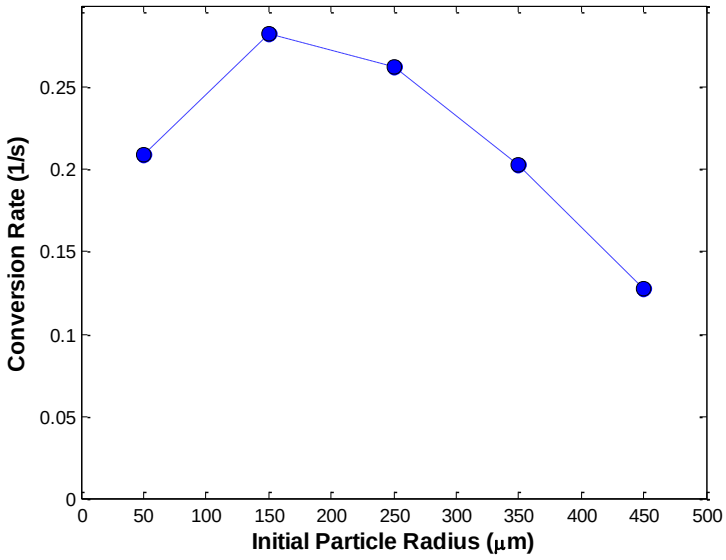

Figure 4.8: Calculated average particle conversion rate $\frac{\Delta X}{\Delta t}$ as a function of initial particle radius $r_{p,0}$ under the conditions shown in Tables 1, 2, and 3.

4.4.4 Effect of radiation intensity

Figure 4.9 presents the calculated particle residence time and conversion as a function of radiation intensity. Because the reference initial particle radius is 50μm, the particles in all radiation intensity cases are entrained into the freeboard immediately after ejection from the bed surface. It can be seen that high radiation intensity has the effect of decreasing residence time and increasing particle conversion. The increase in particle conversion is expected because high radiation intensity delivers increased heat energy to particles, leading to higher particle temperature and conversion rate, shown in Figure 4.10. However, the noticeable reduction in particle residence time is surprising. It appears that the rapid rate reduction in particle mass produced a significant decrease in the centrifugal force acting on the particle. This highlights the importance of the rate of change in particle mass in determining particle residence time, and identifies radiation intensity as a key parameter for improving reactor throughput rate and capital intensification,

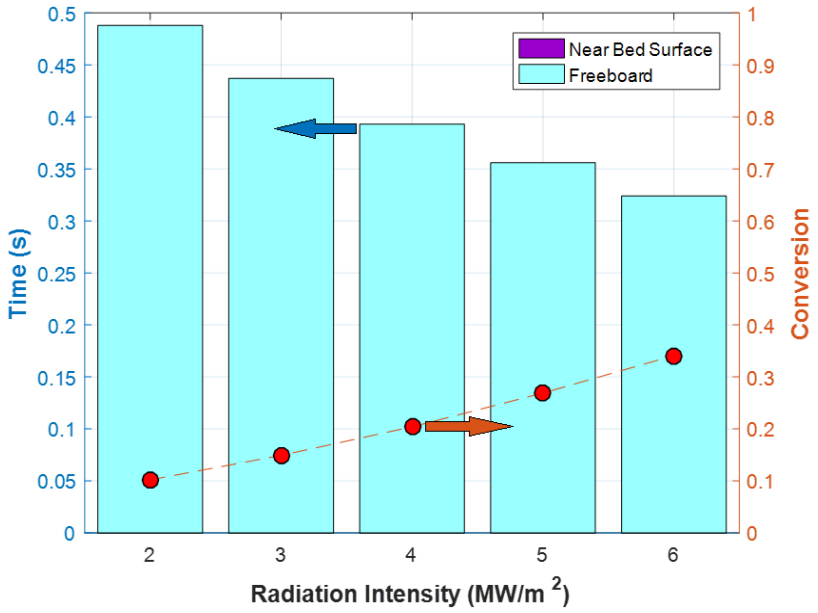

Figure 4.9: Comparison of calculated residence time τ_{res} and conversion X as a function of radiation intensity q_{solar} under the conditions shown in Tables 1, 2, and 3.

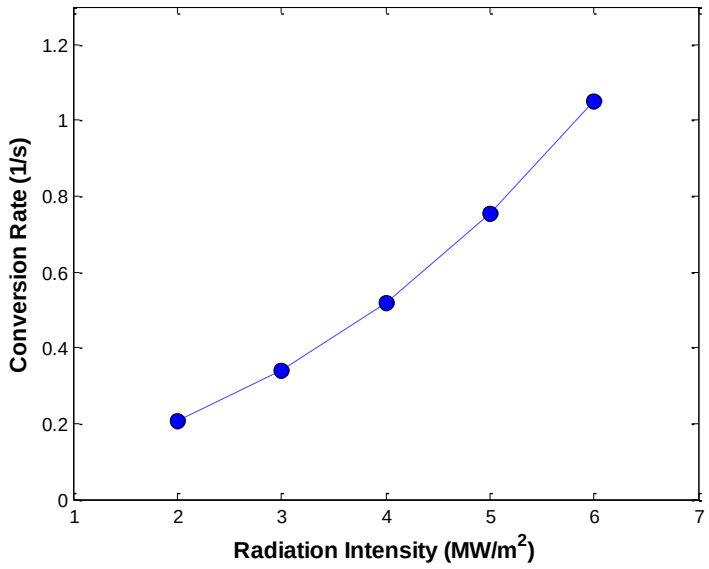

Figure 4.10: Calculated average particle conversion rate $\frac{\Delta X}{\Delta t}$ as a function of radiation intensity q_{solar} under the conditions shown in Tables 1, 2, and 3.

4.4.5 Effect of particle release position

The particle residence time and conversion as a function of the dimensionless particle release position in the Z direction is presented in Figure 4.11. It is apparent that particle release position has relatively little influence on the particle residence in the cavity and almost negligible influence on conversion. The decrease in residence time is seen to diminish with increased Z position. This can be attributed to the expression for the estimating the Z fluid velocity which increases in the positive Z direction due to higher cross section flow rate. It is worth noting that the particle residence time variations caused by the changes in particle release position are insignificant compared to other more effective means such as altering the rotational speed or initial particle radius. Figure 4.12 shows that the average conversion rate is independent of particle release position. This implies that heat and mass transfer are not affected by particle release position as expected.

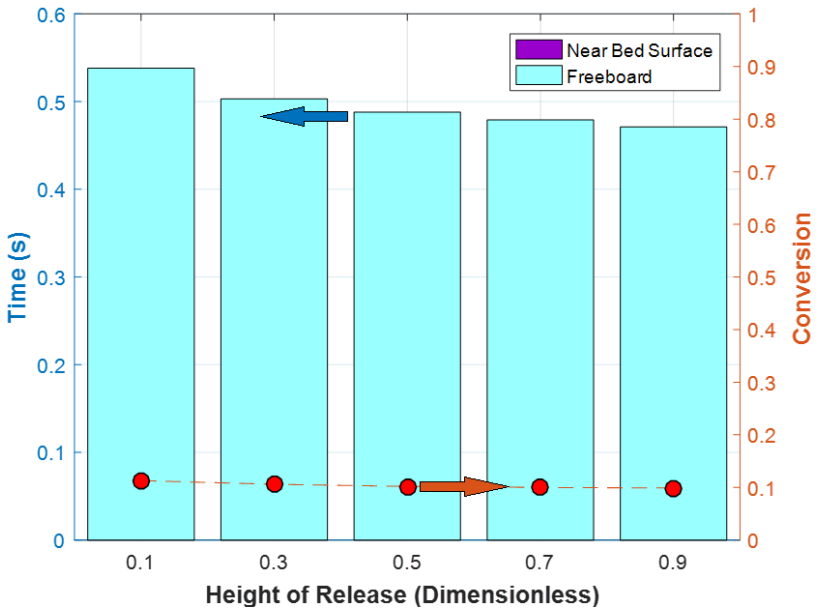

Figure 4.11: Calculated total residence time τ_{res} and conversion X as a function of particle release height $H_{release}$ under the conditions shown in Tables 1, 2, and 3.

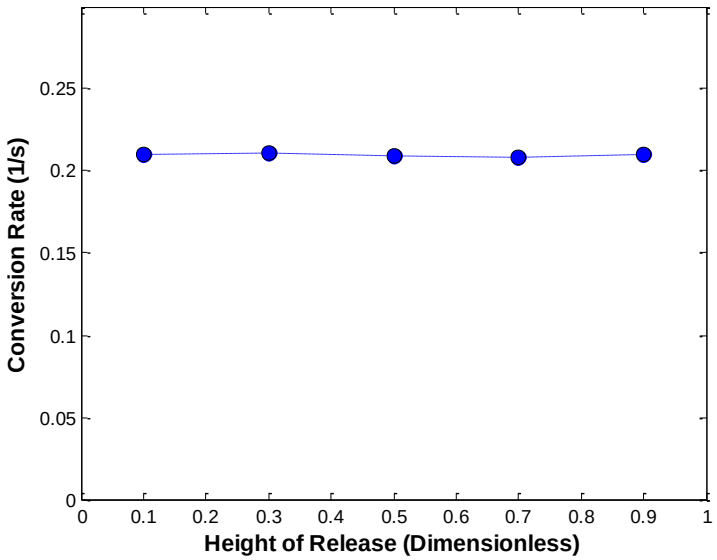

Figure 4.12: Calculated average particle conversion rate $\frac{\Delta X}{\Delta t}$ as a function of particle release height $H_{release}$ under the conditions shown in Tables 1, 2, and 3.

4.5 Conclusion

The results of the present study confirm the suitability of the proposed rotating fluidized bed solar reactor to enable increased residence time and conversion of particles relative to a vertical solar fluidized bed. Precise control of the reactor is possible through adjusting relevant operating parameters. Some of the important findings are as follows:

- Rotational speed is found to be the most important operating parameter controlling particle conversion and residence time, influencing the conversion extent at which particles are retained in the bed before elutriation. Conversion approaches completion as the rotational speed increases.
- Initial particle radius has a complex influence on particle residence time and conversion. Large particles are shown to be trapped in the reactor for longer than small particles due to the greater centrifugal force. This preferential entrapment of large particles limits the percentage of feedstock leaving the reactor unreacted. However, it is important to note that large particles may be converted at slower rates due to the limitations imposed by diffusive mass transfer of gasification agent.
- Radiation intensity significantly increases particle temperature and conversion rate, leading to higher particle conversion. An increased particle conversion rate can causes a rapid loss of particle mass which greatly reduces particle residence time. It is worth noting that the reduction in residence time in this case is not a disadvantage because the significantly increased conversion rate makes up for any reduction in conversion due to decreased residence time. The net effect of increasing radiation intensity is greatly improved conversion, throughput rate and capital intensification.

- Particle released height is found to have negligible influence on residence time or particle conversion. Particle release height may have more influence on particle residence time in practice due to the role of end effects and turbulence.

4.6 Acknowledgement

The authors would like to acknowledge the financial support provided by the Australian Solar Thermal Research Initiative.

4.7 Nomenclature

A_j		Frequency factor
A_{dis}	[m]	Area of the gas distributor
A_p	[m^2]	Particle cross sectional area
B_o		Gas permeability of the porous char particle
C_d		Particle drag coefficient
C_i	[mol m^{-3}]	ith component concentration
C_t	[mol m^{-3}]	Total concentration of gas components
$C_{i,bulk}$	[mol m^{-3}]	ith component concentration in the bulk gas
$c_{p,s}$	[J kg^{-1}]	Specific heat capacity solid
$c_{p,g}$	[J kg^{-1}]	Specific heat capacity gas
$\mathcal{D}_{i,eff}$	[m^2 s^{-1}]	Effective diffusion coefficient of the ith gas component
$\mathcal{D}_{i,K}$	[m^2 s^{-1}]	ith component Knudsen diffusion coefficient
$\mathcal{D}_{i,j}$	[m^2 s^{-1}]	Molecular diffusion coefficient
$D_{Aperture}$	[m]	Diameter of the Aperture
D_{Bed}	[m]	Diameter of the Bed Surface
$D_{Distributor}$	[m]	Diameter of the Gas Distributor
d_{pore}	[m]	Particle pore diameter
g	[m s^{-2}]	Gravitational acceleration
$H_{release}$		Height of release (fraction of cavity length)
h	[m]	Height of the gas distributor
k_i		Gasification kinetic parameter

k_c	[mol m^{-2} s^{-1}]	Mass transfer coefficient
L	[m]	Reactor cavity length
m_{init}	[kg]	Initial mass of particle
M_c	[mol kg^{-1}]	Molecular weight of carbon
M	[mol kg^{-1}]	Molecular weight
N_i	[m^3 mol^{-1} s^{-1}]	ith component net flux
Nu		Nusselt number
P	[Pa]	Pressure
P_t	[Pa]	Total Pressure
p_i	[Pa]	ith component partial pressure
$\dot{Q}_{abs}$	[W]	Absorbed radiative heat
$\dot{Q}_{convection}$	[W]	Convective heat on the particle surface
$\dot{Q}_{conduction}$	[W]	Conductive heat on the particle surface
$\dot{Q}_{re-radiation}$	[W]	Re-radiative heat on the particle surface
$\dot{Q}_{solar}$	[W]	Solar radiation heat incident on the particle surface
q_{solar}	[MW m^{-2}]	Solar heat flux
$\mathcal{R}$	[m^3 Pa Kmol]	Universal gas constant
Re		Reynolds number
R_{char}	[mol m^{-3} s^{-1}]	Rate of char gasification
$R_{intrinsic}$	[mol m^{-3} s^{-1}]	Intrinsic rate of char gasification
$R_{solar,char}$	[mol m^{-3} s^{-1}]	Rate of char gasification corrected for high solar flux
r	[m]	Particle radial position
$\dot{r}$	[m s^{-1}]	Particle radial acceleration velocity
$\ddot{r}$	[m s^{-2}]	Particle radial acceleration
r_p	[µm]	Particle radius
$r_{p,0}$	[µm]	Initial particle radius
r_{bed}	[m]	Fluidized bed radius
r_{exit}	[m]	Exit port radius
$r_{distributor}$	[m]	Gas distributor plate radius
$r_{aperture}$	[m]	Reactor aperture radius
r_m	[m]	Location of the boundary between forced and free vortices
S_r	[m^2]	Internal reactive surface area
S_r^0	[m^2]	Initial internal reactive surface area
Sh		Sherwood number
T	[K]	Particle Temperature
T_{srn}	[K]	Reactor Wall Temperature
T_g	[K]	Bulk Gas Temperature
T_{feed}	[K]	Temperature of particles entering the reactor

u_θ	[m s^{-1}]	Tangential component of the gas velocity in the freeboard
u_r	[m s^{-1}]	Radial component of the gas velocity in the freeboard
u_z	[m s^{-1}]	Axial component of the gas velocity in the freeboard
v_f	[m s^{-1}]	Fluidizing Gas Velocity at the Distributor
v		Stoichiometric coefficient
$y_{i,bulk}$		Mole fraction of ith component in the bulk gas
y_i		Mole fraction of ith component in the particle
z	[m]	Particle axial position
$\dot{z}$	[m s^{-1}]	Particle axial velocity
$\ddot{z}$	[m s^{-2}]	Particle axial acceleration
ΔH_R	[J mol^{-1}]	Enthalpy Change due to Steam Gasification Reaction
α		Effective absorptivity
ε		Effective emissivity
σ	[W m^{-2} K^{-4}]	Stefan-Boltzmann Constant
σ_{ij}	[Å]	Collision diameter
Ω_D		Collision integral
μ	[N s m^{-2}]	Viscosity
$\dot{\theta}$	[rad s^{-1}]	Particle angular velocity
$\ddot{\theta}$	[rad s^{-2}]	Particle angular acceleration
φ		Porosity
φ_{cr}		Critical porosity
τ		Tortuosity of the pores
λ_{eff}	[W m^{-1} K^{-1}]	Effective thermal conductivity
λ_s	[W m^{-1} K^{-1}]	Thermal conductivity of solid char
λ_g	[W m^{-1} K^{-1}]	Thermal conductivity of gas mixture
$\rho_{particle}$	[kg m^{-3}]	Apparent density of the particle
ρ_{char}	[kg m^{-3}]	Density of solid phase char
ρ_{gas}	[kg m^{-3}]	Density of the gas mixture in the particle
ρ_{fluid}	[kg m^{-3}]	Density of the gas mixture in the freeboard
ω	[rad s^{-1}]	Rotational Speed of the Reactor

Chapter 5

RFBR Flow Field and Particle Deposition

This chapter reports the numerical analysis of the RFBR concept's potential to mitigate and control particle deposition onto the receiver window. It is known that the rotation of the fluidized bed in the RFBR concept could generate a high intensity vortex flow in the freeboard and prevent entrained particles from entering the secondary concentrator volume and depositing onto the window. However, the range of suitable rotational speeds required to generate such a high intensity vortex flow in the RFBR concept is yet to be determined. Low rotational speeds are unlikely to generate a vortex flow that mitigates particle deposition onto the receiver window. On the other hand, high rotational speeds .may yield unnecessary kinetic energy loss and rotating component wear. Therefore, gaining an understanding of the influence of bed rotational speed and inlet fluidizing gas velocity on the flow field and particle deposition behaviour in the RFBR concept is important for evaluating its feasibility and identifying operating regimes in which particle deposition on the window is minimised.

The numerical analysis in the present chapter involved coupling Computational Fluid Dynamics (CFD) model for flow field prediction with Discrete Phase Model (DPM) for particle tracking. Because the focus of the numerical analysis is on particle entrainment and

deposition behaviour, the fluidized bed volume was not considered, and the modelled domain consisted of a vastly simplified RFBR geometry. The fluidized bed surface was set to be the inlet for the injected mono-disperse particles and working fluid, which is steam at 1000 K. Due to the lack of information about the radiative flux distribution inside the RFBR concept, heat transfer was not considered, and the modelled domain was assumed to be isothermal. Ozalp et al. (2013) and Chinnici et al. (2016) used similar CFD-DPM approaches to study the particle deposition behaviour in vortex flow solar receivers and obtained numerical predictions that were in good agreement with experimental measurements.

The sensitivity of the flow field in the RFBR to variations in bed rotational speed and fluidizing gas velocity was investigated in the present numerical analysis. The influence of these parameters on the flow field and particle deposition behaviour was found to be linked to their ability to affect the vortex flow intensity in the RFBR freeboard and subsequently the centrifugal force acting on entrained particles. The results of the analysis identified physical mechanisms affecting the particle deposition onto the receiver window and highlighted the unexpected effects of the tangential outlet geometry on the flow field at high fluidizing gas velocities and flow rates.

The numerical analysis in the present chapter confirmed the RFBR concept's potential to control and significantly reduce particle deposition through the adjustment of bed rotational speed. The RFBR concept shows potential in achieving cost effective window maintenance and the required technical robustness for CST systems.

Statement of Authorship

Title of Paper	Numerical Investigation of the Isothermal Flow Field and Particle Deposition in a Rotating Fluidized Bed Solar Receiver
Publication Status	☐ Published ☐ Accepted for Publication ☑ Submitted for Publication ☐ Unpublished and Unsubmitted work written in manuscript style
Publication Details	Z. Lu, A. Chinnici, M. Jafarian, M, Arjomandi & G. Nathan, 2017, "Numerical Investigation of the Isothermal Flow Field and Particle Deposition in a Rotating Fluidized Bed Solar Receiver", Solar Energy, (Under Review)

Principal Author

Name of Principal Author (Candidate)	Zhao Lu
Contribution to the Paper	Developed ideas, performed numerical simulations, interpreted data, wrote manuscript, and acted as the corresponding author.
Overall percentage (%)	70
Certification:	This paper reports on original research I conducted during the period of my Higher Degree by Research candidature and is not subject to any obligations or contractual agreements with a third party that would constrain its inclusion in this thesis. I am the primary author of this paper.
Signature	Date 17/04/2018

Co-Author Contributions

By signing the Statement of Authorship, each author certifies that:

i. the candidate's stated contribution to the publication is accurate (as detailed above);
ii. permission is granted for the candidate in include the publication in the thesis; and
iii. the sum of all co-author contributions is equal to 100% less the candidate's stated contribution.

Name of Co-Author	Mehdi Jafarian
Contribution to the Paper	Supervised development of work, interpreted data, and edited manuscript
Signature	Date 17/04/2018

Name of Co-Author	Alfonso Chinnici
Contribution to the Paper	Supervised development of work, interpreted data, and edited manuscript
Signature	Date 17/04/2018

Name of Co-Author	Maziar Arjomandi		
Contribution to the Paper	Supervised development of work, interpreted data, and edited manuscript		
Signature		Date	17/04/2018

Name of Co-Author	Graham Nathan		
Contribution to the Paper	Supervised development of work, interpreted data, and edited manuscript		
Signature		Date	17/04/2018

Numerical Investigation of the Isothermal Flow Field and Particle Deposition Behaviour in a Rotating Fluidized Bed Solar Receiver

Zhao Lu*

Alfonso Chinnici

Mehdi Jafarian

Maziar Arjomandi

Graham J. Nathan

Centre for Energy Technology, School of Mechanical Engineering, The University of Adelaide, SA 5005, Australia

*Corresponding author: zhao.lu@adelaide.edu.au

Keywords: CFD; particle tracking; rotating fluidized bed; solar receiver.

Abstract

A numerical analysis of the isothermal flow field within a directly irradiated Rotating Fluidized Bed Receiver (RFBR), is presented to provide a systematic assessment of the influence of key receiver control parameters, namely fluidized bed rotational speed and radial fluidizing gas velocity, on the flow field inside the receiver and particle deposition onto the receiver window. To achieve these aims, a Computational Fluid Dynamics (CFD) model of the RFBR was developed and coupled with Discrete Phase Model (DPM) to analyse the fluid flow and particle trajectory in the receiver cavity for the systematic variations of the key control parameters. The fluid flow modelling approach was partially verified by comparing the numerical predictions with previously published experimental flow measurements in a rotating vortex flow device that is geometrically similar to the RFBR. Using the reported modelling approach, the sensitivity of the flow field and particle deposition to the variations in key control parameters was determined. Flow features and physical mechanisms linked to particle deposition onto the receiver window were identified with the view to better understand the operation of the RFBR and identify operating regimes that achieve a low risk of particle deposition onto a window.

5.1 Introduction

Concentrated Solar Thermal (CST) technology is receiving growing attention due to its potential to reduce CO_2 emissions and facilitate the transition from a fossil fuel-based economy to a hydrogen-based economy (Steinfeld, 2005; Gordillo & Belghit, 2011). CST can be coupled with combustion hybrids technologies for continuous power generation or applied to thermochemical processes for chemical production, which essentially converts solar energy to chemical energy in storable compounds. Several examples of solar thermochemical processes that have been demonstrated at lab scale include gasification, methane decomposition and thermal production of metals and minerals. The lack of combustion products in solar heat driven thermochemical processes offers reduced CO_2 emission and potential to improve chemical product quality. For this reason, a range of lab scale solar thermochemical receivers have been developed to harness concentrated solar radiation and turn it into the process heat to drive thermochemical reactions (Steinfeld, 2005; Nathan et al., 2018). These receivers span from simple tubular receivers to complex particle receivers, each suitable for a particular range of feedstock properties and operating conditions (Nathan et al., 2017; Jafarian et al., 2013). For instance, entrained flow receivers such as the Solar Vortex Receiver configuration (SVR; Z'Graggen & Steinfeld, 2008) and its refined configuration termed the Solar Expanding-Vortex Receiver (SEVR; Chinnici et al., 2015, 2016, 2017) are particularly suited for small particles that can be suspended in particle clouds for effective solar radiation absorption. In contrast, the packed bed solar gasifier developed by Piatowski & Steinfeld (2008) is well suited for large particles of a very wide range of sizes that are too heavy to be suspended by a heat transfer fluid. Fluidized bed solar receivers require feedstock particles with properties that fall between the feedstock

particle requirements for the entrained flow and packed bed receivers whilst offering relatively high mass and heat transfer rates comparable to those found in entrained flow receivers (Higman, 2011). For a typical fluidized bed, the feedstock particle size can range from a few hundred microns to a few thousand microns depending on particle density (Geldart, 1973). The particle size distribution required is also less stringent than that for an entrained flow receiver. Hence, potential cost savings can be achieved in the feedstock preparation stage. For these reasons, the application of fluidized bed for solar thermochemical processes has been investigated experimentally by Taylor et al. (1983), Kodama et al. (2002), Trommer (2006) and Kodama et al. (2008). More research is still needed to better understand the operation and limitations of fluidized bed exposed to concentrated solar radiation at extreme temperature conditions (>1200K) that are not found in conventional non-solar fluidized bed chemical reacting systems. Therefore, the overall objective of the present paper is to support the development of more technologically robust fluidized bed receivers.

Whilst possessing many advantageous characteristics, fluidized bed is associated with many unique challenges that act as barriers to its implementation in solar thermochemical processes. The first major barrier is the limited bed surface area for solar radiation absorption. The large volume-to-surface ratio in a typical fluidized bed is undesirable because it limits the maximum temperature that can be achieved in the bed volume uniformly. For uniformity of temperature to occur within a fluidized bed, the rate of heat transfer within the bed volume must be sufficiently high to quickly dissipate any radiative heat absorbed on the bed surface. If the rate of heat absorbed on the top surface is higher than the rate of heat dissipation in the bed volume, hotspots can form on the top surface, and

the feedstock particles there may melt or thermally anneal, both of which may negatively alter reaction kinetics and pathway. In addition, the maximum gas-solid slip velocity in a fluidized bed, important for the mass and heat transfer rates between gas and solid phases, is limited by the constant gravitational force acting on the feedstock particles. At excessively high fluidizing gas velocities, the gravitational force becomes insufficient to counteract against the fluidizing gas drag force acting on the particles. As a result, fine particles are elutriated out of the bed. This elutriation increases the concentration of particles in the freeboard above the bed, influencing the radiative heat transfer in the receiver cavity and potentially reducing the solar radiative heat flux on the bed surface. For directly irradiated fluidized bed receivers, this elutriation is hazardous to the receiver window because it could affect the window's transparency and cause overheating and subsequent structural failure (Hirsch & Steinfeld, 2004; Kodama et al., 2008). Furthermore, due to the reliance on gravity, a fluidized bed receiver can only operate in the vertical orientation and thus is limited to less optically efficient beam-down solar radiation concentrating methods. Because of these limitations, fluidized bed solar receivers are difficult to operate on a large scale. There is a need for the development of an alternative fluidized bed configuration that could overcome or mitigate the negative impacts of these limitations.

To address the limitations of conventional fluidized bed solar receivers, a directly irradiated Rotating Fluidized Bed Receiver (RFBR) concept has been reported by Lu et al. (2016) for steam gasification of biomass char. A schematic representation of the RFBR concept is shown in Figure 5.1. In operation, the rotation of the RFBR generates a centrifugal acceleration which pushes the feedstock particles radially outwards from the central screw feeder and forms a relatively thin particle bed on the cylindrical wall. Unlike conventional

fluidized bed, fluidizing gas is injected radially through the porous cylindrical wall into the RFBR cavity. The cylindrical wall functions as a fluidizing gas distributor, thereby significantly increasing the available bed surface area for solar radiation absorption. This combined with a relatively thin bed thickness results in greatly reduced fluidized bed volume-to-surface ratio and helps to create a uniform distribution of bed temperature even under intense radiative heat flux.

In addition, the centrifugal force generated through rotation is both adjustable and configurable to significantly exceed the gravitational force, meaning that the orientation of a rotating fluidized bed is not limited by the direction of gravitational acceleration or beam-down optical systems, although a beam-down system is used in the current concept for the ease of scaling infrastructure on the ground. The additional control parameter of fluidized bed rotational speed gives RFBR more controllability over conventional fluidized bed because it can be used to shift the bed fluidization regime as well as fluidizing gas velocity. Qu et al. (2001) through a series of experiments demonstrated that even cohesive fine particles in the "Geldart Group C" category can be uniformly fluidized in an RFB if there is sufficient centrifugal force. The slugging and channeling of fluidizing gas through cohesive fine particle beds have been shown to decrease with increasing centrifugal force (Qu et al., 2001). Moreover, by adjusting the magnitudes of the centrifugal and fluidizing gas drag forces, the gas-solid slip velocity in an RFB can be increased to potentially achieve higher rates of heat and mass transfer. Hao et al. (2000) demonstrated in an RFB food dryer that increasing the rotational speed and fluidizing gas velocity improves the rates of heat transfer and drying of food particles. However, as with conventional fluidized bed, RFB also suffers from the problem of particle elutriation, albeit to a lesser extent due to the

stronger centrifugal acceleration that can be adjusted to limit the size of elutriated particles. The elutriation of non-reacting particles in RFB has been studied both numerically and experimentally by Chevray et al. (1980) and Saunders (1986), both of whom verified the effectiveness of rotational speed in limiting the mass flow rate and maximum size of elutriated particles for non-solar devices. As mentioned previously, particle elutriation in a solar fluidized bed receiver can affect the radiative heat transfer within the receiver cavity and loss through the receiver aperture. Hence, it is important to develop an understanding of the influence of dominant receiver control parameters, notably fluidized bed rotational speed and radial fluidizing gas velocity, on the fluid flow field and distribution of elutriated particles in the receiver cavity.

Previous assessment of the potential benefits of the RFBR concept on particle residence time and gasification conversion (Lu et al., 2016) utilized an analytical model based on an idealised semi-empirical flow field derived from the experimental flow velocity measurements of Donaldson & Snedeker (1962) in a geometrically similar rotating vortex flow device. This idealised flow field assumption severely constrains the geometrical configurations that can be investigated and prevents the assessment of variables that may heavily depend on flow features, such as the potential for particles to propagate through the aperture to either deposit on the receiver window. Therefore, there is a need for an investigation of the flow-field and particle entrainment behaviour inside the RFBR with tools that do not require this idealised flow field assumption. To meet this need, the present study reports a systematic investigation conducted using Computational Fluid Dynamics (CFD) coupled with Discrete Phase Model (DPM) to investigate the effects of key receiver control parameters, bed rotational speed and radial fluidizing gas velocity, on the flow-field

and entrained particle trajectory within the receiver cavity, with the aims of assessing the particle deposition onto the window of the RFBR concept and providing new understanding of the underlying mechanisms.

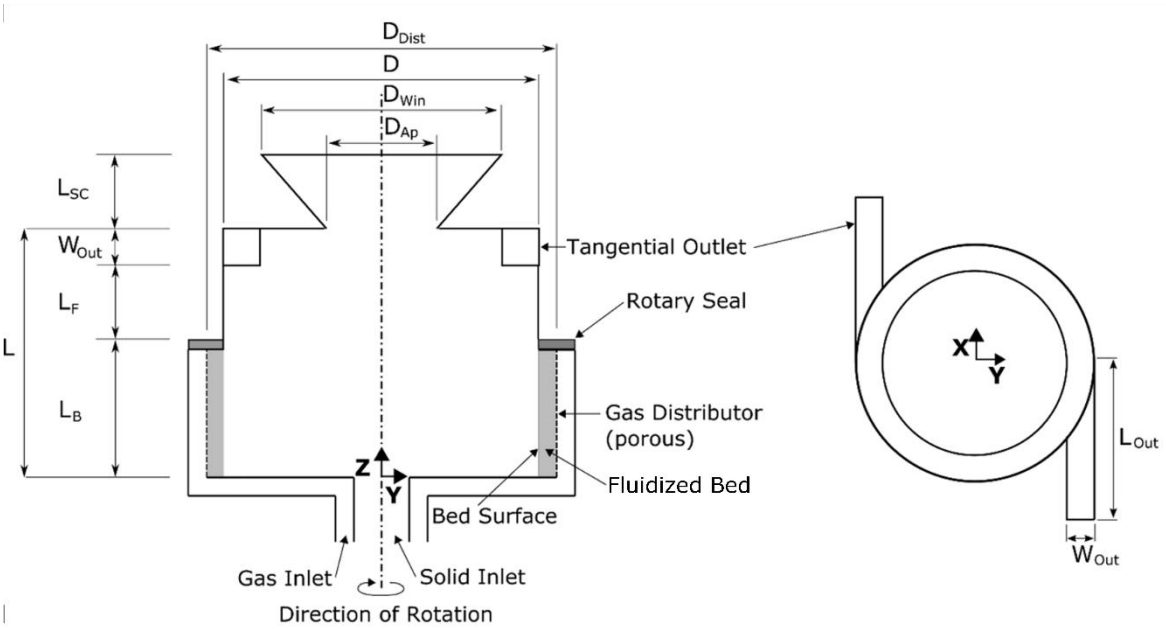

Figure 5.1: Schematic diagram of the Rotating Fluidized Bed Receiver.

5.2 Methodology

The physical dimensions of the RFBR investigated here are listed in Table 1. This configuration differs from that reported previously by the authors (Lu et al., 2016) due to small iterative changes made to the concept based on previous findings. The RFBR concept is configured for a beam-down solar radiation concentrating system which allows the receiver to be placed on the ground. This eases the weight limitation on the receiver which is expected to be heavier than other solar receiver concepts due to the need for additional components to generate rotation. The RFBR consists of two separate sections joined with a

rotary seal. This configuration allows the heaviest components to be fixed and the lighter components to be rotated for minimal kinetic energy loss. The top stationary section contains a secondary concentrator, which is assumed to be conical, and two diametrically opposed tangential outlets, each of square cross section and selected based on considerations of manufacturability and geometrical simplicity. The present paper also only considers the case which the secondary concentrator is sealed with a transparent quartz window following earlier work (Lu et al., 2016). The rotating bottom section contains a porous cylindrical wall which acts as a gas distributor for the fluidized bed and a centrally positioned screw feeder at the bottom surface for feeding particles into the receiver cavity. Concentrated solar radiation enters the receiver cavity through the aperture and is absorbed by the particle bed surface to drive the gasification process within the bed volume. Ash and other fine particles derived from the gasification process are entrained from the bed surface and carried out of the receiver domain by the radially injected fluidizing gas

The surface profile of the bed is shown schematically as being of uniform radial thickness (Fig 1) based on the observations of Kroger et al. (1979), Saunders (1986) and Watano et al. (2003) for RFB operating at high rotational speeds (> 26 rad/s). Some departure from the uniform bed thickness can be expected under low rotational speed conditions but this is not considered in the present paper due to limited understanding of the effect of rotational speed on bed surface profile. For the systematic investigation of the effects of bed rotational speed and radial inlet gas velocity on flow field and participle deposition on the receiver window, 25 combinations of these two key control parameters are selected and listed in Table 2. This selection covers most of the expected operating regime of the RFBR, which is the bubbling

fluidized bed regime for carbonaceous materials (< 1000 kg/m^3) and particle sizes between 100 and 500 microns.

Table 1: Dimensions of the RFBR configuration investigated in the present study.

Variable	Unit	Value
D_{Win}	[m]	0.4
D_{Ap}	[m]	0.2
D	[m]	0.5
D_{Dist}	[m]	0.6
W_{out}	[m]	0.05
L_{Out}	[m]	0.6
L_B	[m]	0.25
L_F	[m]	0.2
L	[m]	0.5
L_{SC}	[m]	0.15

Table 2: RFBR operating conditions investigated in the present study.

Rotational Speed (rad/s)	Radial Inlet Velocity (m/s)	Rotational Reynolds Number
15.7 (150 RPM)	0.1-0.3 (0.05 increments)	5.9818×10^3
23.6 (225 RPM)	0.1-0.3	8.9727×10^3
31.4 (300 RPM)	0.1-0.3	1.1964×10^4
39.4 (375 RPM)	0.1-0.3	1.4955×10^4
47.1 (450 RPM)	0.1-0.3	1.7945×10^4

The modelled receiver domain is shown in Figure 5.2. The rotating fluidized bed volume, gas distributor, and upstream components were not included in the model domain because the main objectives of the present study are to assess the flow field inside the receiver cavity and the particle deposition onto the receiver window. To simplify the receiver geometry for CFD investigation, the thickness of the rotary seal was assumed to be physically insignificant, having negligible effect on the flow within the cavity, and the fluidized bed surface was treated as a flat static surface to provide an inflow boundary to the model domain. The fluid flow at the inlet boundary (bed surface) is characterised by its radial and tangential velocity components which are related to the radially injected fluidizing gas

velocity at the bed surface and bed rotational speed respectively. The axial velocity component is assumed to be zero. In addition, the walls of the receiver were assumed to be adiabatic, and the entire flow field within the receiver cavity was considered isothermal at a temperature of 1000K. The working fluid is selected to be steam because it makes up the most volume in a typical solar steam gasification receiver.

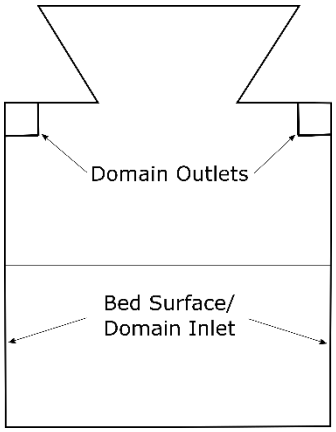

Figure 5.2: ZY plane projection of the modelled geometrical representation of the RFBR.

A commercial CFD code, Fluent 17.1 was used for the simulations of the turbulent fluid flows, species transport and particle tracking in the proposed RFBR. The three-dimensional geometrical representation of the RFBR domain was developed and meshed with ANSYS Workbench 17.1 and smoothed in Fluent 17.1. The mesh quality was checked for mesh independence, skewness, aspect ratio, and orthogonality. All transport equations were discretised employing a second order upwind scheme. The final mesh comprises of approximately 1.6 million elements. The discretised equations were then solved using SIMPLE solver. Simulations were considered converged when the residuals reach below 1 x 10^{-5} and the monitored fluid flow variables at locations of interest cease to fluctuate with further iterations.

Fluent 17.1 offers a variety of Reynolds-averaged Navier–Stokes (RANS) equations based turbulence models with which the fluid flow in the receiver cavity could be numerically predicted. For applications involving internal rotating flow with particle entrainment, two commonly used Fluent turbulence models in literature are Reynold Stress Model and Re-Normalization Group (RNG) k-ε model (Gimbun et al., 2005). Azadi et al. (2010) used the aforementioned turbulence models with Discrete Phase Model (DPM) to study the effect of cyclone size on its performance. They were able to predict the minimum particle cut-off diameters in different sized cyclones within 8% of experimentally measured values. Chuah et al. (2006) also used the Reynold Stress and RNG k-ε models with DPM to study the effect of cone tip dimensions on cyclone performance. Their numerical predictions showed close agreement with experimentally measured cyclone collection efficiencies and deviations less than 10%. Both studies analysed vortex flows with equivalent Rotational Reynolds Numbers in the 10^5 range and provide confidence in the use of Fluent turbulence models with DPM for investigating particle entrainment in vortex flow devices.

More recently, Chinnici et al. (2015) and Chinnici et al. (2016) used the RNG k-ε model with DPM to study the particle trajectory, residence time and deposition rate on the receiver window in the Solar Expanding Vortex Receiver, SEVR. A comparison of their numerically predicted and experimentally obtained particle deposition rates on the receiver window showed deviations than 12%.

To the authors' knowledge, there currently lacks publicly available experimental flow measurements in the freeboard of an RFB. However, there exists experimental flow measurements in a geometrically similar vortex flow device studied by Donaldson and

Snedeker (1962). Their device consists of a rotating porous cylinder that enables the radial injection of air into the cylinder cavity and an axially movable disc that closes one end of the cylinder and turns the opened end of the cylinder into an exit for the injected air flow. The rotation of the cylinder generates a vortex flow within the cylinder cavity, similar to how the rotating bed surface in an RFB generates a vortex flow. Therefore, the flow in the device of Donaldson and Snedeker (1962) should resemble the flow in the freeboard of an RFB and was used to help select a turbulence model and partially verify Fluent's reliability in the present investigation.

Figure 5.3 presents a comparison of turbulence model predictions and experimental velocity measurements made at the opening plane of the device of Donaldson and Snedeker (1962). Both the Reynold Stress and RNG k-ε turbulence models predicted with sufficient accuracy the combined free and forced vortex structure. The Reynold Stress Model shows slightly better agreement with the experimental measurements than the RNG k-ε model due to it being able to better predict the slight dip in tangential velocity at r/R = 0.6. However, this improvement in accuracy comes with a more significant computational cost because the Reynold Stress Model solves for 7 equations rather than the 2 equations required by the RNG k-ε model. Hence, the RNG k-ε model is selected to model fluid flow in the present investigation.

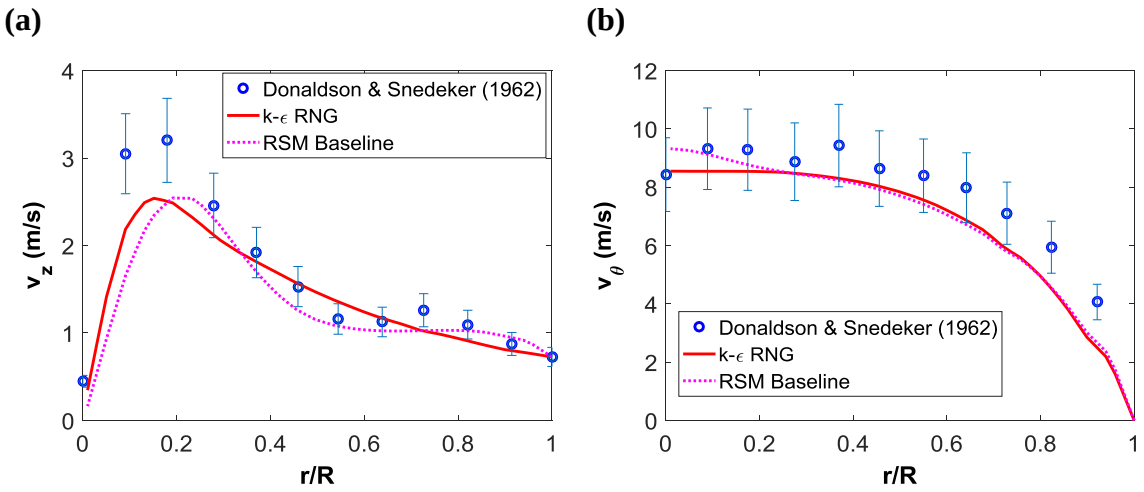

Figure 5.3: Comparison of measured and calculated velocity profiles, (a) tangential and (b) axial, for the vortex chamber experiment conducted by Donald & Snedecker (1962), with a length to diameter ratio of 5 and rotational speed of 25.23 rad/s. The error bars show deviations of 15% accounting for the uncertainty of the conical 5-point pressure probe and experimental set up.

The Discrete Phase Model (DPM) in Fluent 17.1 was implemented to track the particles injected from the fluidized bed surface, assess their trajectories relative to the fluid phase and investigate the particle deposition rates onto the window. The volume fraction of particles entrained at the inlet was kept constant at 2 x 10^{-5}, similar to other entrained flow receiver CFD-DPM investigations (Chinnici et al, 2016). This results in an inlet particle mass loading of 0.045 and prompts the use of Two-way coupled gas-solid interaction in Fluent.

Injected particle sizes of 10 µm, 20 µm, and 40 µm were selected for the DPM analysis because they are sufficiently small to be entrained out of the fluidized bed under the conditions listed in Table 2 and large enough to cause severe particle deposition rates on the receiver window. The injected particles were assumed to be spherical and have a density of 500 kg/m^3 based on the char density measurements of Mermoud et al. (2006). It is important to note that for each combination of rotational speed and radial inlet gas velocity in Table

2, three DPM simulations were conducted to separately assess the particle entrainment behavior of the three monodisperse particle sizes.

The surface injection option in Fluent was used to inject particles into the modelled domain. The injection surface is the fluidized bed surface and has a constant mesh density which leads to a constant number of particle parcel injection points. Particle dispersion due to fluid turbulence was accounted for using Fluent's Discrete Random Walk Model which uses a stochastic method to include the effect of turbulent velocity fluctuations on particle trajectories. To obtain realistic random effects of turbulence on particle dispersion, each injected particle parcel was tracked by the solver 20 times. As a result, for each DPM simulation, 272520 particle parcels were tracked in the model domain.

To facilitate consistent comparisons of flow field features in the vicinity of the aperture, four axial locations of interest were selected in the ZY plane (normal to outlets), as shown in Figure 5.4.

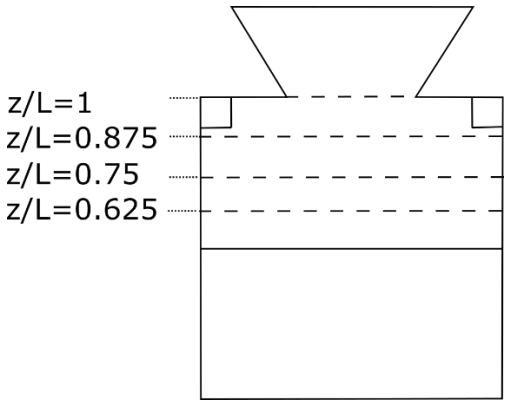

Figure 5.4: Locations of interest in the ZY plane of the modelled domain.

5.3 Results and discussion

5.3.1 Flow Analysis

Figure 5.5 presents the fluid axial (Fig 5a) and tangential (Fig 5b) velocity profiles of the fluid phase at various axial locations, z/L, in the ZY Plane of the RFBR operating at a rotational speed of 15.7 rad/s (150RPM) and a radial inlet velocity of 0.1 m/s. The axial velocity profiles indicate the presence of a complex vortex flow, characterised by multiple axial recirculation zones that can be identified by the pairs of adjacent local axial velocity maxima and minima. Axial recirculation appears to be the strongest nearest to the cavity wall and weakest at the cavity centre. This can be attributed to the tangential outlets which likely enhance the axial flow closest to the cavity wall. The strength of the recirculation is seen to increase as the flow develops in the positive Z direction. This is indicated by the growing difference between adjacent local maxima and minima. It is important to note that the strength of the recirculation in the outer region defined by $-0.5 > r/R > 0.5$ shows much greater variation with increasing z/L than the inner region defined by $-0.5 < r/R < 0.5$. This is favourable for a directly irradiated receiver because entrained particles are primarily recirculated in the outer region that is not directly under the aperture. At the Aperture ($z/L = 1$), the axial velocity profile resembles a compressed and truncated version of the velocity profile before it at $z/L = 0.875$. The sudden contraction of flow produces a noticeable increase in axial recirculation closest to the edge of the aperture. This means that entrained particles in close proximity of the aperture's edge are more likely to be entrained by the axial flow into the secondary concentrator volume.

The tangential velocity profiles in Figure 5.5, on the other hand, show little variations as the flow develops in the positive axial direction. The profiles indicate a vortex structure resembling that of a combined vortex with the forced vortex taking up most of the cavity volume, -0.9 > *r/R* > 0.9. The most notable difference between the tangential velocity profiles is the maximum tangential velocity which is seen to slightly decrease in the positive axial direction as a result of wall friction. This is consistent with the combined vortex flow observed in the numerical and experimental investigation of Chinnici et al. (2016). It is worth noting that the tangential velocity profiles in the region defined by the aperture diameter, 0.4 < *r/R* < 0.4, are remarkably similar. This suggests that entrained particles directly below the aperture are acted upon by similar centrifugal forces throughout the cavity length.

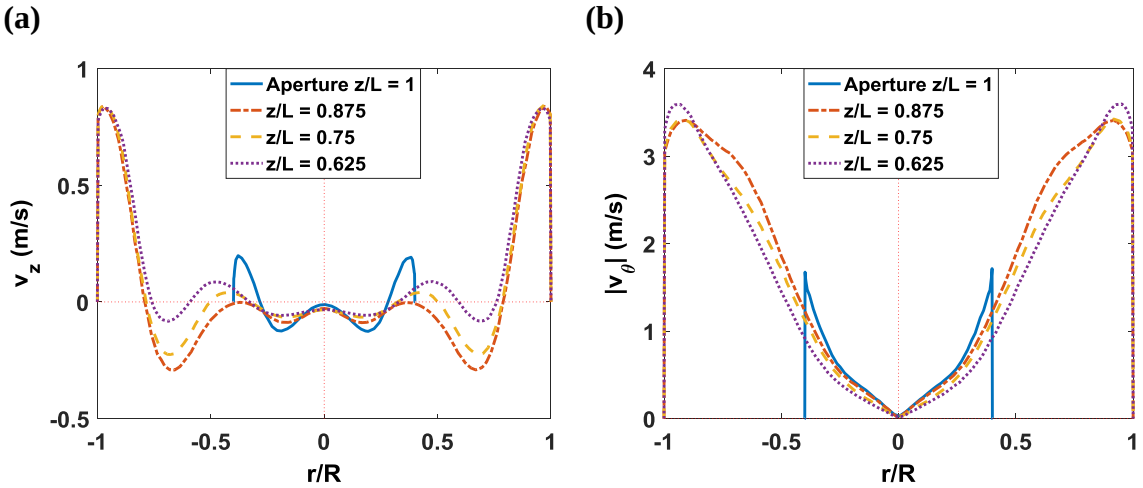

Figure 5.5: Calculated (a) axial and (b) tangential fluid velocity profiles in the ZY plane at various axial locations in the RFBR operating at a rotational speed of 15.7 rad/s and a radial inlet velocity of 0.1 m/s.

Figure 5.6 presents the fluid axial (Fig 5.6a) and tangential (Fig 5.6b) velocity profiles at various axial locations, z/L, in the ZY plane of the RFBR operating at a rotational speed of 15.7 rad/s and a radial inlet velocity of 0.3 m/s. A comparison of Figures 5 and 6 shows that that increasing the radial inlet velocity and fluid flow rate through the cavity has noticeable

effects on the vortex flow structure. For example, the local maxima and minima pairs in the axial velocity profiles (Fig 5.6a) are seen to be closer to the centre and the velocity difference between adjacent local maximum and minimum is noticeably increased, indicating stronger axial recirculation.

The tangential velocity profiles (Fig 5.6b) show that increasing the radial inlet velocity and flow rate increases the magnitude of the maximum tangential velocity, shifts the location of the maximum closer to the centre, enlarges the size of the outer free vortex, and generates a more complex vortex structure with a new local maximum tangential velocity emerging at *r/R* = 0.6 and -0.6. All of these effects bring entrained particles closer to the centre and increase the probability of particles entering the secondary concentrator volume and deposit on the window. However, it should be noted that the maximum tangential velocities at all axial locations appear to be greater than those seen in Figure 5.5. This means that entrained particles while closer to the centre are acted upon by a greater centrifugal acceleration which may reduce the likelihood of particle deposition on the window.

One perculiar feature of Figure 5.6b is that the tangential velocity is seen to noticeably increase from z/L = 0.75 to z/L = 0.875. This feature is not seen in Figure 5b and indicates that increasing the radial inlet velocity has the unintenteded effect of turning the tangential outlets located between z/L >= 0.9 and z/L <= 1 into a vortex generator. Because of the significant difference in the total areas of the fluidized bed surface inlet and tangential outlets, increasing the radial inlet velocity from 0.1 m/s to 0.3 m/s is sufficient to increase the average tangential outlet flow velocity from 7.85 m/s to 23.56 m/s. This high tangential outlet flow velocity is significantly greater than the tangential velocity generated through

bed rotation, which is 11.78 m/s at r/R = 1 for a rotational speed of 15.7 rad/s, and mostly responsible for the flow features seen in Figure 5.6b. Thus, the tangential outlet geometrical configuration and the ratio between total inlet and outlet areas are important design considerations that should be taken into account when determining suitable ranges of radial inlet and bed rotational velocities.

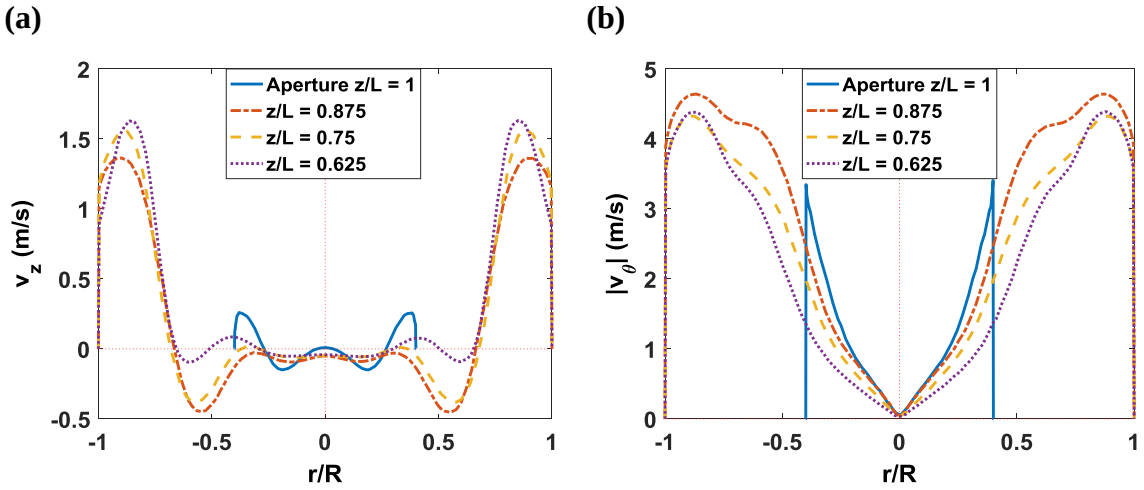

Figure 5.6: Calculated (a) axial and (b) tangential fluid velocity profiles in the ZY plane at various axial locations in the RFBR operating at a rotational speed of 15.7 rad/s and a radial inlet velocity of 0.3 m/s.

Figure 5.7 reports the axial velocity profiles in the ZY plane of the RFBR operating at a rotational speed of 15.7 rad/s inlet velocity of 0.1 m/s for various radial inlet velocities at z/L = 0.75 (Fig 5.7a) and aperture, z/L = 1 (Fig 5.7b). It can be seen that the stepwise increases in radial inlet velocity produce approximately proportional changes in the axial velocity profiles at both locations. The profiles at z/L = 0.75 show more significant changes compared to the profiles at the aperture, z/L = 1. This suggests that the axial flow through through the aperture is relatively insensitive to the radial inlet velocity and flow rate through the cavity. Thus, the radial inlet velocity profile across the height of the fluidized bed surface in the axial direction may have little impact on particle deposition on the window. One important feature to note in Figure 5.7 is that the radial inlet velocity appears to affect the

axial flow near the outer boundary, namely the cavity wall or aperture edge, more than the flow at the centre. This may be attributed to the tangential outlets which facilitate radially outward flow.

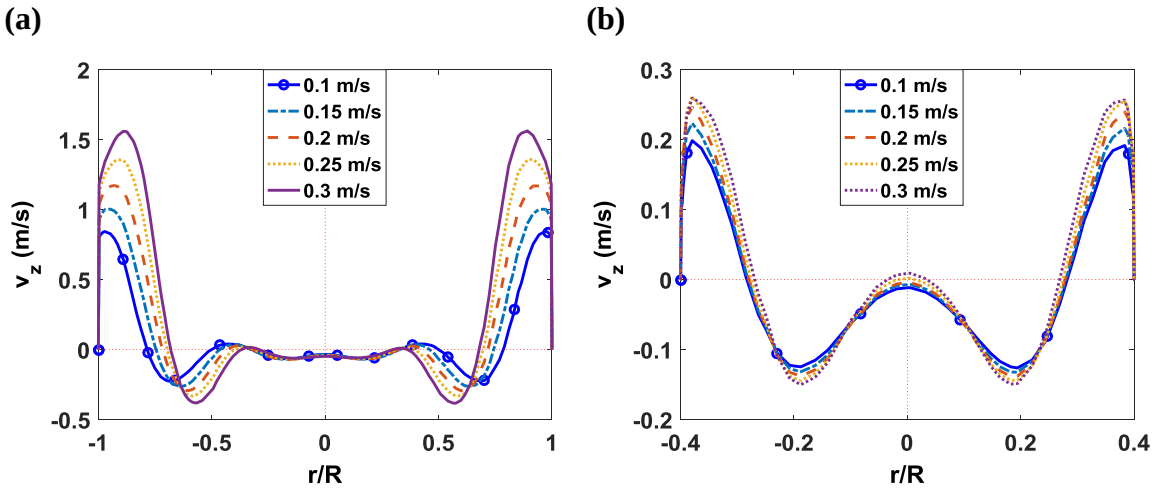

Figure 5.7: Calculated axial velocity profiles in the ZY plane in the RFBR operating at a rotational speed of 15.7 rad/s and axial locations of (a) z/L = 0.75 and (b) z/L = 1.

Figure 5.8 presents the fluid axial (Fig 5.8a) and tangential (Fig 5.8b) velocity profiles in the ZY plane at various axial locations, z/L, in the ZY plane of the RFBR operating at a rotational speed of 47.1 rad/s (450RPM) and a radial inlet velocity of 0.1 m/s. The axial velocity profiles (Fig 5.8a) show that increasing the rotational speed generates a more complex vortex structure with increased number of axial recirculation zones as indicated by the increased number of pairs of local velocity maximum and minimum. To accommodate the increased number of recirculation zones, each zone is squeezed and takes up less space in the radial direction. As a result, the location of the strongest axial recirculation zone closest to the wall is shifted further away from the centre. This may lead to reduced amount of entrained particles below the aperture and decreased probability of particle deposition on the window. It is worth noting that increasing the rotational speed also greatly increases the strengths of the axial recirculation zones. The maximum difference between adjacent local

axial velocity maximum and minimum is approximately 2.3 m/s in Figure 8a compared to approximately 1.2 m/s in Figure 5.5a. This may have implications on the average time that entrained particles are exposed to concentrated solar radiation under the aperture and other relevant gasification conversion parameters. Similar to Figures 5.5a and 5.6a, axial recirculation is also seen to increase in strength as the flow develops in the positive axial direction. This can be attributed to the tangential outlets located between z/L >= 0.9 and z/L <= 1 and highlights the importance of the axial location of the tangential outlets and its influence on the axial flow development within the receiver cavity.

The tangential velocity profiles (Fig 5.7b) show that increasing the rotational speed significantly increases the maximum tangential velocity and shifts its location further away from the centre. As expected, the increase in maximum tangential velocity is approximately proportional to the increase in rotational speed. Increasing the rotational speed from 15.7 rad/s to 47.1 rad/s resulted an increase in maximum tangential velocity from 3.6 m/s to 9.7 m/s at z/L = 0.625. This proportionality decreases as the axial location is increased due to the more pronounced effect of wall fricition on the faster rotating flow. At z/L = 0.875, the maximum tangential velocities for the two rotational speeds are reduced to 3.4 m/s and 8.1 m/s respectively.

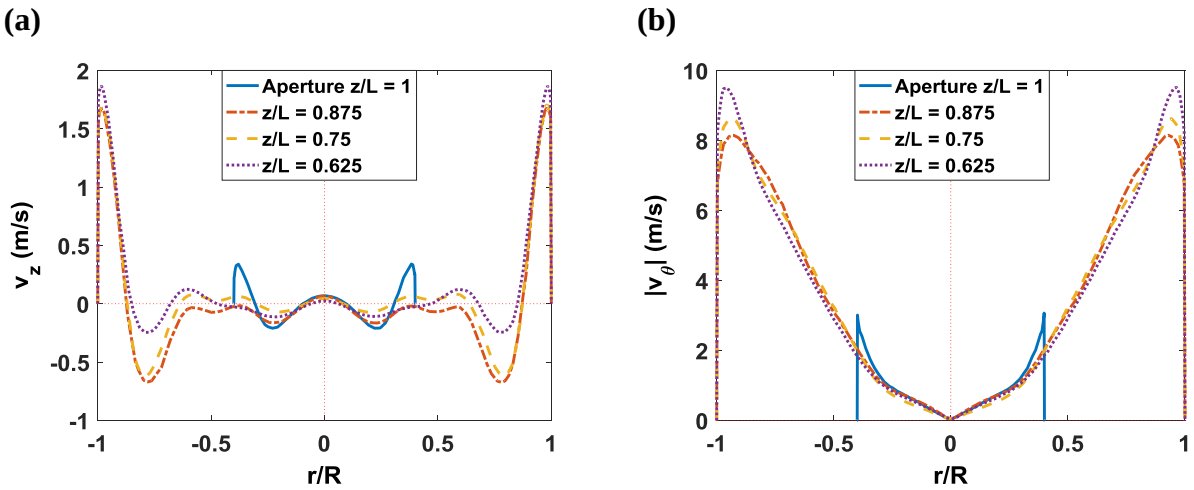

Figure 5.8: Calculated (a) axial and (b) tangential fluid velocity profiles in the ZY plane at various axial locations in the RFBR operating at a rotational speed of 47.1 rad/s and a radial inlet velocity of 0.1 m/s.

Figure 5.9 reports the axial velocity profiles in the ZY plane in the RFBR operating with a radial inlet velocity of 0.1 m/s for various rotational speeds at z/L = 0.75 (Fig 5.9a) and aperture, z/L = 1 (Fig 5.9b). It can be seen that rotational speed has significant influence on the axial velocity profiles at both locations. As the rotational speed increases, the vortex structure appears to become increasingly complex at z/L = 0.75, and the strength of axial recirculation at the aperture, z/L = 1, greatly increases. Figure 5.9b shows that at the aperture boundary, *r/R* = 0.4 and -0.4, the positive axial velocity is almost doubled from 0.2 m/s to 0.38 m/s for an increase in rotational speed from 15.7 rad/s to 47.1 rad/s. This could result in a significant increase in entrained particles entering the secondary concentrator volume and depositing on the window.

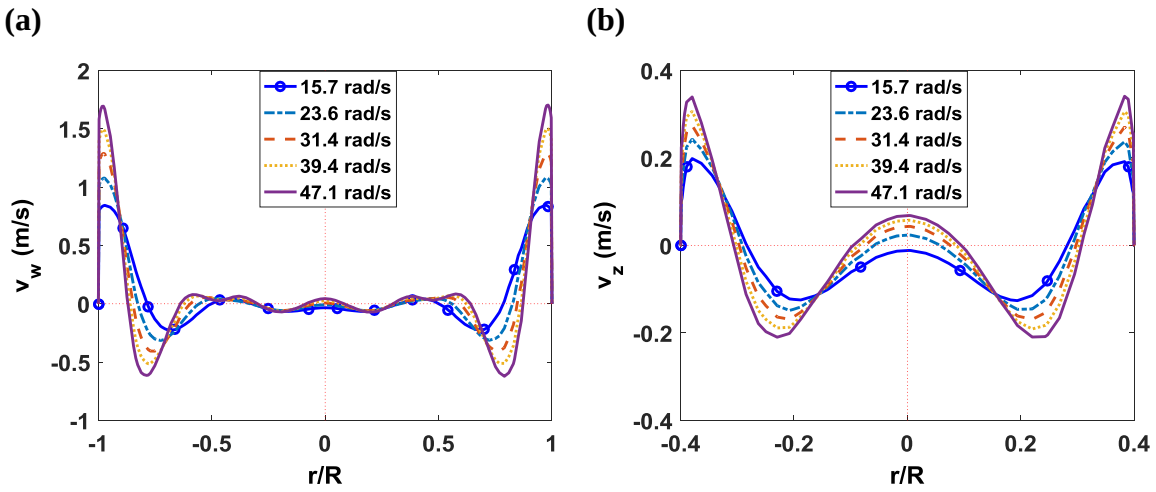

Figure 5.9: Calculated axial velocity profiles in the ZY plane of the RFBR operating with radial inlet velocity of 0.1 m/s at axial locations of (a) z/L = 0.75 and (b) z/L = 1.

Figure 5.10 presents the coordinates for which the axial velocity v_w = 0 m/s in the XY plane at the aperture, z/L = 1, in the RFBR opearting at a rotational speed of 15.7 rad/s for various radial inlet velocities (Fig 5.10a) and a radial inlet velocity of 0.1 m/s for various rotational speeds (Fig 5.10b). These coordinates provide information about the vortex structure at the aperture plane and the locations for positive (+Z) and negative (-Z) axial flows into the secondary concentrator volume. It can be seen that the vortex is non-uniform and appears to be warped by the tangential outlets located in the lower left (X & Y = -0.15) and upper right (X & Y = 0.15) corners . Figure 5.10a shows that as the radial inlet velocity and outlet flow rate increase, the vortex structure becomes increasingly warped and elongates in the directions of the tangential outlets. At a radial inlet velocity of 0.3 m/s, a small positive axial flow region appears in the centre of the aperture. According to Figure 5.7b, the positive flow entering the secondary concentrator through this central region is almost negligible compared to the positive flow near the boundary of the aperture. In Figure 5.10b, increasing the rotational speed is seen to also warp the coordinates at which v_w = 0 m/s, though to a lesser extent, and generate a positive axial flow region in the central region of the aperture.

The magnitude of the positive flow through the newly generated central region is more sensitive to changes to rotational speed than radial inlet velocity (Figs 5.7b & 5.9b). This can be attributed to the greater influence of rotational speed on the vortex structure and the number of axial recirculation zones in the radial direction. Therefore, if the entrained particle concentration in the central region of the cavity is significant, increasing the rotational speed is likely to have a more severe impact on the number of particles entering the secondary concentrator and depositing on the window than radial inlet velocity.

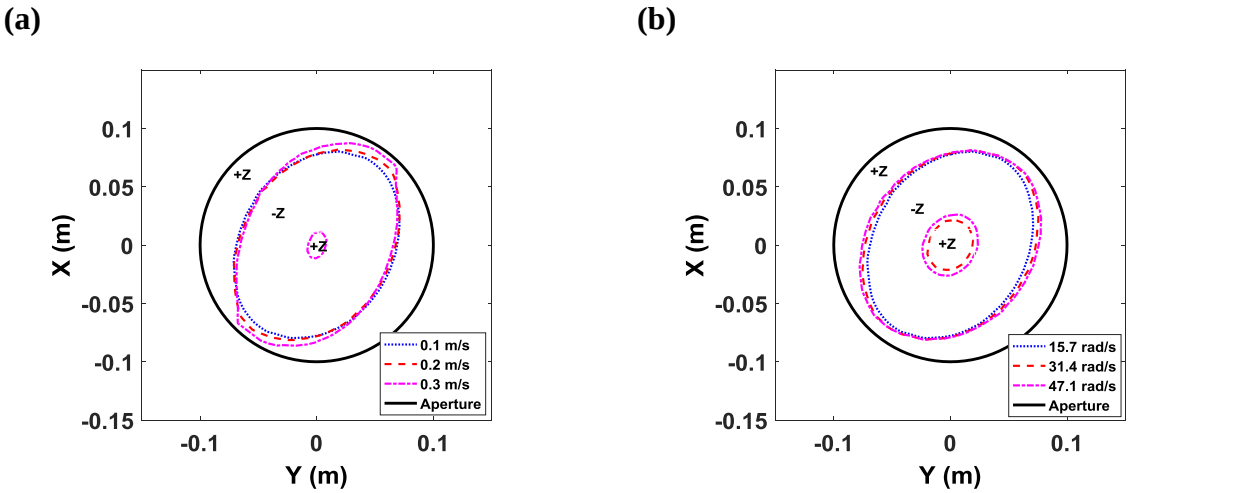

Figure 5.10: Boundaries between positive (+Z) and negative (-Z) axial fluid flow at the aperture plane (z/L = 1) for the RFBR with the following operating conditions: (a) rotational speed of 15.6 rad/s and various radial inlet velocities and (b) radial inlet velocity of 0.1 m/s and various rotational speeds.

Figure 5.11 presents the normalised positive fluid flow rate through the aperture as a function of rotational speed for various radial inlet velocities. This normalised flow rate is the ratio of the positive fluid flow rate through the aperture, $\dot{Q}_{ap}$, to the total inlet fluid flow rate, $\dot{Q}_{in}$. The bed rotational speed is seen to be positively correlated to the normalised flow rate and has greater influence at low radial inlet velocities where the total inlet flow rate is relatively low. The increase in flow rate due to increasing rotational speed may be attributed to the drastically changed vortex structure at high rotational speeds where new axial

recirculation zones emerge and more positive flow areas appear at the aperture plane (Figs 5.9 & 5.10). Increasing the radial inlet velocity, on the other hand, is shown to decrease the normalised flow rate which suggests that the positive flow rate through the aperture not as sensitive to variations in the radial inlet velocity as the total inlet flow rate. There appears to be no significant changes to the vortex structure and axial recirculation with increasing radial inlet velocity (Fig 5.7).

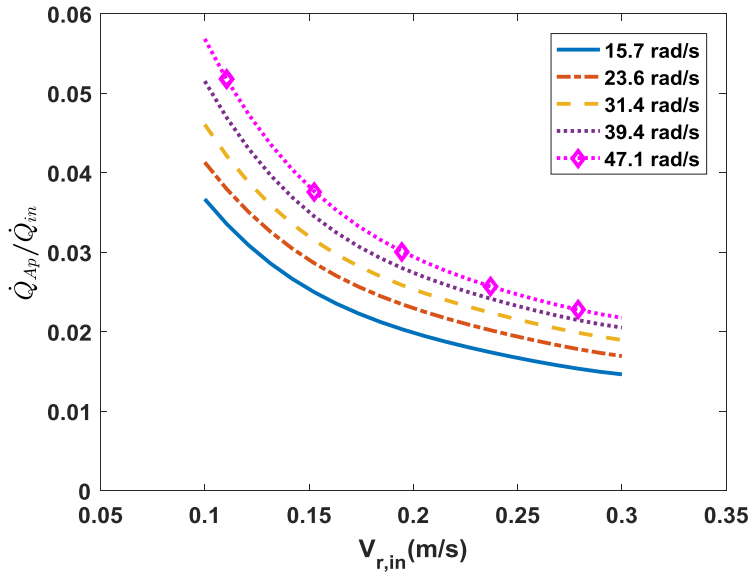

Figure 5.11: Normalised positive fluid flow rate through the aperture as a function of radial inlet velocity in the RFBR operating at various rotational speeds.

Figure 5.12 presents the swirl number of the fluid flow as a function of axial location z/L in the RFBR operating at a rotational speed of 15.7 rad/s (Fig 5.12a) and 47.1 rad/s (Fig 5.12b) for various radial inlet velocities. The swirl number provides the ratio of the fluid axial to tangential momentum and an indication of the strength of the vortex flow throughout the receiver cavity. It can be seen that the swirl number gradually decays in the positive Z direction as a result of increased wall friction. For the lower rotational speed of 15.7 rad/s (Fig 5.12a), the rates of decay between z/L = 0.5 and z/L = 0.9 appear to be similar for all

radial inlet velocities. For the higher rotational speed of 47.1 rad/s (Fig 5.12b), steeper rates of decay can be seen for lower radial inlet velocities between z/L = 0.5 and z/L = 0.9. The swirl number at the aperture, z/L = 1 appears to be unaffected by the rotational speed. For both rotational speeds, the swirl number falls between 2 and 3 depending on the corresponding radial inlet velocity. A higher radial inlet velocity is seen to lead to a higher swirl number at the aperture. This confirms the tangential outlets' secondary function as a vortex generator and highlights its significant influence on the vortex flow around the aperture, and thus, particle deposition on the receiver window.

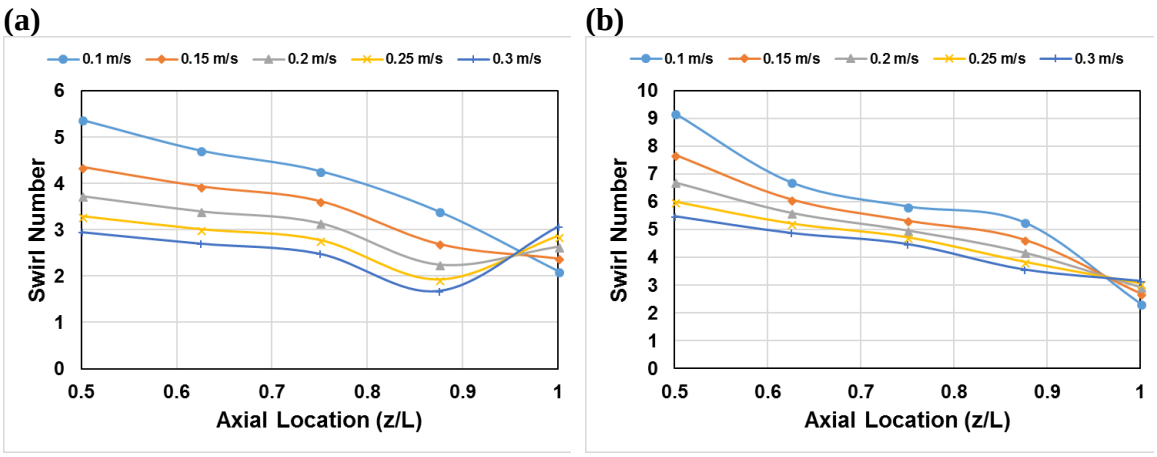

Figure 5.12: Swirl Number as a function of axial location for various radial inlet gas velocities in the RFBR operating at rotational speeds of (a) 15.7 rad/s and (b) 47.1 rad/s.

5.3.2 Particle Deposition Analysis

Figure 5.13 presents the normalised rate of particle deposition onto the receiver window as a function of the fluid radial inlet velocity for various rotational speeds and injected particle sizes of 10 μm (Fig 5.13a), 20 μm (Fig 5.13b), 40 μm (Fig 5.13c). It is clear that the normalised particle deposition rate increases with increasing radial inlet velocity and decreases with increasing rotational speed. The gradients of the particle deposition curves show that the deposition rates of larger particles are more sensitive to variations in radial

inlet velocity compared to smaller particles. At the lowest rotational speed of 15.7 rad/s, the deposition rate curve changes from concave downward to concave upward as the injected particle size is increased from 10 μm to 40 μm. The change of concavity becomes less noticeable as the rotational speed is increased. At a rotational speed of 31.4 rad/s or greater, the deposition rate curves for all particle sizes exhibit a concave downward shape, and the normalised particle deposition rates for both 10 μm to 20 μm reach a plateau for radial inlet velocities greater than 0.2 m/s. The plateau may be attributed to the decreasing normalised positive flow rate through the aperture at high radial inlet velocities shown in Figure 5.11. The deposition rate for 40 μm injected particles is so low at those rotational speeds that it becomes negligible. This can be explained with the fact that compared to smaller particles, larger particles contain more mass and are influenced to a greater extent by centrifugal acceleration which pushes entrained particles away from the cavity centre and prevents particles from entering the aperture. It should be noted that the reductions in particle deposition rate seen are not proportional to variations in rotational speed. The reduced effectiveness of bed rotational speed in controlling particle deposition could be caused by the increasingly complex vortex structure, which provides new pathways for entrained particles to flow through the aperture, and greatly increased normalised positive flow rate through the aperture at high rotational speeds (Figs 5.10 & 5.11).

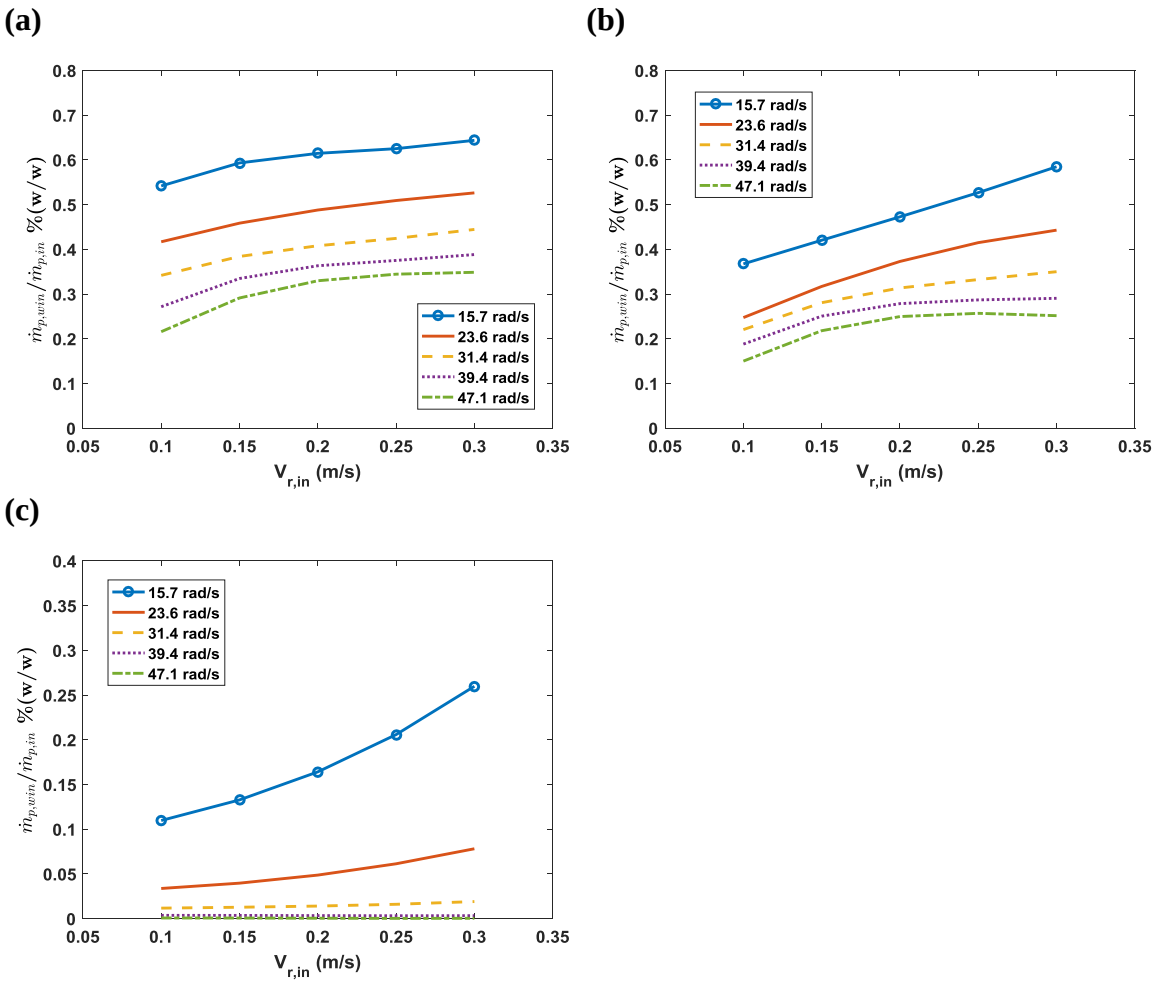

Figure 5.13: Normalised particle deposition rate on the window as a function of radial inlet velocity for various rotational speeds and injected particle sizes of (a) 10 µm, (b) 20 µm and (c) 40 µm.

Figure 5.14 presents the normalised particle mass loading in ZY plane directly below the aperture at z/L = 0.99 for various combinations of radial inlet velocity and injected particle size. The normalised particle mass loading is defined as the ratio of particle mass loading, ϕ to particle mass loading at the inlet, ϕ_{in} which is 0.045 for the volume fraction of 2e^{-5} used in this investigation. Figure 5.14 shows that the injected particle size has an effect on how normalised particle mass loading changes with increasing radial inlet velocity. For the small 10 µm particles, increasing the radial inlet velocity leads to almost uniform increase in particle loading in the radial direction within the receiver cavity. In contrast, for the larger

20 μm and 40 μm particles, particle loading is seen to increase disproportionately in the region close to the aperture's edge, r/R = -0.4 and 0.4, with increasing radial inlet velocity. The reduced mass loading of larger particles in the center can be attributed to the greater centrifugal force acting on the larger particles which pushes them away from the center and to the radial location of maximum tangential velocity. The disproportionate increase in the mass loading of 40 μm particles at the aperture's edge may be attributed to the radially inward shift of the location of maximum tangential velocity and axial recirculation zones (Figs 5.6 & 5.7). A comparison of the areas under the radial mass loading profiles for the three particle sizes shows that for the same increase in radial inlet velocity, the proportional increase in the area under the profile is the greatest for 40 μm particles and the smallest for 10 μm particles. This implies that the mass loading for 10 μm particles is less sensitive to radial inlet velocity compared to 40 μm particles and provides an explanation for the concavity changes seen in the normalised particle deposition rate curves in Figure 5.13.

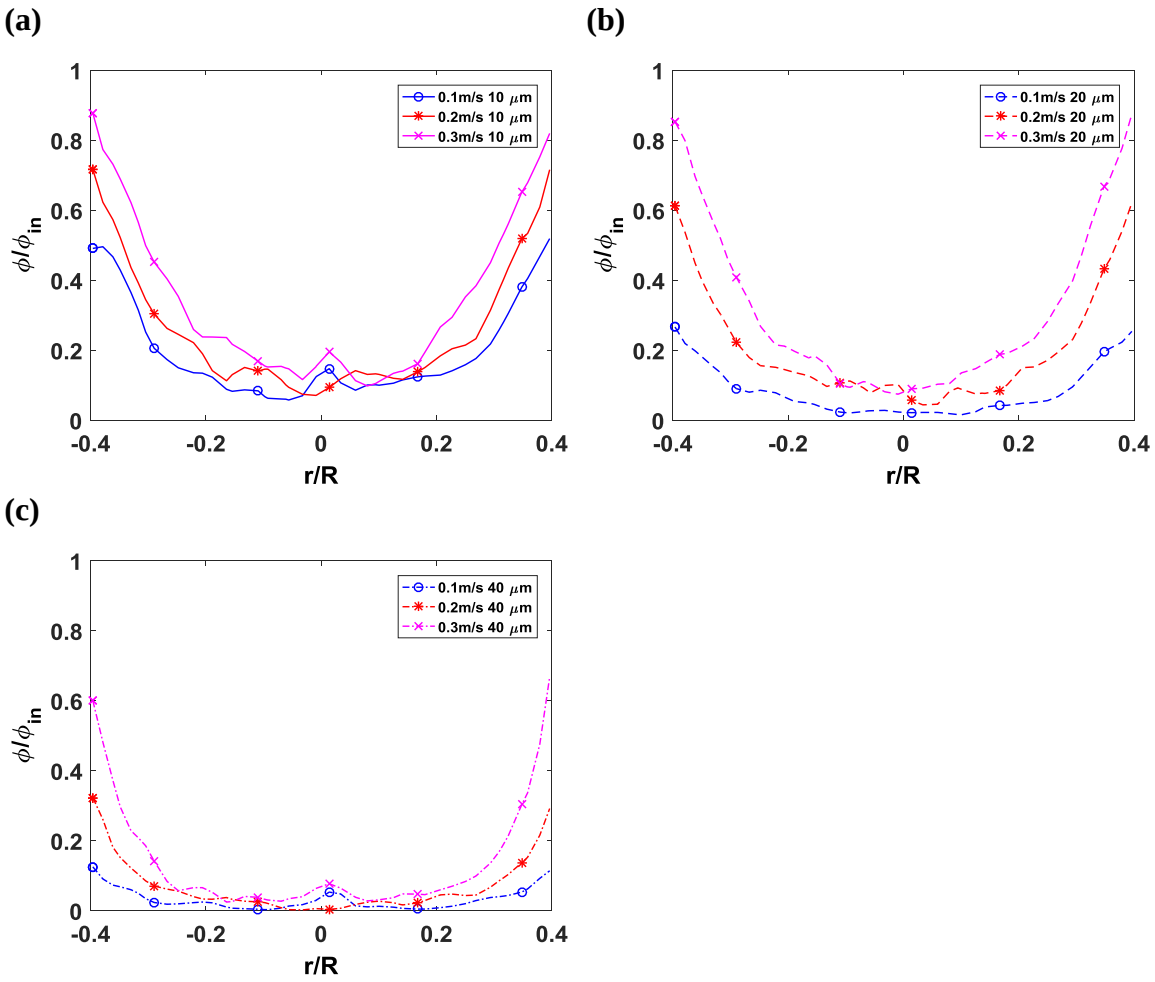

Figure 5.14: Normalised particle mass loading in the ZY plane at z/L = 0.99 in the RFBR operating at a rotational speed of 15.7 rad/s for various radial inlet velocities and injected particle sizes of (a) 10 μm, (b) 20 μm and (c) 40 μm.

Figure 5.15 reports the normalised particle mass loading in the ZY plane at z/L = 0.99 for various rotational speeds and injected particle sizes of 10 μm and 20 μm. It can be seen that adjusting the bed rotational speed is a very effective means of controlling particle mass loading, especially at relatively low rotational speeds. However, it should be noted that as the rotational speed is increased, the sensitivity of particle mass loading to rotational speed decreases, as shown by the diminishing changes in the area under the radial particle loading

profile. This growing insensitivity may contribute to the diminished effectiveness of rotational speed in reducing the normalised particle deposition rate seen in Figure 5.13.

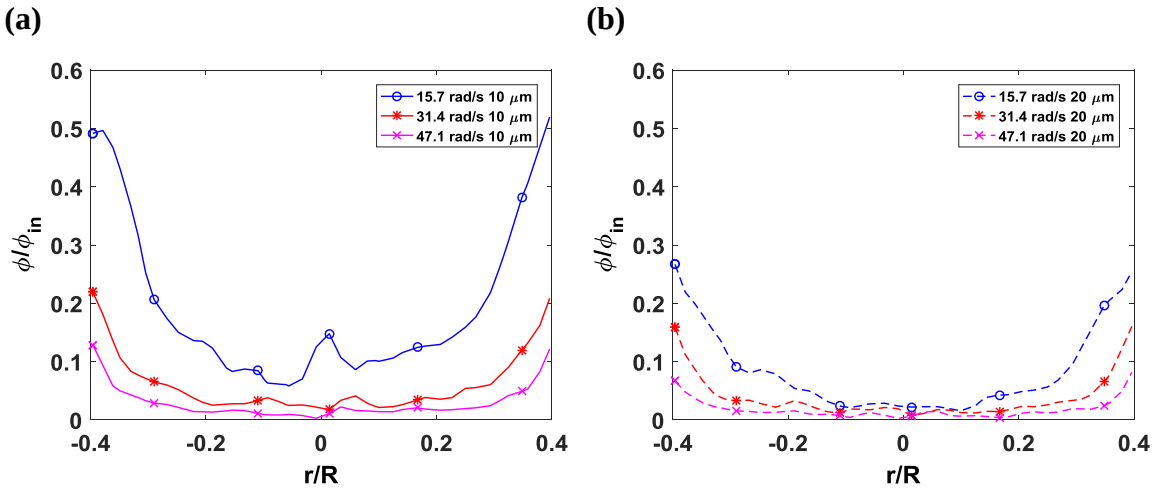

Figure 5.15: Normalised particle mass loading in the ZY plane at z/L = 0.99 in the RFBR operating with a radial inlet velocity of 0.1 m/s for various rotational speeds and injected particle sizes of (a) 10 μm and (b) 20 μm.

Figure 5.16 presents the normalised particle deposition rates as a function of the ratio of centrifugal, $F_{C,in}$ and Stokes drag, $F_{D,in}$, forces acting on an entrained particle at the inlet. It is an alternative visualization of the data points presented in Figure 5.13 because both the centrifugal and Stokes drag forces are calculated using inlet fluid tangential and radial velocities. It is clear that there is a strong correlation between the inlet force ratio and normalised particle deposition rate, and that the gradient of the inlet force ratio versus particle deposition curve appears to be independent of particle size. This confirms the importance of the balance of forces in controlling particle trajectory and deposition on the receiver window. It also implies that the gradient of curves in Figure 5.16 may depend only on the RFBR geometrical configuration. If this is the case, then this gradient can be used as a tool to compare the relative effectiveness of RFBR geometrical configurations in controlling particle deposition and estimate the particle deposition rate for a range of operating conditions and particle sizes.

It is worth noting that if the curves of best fit in Figure 5.16 were extended, they would meet the X axis at inlet force ratios greater than 1 which seems physically impossible. This may be caused Fluent's implementation of the Discrete Random Walk Model which gives injected particle parcels random velocity fluctuations to simulate the effect of turbulence. The ratio of forces is calculated using fluid radial and tangential velocity components which may be different to the actual particle velocity components in Fluent simulation. Smaller particles with less mass are more susceptible to the influence of turbulence, as shown by the expected intersection points of the curves for 10 μm and 20 μm particles which are further away from $F_{C,in}/F_{D,in}$ = 1.

Another peculiar feature in Figure 5.16 is that the normalised particle deposition rates for 20 μm particles are consistently higher than smaller 10 μm particles across their shared range of inlet force ratios. This suggests the presence of an unidentified aerodynamic mechanism that favours the deposition of larger particles onto the receiver window. However, since the deposition rates for 40 μm particles are seen to be consistently lower than 10 μm particles in Figure 5.16 so this unidentified mechanism is likely to only affect the particles entrained in the central region, -0.4 > *r/R* > 0.4, directly below the aperture where the mass loading of 40 μm particles is insignificant compared to 10 μm and 20 μm particles (Fig 5.14). The axial fluid velocity profiles in Figure 5.7 show that axial recirculation zones extend across the aperture and into the secondary concentrator volume. It is possible that the larger 20 μm particles follow the flow recirculation pattern inside the secondary concentrator less closely than 10 μm particles due to its quadrupled particle relaxation time, and therefore, are more likely to deposit on the receiver window.

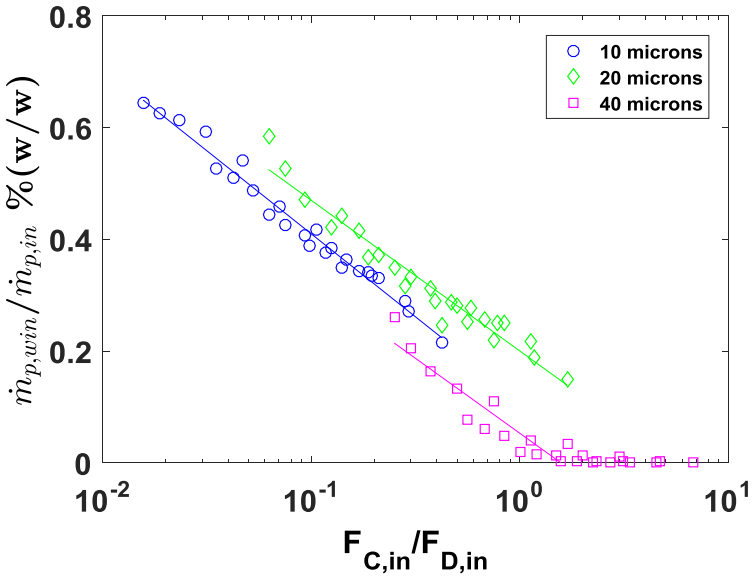

Figure 5.16: Normalised particle deposition rate on the window as a function of the ratio of centrifugal to Stokes drag forces acting on the injected particles at the inlet surface.

5.4 Conclusion

A numerical analysis of the isothermal flow field within a directly irradiated Rotating Fluidized Bed Receiver is presented. The effects of dominant operating parameters, namely fluidized bed rotational speed and radial inlet gas velocity, on the flow field inside the receiver and particle deposition rate onto the window are assessed with the aim of gaining an understanding of the mechanisms controlling particle deposition and exploring the RFBR's potential to be used as a windowed or windowless solar receiver. The key findings of the present investigation are as follows:

The particle deposition rate on the RFBR window can be strongly correlated with the ratio of centrifugal (determined by bed rotational speed) to Stokes drag (determined by radial inlet gas velocity) forces acting on the particles at the bed surface. The gradient of the particle deposition rate versus ratio of forces curve remains almost the same for all three

injected particle sizes. This gradient could be potentially used to quantitatively estimate the particle deposition rates for various combinations of particle sizes and operating conditions.

The particle deposition rate can also be qualitatively estimated by examining the normalised positive fluid flow rate into the secondary concentrator volume and radial profile of particle mass loading directly under the aperture.

Increasing the radial inlet gas velocity appears to affect the deposition rate of large particles more than small particles due to its ability to radially shift the axial recirculation zones and location of maximum tangential where large particles are more prominently concentrated.

Increasing the rotational speed also affects the deposition rate of large particles more significantly than small particles because large particles contain more mass and are more susceptible to the effect of centrifugal acceleration.

The tangential outlets could function as a vortex generator at high radial inlet gas velocities and inlet/exit flow rates. The Swirl Number at the aperture plane appears to be heavily influenced by the radial inlet velocity and seems almost independent of rotational speed. This means that smart outlet design could have as much of an impact on particle deposition as the dominant receiver operating parameters.

5.5 Nomenclature

D	Diameter (m)
e	Error
F	Force (N)
L	Length (m)
$\dot{m}$	Mass flow rate (kg/s)
$\dot{Q}$	Fluid volume flow rate (m^3/s)
r	Radial location (m)
R	Receiver cavity radius (m)

v	Fluid velocity (m/s)
w	Weight (kg)
W	Width (m)
X	X coordinate (m)
Y	Y coordinate (m)
z	Positive axial location (m)
Z	Z coordinate (m)
ω	Fluidized bed rotational speed (rad/s)
$\emptyset$	Particle mass loading

Subscripts

Ap	Aperture
B	Fluidized bed
C	Centrifugal
D	Stokes Drag
$Dist$	Gas distributor
F	Freeboard
in	Inlet
r	Radial component of inlet variable
p	Particle
Out	Outlet
SC	Secondary concentrator
Win	Window
z	Axial direction
θ	Tangential component of inlet variable

5.6 Acknowledgements

The authors would like to acknowledge the support provided by the Australian Government Research Training Program (RTP), the Australian Solar Thermal Research Initiative (ASTRI), the Australian Renewable Energy Agency (ARENA), and the supercomputing resources of the Phoenix HPC service at the University of Adelaide.

Chapter 6

RFBR at Low Rotational Speeds

This chapter reports the experimental investigation of the bed surface profile and fluidization characteristics within the bed volume at low rotational speeds. As mentioned in Chapters 1 and 2, the bed surface profile is of critical importance in the RFBR because it affects the radiative heat exchange in the receiver cavity and axial distribution of bed radial thickness, which in turn affects the pressure differential distribution and uniformity of fluidization.

Unlike previous experimental investigations on RFB fluidization, the current experimental set up consists of a sliced RFB confined in a rectangular transparent acrylic chamber. This was done to enable the observation of the tangential cross-section of the bed volume which would provide insights about the bed surface profile and fluidization boundary (boundary between packed and fluidized regions in the bed). The pressure differential across the sliced RFB was calculated using measurements from a digital manometer at the inlet of the experimental set up. The flow of fluidizing air was controlled with a pair of digital flow controllers.

The experimental investigation found that the propagation of the fluidization boundary within the bed volume is two dimensional in the low rotational speed sliced RFB where the

effect of gravity cannot be conveniently ignored. Existing theoretical models on the bed pressure differential derived from the assumption of one dimensional radially moving fluidization boundary are inadequate for low rotational speed RFBs. This highlights the need for the development of two dimensional fluidization boundary movement model.

Moreover, operating the sliced RFB at low rotational speeds was found to generate highly skewed initial bed surface profiles and pressure differential distributions in the axial direction. This in turn affected the uniformity of bed expansion and fluidization. The skewed initial bed surface profiles could be made more uniform through a specially devised particle redistribution procedure which involves temporarily fluidizing the bed at a higher rotational speed and fluidization gas flow rate. The redistribution procedure creates more evenly shaped initial bed surface profiles that could lead to improved distribution of pressure differential and radial air flow across the bed. A comparison of surface profiles at varying flow rates for a redistributed bed and a normal bed found the that the uniformity of fluidization could be greatly improved using the redistribution procedure.

The experimental investigation in the present chapter physically confirms the feasibility of the RFBR concept and its ability to operate at low rotational speeds which are beneficial to component wear and energy efficiency. The results of the investigation provide support for further development of the RFBR concept and the construction of a cold case prototype.

Statement of Authorship

Title of Paper	Fluidization Characteristics in a Rotating Fluidized Bed at a Low Rotational Speed
Publication Status	☐ Published ☐ Accepted for Publication ☑ Submitted for Publication ☐ Unpublished and Unsubmitted w ork w ritten in manuscript style
Publication Details	Z. Lu, A. Chinnici, M. Jafarian, M, Arjomandi & G. Nathan, 2017, "Fluidization Characteristics of a Low Speed Rotating Fluidized Bed", Experimental Thermal and Fluid Science, (Under Review)

Principal Author

Name of Principal Author (Candidate)	Zhao Lu
Contribution to the Paper	Developed ideas, performed experiments, interpreted data, wrote manuscript, and acted as the corresponding author
Overall percentage (%)	70
Certification:	This paper reports on original research I conducted during the period of my Higher Degree by Research candidature and is not subject to any obligations or contractual agreements with a third party that would constrain its inclusion in this thesis. I am the primary author of this paper.
Signature	Date 17/04/2018

Co-Author Contributions

By signing the Statement of Authorship, each author certifies that:

i. the candidate's stated contribution to the publication is accurate (as detailed above);
ii. permission is granted for the candidate in include the publication in the thesis; and
iii. the sum of all co-author contributions is equal to 100% less the candidate's stated contribution.

Name of Co-Author	Mehdi Jafarian
Contribution to the Paper	Supervised development of work, interpreted data, and edited manuscript
Signature	Date 17/04/2018

Name of Co-Author	Maziar Arjomandi
Contribution to the Paper	Supervised development of work, interpreted data, and edited manuscript
Signature	Date 17/04/2018

Name of Co-Author	Graham Nathan		
Contribution to the Paper	Supervised development of work, interpreted data, and edited manuscript		
Signature		Date	17/04/2018

Fluidization Characteristics of a Low Speed Rotating Fluidized Bed

Zhao Lu*

Mehdi Jafarian

Maziar Arjomandi

Graham J. Nathan

Centre for Energy Technology, School of Mechanical Engineering, The University of Adelaide, SA 5005, Australia

*Corresponding author: zhao.lu@adelaide.edu.au

Keywords: rotating fluidized bed; solar receiver; fluidization; rotational speed.

Abstract

An experimental investigation of the fluidization characteristics in a low rotational speed (<300 RPM) Rotating Fluidized Bed (RFB) is presented to provide a systematic assessment of the operating parameters, namely bed rotational speed (200 RPM, 250 RPM and 300 RPM), inlet air flow rate (0 to 100 Standard Litres Per Minute) and particle size (120 μm, 240 μm and 330 μm), on the fluidization characteristics, indicated by the bed surface profile and fluidization boundary within the bed volume, and pressure differential across the fluidized bed in a vertically oriented RFB. Potential issues with achieving uniform fluidization at low rotational speeds are identified and discussed. A special particle redistribution procedure was implemented to address non-uniform bed expansion and fluidization observed in the RFB due to skewed axial distribution of radial bed thickness. The overall aim of the present investigation is to provide a better understanding of the fluidization characteristics in a low rotational speed RFB which forms an integral part of the Rotating Fluidized Bed Receiver (RFBR) concept proposed by the authors for solar gasification.

6.1 Introduction

The renewable energy sector is growing at a rapid rate due to anthropogenic climate change and the need to reduce reliance on fossil fuels and CO_2 emission (Edenhofer et al., 2011). While solar energy is an abundant resource, its intermittent nature makes it difficult to be utilised on a large scale (Saw et al., 2017). Concentrated Solar Thermal (CST) technologies coupled with thermochemical processes provide a means to convert variable solar resources into chemical energy in long term storable chemical compounds (Nathan et al., 2017). A prominent example of solar driven thermochemical process is solar gasification of carbonaceous materials such as petroleum coke, biomass char and coal. The process harnesses concentrated solar heat through an optical concentrating system and uses the solar heat to drive gasification reactions in a solar receiver. Compared to the conventional autothermal gasification process which relies on the combustion of feedstock materials for process heat, the syngas produced through solar gasification is usually of higher purity and requires less feedstock materials (von Zedtwitz & Steinfeld, 2005). The lack of combustion simplifies the downstream filtering process of a solar gasification receiver and eliminates the need to remove combustion product gases and unused oxygen from the syngas. Gregg et al. (1980) estimated that eliminating the energy intensive oxygen separation unit in the conventional autothermal Lurgi coal gasification process can potentially lower the specific costs per unit syngas produced by 13% and feedstock coal consumption by 43%. Furthermore, von Zedtwitz & Steinfeld (2003) estimated that using solar energy could reduce the net CO_2 emission from the autothermal gasification process by up to 50% for power generation applications. Therefore, combining CST technologies with the

gasification process offers an attractive means of harnessing and storing intermittent solar energy.

A number of solar receiver concepts have been developed in recent decades to facilitate the solar gasification process (Taylor et al., 1980; Kodama et al., 2008; Z'Graggen & Steinfeld, 2008; Melchior & Steinfeld, 2008; Piatowski & Steinfeld, 2008). These receiver concepts can be broadly divided into two categories, directly irradiated and indirectly irradiated configurations (Steinfeld, 2005). The directly irradiated configuration has the advantages of high heat transfer rate and fast reaction kinetics. Due to the direct exposure of feedstock particles, a quartz window is often employed in directly irradiated receivers to reduce convective heat loss and feedstock particle leakage (Nathan et al., 2017). Nevertheless, the use of quartz window introduces the problem of window contamination by entrained feedstock particles (Chinnici et al., 2016). Window contamination poses a serious risk to the operation of a directly irradiated receiver because it can severely decrease the amount of solar radiation entering the receiver cavity and cause the receiver window to overheat, leading to mechanical failure. One method of mitigating window contamination is the injection of an auxiliary stream of inert cleaning gas near the window. This method has been successfully demonstrated in lab scale solar receivers at the expenses of diluted product syngas and reduced receiver solar-to-chemical energy conversion efficiency (Kogan & Kogan, 2002). Alternatively, the indirectly irradiated configuration can be used to avoid window contamination. This configuration physically separates the feedstock particles from the receiver aperture and window. Concentrated solar heat is indirectly transferred to feedstock particles via receiver wall conduction and radiation. The indirect heat transfer method greatly improves receiver operational reliability which is essential for commercial

operation but it also increases exergetic losses and imposes strict requirements on the properties of construction materials (Steinfeld, 2005). In summary, both solar receiver configurations are associated with unique advantages and technical challenges. However, further research is required to overcome the technical challenges associated with each receiver configuration. There is a need to develop efficient, reliable and technically robust solar receiver concepts for solar gasification.

The authors proposed a solar receiver concept termed Rotating Fluidized Bed Receiver (RFBR) which utilises a vertically oriented Rotating Fluidized Bed (RFB) to facilitate the mixing of feedstock particles and steam in solar gasification (Lu et al., 2016). Similar to conventional fluidized beds, the solid phase in RFB is semi-suspended in turbulent motion by the fluidizing gas, and this in turn enables relatively high heat and mass transfer rates between the gas and solid phases. In addition, the centrifugal force due to rotation in RFB is adjustable and offers more controllability over the fluidization and particle elutriation characteristics compared to conventional fluidized bed (Chevray et al., 1980; Saunders, 1986). Moreover, the use of centrifugal force allows the cylindrical wall of the rotating fluidized bed to be used as the gas distributor and thus significantly increases the particle bed surface area which is beneficial to solar radiation absorption and can potentially reduce the conductive heat loss through the receiver wall. Analytical and numerical assessments by the authors found that the adjustable centrifugal force is an effective operating parameter for controlling particle gasification conversion and deposition on the receiver window (Lu et al., 2016). Nevertheless, RFB is not as well established and understood as conventional fluidized bed. Significant gaps remain in the understanding of the physical phenomena in RFB. Most of the investigations on RFB's in literature employ relatively high rotational

speeds (>26 rad/s or 250 RPM) where the radial thickness of the particle bed is approximately uniform, and the high centrifugal force renders the effect of gravity negligible (Kroger et al., 1979; Takahashi et al., 1984; Fan et al, 1985; Chen, 1987). There is little information on the bed surface profile and fluidization characteristics in RFB's operating at lower rotational speeds. For the RFBR concept to be feasible and technically robust, it must be able to operate in a wide range of rotational speeds including low speeds where the maintenance requirements for the rotating components are more relaxed, and there is less kinetic energy lost due to rotation. Kroger et al. (1979) studied RFB fluidization in a vertically oriented RFB and found that as the rotational speed decreases, the bed surface profile becomes increasingly skewed with a greater variation of bed radial thickness in the axial direction. Since the pressure differential across the bed is dependent on the bed radial thickness, a non-uniform distribution of radial thickness may cause ill-distributed radial gas flow through the bed and cause non-uniformity in fluidization characteristics. This non-uniformity is undesirable and may negatively impact the mixing of solid and gas phases and subsequently, the gasification process. In addition, the slumped bed surface may also influence the radiation heat exchange within the receiver cavity and affect the re-radiation heat loss through the aperture. For these reasons, the first objective of the present paper is to support the development of the RFBR concept through investigating the effects of rotational speed as well as gas flow rate and particle size on the bed surface profile and fluidization characteristics in a vertically oriented RFB.

Two types of pressure differential responses have been reported in literature for RFB at minimum fluidization. Takahashi et al. (1984) and Fan et al. (1985) reported that the pressure differential across the bed reaches its maximum value at minimum fluidization and

decreases for any subsequent increase in fluidizing gas flow rate thereafter. Metcalfe et al. (1977), on the other hand, found the pressure differential at and after minimum fluidization to be a flat plateau. Kao et al. (1987) suggested that the decreasing pressure differential after minimum fluidization could be caused by the elutriation of bed particles and loss of effective bed mass. Their experimental results on RFB's of various uniform bed radial thicknesses provided support for their hypothesis. More recently, Qian et al. (1998) studied the effects of sintered and slotted metal distributors on the pressure differential in a horizontally oriented RFB and discovered that at minimum fluidization, the fluidizing gas could shift a portion of particles onto the closed area of the slotted distributor, reduce the mass of particles on the distributor and in turn, produce a hysteresis in the pressure differential plot. It is important to note that these investigations were conducted in RFBs operating at high rotational speeds that produce an approximately uniform bed radial thickness. There is little information on the pressure differential response in a slumped bed at low rotational speeds. Thus, the second objective of the present paper is to investigate the pressure differential response in a low rotational speed RFB with non-uniform bed radial thickness and examine the relationship between bed surface profile and pressure differential response. The overall aim of the present paper is to support the development of solar gasification reactors through gaining a better understanding of the operation of a vertically oriented RFB at low rotational speeds.

6.2 Methodology

A schematic diagram of the experimental set up is shown in Figure 6.1. The experimental system is designed with the aim of facilitating easy observation of the RFB surface profile

and fluidization boundary, where packed and fluidized portions of the particle bed meet, within the bed volume. To achieve this, the experimental system approximates the geometry of a sliced RFB using a rectangular transparent acrylic chamber. This chamber is enclosed within a larger acrylic chamber filled with pressurized air. One side of the smaller acrylic chamber is open and covered with a vacuum cleaner filter, allowing the pressurized air from the larger plenum chamber to pass through and fluidize the particles. The dimensions of the space confining the RFB slice are shown in Figure 6.2.

The acrylic chambers are mounted on a rotating platform that is capable of rotating at a maximum rotational speed of 400 RPM. Dry air is supplied to the chambers by a pair of digital flow controllers linked in parallel, giving a precise flow rate up to 100 Standard Litres per Minute (SLM). The pressure in the pressurised chamber is measured by a digital manometer and termed $P_{chamber}$. The pressure differential of the experimental system without particles was measured as a function of gas flow rate and given the symbol, ΔP_{system}. The pressure differential across the particle bed ΔP_{bed} can be found using Eq. 1.

$$\Delta P_{bed} = P_{chamber} - P_{atm} - \Delta P_{system} \qquad \text{Eq. 1}$$

The particles used in the present investigation are glass beads of three different mean diameters, 120μm, 240μm, and 330μm. The density of the glass beads is 2470kg/m^3 as reported by the manufacturer. The void fraction ε of the packed bed with no air flow is calculated to be 0.41 through Eq. 2 given in Kao et al. (1987) based on the assumed glass bead sphericity ϕ_s of 1.

$$\frac{1}{\phi_s \varepsilon^3} \approx 14 \qquad \text{Eq. 2}$$

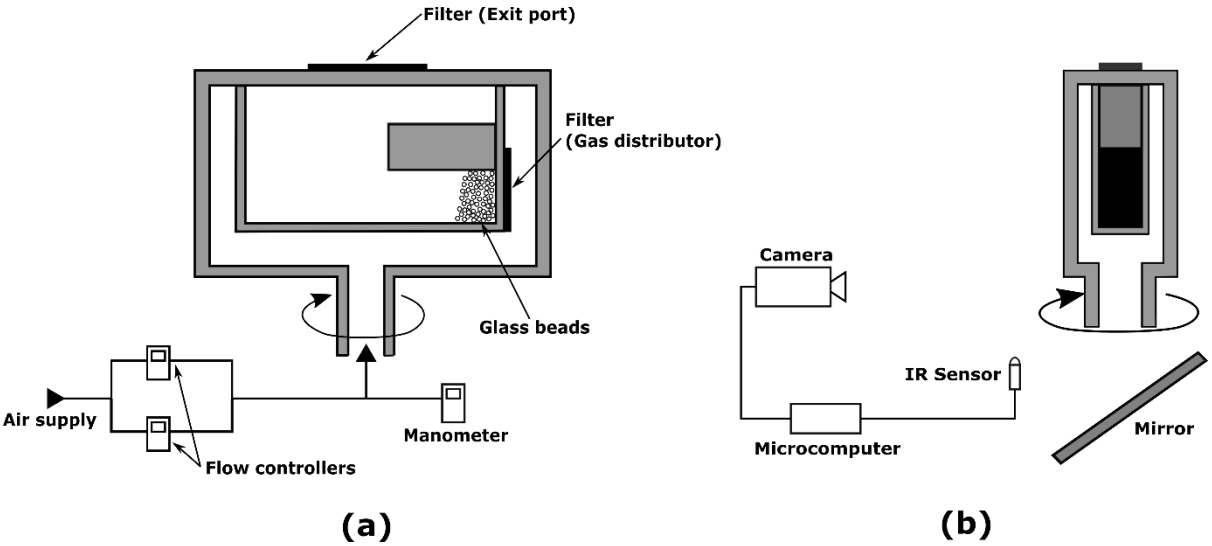

Figure 6.1: Schematic diagrams of the experimental set up: (a) air supply system and (b) camera observation system.

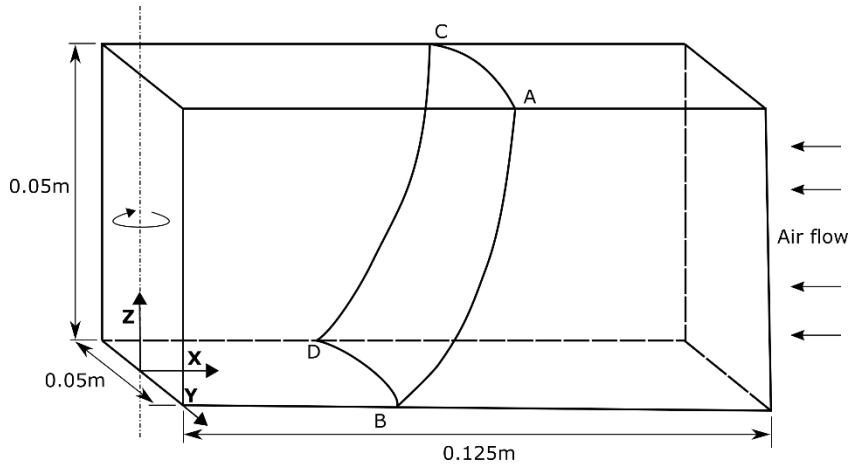

Figure 6.2: Dimensions of the space containing the rotating fluidized bed slice.

For the observation of the RFB surface profile and fluidization boundary, a special camera system was set up as shown in Figure 6.1. The IR sensor detects the position of the rotating acrylic chambers and triggers the camera when the vertical chamber surfaces containing the points A, B, C, and D are approximately perpendicular to the direction of the camera. A mirror is placed below the rotating chambers to record the horizontal surface containing the

points B and D. All three surfaces are covered with a fine grid which allows the profiles of the particle bed to be interpolated.

To create an approximately consistent particle bed volume and shape at the start of every experiment, after the insertion of particles, the inner chamber is rotated 90 degrees clockwise such that the particles form a rectangular bed volume with a flat surface on top of the gas distributor. The inner chamber is then slowly rotated 90 degrees counter clockwise and installed into the larger chamber. This procedure ensures that the initial slope of the bed surface is similar for all experiments regardless of how the particles are inserted.

6.3 Results and discussion

Figure 6.3 presents the pressure differential across a particle bed consisting of 100 g of 120 μm mean diameter glass beads for rotational speeds of 200 RPM, 250 RPM and 300 RPM. It can be seen that the initial increase in pressure differential as a function of air flow rate is almost linear which suggests that the whole bed is initially in the packed bed regime. A drop in pressure differential is observed as the air flow rate reaches a specific point for each rotational speed. This drop can be explained by the bed undergoing packed to fluidized bed transition. As shown in Figure 6.3, the air flow rate at which the drop occurs is proportional to the rotational speed and centrifugal force acting on the glass beads. Increasing the rotational speed delays the packed to fluidized bed transition to a higher air flow rate. After the drop, the pressure differential increases at a much slower rate and gradually reaches a stead state which signals the end of the packed to fluidized bed transition. Another observation worth noting in Figure 6.3 is the magnitude of the drop in pressure differential which is also proportional to rotational speed. The pressure differential plot for the bed

rotating at 300 RPM shows a significant drop of 400 Pa, whereas the plot for the 200 RPM bed displays a relatively minor drop of 100 Pa.

The pressure differential as a function of decreasing flow rate in the backward direction is also shown in Figure 6.3. No significant difference is seen between the forward and backward pressure differential plots. This indicates that there is little loss of bed mass due to particle elutriation for all three rotational speeds.

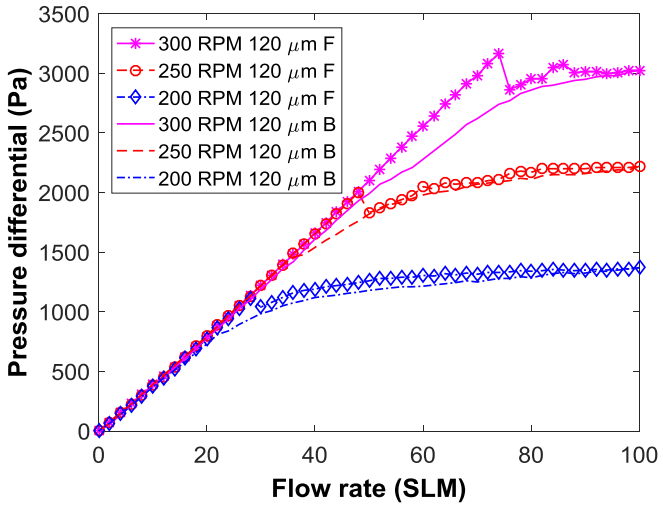

Figure 6.3: Pressure differential as a function of air flow rate. F and B denote forward (increasing) and backward (decreasing) changes in air flow rate.

A comparison of the surface profiles observed on the bottom acrylic surface containing Points B-D also supports the observation that increased rotational speed improves uniformity of bed expansion and fluidization (Figs 6.4c, 6.5c & 6.6c). In the 300 RPM case, the glass beads on the B-D surface appear parabolic with Points B and D moving at approximately the same rate in the radial direction with increasing air flow rate. The gradual radially outward movement of the profiles on the B-D surface hint a reduction in the volume of glass beads at the bottom and an upward movement of glass beads to the top portion (Fig 6.6c). The 200 RPM bed on the other hand shows more skewed profiles on the B-D surface

(Fig 6.4c). Point B is seen to move further in the radial direction than Point D as the flow rate increases. This implies that the glass beads at Point B move more freely and are better fluidized than the glass beads in mostly packed bed state at Point D.

The surface profiles in Figures 6.4b, 6.5b and 6.6b show little expansion and almost no fluidization, indicating that there is little radial gas flow through the region close to the surface containing Points C and D. This is possibly due to the particles being packed denser in the volume near the C-D surface due to the compression by the tangential component of the inertial force.

Figures 6.4, 6.5 and 6.6 present the bed surface profiles, observed on the chamber surfaces containing Points A, B, C, and D, for various flow rates at rotational speeds of 200 RPM, 250 RPM and 300 RPM respectively. It can be seen that bed rotational speed has significant influence on the uniformity of bed expansion and fluidization. As expected, the low rotational speeds used in the experiments created skewed initial (0 SLM) packed bed surface profiles with large variations in radial bed thickness along the axial direction. At a low rotational speed of 200 RPM, the top portion of the bed, which is least influenced by gravity, appears to expand and fluidize much more readily with increasing flow rate than the bottom portion (Fig 6.4a). At the maximum flow rate of 100 SLM, the top portion appears to be in the turbulent bubbling regime, whereas the bottom portion below $z/Z = 0.2$ shows no expansion at all. The difference in fluidization regime can be largely attributed to the skewed surface profile where the bottom portion is significantly thicker than the top portion and thus, is more difficult for air flow to penetrate. The thick bottom portion creates such a high

pressure drop that air is forced to flow through the particle bed mainly through the top portion, causing a non-uniform radial air velocity in the axial direction.

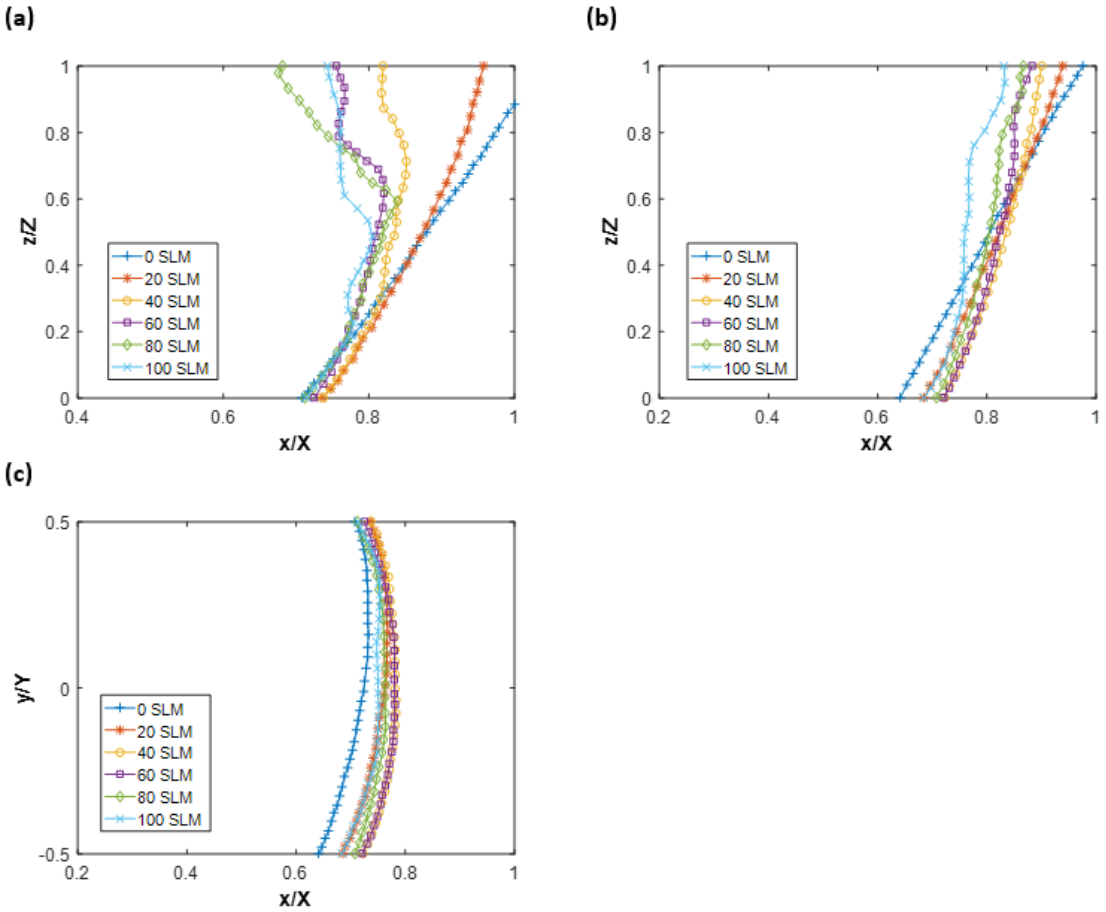

Figure 6.4: Particle bed surface profiles for varying air flow rates on the inner chamber surfaces containing points (a) A-B, (b) C-D and (c) B-D. The bed consisted of 100 g of 120 µm mean diameter glass beads and was rotated at a constant speed of 200 RPM.

As the rotational speed is increased to 250 RPM and 300 RPM as shown in Figures 5 and 6 respectively, the top portion of the bed shows less expansion with increasing flow rate. The surface profiles at 100 SLM also show smaller fluctuations, fewer signs of bubbling and more uniformly distributed radial bed thickness. At 300 RPM, the top and bottom portions are almost equal in thickness, indicating significantly reduced variation in pressure differential across the bed in the axial direction and more uniformed distribution of air flow

and fluidization quality. The greater uniformity of bed expansion at 300 RPM also causes more volume and mass of the bed to undergo the packed to fluidized bed transition at minimum fluidization than the 200 RPM bed. This combined with the increased centrifugal acceleration likely generated the more noticeable drop in the pressure differential for the 300 RPM bed in Figure 6.3.

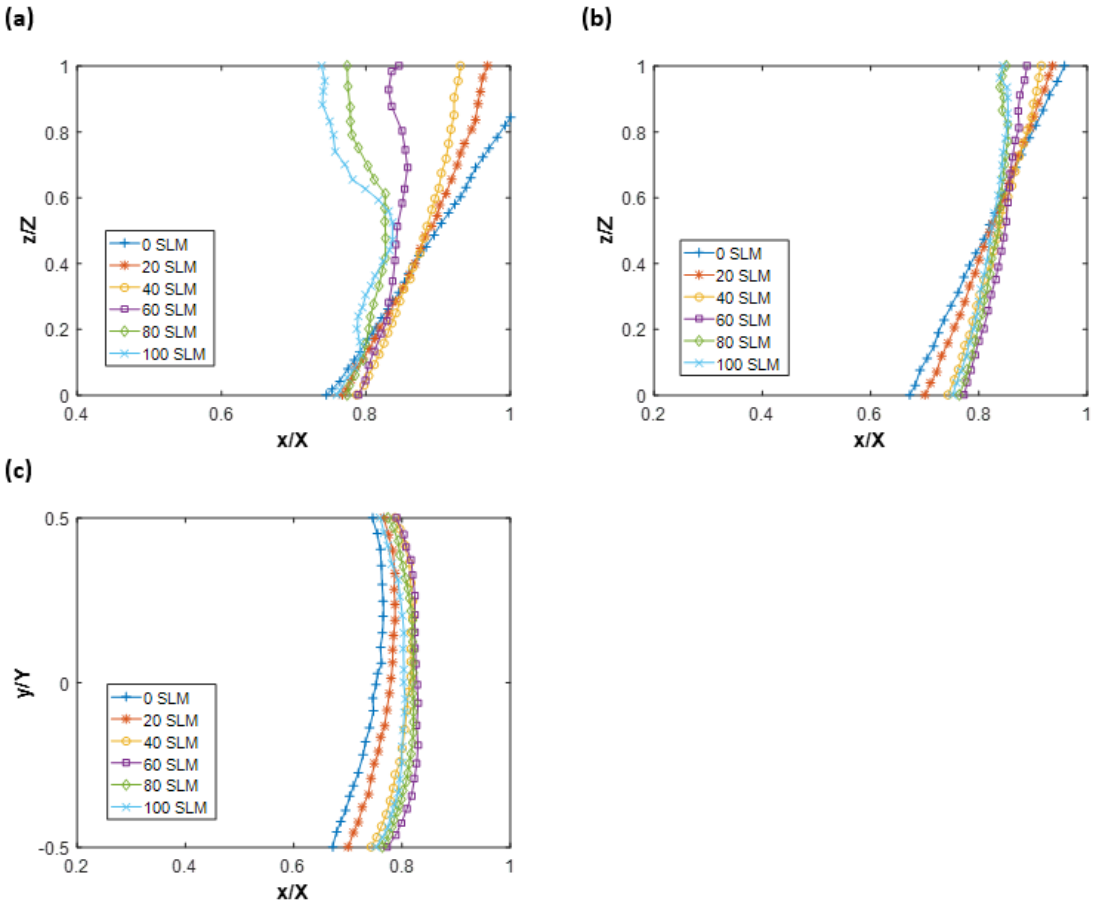

Figure 6.5: Particle bed surface profiles for varying air flow rates on the inner chamber surfaces containing points (a) A-B, (b) C-D and (c) B-D. The bed consisted of 100 g of 120 µm mean diameter glass beads and was rotated at a constant speed of 250 RPM.

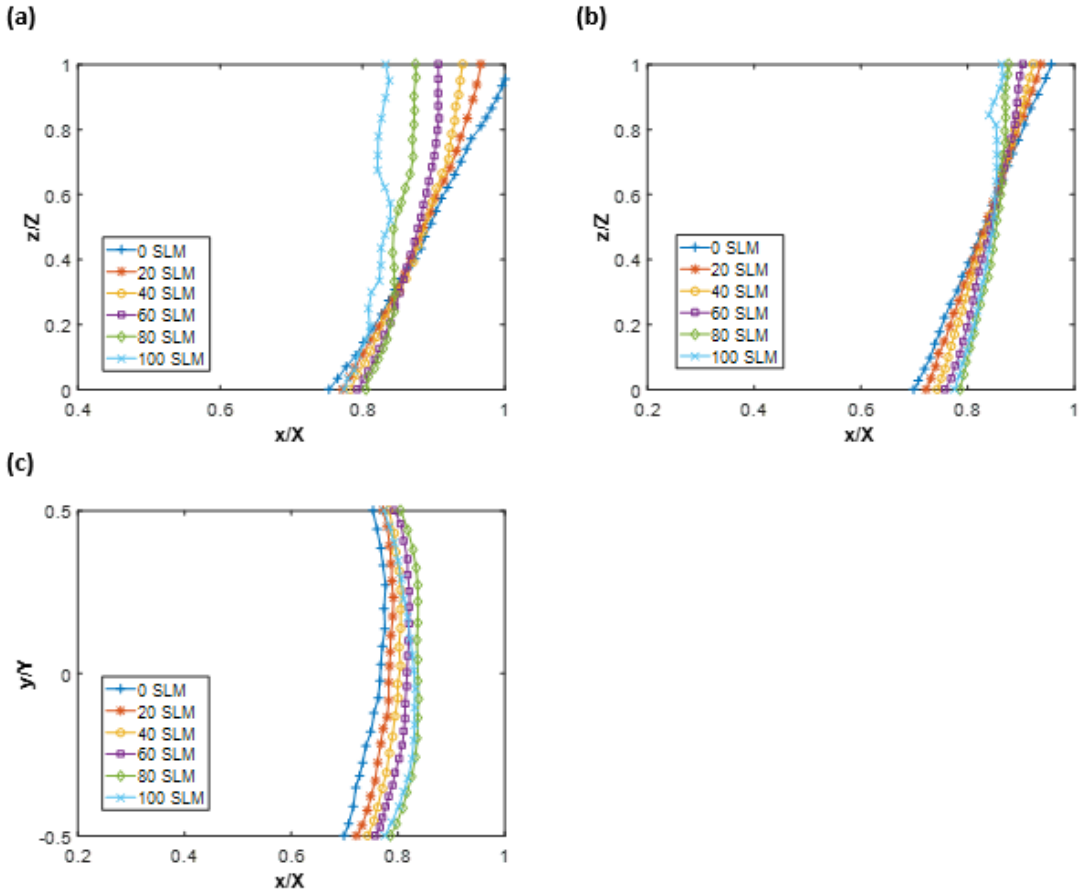

Figure 6.6: Particle bed surface profiles for varying air flow rates on the inner chamber surfaces containing points (a) A-B, (b) C-D and (c) B-D. The bed consisted of 100 g of 120 µm mean diameter glass beads and was rotated at a constant speed of 300 RPM.

Figure 6.7 presents the pressure differential across the bed as a function of air flow rate for beds rotating at a speed of 200 RPM and containing 100g of bed mass for mean glass bead diameters of 120 µm, 240 µm and 330 µm. Increasing the particle diameter is seen to delay minimum fluidization to a higher air flow rate due to larger particles containing more mass and being acted upon by a greater centrifugal force. The gradients for the pressure differential curves for 240 µm and 330 µm mean diameter glass beads appear to be non-zero and decreasing even at 100 SLM, suggesting that those two particle beds are still in the early stages of the transition to the fluidized bed regime. It is worth noting that despite the increased centrifugal force, the pressure differential curves for the beds consisting of 240

μm and 330 μm mean diameter glass beads show no obvious drop in differential pressure unlike in Figure 6.3 where increased rotational speed and centrifugal force were seen to have an effect on the pressure drop after minimum fluidization. One possible explanation for this observation is that the interstitial spacing is greater for larger particles, and this allows air flow to pass more easily, resulting in smaller increase in pressure gradient as a function of flow rate (Fig 6.7). This may prevent the build up of pressure prior to minimum fluidization and facilitate a more smooth transition from the packed to fluidized bed regime.

Figure 6.7 also presents the pressure differential as a function of air flow rate in the backward direction. The forward and backward curves of the bed containing 120 μm mean diameter glass beads show a bigger difference than the plots of the beds with larger glass beads. This suggests that there is some loss of bed mass due to elutriation in the bed containing 120 μm mean diameter glass beads, and this loss of bed mass can be mitigated with increased particle size and corresponding increase in centrifugal force.

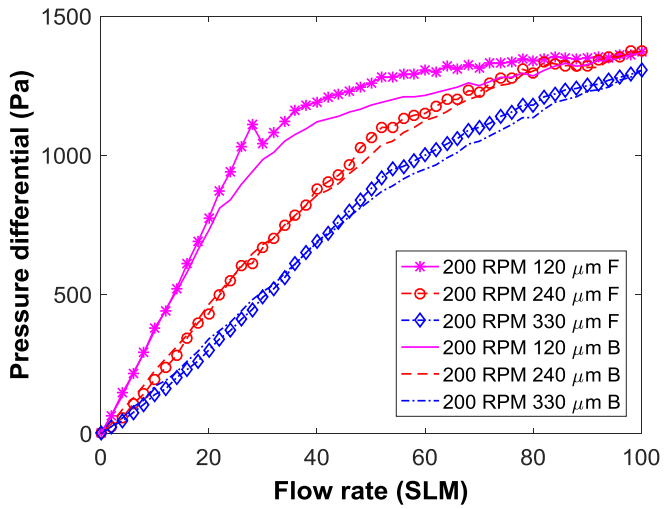

Figure 6.7: Pressure differential as a function of air flow rate. F and B denote forward (increasing) and backward (decreasing) changes in air flow rate.

Figures 6.8 and 6.9 present the surface profiles for various flow rates in beds rotating at 200 RPM and consisting of 100g of 240 μm and 330 μm mean diameter glass beads respectively. It can be seen that both beds expand and fluidize more gradually than the bed consisting of smaller 120 μm mean diameter glass beads in Figure 6.4. This is consistent with the effect of increased centrifugal force as seen in Figures 6.5 and 6.6. However, unlike Figure 6.6, the centrifugal force is insufficient to overcome the effect of gravity, and significant distinction still exists in the fluidization quality between the top and bottom portions of the bed. The fluctuations in the surface profiles in Figures 6.8a and 6.9a are seen to expand downward with increasing flow rate which indicates that non-uniform bed expansion and fluidization start at the top and gradually moves downward. As more portion of the bed becomes fluidized, the particles in the bottom portion of the bed can be seen to move upward as shown by the radially outwards shift of the Points B and D in Figures 6.8c and 6.9c. This again can be attributed to the increased centrifugal force which helps particles to pile over reach other.

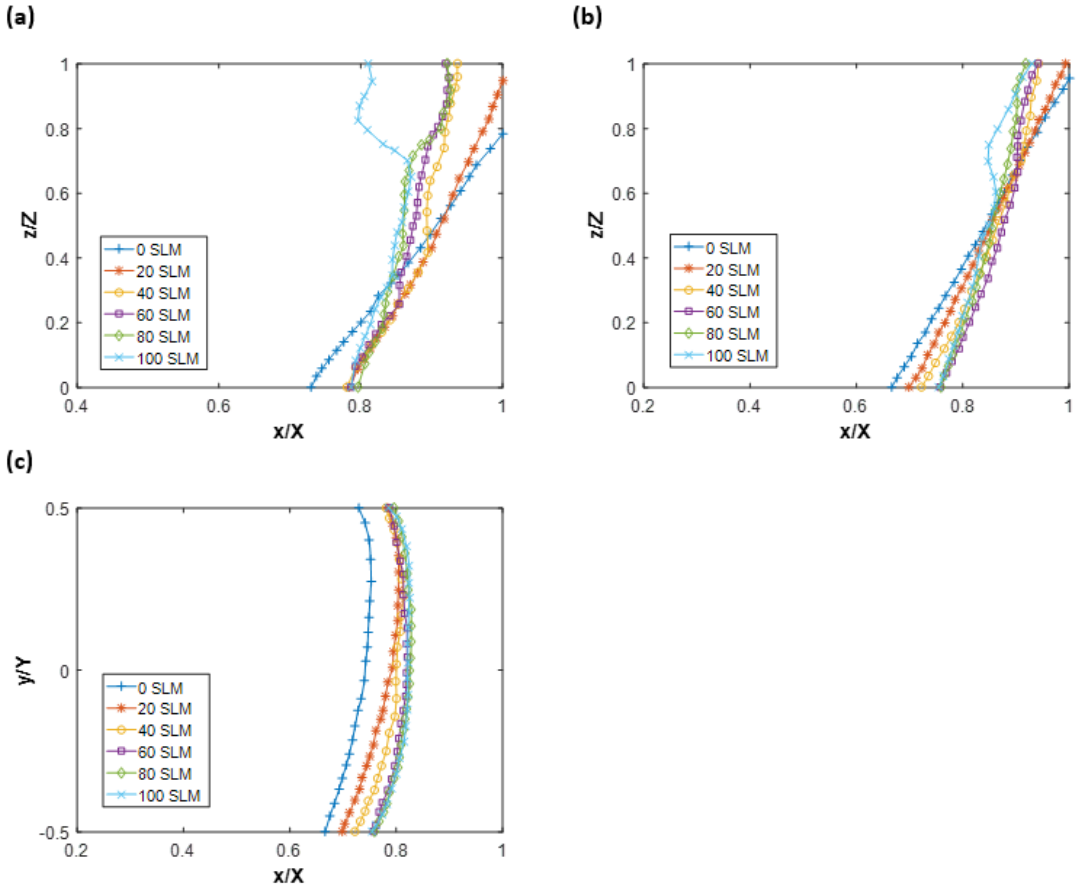

Figure 6.8: Particle bed surface profiles for varying inlet flow rates on the inner chamber surfaces containing points (a) A-B, (b) C-D and (c) B-D. The bed consisted of 100 g of 240 µm mean diameter glass beads and was rotated at a constant speed of 200 RPM.

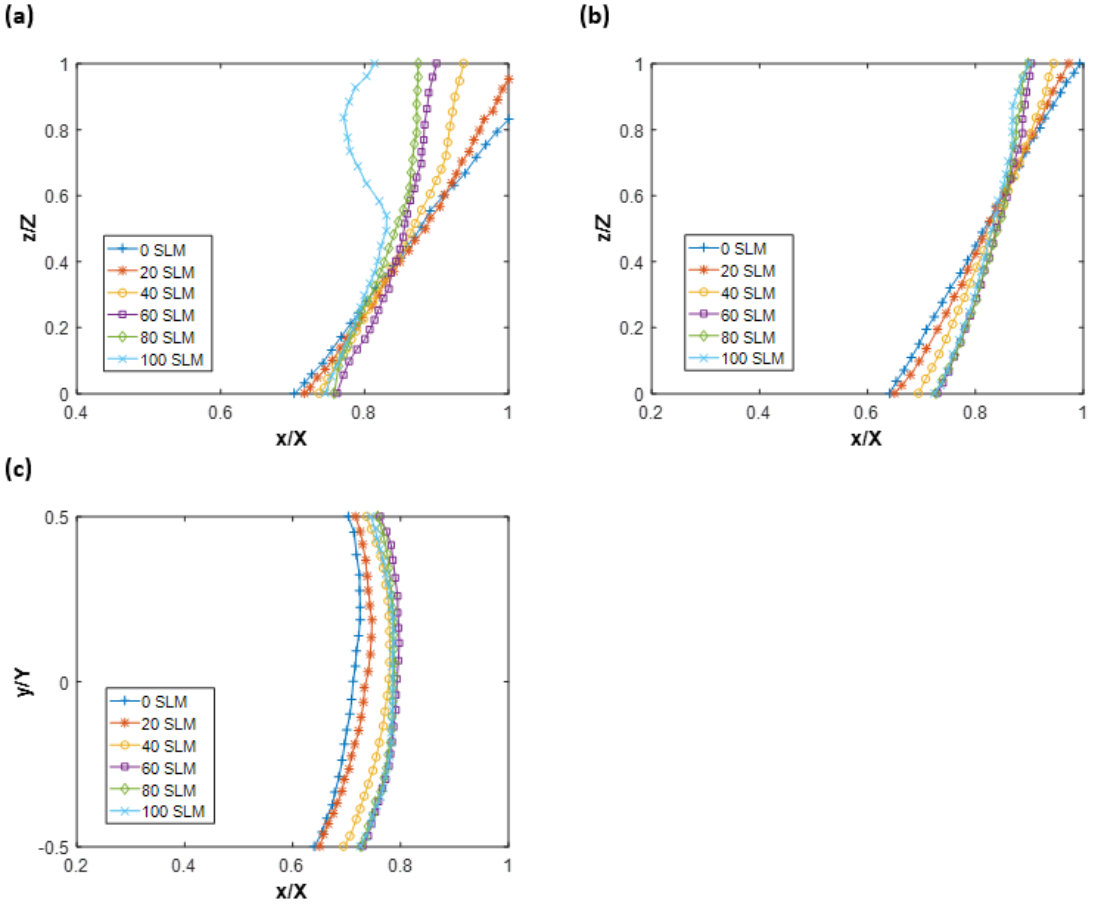

Figure 6.9: Particle bed surface profiles for varying air flow rates on the inner chamber surfaces containing points (a) A-B, (b) C-D and (c) B-D. The bed consisted of 100 g of 330 µm mean diameter glass beads and was rotated at a constant speed of 200 RPM.

Figures 6.10 and 6.11 present the fluidization boundaries for various air flow rates within 100g beds containing 240 µm and 330 µm mean diameter glass beads respectively. It should be noted that the fluidization boundary is only observable for these two particle sizes because they are sufficiently large for the camera's resolution to differentiate between packed and fluidized volumes. The most noticeable feature in Figures 6.10 and 6.11 is that the movement of fluidization boundaries appears to be staggered and not proportional to air flow rate. Due to the influence of gravity and low rotational speed, the fluidization boundaries move both in the radially outward and axially downward directions unlike in the high rotational speed RFB's in literature where they have been speculated to move in

radially outwards only. The gradients of the fluidization boundaries for the both glass bead sizes appear to be the same. This implies that the gradient of the fluidization boundary is not overly sensitive to particle size.

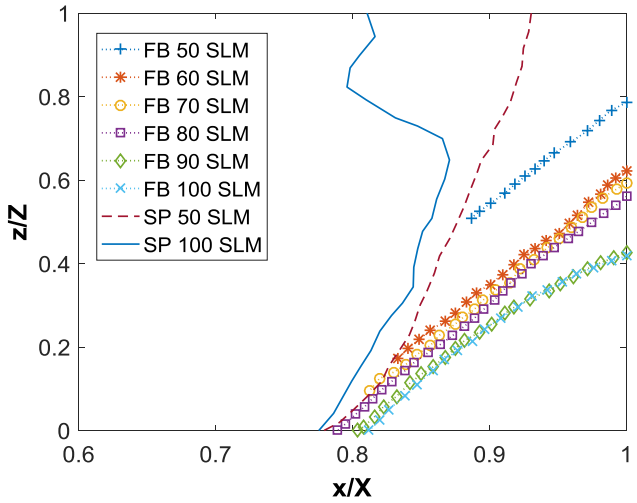

Figure 6.10: Particle bed surface profiles, denoted by SP, and fluidization boundaries, denoted by FB, for varying air flow rates on the inner chamber surface containing points A-B. The bed was rotated at a constant speed of 200 RPM and consisted of 100 g of 240 µm mean diameter glass beads.

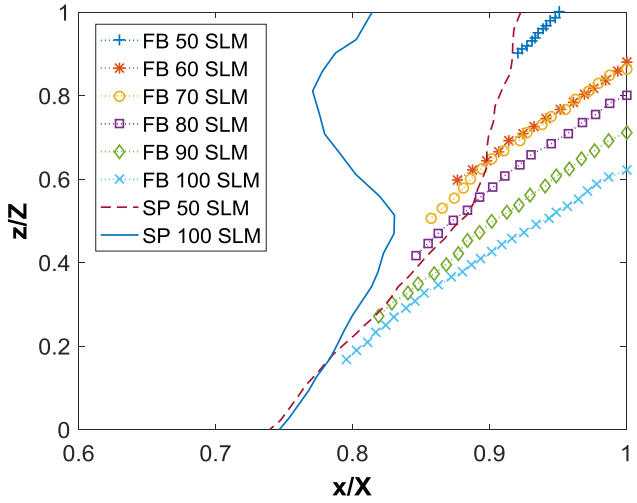

Figure 6.11: Particle bed surface profiles, denoted by SP, and fluidization boundaries, denoted by FB, for varying air flow rates on the inner chamber surface containing points A-B. The bed was rotated at a constant speed of 200 RPM and consisted of 100 g of 330 µm mean diameter glass beads.

The diagonal fluidization boundaries in Figures 6.10 and 6.11 provide further evidence that the axial distribution of radial air flow through the bed is non-uniform. The radial air flow appears to be the highest at the top portion of the bed and almost zero at the bottom portion where the bed remains largely packed with little expansion throughout the range of flow rates. The bottom packed region can be minimized through increasing the air flow rate (Fig 6.10). However, continuously increasing the flow rate may result in the top portion being shifted to the pneumatic transport regime and cause severe loss of bed mass. Thus, to facilitate uniform fluidization of particles in the whole bed, an angled porous surface could be installed in the corner of the bottom surface and the vertical gas distributor to reduce the volume of the bottom packed bed region.

Previous discussion highlights the effect of centrifugal force on the uniformity of bed expansion and fluidization. One of the ways that centrifugal force improves fluidization uniformity is by redistributing fluidized particles upward and creating a more uniform axial distribution of radial bed thickness and air flow as seen in Figure 6.6. Therefore, if the same redistribution of particles could be achieved through another method, the positive effect of redistribution on fluidization uniformity would likely remain. It has been reported in literature that properly fluidized particles can behave like a fluid and form an almost annular bed in RFB operating at high rotational speeds regardless of RFB orientation and gravitational force. Thus, a special particle redistribution procedure was devised for the present experimental set up to investigate the effects of particle redistribution on fluidization. The redistribution procedure involves increasing the bed rotational speed to 400 RPM and air flow rate to 50 SLM before shutting off the air flow and changing the rotational speed to the desired rotational speed for the experimental run.

Figure 6.12 presents the comparison of the pressure differential as a function of air flow rate in a redistributed and a normal 100g bed rotating at 200 RPM and consisting of 120 μm mean diameter glass beads. It can be seen that the curve for the redistributed bed shows a much larger delayed drop in pressure differential than the normal bed. The magnitude of the drop is approximately 400 Pa which is comparable to the drop shown in Figure 6.3 produced by rotating a bed also consisting of 120 μm mean diameter glass beads at a speed of 300 RPM. After the noticeable drop, the pressure differential curve for the redistributed bed bears close resemblance to that of the normal bed. The difference between the forward and backward pressure differential curves of the redistributed bed appears to be slightly smaller than the difference between the curves of the normal bed. This indicates that less bed mass is lost due to particle elutriation in the redistributed bed, possibly because of more evenly distributed radial air flow.

Figure 6.13 presents the surface profiles of a 100g redistributed bed rotating at 200 RPM and consisting of 120 μm mean diameter glass beads for various flow rates. Comparing the surface profile at 0 SLM of the redistributed bed to that of the normal bed in Figure 6.4, it can be seen that the redistribution procedure was very effective in moving glass beads upward and decreasing the variation in radial bed thickness in the axial direction. This relatively uniform surface profile at 0 SLM is seen to lead to more uniform bed expansion and fluidization at higher flow rates. Unlike the skewed surface profile expansion seen in Figure 6.4, the profiles in Figure 6.13 show that both top and bottom portions of the bed expand at similar rates. A significant expansion in bed volume is seen between the flow rates of 20 SLM and 40 SLM. This difference in bed volume is much larger than that between 0 SLM and 20 SLM and signals the transition from packed to minimally fluidized

regime which could explain the significant pressure drop seen in Figure 6.12. Examining the surface profiles in Figures 6.4a and 6.13a shows that the packed region of the bed at 100 SLM in the redistributed bed was confined to $z/Z < 0.08$ compared to $z/Z < 0.2$ in the normal bed. This indicates the redistribution procedure markedly improved the uniformity of fluidization and highlights the importance of the starting surface profile at zero flow rate in low rotational speed RFB's.

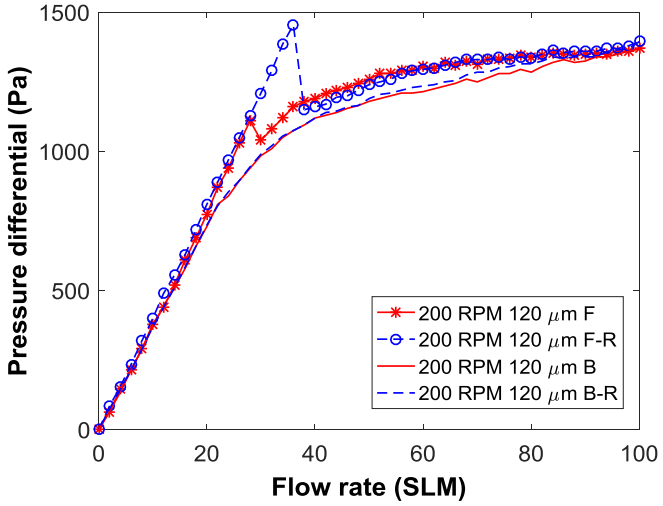

Figure 6.12: Pressure differential as a function of air flow rate. F and B denote forward (increasing) and backward (decreasing) changes in air flow rate. R denotes redistribution procedure at the start of the experimental run.

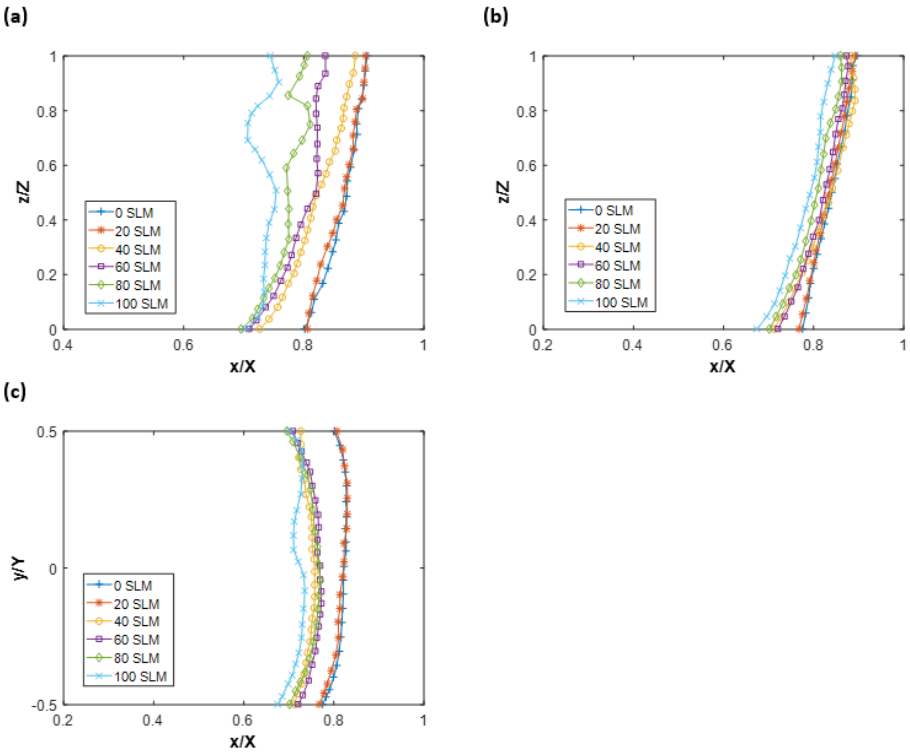

Figure 6.13: Particle bed surface profiles for varying air flow rates on the inner chamber surfaces containing points (a) A-B, (b) C-D and (c) B-D. The bed was rotated at a constant speed of 200 RPM and consisted of 100 g of 120 µm mean diameter glass beads which were redistributed through a special procedure.

Figure 6.14 presents the comparison of the pressure differential as a function of air flow rate across a bed consisting of 240 µm mean diameter glass beads that underwent the redistribution procedure and a normal bed that did not. It can be seen that redistributing bed particles had a positive effect on the uniformity of fluidization. The pressure differential curve for the redistributed bed shows a drop in pressure at minimum fluidization compared to the smooth increase of the normal bed. This suggests that more portion of the bed is fluidized at minimum fluidization in the redistributed bed compared to the normal bed. After the drop in pressure differential, the curves for the both beds appear almost the same, similar to the curves of beds consisting of smaller particles shown in Figure 6.12. The backward and forward pressure differential plots show very little difference for both, meaning that there is very little loss of particle bed mass due to elutriation for both beds. This is due to

the 240 μm glass beads being larger and harder to be entrained than the 120 μm glass beads in Figure 6.12.

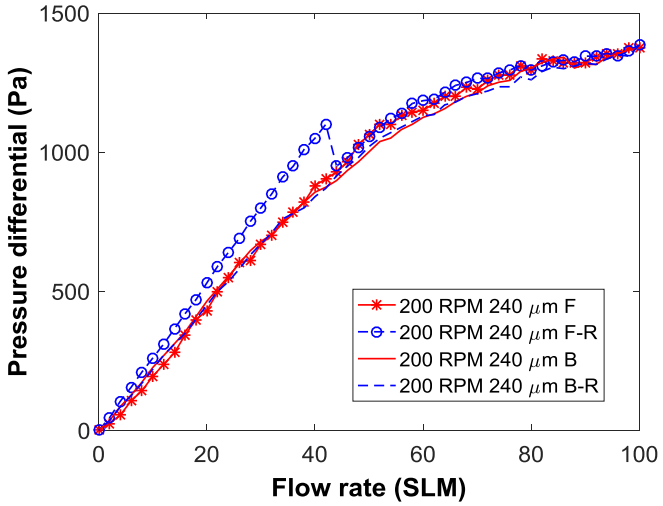

Figure 6.14: Pressure differential as a function of air flow rate. F and B denote forward (increasing) and backward (decreasing) changes in air flow rate. R denotes redistribution procedure at the start of the experimental run.

Figure 6.15 presents the surface profiles of a 100g bed rotating at 200 RPM and consisting of 240 μm mean diameter glass beads for varying flow rates. These profiles appear distinctly different to the profiles of the normal bed shown in Figure 6.8. For example, here Points B and D do not move radially outwards with increasing flow rate because the particles are already redistributed at the start. In Figure 6.8, Points B and D move with increasing flow rate because the process of redistributing particles upward occurs as the flow rate is increased and more portion of the bed becomes fluidized. Another obvious difference is the more uniform expansion of bed surface profiles with increasing flow rate. The average gradients of the surface profiles in Figure 6.15 remain similar throughout the range of flow rates, indicating that the whole bed expands almost as one. The most noticeable expansion happens between the flow rates of 40 SLM and 60 SLM. This expansion corresponds to the drop in differential pressure seen in Figure 6.14 and likely marks the point at which a portion

of the bed becomes minimally fluidized. At flow rates greater than 60 SLM, the profiles for the redistributed bed show signs of bubbles emerging from the surface for z/Z > 0.7, whereas for the normal bed in Figure 6.8, the profiles show signs of turbulent bubbling. This again shows that the redistribution procedure has positive effects on the uniformity of radial air flow, bed expansion and fluidization quality.

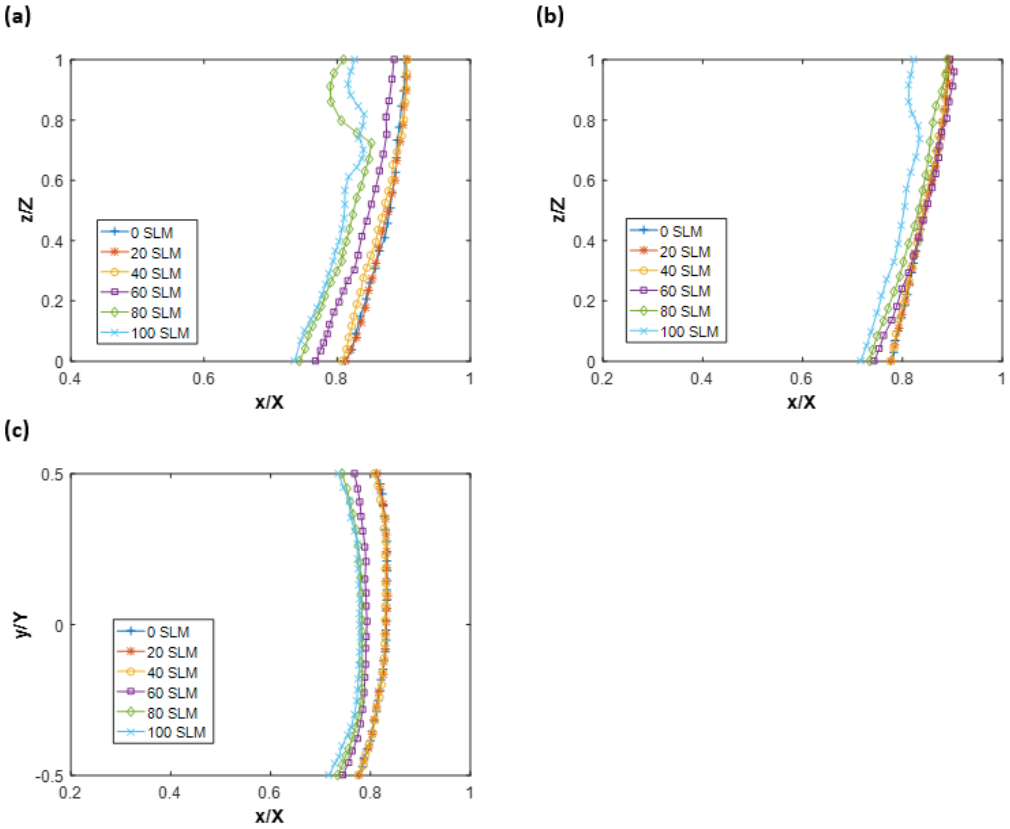

Figure 6.15: Particle bed surface profiles for varying air flow rates on the inner chamber surfaces containing points (a) A-B, (b) C-D and (c) B-D. The bed was rotated at a constant speed of 200 RPM and consisted of 100 g of 240 µm mean diameter glass beads which were redistributed through a special procedure.

Figure 6.16 presents the fluidization boundaries and surface profiles for varying flow rates in a bed consisting of 240 µm mean diameter glass beads that underwent the redistribution procedure. The conditions are the same as those of Figure 6.10. The movement of the fluidization boundaries here appear less staggered with increasing flow rate, and the gradients for these boundaries are steeper, indicating a greater uniformity of radial air flow

through the bed. One interesting observation to note here is that the gradient of every fluidization boundary that touches the bottom surface becomes increasingly steeper as z/Z approaches 0 or the bottom surface. This gives the fluidization boundary a curved appearance and implies that the bottom surface in the redistributed bed has the effect of making the radial air flow near it more uniform. The steepening effect is also seen in Figure 6.10, albeit to a lesser extent and only for high flow rates of 80 SLM and 100 SLM. Comparing the surface profile and fluidization boundary in Figure 6.16 and those in Figure 6.10 provides support for the positive effects of the redistribution procedure in creating a more uniformly expanded and fluidized bed.

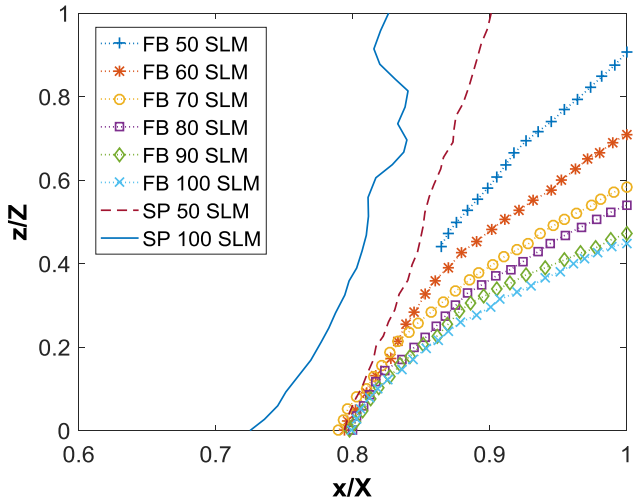

Figure 6.16: Particle bed surface profiles, denoted SP, and fluidization boundaries, denoted FB, for varying air flow rates on the inner chamber surface containing points A-B. The bed was rotated at a constant speed of 200 RPM and consisted of 100 g of 240 µm mean diameter glass beads which were redistributed through a special procedure.

6.4 Conclusion

The present investigation report the pressure differential, bed surface profile and fluidization boundary for systematically varied operating parameters, namely rotational speed, particle size and fluidizing gas flow rate, in a sliced RFB. A special redistribution procedure was trialled to assess the influence of the axial distribution of bed radial thickness on fluidization

characteristics. The key findings derived from the investigation can be summarised as follows:

The pressure differential response in a vertically oriented RFB can be significantly altered through manipulating the initial bed surface profile or the movement of particles within the bed through rotational speed. The size of the initial portion of the bed that undergoes the packed to fluidized bed transition determines the magnitude of the observed drop in pressure differential at minimum fluidization. For large particles that fluidize very gradually, there may not be an observable drop. This phenomenon may help explain the two distinct pressure differential responses reported in literature (Takahashi et al. 1984; Fan et al. 1985).

The fluidization boundary between the fluidized and packed volumes of the bed is highly non-uniform and very sensitive to the balance of forces acting on the particles. One dimensional fluidization models that assume the boundary moves only in the radial direction cannot adequately predict the pressure differential in a low rotational speed RFB. Thus, the development of two dimensional theoretical models for partially fluidized RFB is needed to account for the influence of gravity.

A tapered bed design should be implemented to prevent the packed bed region caused by the weight of the bed and to improve the uniformity of fluidization. A tapered bed design also has the benefit of reducing particle elutriation rate from the bed (Nakamura et al., 2014).

Redistributing particles through the reported particle redistribution procedure helps improve the uniformity of bed expansion and fluidization by ensuring that the variation in radial bed thickness and pressure differential across the bed is minimized at the start of flow injection.

6.5 Acknowledgement

This research was performed as part of the Australian Solar Thermal Research Initiative (ASTRI), a project supported by the Australian Government, through the Australian Renewable Energy Agency (ARENA). This research is also supported by the Australian Government Research Training Program (RTP). The views expressed herein are not necessarily the views of the Australian Government, and the Australian Government does not accept responsibility for any information or advice contained herein.

Chapter 7

Conclusion and Future Work

The present thesis introduced a new solar gasification receiver concept termed Rotating Fluidized Bed Receiver (RFBR). Perceived benefits of the proposed RFBR concept namely, its potential to prevent the deposition of entrained particles onto the receiver window and extend particle residence time and gasification conversion were quantified using the analytical and numerical models developed in the present thesis. The influence of key RFBR operating parameters on the extent of these benefits was assessed with the aim of identifying suitable operating regimes and improving the RFBR concept for better technical robustness and commercial viability. Relevant physical mechanisms affecting the particle residence time, gasification conversion and particle deposition behaviour in the RFBR were identified and investigated to provide a better understanding of the operation of the RFBR and other similar entrained flow solar receivers.

In addition, the feasibility of the RFBR was further explored in the experimental campaign designed to observe the physical operation and fluidization characteristics of an RFB operating at low rotational speeds. This experimental campaign confirmed that the RFBR concept is capable of operating and achieving sufficient fluidization quality at low rotational speeds which are beneficial to reducing the rotating component wear and kinetic energy loss via rotation. The present thesis demonstrated that the RFBR concept is feasible and its advantageous benefits could be realised under operating conditions that do not incur

significant penalties such as low energy conversion efficiency or excessive maintenance requirements. Hence, there is justification for further development and investigation of the RFBR concept. The following sections outline the key findings and outcomes derived from each major investigation of the present thesis.

7.1 Feedstock Particles for Solar Gasification

A single particle model for the steam gasification of wood char was developed and verified with experimental measurements in this chapter. The particle surface temperature and relative dominance of heat transfer mechanisms on the particle surface were assessed using the model for their sensitivity to key solar gasification receiver parameters, namely initial particle size, radiation intensity and concentration of steam (H_2O).

The initial feedstock particle size was found to increase the particle surface temperature due to increased surface area for solar radiation absorption and reduced convection heat loss in an environment where the particulate phase is highly diluted and there is little negligible heat transfer between particles. However, this temperature increase significantly diminishes as the particle size increases because of the rapidly increasing re-radiation heat loss from the surface. Increasing the initial particle size from 100 μm to 700 μm and 700 μm to 1300 μm was predicted to increase the particle surface temperature by approximately 155 K and 30 K respectively. Changing the particle surface temperature was found to shift the relative dominance of heat transfer modes on the particle surface. For instance, for a 100 μm diameter particle, about 80% and 19.9% of the absorbed solar heat on the particle surface was lost through convection and re-radiation respectively. In contrast, for a 700um diameter particle, the convective and re-radiation heat losses on the particle surface made up of about

34% and 64% of the absorbed solar heat respectively. For these two initial particle sizes, the proportions of solar heat conducted into the particle volume were calculated to be 0.115% and 2.4% respectively. It is worth noting that large particles with skewed radial distribution of temperature and reactant concentration exhibit a different peripheral fragmentation behaviour to small particles with almost uniform radial distribution of temperature and reactant concentration. Large particles were predicted to shrink gradually whereas small particles were predicted to disintegrate almost instantaneously.

Increasing the radiation intensity on the particle surface was found to increase the absorption of solar heat which causes the particle surface temperature to rise. The stepwise variations in radiation intensity simulated in the model produced almost stepwise increases in particle surface temperature. This increase in particle surface temperature is beneficial to gasification conversion rate. A reduction of approximately 250 s in complete gasification conversion time was calculated for an increase of particle surface temperature from 1303K ($1\,\mathrm{MW/m^2}$) to 1563K ($4\,\mathrm{MW/m^2}$) for a 100 μm diameter char particle. The faster gasification kinetics were predicted to increase the amount of absorbed solar heat that is conducted into the particle to drive the gasification process. The proportion of absorbed solar heat being conducted into the particle was predicted to increase from 0.115% to 0.15% for an increase of radiation intensity from 1 $\mathrm{MW/m^2}$ to 4 $\mathrm{MW/m^2}$.

The concentration of steam was found to have little effect on particle surface temperature and convection and re-radiation heat losses. However, it appears to have a noticeable influence on the conduction of absorbed solar heat into the particle volume. The proportion of heat conducted was calculated to increase from 0.115% to 0.137% for an increase of

steam concentration from 0.2 mole fraction to 0.8 mole fraction. This increase in steam concentration was also predicted to lead to a reduction of 50 s in the complete gasification conversion time of a 100 μm diameter particle.

Overall, this investigation showed that increasing the rate of reaction (through temperature or concentration of reactant) or volume of reaction (through initial particle size) can be beneficial to the solar to chemical energy conversion efficiency of a solar gasification receiver. This investigation also found that the convection heat loss on the particle surface to be prominent at low gasification temperatures for small feedstock particle sizes, accounting for approximately 80% of the heat lost on the particle surface of a 100 μm diameter char particle at a temperature of 1303K. Re-radiation heat loss becomes more dominant as the particle size and surface temperature increase. Thus, the solar receiver sensible heat recovery system needs to be designed with consideration about the feedstock particle size and temperature. It is worth noting that the single particle model does not account for volumetric effects, and the conclusions derived should be considered in conjunction with the limitations of the model.

7.2 Particle Residence Time and Gasification Conversion in the RFBR

The single particle model developed in Chapter 3 was combined with equations of motion describing the particle trajectory in an idealised RFBR flow field to assess the sensitivity of particle residence time and conversion to important RFBR parameters, namely rotational speed, initial particle size, radiation intensity, and particle release position.

Rotational speed was found to be a very effective means of controlling particle conversion and residence time at low rotational speeds. Increasing the rotational speed from 30 rad/s to 40 rad/s was calculated to increase the particle residence time from 0.5 s to 2.2 s and gasification conversion from 0.11 to 0.55 for a 100 μm diameter char particle. However, the effectiveness of rotational speed quickly diminishes with increasing rotational speed. For example, increasing the rotational speed from 60 rad/s to 70 rad/s only resulted in a predicted increase of 0.4 s in particle residence time and 0.1 in gasification conversion. The diminished effectiveness of rotational speed at high rotational speeds is largely due to high gasification conversion and limited particle mass for the centrifugal accelerate to influence.

The effect of initial particle size on particle residence time and conversion was found to vary significantly depending on the particle size and rate of gasification conversion. In general, increasing the particle size was predicted to increase particle residence time and conversion because a larger mass equates to more centrifugal force and longer entrainment. However, as the particle size increases, the gasification process shifts gradually to the diffusion limited reaction regime with the rate of diffusive transport of reactants becoming the key limiting factor instead of temperature. At this point, the rate of gasification conversion slows down, and further increases in particle size and residence time do not necessarily lead to more conversion. This is further complicated by the inconsistent relationship between particle size and residence time. The developed model shows that particle size greatly influences the particle's shrinking behaviour which in turn affects the fluid drag acting on the particle. The peripheral fragmentation approach to modelling particle shirking are heavily dependent on the radial distribution of temperature and reactant concentration within the particle volume. The skewness of these radial distributions

determines the rate of particle shrinking. Thus, small particles shrink in a different manner to large particles and subsequently, show a different trend between particle size and residence time. For instance, increasing the particle size from 100 μm to 300 μm resulted in an increase of freeboard residence time from 0.5 s to 0.8 s whereas increasing the particle size from 300 μm to 500 μm resulted in a reduction of freeboard residence time from 0.8 s to 0.3 s. However, it should be noted that the predicted total residence times for these three particle sizes were 0.5 s, 3.3 s and 3.6 s due to larger particles taking longer to escape the fluidized bed.

Radiation intensity was found to decrease particle residence time because increasing the radiative heat transfer leads to a higher particle temperature and gasification conversion rate which in turn, accelerates the loss of particle mass and decreases the time taken for a particle to be entrained out of the receiver. However, it is worth noting that the increase in conversion rate is sufficiently great to compensate for any conversion lost due to reduced residence time. In fact, particle conversion was found to increase with increasing radiation intensity despite of decreased residence time. For example, increasing the radiation intensity from 2 $\mathrm{MW/m^2}$ to 6 $\mathrm{MW/m^2}$ was predicted to increase the conversion from 0.1 to 0.35 and decreases the residence time from 0.5 s to 0.32 s.

The axial position at which the particle is release from the bed appears to have very little influence on particle residence time or conversion. The axial release position may have more influence on particle residence time in a physical, non-idealised flow field with end effects and fluid turbulence.

In summary, this investigation confirmed that the aforementioned key RFBR parameters can be adjusted to achieve precise control of particle residence time and gasification conversion. This investigation also identified operating regimes where the effectiveness of these key parameters is greatly diminished.

7.3 Flow Field and Particle Deposition in the RFBR

The combined analytical model developed in Chapter 4 utilised a set of idealised flow field equations which were inadequate to account for the effects of RFBR receiver geometrical features such as the tangential outlets, aperture and secondary concentrator volume. Therefore, a CFD-DPM model was created to assess the sensitivityse of the flow field and particle deposition onto the receiver window to variations in bed rotational speed, cavity length to diameter ratio and fluidizing gas velocity.

The bed rotational speed was found to be an effective parameter in controlling the tangential velocity and intensity of the vortex flow in the RFBR. Increasing the rotational speed increases the ratio of the centrifugal to radial fluid drag forces acting on the entrained particles and thus, shifts the peak concentration of particles radially outwards and away from the centre. This resulted in a significant reduction of particles being entrained through the central aperture and depositing on the receiver window. For instance, increasing the rotational speed from 15.7 rad/s to 47.1 rad/s was predicted to decrease the normalised rate of particle deposition on the window from 0.55 % to 0.2 % of the injected 10 μm diameter particles. Increasing the rotational speed was also calculated to significantly increase the positive fluid flow rate into the secondary concentrator volume. For an increase of rotational speed from 15.7 rad/s to 47.1 rad/s, the positive fluid flow rate into the secondary

concentrator increased from 3.5% to 5.8% of the inlet flow rate. The additional fluid flow into the secondary concentrator increases the probability of particle deposition and counters the particle mitigation effect of increased centrifugal force, rendering bed rotational speed less effective in reducing particle deposition.

Increasing the radial fluidizing gas velocity and flow rate was found to add more tangential momentum to the receiver cavity which resulted in increased tangential velocity and intensity of the vortex flow in the receiver. This increases the centrifugal force acting on the entrained particles and effectively decreases the particle deposition onto the receiver window. The fluidizing velocity was also found to increase the average flow velocity in the tangential outlets by a factor equal to the ratio of the total inlet and outlet areas. This has the unintended effect of re-energising the vortex flow near the aperture where the outlets are located. As a result, the Swirl Number of the flow at the aperture plane was found to be heavily influenced by the fluidizing gas velocity and total inlet/outlet flow rate. This highlights the importance of selecting suitable outlet geometry and dimensions to match the flow conditions inside the RFBR cavity.

In conclusion, this investigation showed that the particle deposition onto the receiver window can be effectively controlled through adjusting the radial fluidising gas velocity and bed rotational speed of the RFBR. Several particle deposition related mechanisms were identified and investigated to better understand the operating regimes where the deposition of particles onto the receiver window is minimised.

7.4 Fluidization Characteristics in the RFBR at Low Rotational Speed

An experimental campaign was conducted to observe the fluidization characteristics in the particle bed section of the RFBR at low rotational speeds. The initial bed surface profile was found to be an important parameter affecting the uniformity of bed expansion and fluidization. A highly skewed surface profile was seen to cause significant maldistribution of radial air flow through the bed and consequently, greatly varied fluidization quality in the axial direction. The top portion of the bed was observed to expand and fluidize at lower flow rates than the bottom portion due to being radially thinner, which leads to smaller pressure drop, and being almost unaffected by the weight of the particle bed.

The movement of the fluidization boundary within the bed appeared to be two dimensional, moving in both radial and axial directions. Because of the low rotational speeds. The centrifugal force generated was found to be insufficient gain dominance over gravity. Thus, the commonly adopted one dimensional approach to modelling a partially fluidized RFB cannot be used here. A two dimensional partial fluidization modelling approach is required to account for the skewed bed surface profile and two dimensional fluidization boundary movement in low speed RFBs.

In addition, the pressure differential across the bed at minimum fluidization was observe to be closely linked to the bed surface profile and uniformity of bed expansion and fluidisation. In a uniformly expanded bed, a large amount of the bed undergoes the packed to fluidized bed regime transition at minimum fluidization, and this may cause a sudden drop in the pressure differential curve. In a non-uniformly expanded bed, the initial portion of the bed

undergoing the transition at minimum fluidization is relatively small, and there may not be any observable sudden drop in the pressure differential curve.

Redistributing particles through a special redistribution procedure before low speed fluidization was found to reduce the skewness in the initial bed surface profile and improve the uniformity of bed expansion and fluidization quality. With the implementation of the redistribution procedure, sufficiently uniform fluidization was observed a low rotational speed of 21 rad/s (200 RPM) in a bed containing 100 g of 120 μm mean diameter glass beads. At this low rotational speed, the kinetic energy loss through rotation and mechanical wear of the RFBR are expected to be insignificant.

Lastly, a packed bed volume were observed to form in the corner between the vertical gas distributor and bottom RFB surface. This packed bed volume persists even at high flow rates that could cause significant elutriation in other regions of the bed. A tapered bed design should be considered for the RFBR concept because it could eliminate the corner between the gas distributor and bottom surface, subsequently removing the space for the packed bed volume. A tapered bed design may also reduce the rate of particle elutriation through reducing the radial gas velocity at the bed surface (Nakamura et al. 2014).

7.5 Future Work

The present work quantified many of the perceived benefits of the RFBR concept through theoretical modelling and demonstrated that these benefits can be realized through controlling various key RFBR parameters under typical solar receiver conditions. For example, Chapter 4 showed that a high gasification conversion up to 0.85 was achievable at a rotational speed of 70 rad/s for 100 μm diameter char particles in a receiver operating at a

temperature of 1200K with an incident radiative flux of 1 MW/m^2 on the particle surface. A further increase in rotational speed is expected to increase the particle residence time and conversion extent further. Moreover, Chapter 5 reported that very low dimensionless particle deposition rates (<0.02 % of the injected 10 μm diameter particles) could be achieved for rotational speeds less than 94.2 rad/s. In addition, Chapter 6 experimentally demonstrated that the bed section of the RFBR could be uniformly and adequately fluidized at a rotational speed as low as 21 rad/s if the particle bed undergoes a special particle redistribution procedure. Hence, the present work alleviates the concern that the perceived benefits of the RFBR concept could only be achieved at unrealizably high rotational speeds.

However, since the present work is based on many idealised assumptions, further verification in the real world is required to confirm the theoretical findings and various identified mechanisms. A cold case lab scale prototype RFBR would need to be constructed for an experimental campaign to be carried out to further investigate the flow field, onset of particle elutriation from the bed, particle deposition on the window, and the radial concentration of entrained particles in the freeboard. The knowledge gained from this experimental campaign would enable a detailed whole receiver model to be created to simulate the receiver's hot case operation. Then, iterative changes to the RFBR receiver concept could be implemented and result in the production of a lab scale hot case prototype receiver which could be used to verify and tune the models as well as testing the concept for technical robustness and potential to be used in a large scale commercial system.

References

Abrahamsen, AR & Geldart, D 1980, 'Behaviour of gas-fluidized beds of fine powders part I. homogeneous expansion', *Powder Technology*, vol. 26, no. 1, pp. 35-46.

Ahmadzadeh, A & Arastoopour, H 2008, 'Three-dimensional numerical simulation of a horizontal rotating fluidized bed', *Powder Technology*, vol. 183, no. 3, pp. 410-416.

Ahmadzadeh, A, Arastoopour, H & Teymour, F 2003, 'Numerical simulation of gas and particle flow in a rotating fluidized bed', *Industrial & Engineering Chemistry Research*, vol. 42, no. 12, pp. 2627-2633.

Azadi, M, Azadi, M & Mohebbi, A 2010, 'A CFD study of the effect of cyclone size on its performance parameters', *Journal of Hazardous Materials*, vol. 182, pp. 835-841.

Basu, P 2010, Biomass gasification and pyrolysis: practical design and theory, Academic Press.

Baykara, S & Bilgen, E 1985, 'Synthesis gas and H 2 production from solar gasification of Albertan coal', *Energy Conversion and Management*, vol. 25, no. 4, pp. 391-398.

Beattie, WH, Berjoan, R & Coutures, J-P 1983, 'High-temperature solar pyrolysis of coal', *Solar Energy*, vol. 31, no. 2, pp. 137-143.

Belghit, A & Daguenet, M 1989, 'Study of heat and mass transfer in a chemical moving bed reactor for gasification of carbon using an external radiative source', *International Journal of Heat and Mass Transfer*, vol. 32, no. 11, pp. 2015-2025.

Belghit, A, Daguenet, M & Reddy, A 2000, 'Heat and mass transfer in a high temperature packed moving bed subject to an external radiative source', *Chemical Engineering Science*, vol. 55, no. 18, pp. 3967-3978.

Belghit, A & El Issami, S 2001, 'Hydrogen production by steam gasification of coal in gas–solid moving bed using nuclear heat', *Energy Conversion and Management*, vol. 42, no. 1, pp. 81-99.

Berber, R & Fletcher, E 1988, 'Extracting oil from shale using solar energy', *Energy*, vol. 13, no. 1, pp. 13-23.

Bharadwaj, A, Baxter, LL & Robinson, AL 2004, 'Effects of intraparticle heat and mass transfer on biomass devolatilization: experimental results and model predictions', *Energy & Fuels*, vol. 18, no. 4, pp. 1021-1031.

Bhatia, S & Perlmutter, D 1981, 'A random pore model for fluid - solid reactions: II. Diffusion and transport effects', *AIChE Journal*, vol. 27, no. 2, pp. 247-254.

Bhatia, SK & Perlmutter, D 1980, 'A random pore model for fluid - solid reactions: I. Isothermal, kinetic control', *AIChE Journal*, vol. 26, no. 3, pp. 379-386.

Bilbao, R, Mastral, J, Ceamanos, J & Aldea, M 1996, 'Modelling of the pyrolysis of wet wood', *Journal of Analytical and Applied Pyrolysis*, vol. 36, no. 1, pp. 81-97.

Brewster M & Kunitomo T, 1984, 'The optical constants of coal, char, and limestone', *Journal of Heat Transfer*, vol. 106, no. 4, pp. 678-683.

Chandran, R & Chen, JC 1982, 'Bed - surface contact dynamics for horizontal tubes in fluidized beds', *AIChE Journal*, vol. 28, no. 6, pp. 907-914.

Chen, Y 1987, 'Fundamentals of a centrifugal fluidized bed', *AIChE Journal*, vol. 33, no. 5, pp. 722-728.

Chen, Z, Yan, Y & Elnashaie, SS 2004, 'Catalyst deactivation and engineering control for steam reforming of higher hydrocarbons in a novel membrane reformer', *Chemical Engineering Science*, vol. 59, no. 10, pp. 1965-1978.

Chevray, R, Chan, Y & Hill, F 1980, 'Dynamics of bubbles and entrained particles in the rotating fluidized bed', *AIChE Journal*, vol. 26, no. 3, pp. 390-398.

Chinnici, A, Arjomandi, M, Tian, Z & Nathan, G 2016, 'A novel solar expanding-vortex particle reactor: experimental and numerical investigation of the iso-thermal flow field and particle deposition', *Solar Energy*, vol. 133, pp. 451-464.

Chinnici, A, Arjomandi, M, Tian, ZF, Lu, Z & Nathan, GJ 2015, 'A novel solar expanding-vortex particle reactor: influence of vortex structure on particle residence times and trajectories', *Solar Energy*, vol. 122, 12//, pp. 58-75.

Chinnici, A, Xue, Y, Lau, TC, Arjomandi, M & Nathan, GJ 2017, 'Experimental and numerical investigation of the flow characteristics within a solar expanding-vortex particle receiver-reactor', *Solar Energy*, vol. 141, pp. 25-37.

Chuah, T, Gimbun, J & Choong, T 2006, 'A CFD study of the effect of cone dimensions on sampling aerocyclones performance and hydrodynamics', *Powder Technology*, vol. 162, pp. 126-132.

Clift, R 1983, 'An occamist view of fluidized bed reactor modeling ', *Chemical Engineer-London*, no. 388, pp. 29.

Darton, R, LaNauze, R, Davidson, J & Harrison, D 1977, 'Bubble growth due to coalescence in fluidized bed', *Transactions of the Institution of Chemical Engineers*, vol. 55, pp. 274-280.

Dasappa, S, Paul, P, Mukunda, H & Shrinivasa, U 1994, 'The gasification of wood-char spheres in CO 2 N 2 mixtures: analysis and experiments', *Chemical Engineering Science*, vol. 49, no. 2, pp. 223-232.

Davidson, J 1961, 'Symposium on fluidization-discussion', *Transactions of the Institution of Chemical Engineers*, vol. 39, pp. 223-240.

de Diego, LF, García-Labiano, F, Abad, A, Gayán, P & Adánez, J 2002, 'Modeling of the devolatilization of nonspherical wet pine wood particles in fluidized beds', *Industrial & Engineering Chemistry Research*, vol. 41, no. 15, pp. 3642-3650.

Dechsiri, C 2004, 'Particle transport in fluidized beds: experiments and stochastic models', PhD thesis, University of Groningen.

Demircan, N, Gibbs, B, Swithenbank, J & Taylor, D 1978, 'Rotating fluidized bed combustor', *Fluidization: Proceedings of the Second Engineering Foundation Conference, Trinity College, Cambridge, England, 2-6 April 1978*, vol. 2, p. 269.

Desideri U, & Campana PE 2014, 'Analysis and comparison between a concentrating solar and a photovoltaic power plant', *Applied Energy*, vol. 113, pp. 422-433.

Dinc S, Demiroglu M, Turnquist N, Mortzheim J, Goetze G, Maupin J, Hopkins J, Wolfe C & Florin M 2001, 'Fundamental design issues of brush seals for industrial applications', *ASME Turbo Expo 2001: Power for Land, Sea, and Air*.

Dlugokencky, E, Hall, B, Montzka, S, Dutton, G, Mühle, J, Elkins, J 2018, 'Atmospheric composition [in State of the Climate in 2017]', *Bulletin of the American Meteorological Society*, vol. 99, no. 8, S46–S49.

Donaldson, C & Snedeker, R 1962, *Experimental investigation of the structure of vortices in simple cylindrical vortex chambers*, Aeronautical Associates of Princeton.

Dutta, S & Wen, C 1977, 'Reactivity of coal and char. 2. In oxygen-nitrogen atmosphere', *Industrial & Engineering Chemistry Process Design and Development*, vol. 16, no. 1, pp. 31-37.

Dutta, S, Wen, C & Belt, R 1977, 'Reactivity of coal and char. 1. In carbon dioxide atmosphere', *Industrial & Engineering Chemistry Process Design and Development*, vol. 16, no. 1, pp. 20-30.

Edenhofer, O, Pichs-Madruga, R, Sokona, Y, Seyboth, K, Matschoss, P, Kadner, S, Zwickel, T, Eickemeier, P, Hansen, G & Schlömer, S 2011, 'IPCC special report on renewable energy sources and climate change mitigation', *Prepared By Working Group III of the Intergovernmental Panel on Climate Change, Cambridge University Press, Cambridge, UK*.

Edwards, M & Avidan, A 1986, 'Conversion model aids scale-up of mobil's fluid-bed MTG process', *Chemical Engineering Science*, vol. 41, no. 4, pp. 829-835.

Ergun, S 1952, 'Fluid flow through packed columns', *Chemical Engineering Progress*, vol. 48.

Fan, L, Chang, C, Yu, Y, Takahashi, T & Tanaka, Z 1985, 'Incipient fluidization condition for a centrifugal fluidized bed', *AIChE Journal*, vol. 31, no. 6, pp. 999-1009.

Figueroa, JD, Fout, T, Plasynski, S, McIlvried, H & Srivastava, RD 2008, 'Advances in CO_2 capture technology — the US Department of Energy's Carbon Sequestration Program', *International Journal of Greenhouse Gas Control*, vol. 2, no. 1, pp. 9-20.

Flechsenhar, M & Sasse, C 1995, 'Solar gasification of biomass using oil shale and coal as candidate materials', *Energy*, vol. 20, no. 8, pp. 803-810.

Foka, M, Chaouki, J, Guy, C & Klvana, D 1994, 'Natural gas combustion in a catalytic turbulent fluidized bed', *Chemical Engineering Science*, vol. 49, no. 24, pp. 4269-4276.

Fryer, C & Potter, OE 1972, 'Countercurrent backmixing model for fluidized bed catalytic reactors. Applicability of simplified solutions', *Industrial & Engineering Chemistry Fundamentals*, vol. 11, no. 3, pp. 338-344.

Fuertes A & Marban G, 1994, 'Modelling gasification reactions including the percolation phenomenon', *Chemical Engineering Science*, vol. 49, no. 22, pp. 3813-3821.

Geldart, D 1973, 'Types of gas fluidization', *Powder Technology*, vol. 7, no. 5, pp. 285-292.

Geldart, D & Abrahamsen, AR 1978, 'Homogeneous fluidization of fine powders using various gases and pressures', *Powder Technology*, vol. 19, no. 1, pp. 133-136.

Gibilaro, LG & Rowe, P 1974, 'A model for a segregating gas fluidized bed', *Chemical Engineering Science*, vol. 29, no. 6, pp. 1403-1412.

Gimbun, J, Chuah, T, Choong, T & Fakhru'l-Razi, A 2005, 'A CFD study on the prediction of cyclone collection efficiency', *International Journal for Computational Methods in Engineering Science and mechanics*, vol. 6, pp. 161-168.

Gordillo, E & Belghit, A 2011, 'A bubbling fluidized bed solar reactor model of biomass char high temperature steam-only gasification', *Fuel Processing Technology*, vol. 92, no. 3, pp. 314-321.

Grace, J 1981, 'Fluidized bed reactor modeling: an overview', *ACS Publications*.

García-Labiano, F, Luis, F, Adánez, J, Abad, A & Gayán, P 2005, 'Temperature variations in the oxygen carrier particles during their reduction and oxidation in a chemical-looping combustion system', *Chemical Engineering Science*, vol. 60, no. 3, pp. 851-862.

Gregg, D, Taylor, R, Campbell, J, Taylor, J & Cotton, A 1980, 'Solar gasification of coal, activated carbon, coke and coal and biomass mixtures', *Solar Energy*, vol. 25, no. 4, pp. 353-364.

Gregg, DW 1980, *Apparatus and method for solar coal gasification*, Lawrence Livermore National Laboratory (LLNL), Livermore, CA.

Gunardson, HH 1997, *Industrial gases in petrochemical processing: chemical industries*, CRC Press.

Hao, Y, Shi, M & Wang, H 2000, 'Experimental investigation of the heat and mass transfer in a centrifugal fluidized bed dryer', *Chemical Engineering Journal*, vol. 78, no. 2, pp. 107-113.

Hartholt, G, Hoffmann, A & Janssen, L 1996, 'Visual observations of individual particle behaviour in gas and liquid fluidized beds', *Powder Technology*, vol. 88, no. 3, pp. 341-345.

Hasuike H, Yoshizawa Y, Suzuki A & Tamaura Y, 2006, 'Study on design of molten salt solar receivers for beam-down solar concentrator', *Solar Energy*, vol. 80, no. 10, pp. 1255-1262.

He, F, Han, T, Hong, H & Jin, H 2011, 'Solar thermochemical hybrid trigeneration system with CO2 capture using dimethyl ether-fueled chemical-looping combustion', *ASME 2011 5th International Conference on Energy Sustainability*, pp. 1651-1660.

Helsen, L & Van den Bulck, E 2000, 'Kinetics of the low-temperature pyrolysis of chromated copper arsenate-treated wood', *Journal of Analytical and Applied Pyrolysis*, vol. 53, no. 1, pp. 51-79.

Higman, C & Van der Burgt, M 2008, *Gasification*, 2nd edn, Gulf Professional Publishing/Elsevier Science, Boston.

Hirsch, D 2005, 'Decarbonization of fossil fuels - Hydrogen production by the solar thermal decomposition of natural gas using a vortex-flow solar reactor', PhD thesis, ETH Zurich.

Ho CK & Iverson BD, 2014, 'Review of high-temperature central receiver designs for concentrating solar power', *Renewable and Sustainable Energy Reviews*, vol. 29, pp. 835-846.

Hoffmann, A 1983, 'Gas fluidization at elevated pressures', Department of Chemical and Biochemical Engineering, PhD thesis, University College London.

Ingel, G, Levy, M & Gordon, J 1992, 'Oil-shale gasification by concentrated sunlight: an open-loop solar chemical heat pipe', *Energy*, vol. 17, no. 12, pp. 1189-1197.

IPCC 2007, 'The Fourth Assessment Report of the Intergovernmental Panel on Climate Change', Geneva, Switzerland.

Jackson, R 1963, 'The mechanics of fluidized beds: part I', *Transactions of the Institution of Chemical Engineers*, vol. 41, pp. 13-21.

Kantorovich I, & Bar-Ziv E, 1999, 'Heat transfer within highly porous chars: a review', *Fuel*, vol. 78, no. 3, pp.279-299.

Kajitani, S, Hara, S & Matsuda, H 2002, 'Gasification rate analysis of coal char with a pressurized drop tube furnace', *Fuel*, vol. 81, no. 5, pp. 539-546.

Kaniyal, AA, van Eyk, PJ & Nathan, GJ 2016, 'Storage capacity assessment of liquid fuels production by solar gasification in a packed bed reactor using a dynamic process model', *Applied Energy*, vol. 173, pp. 578-588.

Kao, J, Pfeffer, R & Tardos, G 1987, 'On partial fluidization in rotating fluidized beds', *AIChE Journal*, vol. 33, no. 5, pp. 858-861.

Karthikeyan, M, Zhonghua, W & Mujumdar, AS 2009, 'Low-rank coal drying technologies—Current status and new developments', *Drying Technology*, vol. 27, no. 3, pp. 403-415.

Knowlton, T, Karri, S & Issangya, A 2005, 'Scale-up of fluidized-bed hydrodynamics', *Powder Technology*, vol. 150, no. 2, pp. 72-77.

Kodama, T, Kondoh, Y, Tamagawa, T, Funatoh, A, Shimizu, K & Kitayama, Y 2002, 'Fluidized bed coal gasification with CO2 under direct irradiation with concentrated visible light', *Energy & Fuels*, vol. 16, no. 5, pp. 1264-1270

Kodama, T, Enomoto, S, Hatamachi, T & Gokon, N 2008, 'Application of an internally circulating fluidized bed for windowed solar chemical reactor with direct irradiation of reacting particles', *Journal of Solar Energy Engineering*, vol. 130, no. 1.

Kogan, A & Kogan, M 2002, 'The tornado flow configuration-an effective method for screening of a solar reactor window', *Journal of Solar Energy Engineering*, vol. 124, no. 3, pp. 206-214.

Krishna, R & Wesselingh, J 1997, 'The Maxwell-Stefan approach to mass transfer', *Chemical Engineering Science*, vol. 52, no. 6, pp. 861-911.

Kroger, D, Levy, E & Chen, J 1979, 'Flow characteristics in packed and fluidized rotating beds', *Powder Technology*, vol. 24, no. 1, pp. 9-18.

Krusi, M 2014, 'Heat transfer enchancement in a solar biomass gasifier', PhD thesis, ETH Zurich.

Kubiak, H & Lohner, H 1992, 'Study relating to the use of solar energy for the allothermal gasification of coal', *Solar Thermal Energy Utilization*, vol. 6, pp. 327-340.

Kunii, D & Levenspiel, O 2013, *Fluidization engineering*, Elsevier.

Larfeldt J, Leckner B & Melaaen MC, 2000, 'Modelling and measurements of heat transfer in charcoal from pyrolysis of large wood particles', *Biomass and Bioenergy*, vol. 18, no. 6, pp. 507-514.

Lédé, J, Verzaro, F, Antoine, B & Villermaux, J 1986, 'Flash pyrolysis of wood in a cyclone reactor', *Chemical Engineering and Processing: Process Intensification*, vol. 20, no. 6, pp. 309-317.

Leva, M 1959, *Fluidization*, McGraw-Hill.

Levy, E & Chen, J 1977, *Centrifugal fluidization: a review*, Lehigh University, Bethlehem, PA (USA).

Lewis, NS & Nocera, DG 2006, 'Powering the planet: chemical challenges in solar energy utilization', *Proceedings of the National Academy of Sciences*, vol. 103, no. 43, pp. 15729-15735.

Lichty, P, Perkins, C, Woodruff, B, Bingham, C & Weimer, A 2010, 'Rapid high temperature solar thermal biomass gasification in a prototype cavity reactor', *Journal of Solar Energy Engineering*, vol. 132, no. 1, p. 011012.

Lipinski, W, Z'Graggen, A & Steinfeld, A 2005, 'Transient radiation heat transfer within a nongray nonisothermal absorbing-emitting-scattering suspension of reacting particles undergoing shrinkage', *Numerical Heat Transfer, Part B*, vol. 47, no. 5, pp. 443-457.

Lu, Z, Jafarian, M, Arjomandi, M & Nathan, GJ 2016, 'Analytical assessment of a novel rotating fluidized bed solar reactor for steam gasification of char particles', *Solar Energy*, vol. 140, pp. 113-123.

Mahecha-Botero, A, Grace, JR, Elnashaie, S & Lim, CJ 2009, 'Advances in modeling of fluidized-bed catalytic reactors: a comprehensive review', *Chemical Engineering Communications*, vol. 196, no. 11, pp. 1375-1405.

Malburg, W & Treiber, H 1980, 'Solar reactor', Patent DE, vol. 2836179.

Massaquoi, JG & Riggs, JB 1983, 'Mathematical modeling of combustion and gasification of a wet coal slab—I: Model development and verification', *Chemical Engineering Science*, vol. 38, no. 10, pp. 1747-1756.

Melchior, T, Perkins, C, Lichty, P, Weimer, AW & Steinfeld, A 2009, 'Solar-driven biochar gasification in a particle-flow reactor', *Chemical Engineering and Processing: Process Intensification*, vol. 48, no. 8, pp. 1279-1287.

Melchior, T, Perkins, C, Weimer, AW & Steinfeld, A 2008, 'A cavity-receiver containing a tubular absorber for high-temperature thermochemical processing using concentrated solar energy', *International Journal of Thermal Sciences*, vol. 47, no. 11, pp. 1496-1503.

Melchior, T & Steinfeld, A 2008, 'Radiative transfer within a cylindrical cavity with diffusely/specularly reflecting inner walls containing an array of tubular absorbers', *Journal of Solar Energy Engineering*, vol. 130, no. 2, p. 021013.

Mermoud, F, Golfier, F, Salvador, S, Van de Steene, L & Dirion, J 2006, 'Experimental and numerical study of steam gasification of a single charcoal particle', *Combustion and Flame*, vol. 145, no. 1, pp. 59-79.

Merry, J & Davidson, J 1973, 'Gulf stream circulation in shallow fluidized beds', *Transactions of the Institution of Chemical Engineers*, vol. 51, pp. 361-368.

Metcalfe, C & Howard, J 1977, 'Fluidisation and gas combustion in a rotating fluidized bed', *Applied Energy*, vol. 3, no. 1, pp. 65-74.

Metz, B, Davidson, O, De Coninck, H, Loos, M & Meyer, L 2005, *IPCC special report on carbon dioxide capture and storage*, Intergovernmental Panel on Climate Change, Geneva (Switzerland). Working Group III.

Müller, R, Zedtwitz, P, Wokaun, A & Steinfeld, A 2003, 'Kinetic investigation on steam gasification of charcoal under direct high-flux irradiation', *Chemical Engineering Science*, vol. 58, no. 22, pp. 5111-5119.

Murray, J 1965, 'On the mathematics of fluidization Part 1. Fundamental equations and wave propagation', *Journal of Fluid Mechanics*, vol. 21, no. 3, pp. 465-493.

Murray, JP & Fletcher, EA 1994, 'Reaction of steam with cellulose in a fluidized bed using concentrated sunlight', *Energy*, vol. 19, no. 10, pp. 1083-1098.

Naimer, N, Chiba, T & Nienow, A 1982, 'Parameter estimation for a solids mixing| segregation model for gas fluidized beds', *Chemical Engineering Science*, vol. 37, no. 7, pp. 1047-1057.

Nakamura, H, Deguchi, N, Takeuchi, H & Watano, S 2014, 'Numerical analysis of fluid flow and particle entrainment in a novel tapered rotating fluidized bed', *Chemical Engineering Science*, vol. 116, pp. 725-733.

Nakamura, H, Kondo, T & Watano, S 2013, 'Improvement of particle mixing and fluidization quality in rotating fluidized bed by inclined injection of fluidizing air', *Chemical Engineering Science*, vol. 91, pp. 70-78.

Nathan, G, Dally, B, Alwahabi, Z, van Eyk, P, Jafarian, M & Ashman, P 2017, 'Research challenges in combustion and gasification arising from emerging technologies employing directly irradiated concentrating solar thermal radiation', *Proceedings of the Combustion Institute*, vol. 36, no. 2, pp. 2055-2074.

Nathan, G, Jafarian, M, Dally, B, Saw, W, Ashman, P, Hu, E & Steinfeld, A 2018 'Solar thermal hybrids for combustion power plants: a growing opportunity'. *Progress in Energy and Combustion Science*. vol. 64, pp. 4-28.

Navarro, MV, Murillo, R, Mastral, AM, Puy, N & Bartroli, J 2009, 'Application of the distributed activation energy model to biomass and biomass constituents devolatilization', *AIChE Journal*, vol. 55, no. 10, pp. 2700-2715.

Nienow, A, Naimer, N & Chiba, T 1987, 'Studies of segregation/mixing in fluidized beds of different size particles', *Chemical Engineering Communications*, vol. 62, no. 1-6, pp. 53-66.

Orfao, J, Antunes, F & Figueiredo, JL 1999, 'Pyrolysis kinetics of lignocellulosic materials—three independent reactions model', *Fuel*, vol. 78, no. 3, pp. 349-358.

Ozalp, N, Chien, M-H & Morrison, G 2013, 'Computational fluid dynamics and particle image velocimetry characterization of a solar cyclone reactor', *Journal of Solar Energy Engineering*, vol. 135, no. 3, p. 031003.

Pang, S & Mujumdar, AS 2010, 'Drying of woody biomass for bioenergy: Drying technologies and optimization for an integrated bioenergy plant', *Drying Technology*, vol. 28, no. 5, pp. 690-701.

Perkins, C & Weimer, AW 2009, 'Solar‐thermal production of renewable hydrogen', *AIChE Journal*, vol. 55, no. 2, pp. 286-293.

Perkins, C, Jovanovic, Z, Strand, S, Hilton, C & Kelley, D 2015, 'Systems and methods for an indirect radiation driven gasifier reactor and receiver configuration', Google Patents.

Peters, GP, Andrew, RM, Boden, T, Canadell, JG, Ciais, P, Le Quéré, C, Marland, G, Raupach, MR & Wilson, C 2013, 'The challenge to keep global warming below 2 C', *Nature Climate Change*, vol. 3, no. 1, pp. 4-6.

Piatkowski, N & Steinfeld, A 2008, 'Solar-driven coal gasification in a thermally irradiated packed-bed reactor', *Energy & Fuels*, vol. 22, no. 3, pp. 2043-2052.

Piatkowski, N, Wieckert, C & Steinfeld, A 2009, 'Experimental investigation of a packed-bed solar reactor for the steam-gasification of carbonaceous feedstocks', *Fuel Processing Technology*, vol. 90, no. 3, pp. 360-366.

Piatkowski, N, Wieckert, C, Weimer, AW & Steinfeld, A 2011, 'Solar-driven gasification of carbonaceous feedstock—a review', *Energy & Environmental Science*, vol. 4, no. 1, pp. 73-82.

Please, C, McGuinness, M & McElwain, D 2003, 'Approximations to the distributed activation energy model for the pyrolysis of coal', *Combustion and Flame*, vol. 133, no. 1-2, pp. 107-117.

Poling BE, Prausnitz JM, John Paul OC, & Reid RC, 2001, *The properties of gases and liquids (Vol. 5)*, New York: McGraw-Hill.

Puig-Arnavat, M, Tora, E, Bruno, J & Coronas, A 2013, 'State of the art on reactor designs for solar gasification of carbonaceous feedstock', *Solar Energy*, vol. 97, pp. 67-84.

Qader, SA 1981, 'Solar heated fluidized bed gasification system', Google Patents.

Qian, G 2003, 'Fluidization and soot filtration in a rotating fluidized bed', PhD thesis, New Jersey Institute of Technology.

Qian, G, Bagyi, I, Burdick, I, Pfeffer, R, Shaw, H & Stevens, JG 2001, 'Gas–solid fluidization in a centrifugal field', *AIChE Journal*, vol. 47, no. 5, pp. 1022-1034.

Qian, G, Bágyi, I, Pfeffer, R, Shaw, H & Stevens, J 1998, 'A parametric study of a horizontal rotating fluidized bed using slotted and sintered metal cylindrical gas distributors', *Powder Technology*, vol. 100, no. 2, pp. 190-199.

Quaschning, V 2004, 'Technical and economical system comparison of photovoltaic and concentrating solar thermal power systems depending on annual global irradiation', *Solar Energy*, vol. 77, no. 2, pp. 171-178.

Raghuraman, J & Potter, O 1978, 'Countercurrent backmixing model for slugging fluidized-bed reactors', *AIChE Journal*, vol. 24, no. 4, pp. 698-704.

Romero, M & Steinfeld, A 2012, 'Concentrating solar thermal power and thermochemical fuels', *Energy & Environmental Science*, vol. 5, no. 11, pp. 9234-9245.

Roschke E, 1966, 'Experimental Investigation of a Confined, Jet Driven Water Vortex', Jet Propulsion Lab, Pasadena, California.

Segal A, & Epstein M, 2003, 'Solar ground reformer', *Solar Energy*, vol. 75, no. 6, pp. 479-490.

Saunders, J 1986, 'Particle entrainment from rotating fluidized beds', *Powder Technology*, vol. 47, no. 3, pp. 211-217.

Saw, WL, Guo, P, van Eyk, PJ & Nathan, GJ 2017, 'Approaches to accommodate resource variability in the modelling of solar driven gasification processes for liquid fuels synthesis', *Solar Energy*, vol. 156, pp. 101-112.

Schunk L, Lipiński W, & Steinfeld A, 2009, 'Heat transfer model of a solar receiver-reactor for the thermal dissociation of ZnO—Experimental validation at 10kW and scale-up to 1MW', *Chemical Engineering Journal*, vol. 150, no. 2, pp. 502-508.

Shafizadeh, F & Chin, PP 1977, 'Thermal deterioration of wood', *ACS Publications*.

Singer SL & Ghoniem A, 2013, 'Comprehensive gasification modeling of char particles with multi-modal pore structures', *Combustion and Flame*, vol. 160, no. 1, pp. 120-137.

Solomon, PR, Hamblen, DG, Carangelo, R, Serio, M & Deshpande, G 1988, 'General model of coal devolatilization', *Energy & Fuels*, vol. 2, no. 4, pp. 405-422.

Steinfeld, A 2005, 'Solar thermochemical production of hydrogen—a review', *Solar Energy*, vol. 78, no. 5, pp. 603-615.

Steinfeld, A & Palumbo, R 2001, 'Solar thermochemical process technology', *Encyclopedia of Physical Science and Technology*, vol. 15, no. 1, pp. 237-256.

Steinfeld, A & Schubnell, M 1993, 'Optimum aperture size and operating temperature of a solar cavity-receiver', *Solar Energy*, vol. 50, no. 1, pp. 19-25.

Szekely, J & Evans, J 1970, 'A structural model for gas—solid reactions with a moving boundary', *Chemical Engineering Science*, vol. 25, no. 6, pp. 1091-1107.

Szekely, J & Evans, J 1971, 'A structural model for gas-solid reactions with a moving boundary-II: the effect of grain size, porosity and temperature on the reaction of porous pellets', *Chemical Engineering Science*, vol. 26, no. 11, pp. 1901-1913.

Takahashi, T, Tanaka, Z, Itoshima, A & Fan, L 1984, 'Performance of a rotating fluidized bed', *Journal of Chemical Engineering of Japan*, vol. 17, no. 3, pp. 333-336.

Tanimoto, H, Chiba, S, Chiba, T & Kobayashi, H 1981, 'Jetsam descent induced by a single bubble passage in three-dimensional gas-fluidized beds', *Journal of Chemical Engineering of Japan*, vol. 14, no. 4, pp. 273-276.

Tans, P & Keeling, R 2014, 'Trends in atmospheric carbon dioxide', *NOAA/ESRL & Scripps Institute of Oceanography*.

Taylor, R, Berjoan, R & Coutures, J 1983, 'Solar gasification of carbonaceous materials', *Solar Energy*, vol. 30, no. 6, pp. 513-525.

Thurner, F & Mann, U 1981, 'Kinetic investigation of wood pyrolysis', *Industrial & Engineering Chemistry Process Design and Development*, vol. 20, no. 3, pp. 482-488.

Toomey, RD & Johnstone, H 1952, 'Gaseous fluidization of solid particles', *Chemical Engineering Progress*, vol. 48, pp. 220-226.

Trommer, D 2006, 'Thermodynamic and kinetic analyses of the solar thermal gasification of petroleum coke', PhD thesis, ETH Zurich.

Trommer, D, Noembrini, F, Fasciana, M, Rodriguez, D, Morales, A, Romero, M & Steinfeld, A 2005, 'Hydrogen production by steam-gasification of petroleum coke using concentrated solar power—I. Thermodynamic and kinetic analyses', *International Journal of Hydrogen Energy*, vol. 30, no. 6, pp. 605-618.

Ulloa, C, Gordon, AL & García, X 2004, 'Distribution of activation energy model applied to the rapid pyrolysis of coal blends', *Journal of Analytical and Applied Pyrolysis*, vol. 71, no. 2, pp. 465-483.

van Dijk, J-J, Hoffmann, A, Cheesman, D & Yates, J 1998, 'The influence of horizontal internal baffles on the flow pattern in dense fluidized beds by X-ray investigation', *Powder Technology*, vol. 98, no. 3, pp. 273-278.

van Eyk, P, Ashman, P & Nathan, G 2013, 'Mathematical modelling of a hybrid solar entrained-flow gasifier'.

Vermeir, S 2009, 'CFD analysis of a rotating fluidized bed in a static geometry', PhD thesis, Universiteit Gent.

von Zedtwitz, P, Lipiński, W & Steinfeld, A 2007, 'Numerical and experimental study of gas–particle radiative heat exchange in a fluidized-bed reactor for steam-gasification of coal', *Chemical Engineering Science*, vol. 62, no. 1, pp. 599-607.

von Zedtwitz, P & Steinfeld, A 2003, 'The solar thermal gasification of coal—energy conversion efficiency and CO 2 mitigation potential', *Energy*, vol. 28, no. 5, pp. 441-456.

von Zedtwitz, P & Steinfeld, A 2005, 'Steam-gasification of coal in a fluidized-bed/packed-bed reactor exposed to concentrated thermal radiation modeling and experimental validation', *Industrial & Engineering Chemistry Research*, vol. 44, no. 11, pp. 3852-3861.

Wang, FY & Bhatia, SK 2001, 'A generalised dynamic model for char particle gasification with structure evolution and peripheral fragmentation', *Chemical Engineering Science*, vol. 56, no. 12, pp. 3683-3697.

Watano, S, Imada, Y, Hamada, K, Wakamatsu, Y, Tanabe, Y, Dave, RN & Pfeffer, R 2003, 'Microgranulation of fine powders by a novel rotating fluidized bed granulator', *Powder Technology*, vol. 131, no. 2, pp. 250-255.

Welty, JR, Wicks, CE, Rorrer, G & Wilson, RE 2009, *Fundamentals of momentum, heat, and mass transfer*, John Wiley & Sons.

Wu, S & Narayanan, T 1988, *Commercial direct absorption receiver design studies*, Foster Wheeler Solar Development Corp., Livingston, NJ (USA).

Xu, Q 2013, 'Investigation of co-gasification characteristics of biomass and coal in fluidized bed gasifiers', PhD thesis, The University of Canterbury.

Xu, Q, Pang, S & Levi, T 2011, 'Reaction kinetics and producer gas compositions of steam gasification of coal and biomass blend chars, part 2: Mathematical modelling and model validation', *Chemical Engineering Science*, vol. 66, no. 10, pp. 2232-2240.

Yates, J 2013, *Fundamentals of Fluidized-Bed Chemical Processes*, Butterworth-Heinemann.

Yates, JG & Lettieri, P 2016, 'Fluidized-Bed Scaling', *Fluidized-Bed Reactors: Processes and Operating Conditions*, Springer, pp. 175-194.

Z'Graggen, A & Steinfeld, A 2008, 'Hydrogen production by steam-gasification of carbonaceous materials using concentrated solar energy–V. Reactor modeling, optimization, and scale-up', *International Journal of Hydrogen Energy*, vol. 33, no. 20, pp. 5484-5492.

Z'Graggen, A, Haueter, P, Maag, G, Romero, M & Steinfeld, A 2008, 'Hydrogen production by steam-gasification of carbonaceous materials using concentrated solar energy—IV. Reactor experimentation with vacuum residue', *International Journal of Hydrogen Energy*, vol. 33, no. 2, pp. 679-684.

Z'Graggen, A, Haueter, P, Maag, G, Vidal, A, Romero, M & Steinfeld, A 2007, 'Hydrogen production by steam-gasification of petroleum coke using concentrated solar power—III. Reactor experimentation with slurry feeding', *International Journal of Hydrogen Energy*, vol. 32, no. 8, pp. 992-996.

Z'Graggen, A, Haueter, P, Trommer, D, Romero, M, De Jesus, J & Steinfeld, A 2006, 'Hydrogen production by steam-gasification of petroleum coke using concentrated solar power—II Reactor design, testing, and modeling', *International Journal of Hydrogen Energy*, vol. 31, no. 6, pp. 797-811.